Sheldon S. Williamson

Energy Management Strategies for Electric and Plug-in Hybrid Electric Vehicles

Springer

Energy Management Strategies for Electric and Plug-in Hybrid Electric Vehicles

Sheldon S. Williamson

Energy Management Strategies for Electric and Plug-in Hybrid Electric Vehicles

Springer

Sheldon S. Williamson
Electrical and Computer Engineering
Concordia University
Montreal, QC
Canada

ISBN 978-1-4614-7710-5 ISBN 978-1-4614-7711-2 (eBook)
DOI 10.1007/978-1-4614-7711-2
Springer New York Heidelberg Dordrecht London

Library of Congress Control Number: 2013950369

Printed on acid-free paper

Springer is part of Springer Science+Business Media (www.springer.com)

To my dearest wife and loving family members

Preface

In the near future, transportation electrification will become a definite reality. Currently, auto manufacturers as well as transportation industry parts manufacturers are investing immensely on research and development in the areas of clean and efficient electricity production, electric energy storage systems, advanced power electronics, and motor drives. All major transportation industry sectors, such as on-road vehicles, railways/metros/tramways, airways, space, sea, as well as undersea vehicles are moving toward electric-intensive powertrain architectures. In addition, government agencies worldwide are depositing gigantic support into commercialization and adoption of sustainable electric and plug-in hybrid electric vehicle (EV/PHEV) usage.

In addition to the above incentives, renewable energy systems are becoming more popular for smart grid applications. Integration of pure renewables (solar photovoltaics and/or wind energy) with the existing AC grid and future EVs/PHEVs is becoming a popular trend. Pure renewables are also seen as a sole source of energy for charging the immense influx of EVs/PHEVs moving forward. Thus, such a simple all-sustainable approach will make future EV/PHEV battery charging infrastructures completely independent of the AC grid (and fossil fuel).

The book essentially aims at addressing the practical issues for commercialization of current and future EVs/PHEVs. The major book chapters focus principally on advanced power electronics and motor drives solutions for both current as well as future EV/PHEV drivetrains. EV/PHEV power system architectures are discussed in detail, highlighting component-level design particulars. Key EV/PHEV battery technologies are explained as well as corresponding on-board energy management issues are presented. Advanced power electronic converter topologies for current and future battery charging infrastructures are also discussed in detail. Finally, EV/PHEV battery interface with renewable energy as well as the AC grid is discussed in detail, with practical examples. Finally, the book also presents the reader with an idea of "*well-to-wheels*" efficiency analysis of all existing and future more electric drivetrain topologies.

This book is useful for engineers and researchers with entry-level knowledge of electric and plug-in hybrid electric vehicles. The book should also be of interest to university professors as well as graduate-level research students and practicing industry researchers.

Acknowledgments

I would like to express my sincere and heartfelt gratitude toward my wife, Smitha, for her constant encouragement and loving support. I would also like to express my appreciation toward my parents and family members, for their unending support and well wishes.

I would also like to express my sincere gratitude to my graduate student, Mr. Rabbani Basha. Without the help of Rabbani, the completion of this book would never be possible. I would also like to thank my graduate students; Ms. Florence Berthold, Mr. Giampaolo Carli, Mr. Pablo Cassani, and Mr. Arash Shafiei, from whose theses, much of the book contents are extracted. Due to their excellent work and dedication, the contents of this book could be maintained at a high quality.

Last, but not least, I would like to thank the Lord Almighty, for giving me the strength and courage, to bear all impediments that came in the way of completing this book successfully.

Contents

1 Introduction 1
1.1 Background 1
1.2 HEV Fundamentals 2
1.2.1 Concept of HEV 2
1.2.2 Working Principle of an HEV Drive Train 3
1.3 Simulation Platform: The Advanced Vehicle Simulator (ADVISOR) Software 4
References 5

2 Electric and Plug-in Hybrid Electric Vehicle Drive Train Topologies 7
2.1 Concept of Electric, Hybrid Electric and Plug-in Hybrid Electric Vehicles 7
2.1.1 Electric Vehicles 7
2.1.2 Hybrid Electric Vehicle 7
2.1.3 Plug-in Hybrid Electric Vehicle 8
2.2 Hybrid Electric Vehicle Drive Train Topologies 9
2.2.1 Basic HEV Drive Train Configurations 9
2.2.2 Current and Future HEV Topologies 10
2.3 Plug-in Hybrid Electric Vehicle Drive Train Topologies 11
2.4 All-Electric Vehicle Drive Train Topology 13
References 14

3 EV and PHEV Energy Storage Systems 15
3.1 Introduction 15
3.2 Batteries 15
3.2.1 Ideal Model 17
3.2.2 Linear Model 17
3.2.3 Thevenin Model 17
3.3 Electrical Modeling of Ultracapacitors 18
3.3.1 Double Layer UC Model 19
3.3.2 Battery/UC Hybrid Model 20
3.4 Electrical Modeling of Flywheel Energy Storage Systems 22

3.5 Operating Principle of a Fuel Cell 24
3.5.1 Detailed Electrical Modeling of Renewable Fuel Cell Power Sources 26
References 28

4 Hybrid Electric and Fuel Cell Hybrid Electric Vehicles 31
4.1 HEV Fundamentals and Concepts 31
4.1.1 Concept of HEV 31
4.1.2 Working Principle of an HEV Drive Train 32
4.2 Efficiencies of Series and Parallel HEV Drive Trains 33
4.2.1 Introduction 33
4.2.2 Component Stage Based Efficiency Analysis 34
4.3 Varied Driving Patterns and Regenerative Braking Efficiency Analysis 35
4.3.1 Introduction 35
4.3.2 Vehicle Specification and Modeling 36
4.3.3 Overall Efficiency Comparison Based on Varied Driving Patterns 38
4.4 Regenerative Braking Efficiency Analysis 41
4.5 Overall Electric Drive Train Efficiency Analysis 42
4.6 Fuel Cell HEV: Modelling and Control 44
4.6.1 Modeling Environment 44
4.6.2 Modeling and Selection of Power Components 45
4.6.3 Fuel Cell System 45
4.6.4 Battery System 46
4.6.5 Motor-Controller System 48
4.6.6 Baseline Vehicle 50
4.6.7 Summary 50
4.6.8 Control Fuel Cell HEV 51
4.7 Power Electronics Interface of Fuel Cell and Traction System 55
4.7.1 Introduction 55
4.7.2 Power Train Configuration 55
4.7.3 Power Component Modeling 57
4.8 Concept of Fuel Cell Plug-in HEV (FC-PHEV) 60
4.8.1 Fuel Cell-Hybrid Electric Vehicle Architecture 60
References 61

5 EV and PHEV Battery Technologies 65
5.1 Energy Storage Issues of PHEVs and EVs 65
5.1.1 Battery Chemistries 66
5.1.2 Battery Modeling and Simulation 70
5.1.3 Lithium-Ion Batteries 83
5.1.4 Characteristics of Lithium-Ion Batteries 84

5.1.5 Cycle Life Versus State of Charge 85
5.1.6 Solutions to Keys Issues 87
References 88

6 On-Board Power Electronic Battery Management 91
6.1 Battery Cell Voltage Equalization Problem 91
6.1.1 Introduction 91
6.2 Introduction to Classic and Advanced Battery Cell Voltage Equalizers 92
6.2.1 Resistive Equalizers 92
6.2.2 Capacitive Equalizers 92
6.2.3 Inductive Equalizers 93
6.2.4 Cuk Equalizer 94
6.2.5 Transformer-Based Equalizers 95
6.2.6 Novel Cell Voltage Equalizer 96
6.2.7 Summary 97
6.3 Economic Significance of Battery Cell Voltage Equalization 98
6.3.1 Introduction 98
6.3.2 Importance of Battery Cell Equalizers 99
6.3.3 PHEV/EV Cell Equalizers 100
6.3.4 Cost Analyses of Cell Equalizers 100
6.3.5 PHEV Economic and Financial Analysis 102
6.3.6 Summary 106
6.4 Design and Performance of a Novel Power Electronic Cell Equalizer 107
6.4.1 Introduction 107
6.4.2 Design Specifications 108
6.4.3 Circuit Analysis of the Proposed Cell Voltage Equalizer 109
6.4.4 Mathematical Model of the Proposed Cell Voltage Equalizer 113
6.4.5 Comparative Study Between Simulations and Experimental Results 116
6.4.6 Comparison Between Typical Equalizer And Prototype Experimental Results 121
6.4.7 Equalizer Chaining Method 123
6.4.8 Summary 124
6.5 Controller Design for Developed Cell Equalizer 124
6.5.1 Introduction 124
6.5.2 Controller Functions 125
6.5.3 Lithium-Ion Cell Electrical Model 126
6.5.4 VOC Determination 127
6.5.5 VOC Estimation Algorithm 128

6.5.6 Proposed Cell Equalizer Control Strategy 130
6.5.7 Proposed Cell Equalizer Controller Modeling 132
6.5.8 Cell Equalizer Control System Simplification 132
6.5.9 Mathematical Derivation of the Cell Equalizer Controller 135
6.5.10 Cell Equalizer Controller Stability Analysis in Frequency Domain 139
6.5.11 Cell Equalizer Controller Stability Verification in Time Domain 143
6.5.12 Proposed Novel Cell Equalizer Experimental Results 145
6.5.13 Comparison Between Theoretical and Experimental Results 146
6.5.14 Summary 148
References 149

7 EV and PHEV Battery Charging: Grid and Renewable Energy Interface 151
7.1 Introduction 151
7.2 Charging Regimes for Batteries 152
7.2.1 Battery Parameters 152
7.2.2 Charging Methods 154
7.2.3 Termination Methods 156
7.2.4 Charging Algorithm 158
7.3 Charging from Grid 160
7.3.1 Line Stability Issues 160
7.3.2 Inverter Distortion and DC Current Injection 161
7.3.3 Local Distribution Configuration 162
7.4 Charging from Renewable Energy Sources 162
7.4.1 Basic Aspects of Battery Charging from Photovoltaic Systems 162
7.4.2 PV Array Model 163
7.4.3 Control System Design 165
7.4.4 Simulation Results 170
7.4.5 Summary 171
7.5 Power Electronics for EV and PHEV Charging 172
7.5.1 Need of Power Electronics for PHEV Applications 172
7.5.2 Conventional Structures of PV Systems 173
7.5.3 Central Inverters 173
7.5.4 String Inverters 174
7.5.5 Module Integrated Inverters 174

7.6 Topologies for PV Inverters . . . 174
7.6.1 PV Inverters with DC-DC Converter and Isolation . . . 175
7.6.2 PV Inverters with DC-DC Converter and Without Isolation . . . 176
7.6.3 PV Inverters Without DC-DC Converter and with Isolation . . . 177
7.6.4 PV Inverters Without DC-DC Converters and Without Isolation . . . 177
7.6.5 Possible PV Interconnection Schemes . . . 178
7.6.6 Proposed Structure . . . 179
7.7 Power Converters Topology . . . 180
7.7.1 MPPT Stage . . . 181
7.7.2 Rectifier/Inverter Stage . . . 182
7.7.3 Charger Stage . . . 183
References . . . 183

8 Power Electronic Converter Topologies for EV/PHEV Charging . . . 187
8.1 Grid and Photovoltaic (PV) System for EV/PHEV Charging . . . 187
8.1.1 Introduction to Power Electronic Inverter Topologies . . . 187
8.1.2 Proposed Power Conversion Topologies . . . 188
8.1.3 The Z-Converter . . . 189
8.2 DC/DC Converters and DC/AC Inverters for Grid/PV Interconnection . . . 193
8.2.1 Design of the Isolating Bidirectional DC/DC Converter . . . 193
8.2.2 Calculation of the Turns Ratio . . . 196
8.2.3 Derivation of the Equivalent Average Circuit of the DC/DC Converter . . . 196
8.2.4 Design of the Z-Circuit: Capacitor . . . 197
8.2.5 Design of the Z-Circuit: Inductor . . . 198
8.2.6 AC Analysis of the Z-converter . . . 199
8.2.7 Comments . . . 200
8.2.8 Cost . . . 200
8.2.9 Reliability . . . 200
8.2.10 Dynamic Behavior, Interaction with PV Source, Interaction with Grid . . . 201
8.2.11 Design Flexibility . . . 201
8.3 Novel Integrated DC/AC/DC Converter for EV/PHEV Charging . . . 202

8.4 High Frequency Transformer-Based Isolated Charger Topology . . . 202
8.4.1 Background . . . 202
8.4.2 Isolation and DC-Link . . . 203
8.5 Component Design . . . 203
8.5.1 Isolation Transformer Turns Ratio Calculation . . . 203
8.5.2 DC-Link Filter . . . 203
8.5.3 Inverter Bridge and DC/DC Converter Power Devices . . . 204
8.6 Comments . . . 204
8.6.1 Cost . . . 204
8.6.2 Reliability . . . 205
8.6.3 Dynamic Behavior, Interaction with PV Source, Interaction with Grid . . . 205
8.6.4 Design Flexibility . . . 206
8.7 Transformer-Less Charger Topology . . . 206
8.7.1 Background . . . 206
8.7.2 Component Design . . . 208
8.8 Comments . . . 208
8.8.1 Cost . . . 208
8.8.2 Reliability . . . 209
8.8.3 Dynamic Behavior, Interaction with PV Source, Interaction with Grid . . . 210
8.8.4 Design Flexibility . . . 210
8.9 Modeling and Simulation Results of Test System . . . 210
8.9.1 The Z-converter . . . 210
8.9.2 System Without Battery (Scheme 1) . . . 211
8.9.3 System with Battery (Scheme 1) . . . 212
8.9.4 System with Battery (Scheme 2) . . . 214
8.9.5 IPV Ripple, PV Utilization Ratio, and MPPT . . . 215
8.9.6 Power Loss (Efficiency) . . . 219
8.9.7 Efficiency Results for Alternate Z-Converter-Based Topology . . . 224
8.10 Conclusion . . . 226
8.11 High Frequency Transformer-Isolated Topology with DC-Link . . . 226
8.12 Transformer-Less Topology . . . 227
8.12.1 Dynamic Behavior . . . 227
8.13 Efficiency . . . 227
References . . . 229

9 EVs and PHEVs for Smart Grid Applications . . . 231
9.1 Introduction . . . 231
9.2 Vehicle-to-Grid and Grid-to-Vehicle Issues . . . 231

9.3 Ancillary Services from V2G . . . 233
9.4 Vehicle-to-Home and Home-to-Vehicle Concept . . . 233
9.5 Interconnection Requirements . . . 233
9.5.1 Converter Losses Calculation . . . 233
9.5.2 Converter Topology . . . 236
9.6 Study Case . . . 238
9.6.1 Scenario . . . 238
9.6.2 Results . . . 239
9.7 Summary . . . 241
References . . . 242

10 EV and PHEV Well-to-Wheels Efficiency Analysis . . . 243
10.1 Interest in Well-to-Wheels Efficiency Analysis . . . 243
10.2 Theoretical Efficiency Calculations for Advanced Vehicular Drive Trains . . . 244
10.3 Simulation Setup for the Vehicle Under Study . . . 247
10.4 Overall Efficiency Analysis Based on Simulation Results of the HEV and FCV Drive Train Architectures . . . 247
10.5 Acceleration Performance and Well-to-Wheels Greenhouse Gas Emissions for HEV and ECV Drive Trains . . . 250
10.6 Prospective Future Work . . . 252
References . . . 253

Chapter 1
Introduction

1.1 Background

Conventional vehicles (CVs), which use petroleum as the only source of energy, represent a majority of the existing vehicles today. As shortage of petroleum is considered to be one of the most critical worldwide issues, costly fuel becomes a major challenge for CV users. Moreover, CVs emit greenhouse gases (GHG), thus making it harder to satisfy stringent environmental regulations. As one of the major elements of the world economy, the transportation industry plays an important role in daily life, which has effects on, but is not limited to, the worldwide environment, global GHG emissions, and recreation and lifestyle issues. Since the early 1900s, the rudimental model of modern transportation changed the world. It is well known that transportation is a petroleum-based human activity, which consumes approximately more than 21 % of the total energy usage. Since 1998, the usage of petroleum in transportation exceeded that compared to other industries. For example, as shown in Figs. 1.1 and 1.2, transportation consumes almost two-thirds of the petroleum used in North America, and similarly, in case of carbon dioxide emissions, the transportation sector contributes to more than half the total emissions. Moreover, assuming some developing countries will mature in the forthcoming decades, the overall vehicle population is expected to increase tremendously in the next 15–20 years, becoming five times larger than the current vehicle population [1–8]. Serious environmental issues have been brought to the attention of the community. In recent decades, automobile manufactures and researchers have focused their attention on developing an energy-wise, pollution free, and safe land vehicle. The electric vehicle (EV) is believed to be the ultimate category of advanced vehicle (AV). However, due to immature battery technology, the performance of an EV is greatly restrained by its equipped electric energy. Hence, at least for the next few years, hybrid electric vehicles (HEVs) present a practical alternative to the current vast number of CVs.

S. S. Williamson, *Energy Management Strategies for Electric and Plug-in Hybrid Electric Vehicles*, DOI: 10.1007/978-1-4614-7711-2_1,

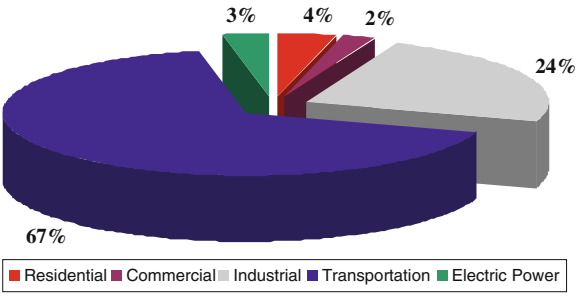

Fig. 1.1 Breakdown of oil usage by sector, 2006

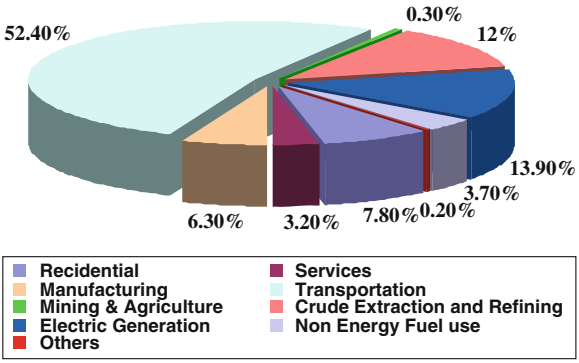

Fig. 1.2 Carbon dioxide emissions, 2006

1.2 HEV Fundamentals

1.2.1 Concept of HEV

Different types of alternate vehicles (AVs) exist, such as EVs, HEVs, and fuel cell vehicles (FCVs). However, HEVs are found to be the most practical and efficient substitutes for CVs in the near future. This is because the characteristics of an electric motor are found to be more favorable, compared to the characteristics of an internal combustion engine (ICE). Different combinations of energy sources exist, for example, electric and mechanical (fly-wheel) energy sources or electric and chemical (fuel cell) energy sources. However, the combination of fuel energy and electric energy sources is found to be the most acceptable, due to the combined usage of mature ICE techniques and well-established modern power electronics.

An HEV is defined as a vehicle whose propulsion energy is usually acquired from more than two types of energy sources, one of them being electric. In addition, an HEV electric drive train employs bidirectional power follow to recapture the heat losses occurring during braking events, which would otherwise be lost in case of a CV. The history of HEVs is surprisingly found to be as old as the automobile itself. However, the initial purpose of employing an electric motor was not to reduce fuel consumption, but to merely help the ICE propel the vehicle. More recently, the purposes of using hybrid drive trains are plentiful:

- To provide sufficient energy to satisfy the required driving range;
- To supply sufficient torque to meet the needs of vehicle performance;
- To achieve higher efficiency compared to CVs and to reduce fuel consumption and GHG emissions as much as possible.

1.2.2 Working Principle of an HEV Drive Train

As mentioned in the above section, the electric drive train of an HEV usually illustrates bidirectional power flow. Figure 1.3 depicts the concept and power flow of a typical HEV. As is clear, the HEV can choose a particular path, in order to combine power flows liberally, to meet the required load demands. The control strategy of an HEV can be designed for different purposes, based on the varied combinations of power flows.

As illustrated in the above figure, considering the drive train is a combination of fuel energy and electric energy, the HEV can work in the following pattern [9]:

- Fuel drive train propels the load alone;
- Electric drive train propels the load alone;
- Both fuel and electric drive trains propel the load at the same time;
- Electric drive train is being charged from load (regenerative braking);
- Electric drive train obtains power from fuel drive train (ICE charging battery);
- Electric drive train is charged by ICE and regenerative braking;
- ICE delivers power to electric drive train, to charge the battery, and propels the vehicle at the same time;
- Fuel drive train delivers power to electric drive train and the electric drive train propels the vehicle (series HEV);
- Fuel drive train propels the load, and load delivers power back to electric drive train.

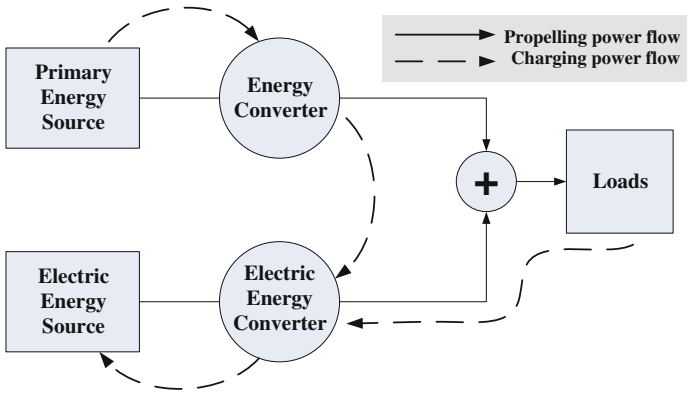

Fig. 1.3 Illustration of power flow within the hybrid drive train

This freedom of choosing a suitable combination of power flows creates enormous flexibility compared to a single drive train, which has been used so far in CVs. However, such an operational characteristic introduces an interesting series of efficiency issues, which entail properly designing the fuel drive train as well as the electric drive train. In essence, the most appropriate and favorable design of the overall system control strategy is of paramount importance.

1.3 Simulation Platform: The Advanced Vehicle Simulator (ADVISOR) Software

There are many existing software packages for modeling HEV drive trains. Most of these packages exist in the Matlab/Simulink environment with either forward or inverse dynamic solution capabilities. However, the Advanced Vehicle Simulator (ADVISOR) combines forward/backward modeling, which allows monitoring the performance of different drive train components, with fairly accurate dynamic solutions [10–12].

ADVISOR models the vehicle by integrating the physical architecture model and the drive train component model, as shown in Fig. 1.4. It is primarily used for the analysis of vehicles rather than vehicle design. The pre-summarized vehicle drive is used as a reference to calculate various outputs by analyzing other user-defined input variables, such as the motor size, fuel converter size, and accessory power.

Modeling is performed to accurately simulate the aerodynamic performance of the vehicle. Thus, the vehicle force can be estimated from the vehicle dynamic equation as shown in Eq. 1.1. It is clear that the vehicle dynamics involves the calculations of required traction as well as the wheel slip model. In order to find out the grade resistance, f_g, some important aerodynamic parameters such as vehicle mass, M_v, frontal area, coefficient of aerodynamic drag, and vehicle wheelbase need to be defined.

$$M_V \frac{\mathrm{d}V}{\mathrm{d}t} = \left(F_{\text{trac\_front}} + F_{\text{trac\_raer}}\right) - \left(f_{\text{resis\_front}} + f_w + f_g\right) \tag{1.1}$$

The required vehicle speed is predefined by the vehicle drive cycle. The dynamic equation of a conventional vehicle, thus, can be used as the basis for vehicle movement. $F_{\text{trac\_front}}$ and $F_{\text{trac\_rear}}$ are traction forces from the frontal and rear wheels, respectively. The terms $f_{\text{resis\_front}}$ and $f_{\text{resis\_rear}}$ are the rolling resistances of the front and rear tires, and f_w is the aerodynamic drag.

The overall modeling of an HEV drive train is a complicated process. In ADVISOR, the drive train components are modeled based on efficiency maps, whose data are pre-tested and saved in multi-dimensional tables. The modeling contains procedures, which include component testing, data acquisition, result analyses, and definition. Finally, the acquired data from tests are analyzed or described by mathematical formulation that can be recognized by the program.

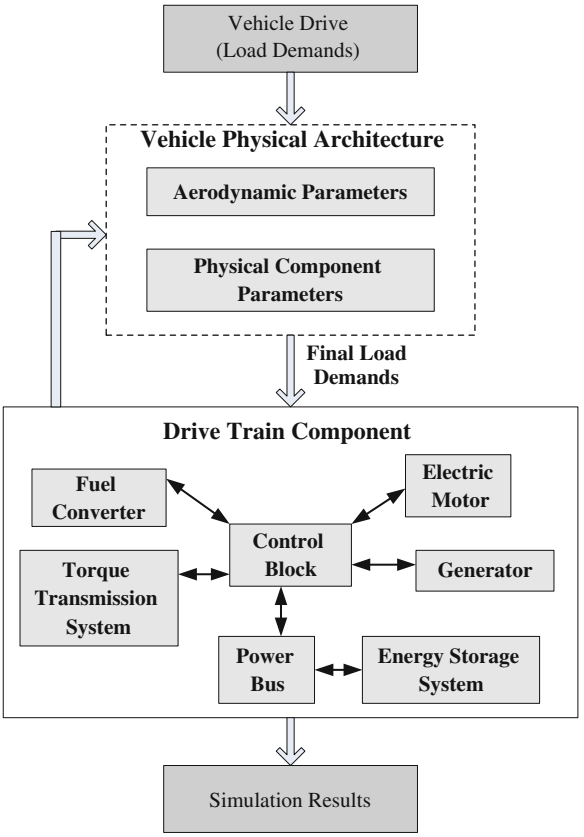

Fig. 1.4 Block diagram of simulation data flow

References

1. X. Li, S. S. Williamson, Assessment of efficiency improvement techniques for future power electronics intensive hybrid electric drive trains. in *Proceedings of IEEE Electrical Power Conference*, (Montreal, Canada, Oct. 2007) pp. 268–273
2. R.D. Strattan, The electrifying future of the hybrid automobile. IEEE Potentials **23**(3), 3–7 (2004)
3. C.C. Chan, An overview of electric vehicle technology. Proc. of the IEEE **81**(9), 1202–1213 (1993)
4. S. S. Williamson, A. Emadi, Fuel cell vehicles: opportunities and challenges. in *Proceedings of IEEE Power Engineering Society (PES) General Meeting*, vol. 2 (Denver, CO, June 2004), pp. 1640–1645
5. C.C. Chan, The state of the art of electric and hybrid vehicles. Proc. of the IEEE **90**(2), 247–275 (2002)
6. T.H. Ortmerey, P. Pillay, Trends in transportation sector technology energy usage and greenhouse gas emission. Proc. of the IEEE **89**(12), 1837–1847 (2001)
7. Annual energy review 2006, *Energy Information Administration*, (Washington DC, June 2007) DOE/EIA-0384 (2006)
8. M.J. Riezenman, Engineering the EV future. IEEE Spectr. **35**(11), 18–20 (1998)

9. M. Ehsani, Y. Gao, S.E. Gay, A. Emadi, *Modern electric, hybrid electric, and fuel cell vehicles: fundamentals, theory and design*, 1st edn. (CRC Press, Dec, 2004)
10. National Renewable Energy Laboratory (NREL), Advanced vehicle simulator (ADVISOR) documentation, http://www.ctts.nrel.gov/analysis/advisor_doc
11. A. Walker, A. McGordon, G. Hannis et al, A novel structure for comprehensive HEV powertrain modeling. in *Proceedings of IEEE Vehicle Power and Propulsion Conference*, (Windsor, UK, Sept. 2006)
12. J. Wu, A. Emadi, M. J. Duoba, T. P. Bohn, Plug-in hybrid electric vehicles: testing, simulations and analysis. in *Proceedings of IEEE Vehicle Power and Propulsion Conference*, (Arlington, TX, Sept. 2007)

Chapter 2
Electric and Plug-in Hybrid Electric Vehicle Drive Train Topologies

2.1 Concept of Electric, Hybrid Electric and Plug-in Hybrid Electric Vehicles

2.1.1 Electric Vehicles

Among all AFVs, electric vehicles (EVs) seems to be the future most viable vehicle option for reducing the rate of oil usage and improving air quality and less emission. Basically, driving an electric vehicle would feel very similar to drive a conventional car but it can be much quitter.

Electric vehicles stores electrical energy in their on board battery pack and then uses that energy to drive the vehicle. Electricity can be taken from either non renewable or renewable sources and stored in the battery pack. While driving, stored energy in battery can be used in an electric motor to run the wheels and move the car [1]. However, EVs have not had same support as HEVs because, EVs purely powered with electricity that supplied by the grid. Long charge time, limited drive range due to limited on board battery pack are concerns, that needs to be considered.

Different components such as, the battery pack, chargers, power electronic converters and electric motor technologies are vary in efficiency and costs. But with the modern and developed technology, these components have high efficiency and drive train efficiency of modern EVs can be up to 90 %. Schematic and theoretical back-of-envelope drive train efficiency of EV is shown in Fig. 2.1.

ADVISOR software, developed by National Renewable Energy Laboratory (NREL) or PSAT software, developed by Argonne National Laboratory can be used to calculate the VTW efficiency and emission of vehicles.

2.1.2 Hybrid Electric Vehicle

Compared to conventional vehicles, hybrid electric vehicles are more fuel efficient since they combine the advantage of an electric motor drive and the existing

S. S. Williamson, *Energy Management Strategies for Electric and Plug-in Hybrid Electric Vehicles*, DOI: 10.1007/978-1-4614-7711-2_2,

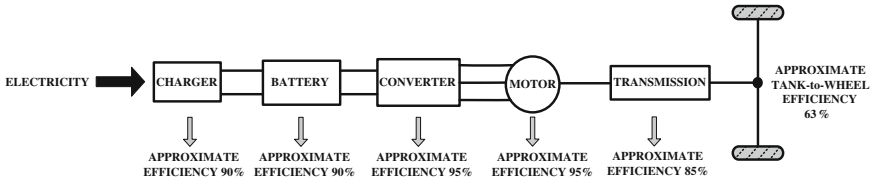

Fig. 2.1 Approximate calculation of theoretical drive train efficiency for EV, based on power component stage analysis

internal combustion engine (ICE) to propel the vehicle. With this arrangement, the ICE operation can be optimized and regenerative braking energy can be recovered, thereby significantly increasing the overall vehicle efficiency [2]. The HEV power train can be divided into three categories based on their configurations: series hybrids, parallel hybrids, and parallel-series combined hybrids.

2.1.3 Plug-in Hybrid Electric Vehicle

Recently, much of the automotive industry's research has been focused on Plug-in hybrid electric vehicles (PHEVs). PHEVs are hybrid electric vehicles that can draw and store energy from an electric grid (or a renewable energy source), to eventually propel the vehicle. The architecture of a typical PHEV is shown in Fig. 2.2.

This simple functional change allows a PHEV to displace petroleum with multi-source electrical energy, including renewable energy resources, such as wind and solar energy. Such a change has critical beneficial impacts on the overall transportation sector petroleum consumption, total emissions, as well as on the performance and makeup of the electrical grid. PHEVs are seen as one of the most promising means to improve the near-term sustainability of the transportation as well as stationary energy sectors. Surveys have shown that there exists a considerable market for PHEVs. *Renault* and *Daimler-Chrysler* have produced limited production PHEVs. *General Motors* and *Ford Motor Co.* have recently developed and displayed PHEV concept vehicles [3].

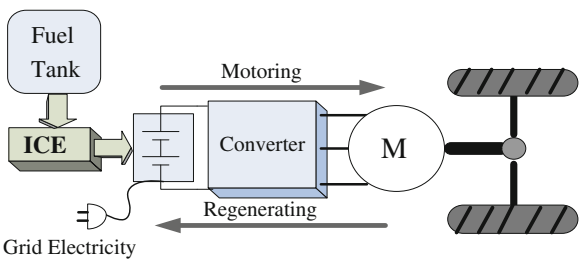

Fig. 2.2 Typical plug-in HEV drive train configuration

2.2 Hybrid Electric Vehicle Drive Train Topologies

2.2.1 Basic HEV Drive Train Configurations

As the name suggests, the propulsion energy of an HEV comes from more than two types of sources, and one of them must be an electric source. In addition, combining an electric motor with the internal combustion engine (ICE) is the most feasible means of realizing a hybrid topology, before the pure EV eventually becomes commercial. Based on different combinations of electric traction and mechanical traction, HEV drive trains are usually divided into three basic arrangements: series, parallel, and series–parallel combined hybrids, as shown in Fig. 2.3a, b and c, respectively [14].

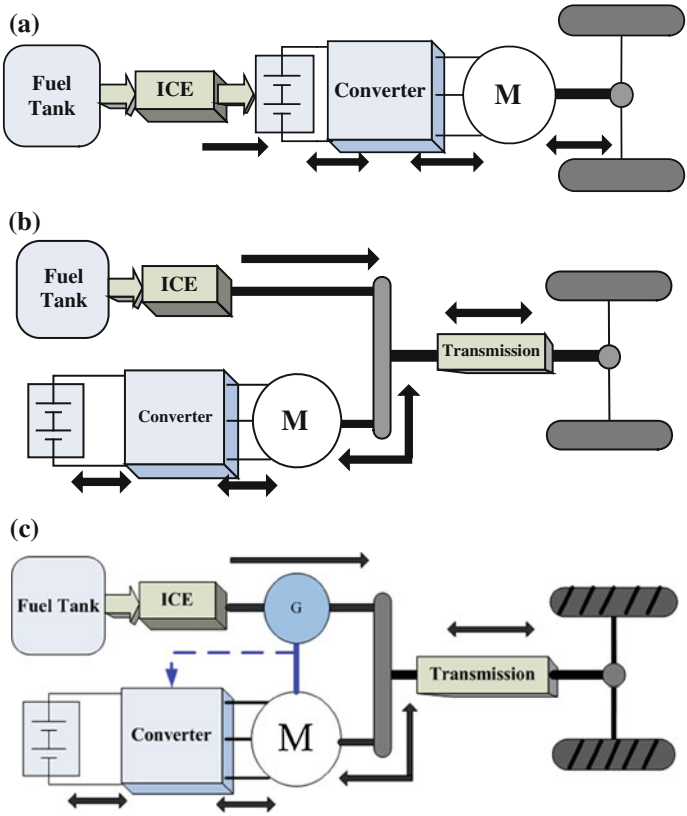

Fig. 2.3 Schematics of different types of HEV drive train configurations. **a** Series HEV drive train configuration. **b** Parallel HEV drive train configuration. **c** Series–parallel combined HEV drive train configuration

For the series HEV configuration, as shown in Fig. 2.3a, two different energy sources are combined in series. It is important to note here that the electric motor offers the only traction, making it an electric-intensive vehicle, which is more suitable for city driving. The ICE works at its optimal operation points as an on-board generator, maintaining the battery charge, by meeting the state of charge (SOC) requirements [15]. The overall efficiency of a series HEV is usually around 24 %, because of the low efficiency of the ICE and other technical constraints, such as battery capacity and drive train mass.

For the parallel HEV configuration, as is clear from Fig. 2.3b, the vehicle has two traction sources, both electric and mechanical. This type of configuration offers freedom to choose a combination of traction sources. By combining the two different traction sources, a smaller engine can be used. In addition, a parallel HEV arrangement requires a relatively smaller battery capacity compared to a series HEV, which results in the drive train mass to be lighter. Therefore, higher efficiency ranges, between 40 and 50 % are easily achieved [16–19]. It is a common notion that a higher overall efficiency for a parallel HEV drive train configuration is easily achieved. However, because of the electric-intensive structure of series HEVs, it is more suited for urban driving. On the other hand, parallel HEVs are more suited for highway driving.

Furthermore, by adding a mechanical unit between the generator and the electric motor, the series–parallel hybrid HEV combines the features of a series HEV as well as a parallel HEV, as shown in Fig. 2.3c. Although it has the advantages of both series and parallel configurations, it also has the drawbacks of these two configurations. In addition, the technical complexity of the general design and development of the combined HEV drive train and its precise control strategy is a major challenge.

It is possible to integrate more than two types of drive trains into one vehicle; however, an HEV drive train usually consists no more than two power trains. In fact, by integrating two drive trains into one vehicle, the complexity of the drive train design increases, and at the same time, the overall control strategy design becomes more difficult. This, in turn, increases the cost.

2.2.2 Current and Future HEV Topologies

Currently, keeping an environment friendly and a more efficient HEV in mind, any striking progress in the HEV industry is possible. From typical HEV drive train configurations to in-wheel motors, fuel economy improvements and GHG emission reductions are easily achievable. For example, in order to improve drive train efficiency, modified planetary gear systems have been successfully designed and tested, whereby the shaft is placed inside the motor, in order to avoid losses occurring during mechanical power transmission. Although such a trivial change might improve the drive train efficiency with less cost, research is constantly being done, in order to find innovative drive train configurations, which can integrate

overall features of completely making use of the motor power and reducing mechanical losses.

With the advent of the in-wheel motor technology, wherein the electric traction motor is constricted into the wheels, in order to reduce the energy lost in the transmission, HEV design and development is perceptibly moving towards a more efficient future [33]. However, for the in-wheel motor HEV design, some issues need to be taken care of. For example, to realize a 4 × 4 drive, four in-wheel motors will be needed, which would increase the overall drive train mass. Moreover, the synchronization of four, or even more motors, will introduce increased complexity of controller design and on-board power electronics.

2.3 Plug-in Hybrid Electric Vehicle Drive Train Topologies

a. **PHEV Power System** (Fig. 2.4)
b. **Extended Range Series PHEV Powertrain Layout** (Fig. 2.5)

PHEVs are sometimes called range-extended electric vehicles or extended range electric vehicles. They always have onboard gasoline or diesel that can be used to drive the vehicle for an extended distance, when the onboard battery energy is depleted and furthermore, these vehicles can provide high fuel economy during the extended driving range. The large battery pack can accept more regenerative braking energy and provide more flexibility for engine optimization during the extended driving range. The *Chevy Volt* is equipped with a full-sized electric motor so that pure electric driving can be realized for all kinds of driving conditions.

For example, the powertrain motor of a PHEV is rated at 125 kW, and the battery pack has a capacity of 16 kWh. This means that at full powertrain power, the battery needs to supply a power eight times its nominal capacity, or 8 C.

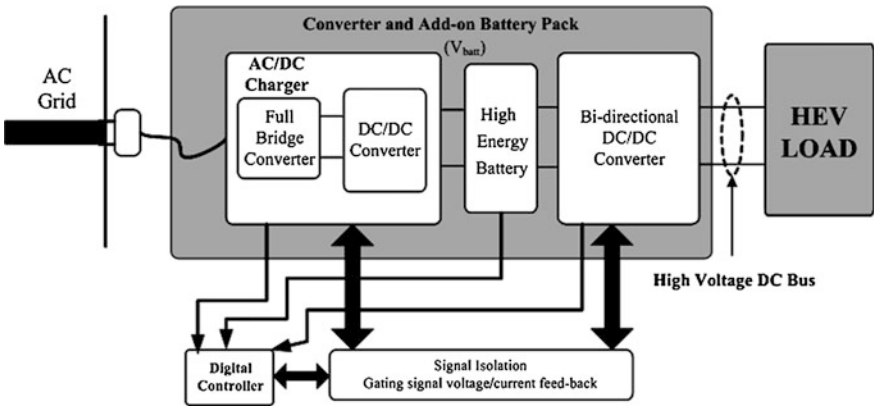

Fig. 2.4 Power System Schematic of a Plug-in HEV (PHEV)

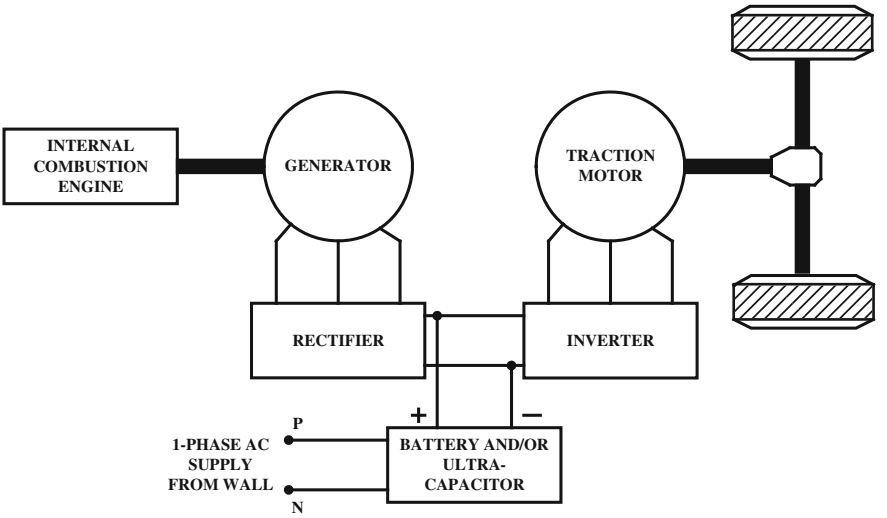

Fig. 2.5 Extended Range Series PHEV Powertrain Layout

This high power requirement not only is difficult to achieve, but also results in inevitable heavy losses inside the battery pack, which makes the drive system very inefficient.

c. **Blended PHEV Powertrain Layout** (Fig. 2.6)

Blended PHEVs have become more popular because of the reduced system cost (smaller electric motor, smaller battery pack, and lower battery power ratings).

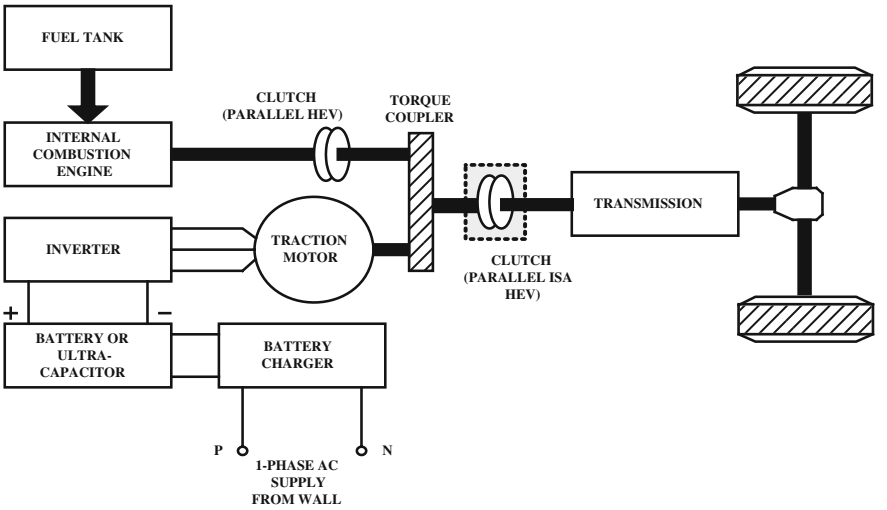

Fig. 2.6 Blended PHEV Powertrain Layout

They also possess the flexibility of optimizing fuel economy for different driving conditions. A blended PHEV usually uses a parallel or complex configuration, wherein the engine and the motor can both drive the wheels directly. Thus, the battery pack can be much smaller than the one in an extended range (series configuration) PHEV. Therefore, cost of the vehicle is comparatively much lesser.

For an extended range EV, the electric range can be easily calculated. For a blended PHEV, there may be no pure electric driving range available for some driving cycles.

To find the equivalent electric range, it is useful to compare the fuel economy of a blended mode PHEV during charge-depletion (CD) mode to that of a comparable HEV.

2.4 All-Electric Vehicle Drive Train Topology

A battery electric vehicle (BEV) is a type of electric vehicle (EV) that uses chemical energy stored in rechargeable battery packs. BEVs use electric motors and motor controllers instead of internal combustion engines (ICEs) for propulsion [11] Fig. 2.7.

Employing a battery alongside the UC, provides an attractive energy storage system, which offers numerous advantages. This is particularly due to the fact, that, the UC provides the necessary high power density, whereas, the battery provides the desired high energy density. Both, the battery and the UC provide power to the motor and power electronic DC/AC inverter during acceleration and overtaking, whereas, they receive power via regenerative braking during slow down/deceleration [12].

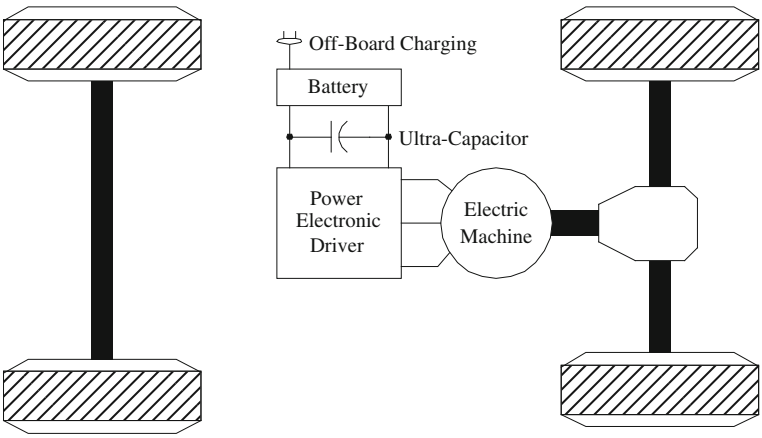

Fig. 2.7 All-electric Vehicle Drivetrain

References

1. Ian Steele, A comparison of ZEM vehicles in well to wheel efficiency, driving range, and fuelling http://cosmos.ucdavis.edu/archives/2009/cluster2/steele_ian.pdf
2. K.T. Chau, Y.S. Wong, Overview of power management in hybrid electric vehicles. Energy Convers. Manage. **43**(15), 1953–1968 (2002)
3. M. Ferdowsi, Plug-in hybrid vehicles—a vision for the future, in *Proceedings. IEEE Vehicle Power and Propulsion Conference*, Arlington, Sept 2007, pp. 457–462
4. H. Y. Cho, W. Gao, and H. Ginn,A new power control strategy for hybrid fuel cell vehicles, in *Proceedings. IEEE Workshop on Power Electronics in Transportation,* Detroit, Oct 2004, pp. 159–166
5. C. Liang and W. Qingnian, Energy management strategy and parametric design for fuel cell family sedan, in *Proceedings SAE Future Transportation Technology Conference and Exposition.*, Costa Mesa, Aug 2001, Paper No. 2001-01-2506
6. H. S. Ahn and N. S. Lee, Power distribution control law for FCHEV-A fuzzy logic-based approach, in *Proceedings IEEE International Conference on Control and Automation*, Budapest, June 2005, pp. 486–490
7. N. S. Lee, G. M. Jeong, and H. S. Ahn, Improvement of fuel economy using fuzzy logic-based power distribution control strategy for a FCHEV, vol. 1, in *Proccedings IEEE International Conference on Computational Intelligence and Security*, Guangzhou, Nov 2006, pp. 891–894
8. J. S. Lai and D. J. Nelson, Energy management power converters in hybrid electric and fuel cell vehicles, Proceedings of the IEEE, **95**(4),766–777, April 2007
9. G. Paganelli, Y. Guezennec, and G. Rizzoni, Optimizing control strategy for hybrid fuel cell vehicles, in *Proceedings SAE International Congress*, Detroit, March 2002, Paper No. 2002-01-0102
10. D. Wu and S. S. Williamson, Performance characterization and comparison of power control strategies for fuel cell based hybrid electric vehicles, in *Proceedings IEEE Vehicle Power and Propulsion Conference*, Arlington, Sept 2007, pp. 55–61
11. https://en.wikipedia.org/wiki/All-electric_vehicle#cite_ref-Leaf65K_1-0
12. X. Yan and D. Patterson, Improvement of Drive Range, Acceleration, and Deceleration Performance in an Electric Vehicle Propulsion System, vol. 2, in *Proceedings IEEE 30th Annual Power Electronic Specialists Conference*, Charleston, June 1999, pp. 638–643

Chapter 3
EV and PHEV Energy Storage Systems

3.1 Introduction

Through prior research results, it is well known, that, energy storage devices provide additional advantages to improve stability, power-quality, and reliability of the power-supply source. The major types of storage devices being considered nowadays, viz., batteries, ultracapacitors, and flywheel energy systems, will be presented in this chapter. It is empirical that precise storage device models are created and simulated for several applications, such as hybrid electric vehicles (HEV) and various power system applications.

The performances of batteries, ultracapacitors, and flywheels have, over the years, been predicted through many different mathematical models. Some of the important factors that need to be considered while modeling these energy storage devices include, storage capacity, rate of charge/discharge, temperature, and shelf life.

The electrical models of two of the most promising renewable energy sources, viz., fuel cells and PV cells, are also described in this chapter. They are recently being studied widely, as they do not produce much emission, and are considered to be environmentally friendly. However, these renewable energy sources are large, complex, and are expensive at the same time. Hence, designing and building new prototypes is a difficult and expensive affair. A suitable solution to overcome this problem is to carry out detailed simulations on accurately modeled devices. Through this chapter, the various types of equivalent electrical models for fuel cells and PV cells will be looked at and analyzed for suitability for operation at system levels.

3.2 Batteries

One of the biggest challenges in electric transportation is storing electrical energy for use in desired times and desired amounts. Batteries are mostly considered because of their high energy density compared to their counterparts and also their

S. S. Williamson, *Energy Management Strategies for Electric and Plug-in Hybrid Electric Vehicles*, DOI: 10.1007/978-1-4614-7711-2_3,

ability to get charged providing regenerative braking capability. The electrochemical nature of batteries has a highly nonlinear behavior and is dependent on many factors such as state-of-charge, state-of-health, runtime, temperature, aging, load profile, and charging algorithm. A very important concern is related to storage, because in order to have a given amount of energy for a reasonable All Electric Range (AER), tens or hundreds of cells should be connected in series and parallel for the desirable voltage and current ratings of the battery pack. This causes the nonlinear behavior of cells to be more prominent. Furthermore, there are some phenomena that are observed only in battery packs and not in single cells, such as thermal unbalance among the cells in pack.

EV and PHEV battery packs are relatively expensive compared to the price of the whole car, because of high number of cells, chemistry types such as Lithium-based, and protection circuits. Accordingly, the life cycle of these battery packs are very important from a cost-effective user's point of view. Therefore, lower cost for final customer can be achieved with increasing the battery pack life cycle, resulting in less frequent replacements of the whole pack. As a real example related to Honda Civic, recently, there has been news [7] about Honda Company regarding the battery packs of Honda Civics produced during 2006–2008. Apparently, some of the battery packs in the second-generation Honda Civic hybrids are failing prematurely after 5 years. According to regulations in California, there is a 10-year, 150,000-mile warranty requirement on the components of the hybrid system. Although Honda Company took recall actions, some customers were not satisfied and preferred to change themselves the battery packs. It has been reported that those battery packs cost about $2,000 excluding tax, shipping, and installation.

This case shows the importance of the battery pack′s price in the commercialization of EVs and PHEVs on a large scale. A factor that highly impacts the life cycle of battery packs is the charging algorithm. There are other factors also involved such as the charging time that plays an important role in high attraction to EVs and PHEVs. These topics and all other ones related to this area should be mainly handled with a multi-level control and power system called Battery Management System (BMS), which takes care of all or some of the aspects affecting batteries in any way. While charging the battery pack, BMS works in collaboration with the charger. Depending on the architecture of the system, BMS can be integrated to the charger. The more accurate and comprehensive the BMS is the more reliable, safer, and faster the charging procedure can be done. Designing a highly efficient BMS needs very good understanding of the behavior of single cells according to the variations of different parameters and also parameter variation and behavior change in a packed large number of cells [7].

Three basic types of battery models shall be presented, viz., the ideal model, linear model, and the Thevenin model. Lastly, a simple lead-acid battery model for traction applications that can be simulated in the PSpice software will also be presented.

3.2.1 Ideal Model

The ideal model of a battery basically ignores the internal parameters, and hence, is very simple. Figure 3.1 depicts an ideal model of a battery, wherein, it is clear that the model is primarily made up of only a voltage source [10].

3.2.2 Linear Model

This is, by far, the most commonly used battery model. As is clear from Fig. 3.1b, this model consists of an ideal battery with open-circuit voltage, Eo and an equivalent series resistance (ESR), Rs [4, 10]. "Vbatt" represents the terminal voltage of the battery. This terminal voltage can be obtained from the open-circuit tests, as well as from load tests, conducted on a fully charged battery [4].

Although this model is quite widely used, it still does not consider the varying characteristics of the internal impedance of the battery with the varying state of charge (SOC) and electrolyte concentration [4].

3.2.3 Thevenin Model

This model consists of electrical values of the open-circuit voltage (Eo), internal resistance (R), capacitance (C), and the overvoltage resistance (Ro) [4, 10]. As observed in Fig. 3.1c, capacitor C depicts the capacitance of the parallel plates and resistor Ro depicts the nonlinear resistance, offered by the plate to the electrolyte [4].

In this model, all the elements are assumed to be constants. But in actuality, they depend on the battery conditions. Thus, this model is also not the most accurate, but the most widely used. In this view, a new approach to evaluate batteries is introduced. The modified model is based on operation over a range of load combinations [11]. The electrical equivalent of the proposed model is as depicted in Fig. 3.2. As is clear from Fig. 3.2, the main circuit model consists of the following five sub-circuits:

(a) E_{batt}: This a simple DC voltage source, designating the voltage in the battery cells.
(b) E_{pol}: It represents the polarization effects, due to the availability of active material in the battery.
(c) E_{temp}: It represents the effect of temperature on the battery terminal voltage.
(d) R_{batt}: This is the battery's internal impedance, the value of which depends primarily on the relation between cell voltage and (SOC) of the battery [11].
(e) V_{sens}: This is basically a voltage source with a value of 0 V. It is used to record the value of battery current.

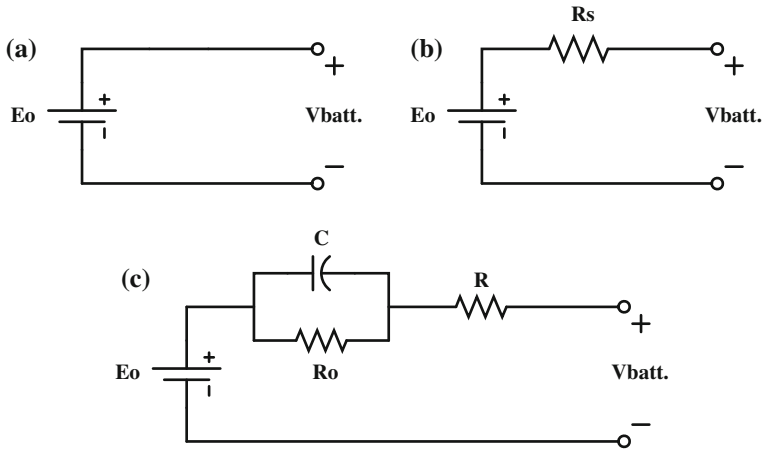

Fig. 3.1 Battery models **a** ideal model, **b** linear model, and **c** Thevenin model

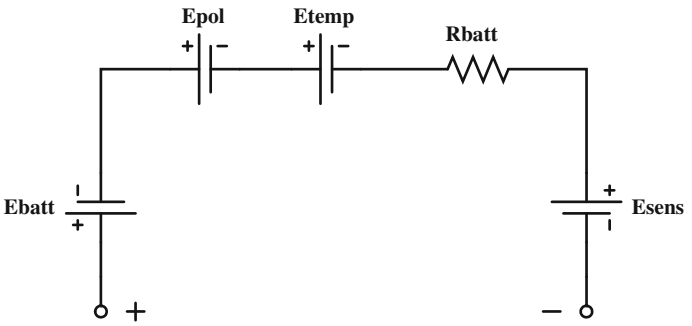

Fig. 3.2 Main circuit representation of modified battery model

Thus, this simulation model is capable of dealing with various modes of charge/discharge. It is comparatively more precise and can be extended for use with Ni–Cd and Li-ion batteries, which could be applied to (HEV) and other traction applications. Only a few modifications need to be carried out in order to vary the parameters, such as load state, current density, and temperature [11].

3.3 Electrical Modeling of Ultracapacitors

Ultracapacitors (UC) (also known as double-layer capacitors) work on the electrochemical phenomenon of very high capacitance/unit area, using an interface between electrode and electrolyte [2]. Typical values of such capacitors range from 400 to 800 F and have low values of resistivity (approximately 10^{-3} Ω cm)

[12, 15]. These UCs operate at high energy densities, which are commonly required for applications, such as space communications, digital cellular phones, electric vehicles (EV), and (HEV). In some cases, usage of a hybridized system, employing a battery alongside the UC, provides an attractive energy storage system, which offers numerous advantages. This is particularly due to the fact that, the UC provides the necessary high power density, whereas the battery provides the desired high energy density. Such a hybridized model will be covered here.

3.3.1 Double Layer UC Model

A simple electrical equivalent circuit of a double layer UC is as shown in Fig. 3.3. Its parameters include ESR, equivalent parallel resistance (EPR), and the overall capacitance. The ESR in Fig. 3.3 is important during charging/discharging, since it is a lossy parameter, which in turn causes the capacitor to heat up. On the other hand, the EPR has a leakage effect, and hence, it only affects the long-term storage performance [13]. For the purpose of simplification in calculations, the EPR parameter is dropped.

Furthermore, the dropping of the EPR parameter does not have any significant impact on the results. The circuit for analysis is, thus, simply an ideal capacitor in series with a resistance and the corresponding load [13]. Hence, the value of resistance can be written as

$$R = n_s \frac{\text{ESR}}{n_p} \tag{3.1}$$

Here, R is the overall resistance (Ω), n_s is the number of series capacitors in each string, and n_p is the number of parallel strings of capacitors. Furthermore, the value for the total capacitance can be expressed as

$$C = n_p \frac{C_{\text{rated}}}{n_s} \tag{3.2}$$

Here, C is the overall value of capacitance and C_{rated} is the capacitance of individual capacitor. This model can be used in conjunction with a DC/DC converter, which in turn acts as a constant power load, as shown in Fig. 3.4.

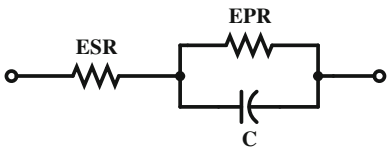

Fig. 3.3 Electrical equivalent circuit of an ultracapacitor (UC)

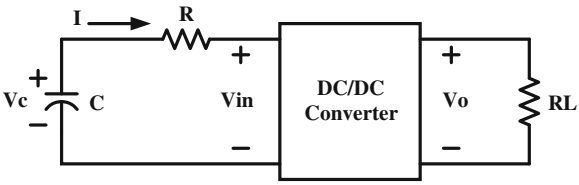

Fig. 3.4 Circuit showing UC connected to a constant power load

The capacitor bank can be used in stand-alone mode or can be operated in parallel with a battery of suitable size for the applications mentioned earlier. A brief description of such a hybrid model is described in the following section.

3.3.2 Battery/UC Hybrid Model

As stated earlier, combining a battery and an UC to operate in parallel makes for an attractive energy storage system with many advantages. Such a hybrid systems uses both, the high power density of the UC, as well as the high energy density of the battery. In this section, an electrical equivalent model of such a system will be presented, which can be used to evaluate its voltage behavior. The model is as depicted in Fig. 3.5.

The equivalent circuit of Fig. 3.5 shows an ESR (*Rc*) and a capacitor (*C*), as a model of the UC, whereas the Li-ion battery can be modeled simply by using a series resistance (*Rb*) and a battery. The values of *Rc* and *C* depend on the frequency, due to the porous nature of the electrodes of the UC [17]. When the pulse-width (T) is varied, the discharge rate of the UC can be varied, and can be shown to be equal to a frequency of $f = {}^{1}/_{T}$. The following equations can be written for Io and Vo from the equivalent circuit model of Fig. 3.3:

$$I_o = I_c + I_b \tag{3.3}$$

$$V_o = V_b - I_b R_b = \left[V_b - \frac{1}{C} \int_0^T I_c \cdot \mathrm{d}t \right] - I_c R_c \tag{3.4}$$

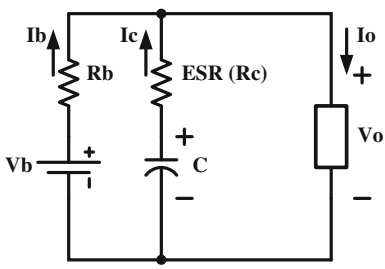

Fig. 3.5 Equivalent circuit model of a battery/UC hybrid system

Here, I_o and V_o are the output current and voltage delivered to the load respectively.

From the above two equations, it is possible to achieve a voltage drop $\Delta V = V_b - V_o$, due to a pulse current of I_o. This voltage drop can be finally expressed as

$$\Delta V = \frac{I_o R_b R_c}{R_b + R_c + \frac{T}{C}} + \frac{I_o R_b \frac{T}{C}}{R_b + R_c + \frac{T}{C}} \tag{3.5}$$

The currents delivered by the battery (I_b) and capacitor (I_c) can also be derived and their ratio can be expressed as

$$\frac{I_c}{I_b} = \frac{R_b}{R_c + \frac{T}{C}} \tag{3.6}$$

It can be seen that for a long pulse, I_c can be limited by the value of C. Furthermore, it can be concluded that during the pulsed discharge, about 40–50 % of the total current is delivered by C. Upon computer simulation of the equivalent circuit model, it is possible to study the fact that, during peak power demand, UC delivers energy to assist the battery, whereas during low power demand, UC receives energy from the battery [17].

Due to the advanced energy storage capabilities of the UC, it can be used for applications requiring repeated short bursts of power, such as in vehicular propulsion systems. In a typical scenario, both the battery and the UC provide power to the motor and power electronic DC/AC inverter during acceleration and overtaking, whereas they receive power via regenerative braking during slow down/deceleration [16]. Two most popular topologies for inserting batteries and UCs into drive trains are as shown in Fig. 3.6a and b.

As is clear in the topology of Fig. 3.6a, the UC bank is placed on the DC bus, whereas in Fig. 3.6b, the DC bus houses the battery. Amongst the two topologies, the one of Fig. 3.6a has a much more degraded energy efficiency, since the whole of the battery energy has to go through the DC/DC converter. Another drawback worth highlighting is that, a very high voltage UC bank is required, which is extremely expensive. Hence, more often than not, the topology of Fig. 3.6b is generally considered for HEV applications [16]. In a typical brushless DC (BLDC) motor driven electric vehicle (EV) propulsion system, a UC bank could be used to achieve a wider drive range, good acceleration/deceleration performance, and to lower the costs.

Future projections with regard to performance of UCs show that energy densities of as high as 10–20 Wh/kg are easily achievable using carbon electrode materials with specific capacitance values of nearly 150–200 F/gm [3]. Currently, extensive R&D on UCs is being carried out in the US, Canada, Europe, and Japan. As aforementioned, most of the research on UCs focuses on EV and HEV applications, as well as medical and power system applications.

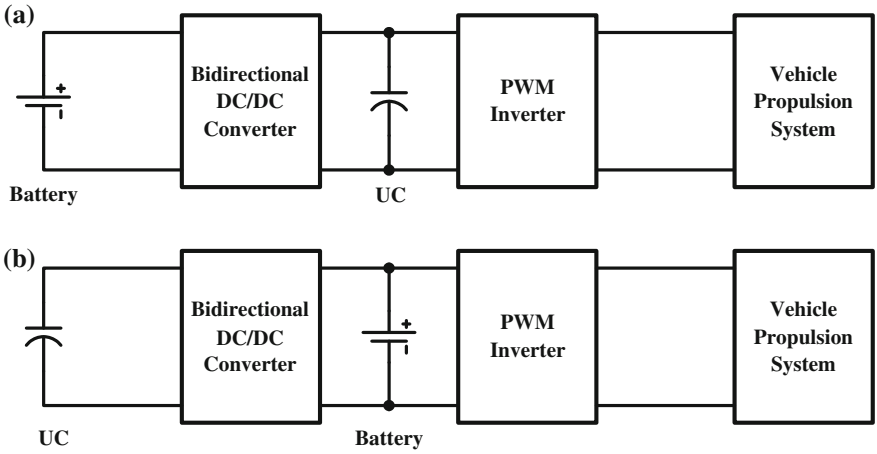

Fig. 3.6 Typical topologies of batteries and UCs in drive trains

3.4 Electrical Modeling of Flywheel Energy Storage Systems

It is a well-known fact that flywheels are most definitely finding numerous applications as energy storage devices in various power system configurations. Furthermore, the constant improvement in digital signal processing (DSP) and Microprocessor technologies, in conjunction with the recent development in magnetic material technology, makes this fact a distinct possibility. A flywheel energy storage system (FESS) is advantageous in a system, comprising other secondary storage devices, such as batteries, since it is capable of generating optimum charge/discharge profiles, for specific battery characteristics [1]. This fact facilitates the exploration of the benefits for optimizing battery management.

A rotating flywheel can store mechanical energy in the form of kinetic energy, based on its inertial properties. Essentially, an FESS consists of a rotor, a motor/generator system, and a suitable enclosure [12]. An example of an FESS, used as a voltage regulator, as well as UPS system, is as shown in Fig. 3.7 below.

The system of Fig. 3.7 essentially operates in three modes, viz., charging mode, voltage regulation mode, and UPS mode [15]. The motor/generator (M/G) set, as shown in Fig. 3.7, is required for energy storage purposes, in the form of the inertia of the rotor. At some suitable point in the operation of the system, it retrieves this stored energy, as demanded by the load. The M/G set is, thus, a high-speed device, which basically operates in the motoring mode, when charging the flywheel, and in the generating mode, when discharging it. The motor used for the M/G set could be a Brushless DC (BLDC) motor, of appropriate rating. The FESS can be easily simulated using the following equation:

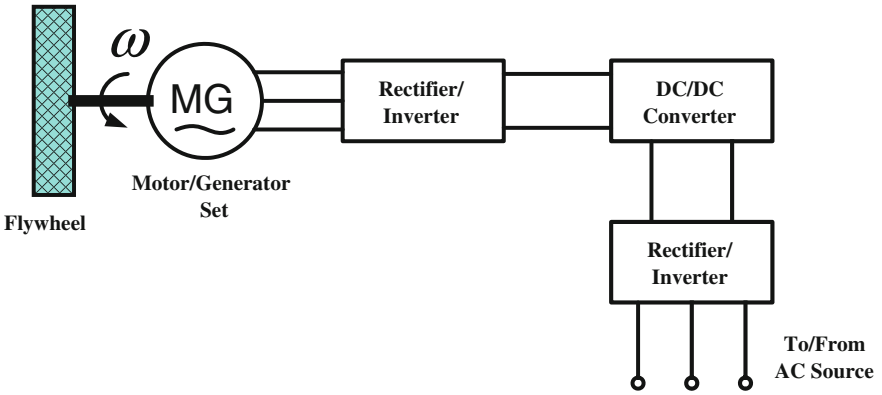

Fig. 3.7 Typical FESS employed as voltage regulator and UPS

$$V_x = R \times i_x + (L - M)\frac{\mathrm{d}i_x}{\mathrm{d}t} + E_x \tag{3.7}$$

Here, V_x, i_x, and E_x are the voltages, stator currents, and back EMFs for the three phases of the BLDC motor. Also, R, L, and M are the resistance, self-inductance, and mutual inductance of the stator winding [2]. The back EMF is directly proportional to the mechanical speed, ω_m, and the rotor angle, θ_r.

In order to electrically simulate the same FESS, operating in conjunction with power electronic intensive systems, it is essential to derive an equivalent electrical model of the same. For this purpose, it is critical to note the important mathematical equations that describe the above system. These are as shown below:

$$v = R \cdot i + L\frac{\mathrm{d}i}{\mathrm{d}t} + a\omega \tag{3.8}$$

$$T_{\mathrm{em}} = a \cdot i = J_r\frac{\mathrm{d}\omega}{\mathrm{d}t} + b\omega + T_L \tag{3.9}$$

$$T_L = J\frac{\mathrm{d}\omega}{\mathrm{d}t} \tag{3.10}$$

Here, v is the voltage across the motor terminals, i is the electric current through the motor, ω is the rotor speed, T_{em} is the electromagnetic torque imposed on the rotor, T_L is the mechanical torque imposed on the rotor by the flywheel, J_r is the equivalent moment of inertia of the rotor, J is the moment of inertia of the flywheel, and R and L are the armature resistance and self-inductance. Also, a indicates the ratio of the rated voltage of the motor to its rated speed, whereas b indicates the mechanical drag coefficient [8]. The electrical equivalent circuit, generated by combining the above three equations, is as depicted in Fig. 3.8.

It is essential to note that the circuit parameters used, are basically the parameters employed for the definition of the mathematical model of the FESS.

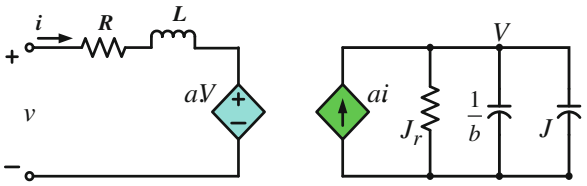

Fig. 3.8 Electrical equivalent circuit of a flywheel energy storage system

Thus, Fig. 3.6 describes the FESS system in its entirety via an electrical equivalent. Again, as aforementioned, the task of simulating an FESS with any electrical system becomes immensely simplified, since such an electrical model can be constructed in any popular electrical CAD simulation software, and can be appropriately analyzed.

3.5 Operating Principle of a Fuel Cell

The application of fuel cells in vehicles has been the focus of auto manufacturers in recent decades. In contrast to a chemical battery, the fuel cell generates electric energy rather than storing it, and continues to do so, as long a fuel supply is maintained. Today, the following five types of fuel cells are currently being developed: the alkaline fuel cell (AFC), the proton exchange membrane fuel cell (PEM), the phosphoric acid fuel cell (PAFC), the molten carbonate fuel cell (MCFC), and the solid oxide fuel cell (SOFC) [13]. The five types of fuel cells differ in terms of efficiency, operating temperatures, and input fuel requirements. Compared to other types of fuel cells, the PEM fuel cell is considered to be a prime candidate for use in automotive applications due to its higher power density (power per fuel cell active area) and lower operating temperature (around 80 °C) as well as faster start-up time (less than 1 min).

The basic operation of a PEM fuel cell is shown in Fig. 3.9 [14]. PEM fuel cells produce electricity via cell reactions, from the chemical energy stored in the fuel source. Separate gas flow channels provide for continuous fuel flow (typically hydrogen) to the anode and continuous oxidant flow (typically air) to the cathode. For automotive applications, hydrogen is provided either directly from on-board storage (direct hydrogen) or by on-board reforming of a hydrogen-bearing fuel. An electrolyte membrane separates the two electrodes. The products of the cell reaction are water, electrical power (electric current with a corresponding voltage), and thermal energy. Several cells are normally connected in series or parallel to form a fuel cell stack, in order to produce sufficient voltage for many practical applications.

The polarization curve is the most important characteristic of any fuel cell. Figures 3.10, 3.11, and 3.12 [6, 9] illustrate typical fuel cell polarization curves.

It can be noticed that, for a given current density, increasing cathode pressure or increasing fuel cell operating temperature generally results in higher voltage,

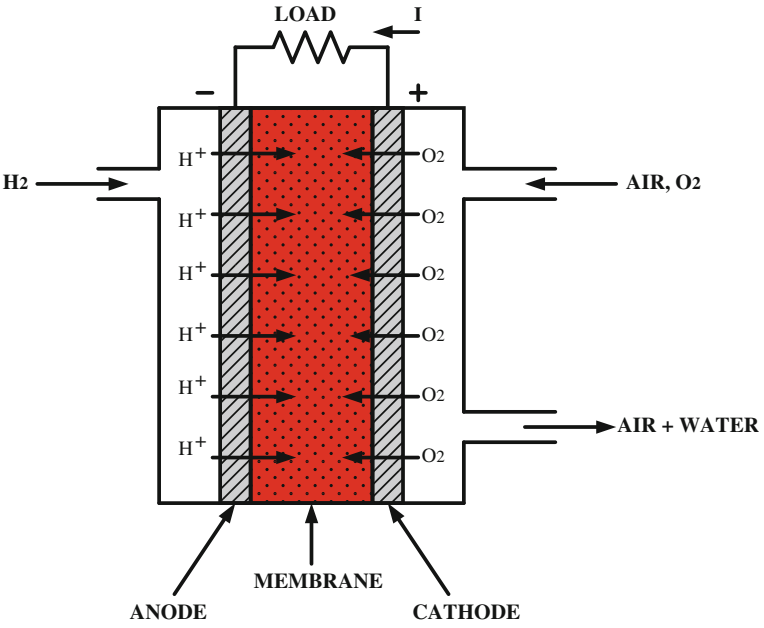

Fig. 3.9 Principle of operation of PEM fuel cells [14]

Fig. 3.10 Typical fuel cell stack I–V and power curve [3]

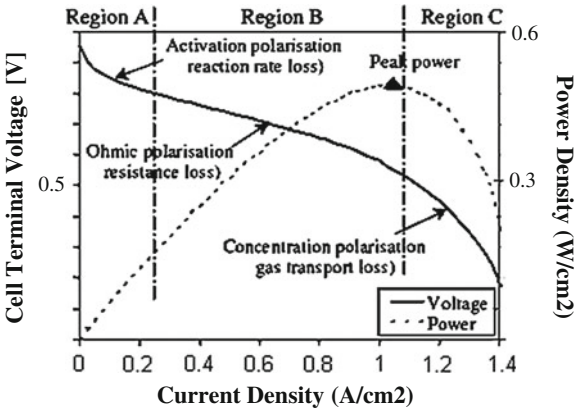

higher power density, and higher energy efficiency. Also, for a given set of conditions, voltage decreases with increasing current density. Furthermore, the power produced increases with increasing current density, until a current density is reached, at which maximum power output occurs.

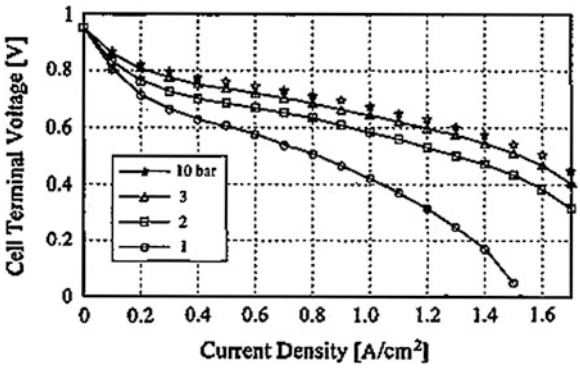

Fig. 3.11 Typical fuel cell polarization characteristics at stack pressure of [7, 8, 13, 17] bar at $T = 80$ °C [9]

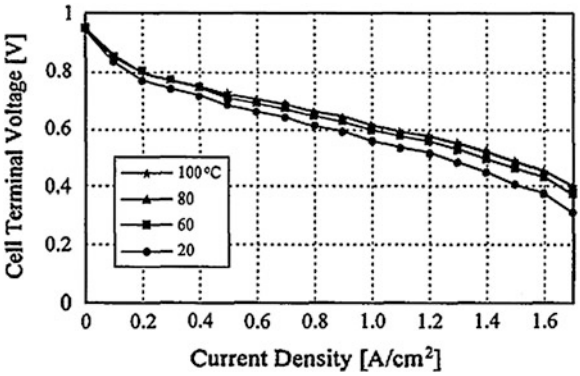

Fig. 3.12 Typical fuel cell polarization characteristics at varying temperatures at $P = 3$ bar

3.5.1 Detailed Electrical Modeling of Renewable Fuel Cell Power Sources

Over the past few years, great environmental concerns have been shown with respect to emissions from vehicles. These concerns, along with the recent developments in fuel cell technology, have made room for the hugely anticipated fuel cell market [5]. Fuel Cells are nowadays being considered for applications in (HEV), portable applications, as renewable power sources for distributed generation applications, and other similar areas, where the emission levels need to be kept to a minimum.

The proton exchange membrane (PEM) fuel cell has the potential of becoming the primary power source for HEVs, utilizing fuel cells. But, such fuel cell systems are large and complex, and hence, need accurate models to estimate the auxiliary power systems, required for use in the HEV. In this section, the fuel cell modeling techniques will be highlighted, thus avoiding the need to build huge and expensive prototypes. To have a clearer picture, refer to Fig. 3.13 showing the schematic representation of a fuel cell/battery hybrid power system.

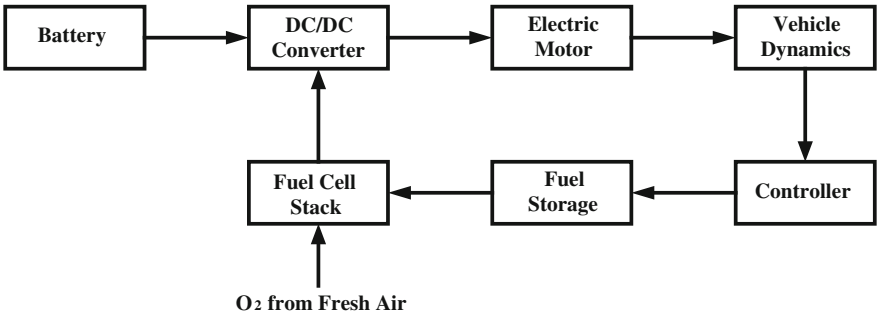

Fig. 3.13 Schematic representation of a fuel cell/battery hybrid power system

The battery pack in Fig. 3.13 is used to compensate for the slow start-up and transient response of the fuel processor [5]. Furthermore, the battery can also be used for the purpose of regenerative braking in the HEV.

As mentioned previously, since fuel cell systems are large, complex, and expensive, designing and building new prototypes are difficult [6, 9]. Hence, the feasible alternative is to model the system and examine it through simulations. The fuel cell power system consists of a reformer, a fuel cell stack, and a DC/DC (buck/boost) or DC/AC power converter. The final output from the power electronic converter is in the required DC or AC form, acquired from the low-voltage DC output from the fuel cell stack. An electrical equivalent model of a fuel cell power system is discussed here, which can be easily simulated using a computer simulation software.

In the electrical equivalent model, a first-order time-delay circuit with a relatively long time-constant can represent the fuel reformer. Similarly, the fuel cell stack can also be represented by a first-order time-delay circuit, but with a shorter time-constant [6].

Thus, the mathematical model of the reformer and stack are represented as

$$\frac{V_{cr}}{V_{in}} = \frac{\frac{1}{Cr \cdot S}}{Rr + \frac{1}{Cr \cdot S}} = \frac{1}{1 + RrCr \cdot S} \tag{3.11}$$

$$\frac{V_{cs}}{V_{cr}} = \frac{\frac{1}{Cs \cdot S}}{Rs + \frac{1}{Cs \cdot S}} = \frac{1}{1 + RsCs \cdot S} \tag{3.12}$$

Here, $RrCr = \tau r$ is the time-constant of the reformer, and $RsCs = \tau s$ is the time-constant of the fuel cell stack [3]. The equivalent circuit is as shown in Fig. 3.12.

By simulating the above equivalent circuit of Fig. 3.14, the system operation characteristics can be investigated. In order to achieve a fast system response, the DC/DC or DC/AC converter can utilize its short time-constant for control purposes. But, eventually, the fuel has to be controlled, despite its long time-delay [6]. The inputs to the chemical model of a fuel cell include mass flows of air (O2) and

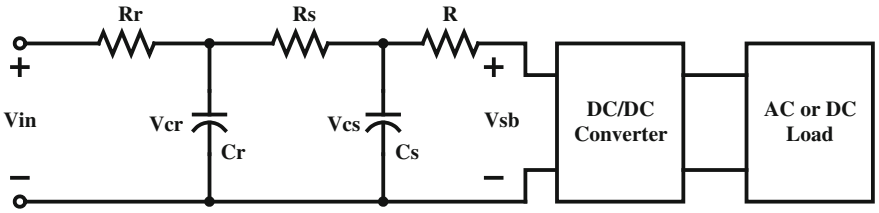

Fig. 3.14 Equivalent circuit model of a fuel cell power system

hydrogen (H2), cooling water, relative humidity of oxygen and hydrogen, and the load resistance. The outputs from the chemical model include temperature of the cell, power loss, internal resistance, heat output, efficiency, voltage, and total power output [9]. Generally, in case of excess of hydrogen supply, it is re-circulated in order to avoid any wastage.

References

1. B.G. Beaman, G.M. Rao, Hybrid battery and flywheel energy storage system for LEO spacecraft, in *Proceedings of IEEE 13th Annual Battery Conference on Applications and Advances*, Long Beach, Jan 1998, pp. 113–116
2. T. Boutot, L. Chang, D. Luke, A low speed flywheel system for wind energy conversion, vol. 1, in *Proceedings of IEEE Canadian Conference on Electrical and Computer Engineering*, Winnipeg, May 2002, pp. 251–256
3. A.F. Burke, Prospects for Ultracapacitors in electric and hybrid vehicles, in *Proceedings of IEEE 11th Annual Battery Conference on Applications and Advances*, Long Beach, Jan 1996, pp. 183–188
4. H.L. Chan, D. Sutanto, A new battery model for use with battery energy storage systems and electric vehicles power systems, vol. 1, in *Proceedings of IEEE Power Engineering Society Winter Meeting*, Singapore, Jan 2000, pp. 470–475
5. M. Ferdowsi, Plug-in hybrid vehicles—A vision for the future, in *Proceedings of IEEE Vehicle Power and Propulsion Conference*, Arlington, Sept 2007, pp. 457–462
6. J.H. Hirschenhofer, D.B. Stauffer, R. R. Engleman, M.G. Klett, *Fuel Cell Handbook*, 4th edn, DOE/FETC-99/1076
7. IEEE spectrum, Software Fix Extends Failing Batteries in 2006-2008 Honda Civic Hybrids: Is Cost Acceptable? (2011) http://spectrum.ieee.org/riskfactor/green-tech/advanced-cars/software-fix-extends-failing-batteries-in-20062008-honda-civic-hybrids-is-cost-acceptable. Accessed 23 August 2011
8. Z. Jiang, Flywheel Energy System Virtual Test Bed (VTB) Model, Available at http://vtb.engr.sc.edu/
9. K. Johansson, P. Alvfors, Steady-state model of a proton exchange membrane fuel cell system for automotive applications, in *Proceedings of International Conference on Efficiency, Costs, Optimization, Simulation, and Environmental Aspects of Energy and Process Systems*, Enschede, The Netherlands, July 2000, pp. 725–736
10. H. Kim, H-D. Ha, Design of interface circuits with electrical battery models, IEEE Trans. Ind. Electron, **44**(1), pp. 81–86, (1997)
11. J. Marcos, A. Lago, C. M. Penalver, J. Doval, A. Nogueira, C. Castro, J. Chamadoira, An approach to real behavior modeling for traction lead-acid batteries, vol. 2, in *Proceedings of*

IEEE 32nd Annual Power Electronic Specialists Conference, Vancouver, June 2001, pp. 620–624
12. L.J. Reinke, Tutorial Overview of Flywheel Energy Storage in a Photovoltaic Power Generation System, vol. 2, in *Proceedings of IEEE Canadian Conference on Electrical and Computer Engineering*, Vancouver, Sept 1993, pp. 1161–1164
13. R.L. Spyker, R.M. Nelms, Double layer capacitor/DC–DC converter system applied to constant power loads, vol. 1, in *Proceedings of IEEE 31st Intersociety Energy Conversion Engineering Conference*, Washington, Aug 1996, pp. 255–259
14. US DOE, *Energy Efficiency and Renewable Energy* (2008), Available at http://www.eere.energy.gov/hydrogenandfuelcells/fuelcells/fc_types.html. Accessed Jan 2008
15. R.S. Weissbach, G.G. Karady, R. G. Farmer, A combined uninterruptible power supply and dynamic voltage compensator using a flywheel energy storage system, IEEE Trans. Power Deliv. **16**(2), 265–270 (2001)
16. X. Yan, D. Patterson, Improvement of drive range, acceleration, and deceleration performance in an electric vehicle propulsion system, vol. 2, in *Proceedings of IEEE 30th Annual Power Electronic Specialists Conference*, Charleston, South Carolina, June 1999, pp. 638–643
17. J.P. Zheng, T.R. Jow, M.S. Ding, Hybrid power sources for pulsed current applications. IEEE Trans. Aerosp. Electron. Syst. **37**(1), 288–292 (2001)

Chapter 4
Hybrid Electric and Fuel Cell Hybrid Electric Vehicles

4.1 HEV Fundamentals and Concepts

4.1.1 Concept of HEV

Different types of alternate vehicles (AVs) exist, such as EVs, HEVs, and fuel cell vehicles (FCVs). However, HEVs are found to be the most practical and efficient substitutes for CVs in the near future. This is because the characteristics of an electric motor are found to be more favorable, compared to the characteristics of an internal combustion engine (ICE). Different combinations of energy sources exist, for example, electric and mechanical (fly-wheel) energy sources or electric and chemical (fuel cell) energy sources. However, the combination of fuel energy and electric energy sources is found to be the most acceptable, due to the combined usage of mature ICE techniques and well-established modern power electronics.

An HEV is defined as a vehicle whose propulsion energy is usually acquired from more than 2 types of energy sources, one of them being electric. In addition, an HEV electric drive train employs bidirectional power follow to re-capture the heat losses occurring during braking events, which would otherwise be lost in case of a CV. The history of HEVs is surprisingly found to be as old as the automobile itself. However, the initial purpose of employing an electric motor was not to reduce fuel consumption, but to merely help the ICE propel the vehicle. More recently, the purpose of using hybrid drive trains are plentiful:

- To provide sufficient energy to satisfy the required driving range;
- To supply sufficient torque to meet the needs of vehicle performance;
- To achieve higher efficiency compared to CVs and to reduce fuel consumption and GHG emissions as much as possible.

S. S. Williamson, *Energy Management Strategies for Electric and Plug-in Hybrid Electric Vehicles*, DOI: 10.1007/978-1-4614-7711-2_4,

4.1.2 Working Principle of an HEV Drive Train

As mentioned in the above section, the electric drive train of an HEV usually illustrates bidirectional power flow. Fig. 4.1 depicts the concept and power flow of a typical HEV. As is clear, the HEV can choose a particular path, in order to combine power flows liberally, to meet the required load demands. The control strategy of an HEV can be designed for different purposes, based on the varied combinations of power flows.

As illustrated in the above figure, considering the drive train is a combination of fuel energy and electric energy, the HEV can work in the following pattern [1]:

- Fuel drive train propels the load alone;
- Electric drive train propels the load alone;
- Both fuel and electric drive trains propel the load at the same time;
- Electric drive train is being charged from load (regenerative braking);
- Electric drive train obtains power from fuel drive train (ICE charging battery);
- Electric drive train is charged by ICE and regenerative braking;
- ICE delivers power to electric drive train, to charge the battery, and propels the vehicle at the same time;
- Fuel drive train deliver power to electric drive train and the electric drive train propels the vehicle (series HEV);
- Fuel drive train propels the load, and load delivers power back to electric drive train.

This freedom of choosing a suitable combination of power flows creates enormous flexibility compared to a single drive train, which has been used so far in CVs. However, such an operational characteristic introduces an interesting series of efficiency issues, which entail properly designing the fuel drive train as well as

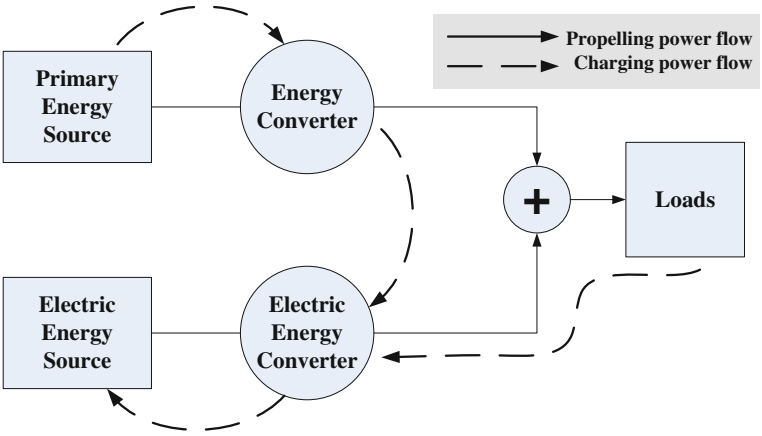

Fig. 4.1 Illustration of power flow within the hybrid drive train

the electric drive train. In essence, the most appropriate and favourable design of the overall system control strategy is of paramount importance.

4.2 Efficiencies of Series and Parallel HEV Drive Trains

4.2.1 Introduction

In order to assess, analyze, and cross-compare efficiencies of HEVs, a true drive train analysis needs to be executed. Generally, the drive train efficiency can be simply yielded out by calculating the losses at each power stage in a series or parallel drive train structure. However, the power component stage-based analysis is a practically deficient method. In order to have a fair efficiency comparison, some parameters that directly affect fuel consumption, such as drive train mass and control strategy should be taken into consideration. This chapter aims at modeling both the series and parallel HEV drive trains, and computing their definite drive train efficiencies, which can be used as a comparative scale for various other HEV topologies. The ADVISOR software is used for modeling, simulation, and parametric analysis of series and parallel HEV drive trains.

In recent years, research results state that vehicle drive train efficiency is considered as an accepted measurement to evaluate and analyse the fuel economy among different types of HEV [2–4]. There exist two popular approaches to calculate drive train efficiencies. One of the methods focuses on the losses occurring at individual drive train components. This loss-oriented analysis is termed as power component stage based analysis. On the other hand, few other analyses concentrate on the influence of critical drive train parameters, such as vehicle mass (glider weight), control strategy, and drive train mass, on the overall fuel economy. These comprehensive analyses are imperative, in order to perform accurate advanced vehicle research, and present a fair comparison between different types of HEVs.

In this chapter, efficiency studies are carried out based on series and parallel HEVs. In order to meet the needs for the required torque, series HEVs usually employ a relatively powerful on-board battery pack and electric motor, which tends to increase the overall drive train mass. However, such an electric-intensive structure liberates the ICE, and allows it to operate at its optimal efficiency points, as an on-board generator. The parallel HEV configuration combines the electric traction with the combustion traction; therefore, the system has the freedom to choose the appropriate propulsion system combination, in order to achieve best efficiency as well as satisfy the load requirement.

This chapter analyzes and compares the drive train efficiencies of series and parallel HEVs by using two different concepts; power component stage based analysis and parametric analysis. Thus, the drive train efficiencies for series and parallel HEV arrangements are fully analyzed and contrasted from the overall efficiency and system performance standpoint.

4.2.2 Component Stage Based Efficiency Analysis

As the name suggests, the power component stage-based drive train efficiency calculation is based on the number of power component stages in a particular drive train. As depicted in Figs. 4.2 and 4.3, the dark arrows indicate the direction of power flow transmitted along the drive train. Bidirectional arrows stand for two power component stages; therefore, there are six power component stages for a series HEV drive train and nine stages for a parallel HEV drive train.

For a commercially available battery and power electronic converter, the maximum efficiency is typically around 80 % each [5–7]. The approximate

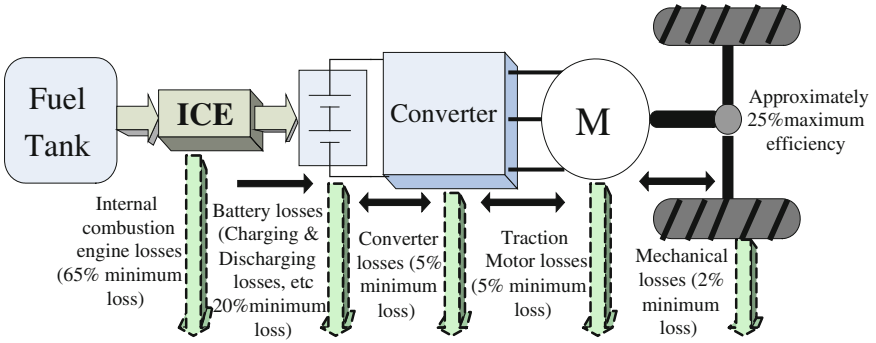

Fig. 4.2 Approximate calculation of maximum theoretical drive train efficiency for series HEVs based on power component stage analysis

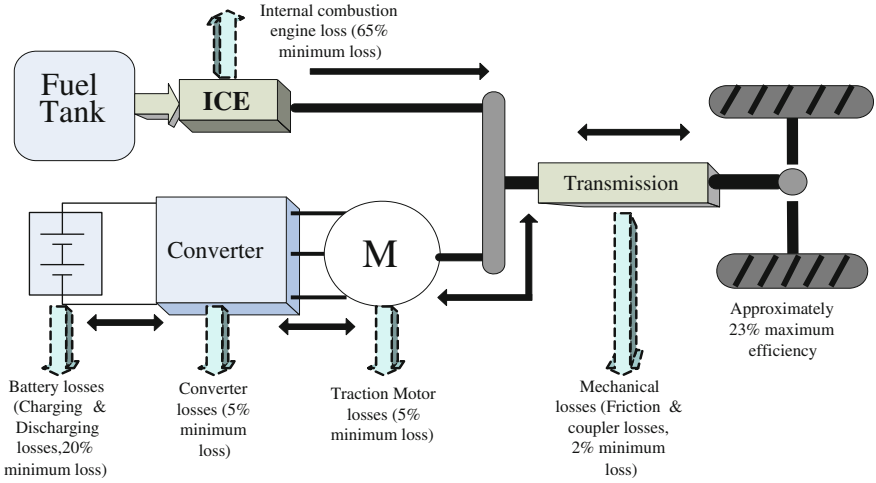

Fig. 4.3 Approximate calculation of maximum theoretical drive train efficiency for parallel HEVs based on power component stage analysis

maximum theoretical drive train efficiency for a typical series HEV is about 25 %, which is yielded out by simply multiplying the efficiencies of the corresponding power component stages. Fig. 4.2 shows the losses occurring at each stage of a parallel HEV drive train.

In order to compare the efficiencies of two different HEV configurations, all the power components used in the representative parallel HEV are assumed to be the same as those used in the series configuration. Considering there are two independent power flow channels (via electric traction and via mechanical traction) for the parallel configuration, the calculated drive train efficiency can be theoretically multiplied by a factor of 2. Thus, based on the power component stage analysis, the approximate maximum theoretical drive train efficiency for a representative parallel HEV is around 45 %.

4.3 Varied Driving Patterns and Regenerative Braking Efficiency Analysis

4.3.1 Introduction

It is a well-understood fact that power electronic converters and electric propulsion motors are extremely critical for every HEV system. It is essential that the traction motor must meet demands of varied driving schedules, and at the same time, it should run at its most optimal operating points to achieve higher drive train efficiency. Therefore, modeling the motor-inverter losses/efficiencies over typical city and highway driving schedules is the key to observe and analyze practical drive train efficiency and vehicle performance.

Currently, land vehicles are transiting from pure gasoline-fuelled to gasoline-electric combined HEV. In fact, there exist about 1,500,000 satisfied HEV users around the world. This number is constantly increasing, based on a yearly rate of roughly about 40 %. A major increase is noticeable in light-duty hybrids, such as passenger cars and SUVs [8, 9]. Majority of these vehicles are used for personal transportation, typically driven in the urban area or on a highway. Therefore, HEVs are not just run in particular routes, but in varied driving patterns. As a complex system, the automobile features vast mobility and variation. It is hard to measure its efficiency by using a simple measurement [10]. Thus, well-rounded measurements, such as well-to-wheel efficiency and tank-to-wheel (drive-train) efficiency are employed to fairly evaluate its efficiency.

However, it is a fact that HEVs cannot be optimally designed for all driving patterns. Various control parameters and efficiency data over particular driving schedules are required to optimize the control strategies for HEVs. Fortunately, because of commuters' regular routes, most of the driving patterns are predictable. In addition, automobile manufactures are tending to design HEVs that can use the electric propulsion motor over all range of load demands. Thus, a motor with high

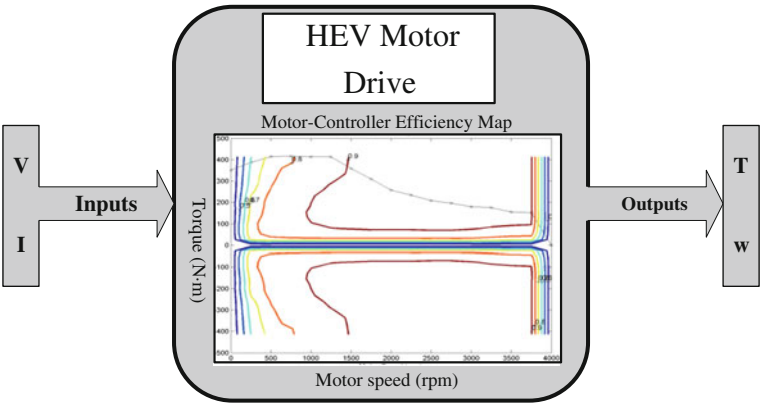

Fig. 4.4 HEV motor drive efficiency modeling concept based on operating efficiency maps

torque density, high efficiency, excellent controllability, and accuracy is needed. Therefore, the efficiency of traction motor-inverter drive system needs to be specifically studied and analysed on the basis of varied load demands [11].

Keeping the above-mentioned constraints in mind, the major focal point of this chapter is to model the traction inverter and motor losses/efficiencies over typical driving patterns. Efficiency maps are usually used to describe total efficiency of traction motors with respect to certain speed/torque combinations. The overall HEV drive train efficiencies are determined by the resultant traction motor-controller efficiency maps during simulation. Consequently, by using efficiency maps, an HEV motor drive can be represented as a "black box" that provides a known output when certain input is applied. The modeling concept is shown in Fig. 4.4. Thus, the traction motor can be studied at all possible torque/speed combinations within the motor's operating envelope by analyzing its operating efficiency.

In this chapter, optimal control strategies are used for parallel HEVs, based on the UDDS driving pattern, which generally represents an average urban driving model. Based on the simulation results, a comparative analysis is carried out for 6 selected different driving patterns, which show varying results in terms of overall drive train efficiency, vehicle performances, and overall emissions.

4.3.2 Vehicle Specification and Modeling

In this chapter, a typical mid-sized SUV is selected to represent the most popular vehicle in the market. The major dimensions and weights of the tested SUV chassis are summarized and revised for simulation purpose based on current commercially available SUVs. The physical parameters of the tested SUV are shown in Table 4.1.

Table 4.1 Physical parameters of tested parallel hybrid SUV

Parameters	Value
Dimensions	
Coefficient of drag	0.34
Frontal area (m^2)	3.15
Wheelbase (m)	2.72
Overall length (m)	4.71
Vehicle mass	
Vehicle weights (kg)	2,701
Cargo weight (kg)	156

As aforementioned, a parallel HEV drive train configuration is chosen for simulation purposes. Parallel HEV drive train configuration in Fig 2.1b shows the block diagram of the modeled parallel SUV. It is clear that a parallel HEV structure is a combined traction source arrangement [12, 13]. Thus, the hybridization factor (HF), which is defined as the ratio of the total electric power to the total propulsion power, plays an important role in the overall efficiency.

The fuzzy logic drive train control strategy is selected for simulation purpose and it is optimized based on UDDS, by adjusting its SOC and HF to have better city-driving efficiency. The tested drive train components were optimized by using the auto-size routine, which employs a bisection method to optimize the component size, based on the required vehicle performance. For the simulated parallel SUV, first the entire energy storage system size is minimized, and then its minimum fuel converter (FC) size is determined, according to the vehicle performance criteria. Finally, the FC size is fixed by a suitable HF, based on the following equation.

$$fc\_pwr = fc\_pwr\_\min + HF * (fc\_pwr\_\max - fc\_pwr\_\min) \tag{4.1}$$

Here, fc_pwr = new fuel converter size; $\min\_fc\_pwr$ = required minimum fuel converter size to meet the vehicle performance; $\max\_fc\_pwr$ = required maximum fuel converter size to meet the vehicle performance; HF = hybridization factor.

Once the FC size has been determined, the routine resizes the energy storage once again, to meet the acceleration requirements. The UDDS driving pattern, which is equivalent to the first 2 cycles of the Federal Test Procedure (FTP-75) driving schedule, represents general city driving conditions. Thus, UDDS is selected as a reference, for optimizing the drive train components [14]. The optimized drive train components are listed in Table 4.2.

The selected drive train was tested over 6 different driving schedules, which include 3 stop-and-go type low-speed driving patterns and 3 high-speed driving patterns. The driving patterns include the West Virginia Suburban (WVU-SUB), the Urban Dynamometer Driving Schedule (FUDS), 10–15 Japan driving schedule, the Highway Fuel Economy Test (HWFET), US06 Highway Driving Schedule (US06 HWY), and the Extra-Urban Drive Cycle (EUDC) [15]. The

Table 4.2 Summary of parallel HEV drive train components

Parameters	Value
Fuel converter	
Max. power	17kw @ 4,000 rpm
Max. torque	45Nm @ 4,000 rpm
Fuel converter mass	70 kg
Battery (Nickel-Metal Hydride)	
Single module voltage	12 V
Number of modules	25 modules
Nominal capacity	60 Ah
Peak power (10 s pulse @ 50 % DOD @ 35 deg. C)	4.9 kW
Mass	290 kg
Motor-controller (PM)	
Continuous power	48 kW
Peak torque	370 Nm
Motor-controller mass	58 kg
Maximum speed	4000 rpm

speed profile versus time for each of the above-mentioned 6 driving schedules and their detailed characteristics are summarized in Fig. 4.2 and Table 4.3, respectively.

The modeled mid-sized hybrid SUV is simulated over 3 reiterations of each driving schedule. The overall efficiency and vehicle performance will be compared in the ensuing sections, which are directly influenced by the different driving patterns.

4.3.3 Overall Efficiency Comparison Based on Varied Driving Patterns

As aforementioned, the ADVISOR software is used in order to determine the overall efficiency based on above-mentioned driving schedules. The comparative overall efficiencies of different driving schedules are shown in Fig. 4.6.

As explained earlier, a parallel HEV is the combination of different traction sources, and hence, the system has the freedom to choose the suitable propulsion

Table 4.3 Summary of the 6 different driving schedules

Driving Schedule	Dist. (miles)	Stops	Max. Spd. (mph)	Ave. Spd. (mph)	Max. Accel. (ft/s^2)
UDDS	7.45	17	56.7	19.58	4.84
WVU-SUB	7.44	9	44.8	16.7	4.25
10–15 Japan	2.61	14	43.96	14.24	3.89
HWFET	10.26	1	59.9	48.2	4.69
US06 HWY	6.24	1	80.3	60.84	10.12
EUDC	4.32	1	74.56	38.8	3.46

system combination. For city driving, the number of stops and starts is 10 times more than that in case of highway driving. Thus, the ICE is more frequently used in city driving patterns than highway driving patterns, which results in a lower efficiency. Moreover, steep decelerations are harmful for regenerative braking energy recovery. Especially in the case of 10–15 Japan, there are 14 stops-and-starts in only 2.61 miles, as shown in Table 4.3, and the average deceleration is the greatest amongst the 3 city driving patterns. Therefore, less energy is recovered from regenerative braking and the overall drive train efficiency over 10–15 Japan is the lowest, although the driving distance and acceleration is much less compared to other city driving schedules [16].

The overall fuel economy over the designated 6 driving schedules is shown in Fig. 4.5. It can be easily observed that the overall drive train efficiency is not necessarily proportional to fuel economy. For example, the fuel economy under 10–15 Japan driving conditions is higher than that under UDDS conditions, but the overall drive train efficiency is lower. The higher fuel economy of 10–15 Japan is because it possesses lower average speed as well as maximum acceleration, which leads to less usage of the ICE and leads to higher motor-controller efficiency. In the case of drive train efficiency, UDDS has a higher efficiency, because of the efficient usage of regenerative braking. As is clear from Table 4.3, there are a total of 51 stops in UDDS, but only 42 stops in 10–15 Japan. The simulation data also shows that the energy generated by regenerative braking under UDDS conditions is 2 % higher than that of 10–15 Japan, which indicates that more energy is saved in the drive train, as shown in Fig. 4.6. In addition, the electric motor is more frequently used in UDDS, which leads to a higher efficiency.

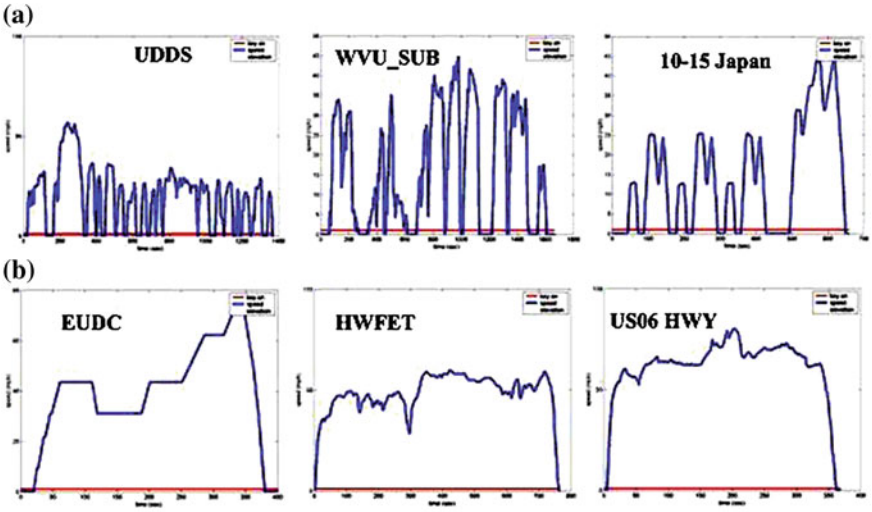

Fig. 4.5 Simulated driving schedules for test purposes **a** City driving patterns, **b** Highway driving patterns

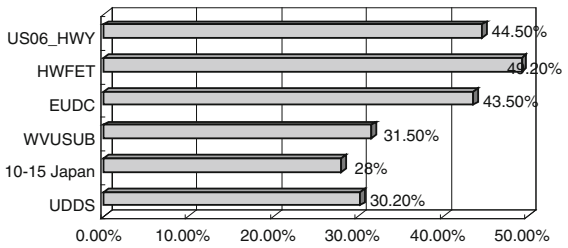

Fig. 4.6 Overall drive train efficiency over different driving schedules

Moreover, it is easy to notice that a single cycle distance of UDDS is 3 times greater than that of 10–15 Japan. Since the simulation is carried out over 3 repetitions for each driving schedule, the simulated distance of UDDS is approximately 9 times longer than that of the 10–15 Japan. On the other hand, the tested SUV runs as an electric vehicle because the high (80 %) initial SOC. The ICE starts working when the SOC decreases to a designated value. For these reasons, the SUV tested over 10–15 Japan is more likely to stay in electric mode longer than UDDS, which contributes a higher fuel economy. This result also suggests that a higher fuel economy can be obtained by maintaining the ESS in its high SOC range and driving the vehicle for shorter distances (Figs. 4.7, 4.8).

According to the simulation results, it is easy to see that the parallel drive train system is more suitable for highway driving. Both the fuel economies as well as the overall drive train efficiencies, under highway driving, are comparatively higher than in case of city driving patterns. This is mainly because the ICE nearly reaches its maximum efficiency (around 40 %). When the vehicle is running on the highway, the smooth driving patterns allow either the ICE or the electric motor to operate at its respective optimal operating point. Although the recovered energy from regenerative braking is much less compared to city drive cycles, as a low-efficiency power component, the ICE running at its most efficient operating points is a significant factor in improving the drive train efficiency.

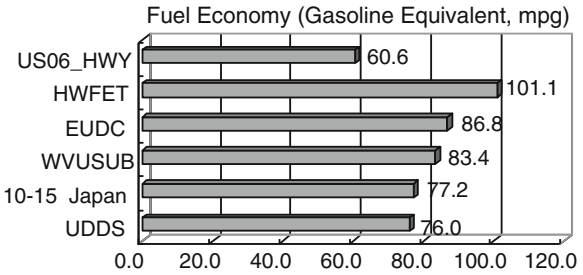

Fig. 4.7 Fuel economy over different driving schedules

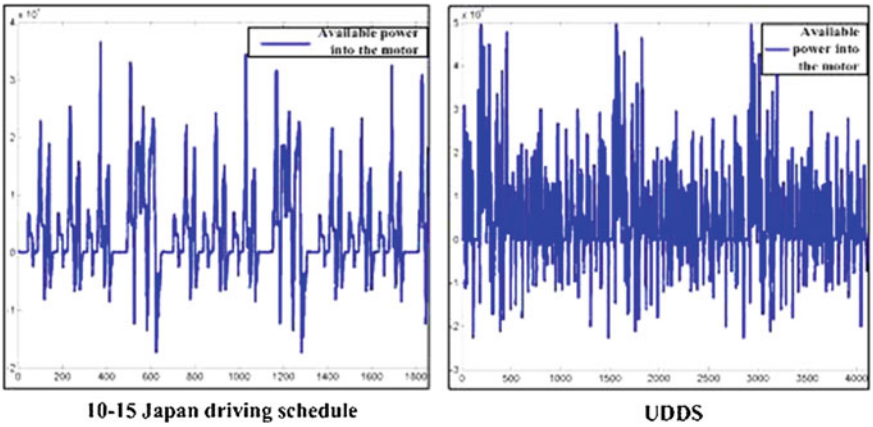

Fig. 4.8 Comparison of available power into the motor under UDDS and 10–15 driving patterns

4.4 Regenerative Braking Efficiency Analysis

According to the definition of regenerative braking efficiency in the previous section, the regenerative braking efficiency for each control strategy is calculated by retrieving the current that flows into motor for regenerative braking and the energy used by accessory loads, during regenerative braking events. The results are calculated based on equation $\eta_{REGEN} = \frac{E_{regen}}{E_{neg.trac}} \bullet 100\%$ and summarized in Fig. 4.9.

The considerable improvement of regenerative braking efficiency in electric assist mode indicates the flexibility of this control strategy, as it is originally designed to use electric traction, when needed. Therefore, increase of the possibility of using electric traction is allowed. As shown in Fig. 4.10, the modification

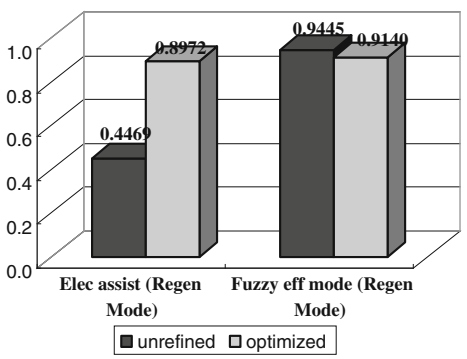

Fig. 4.9 Comparative electric drive train regenerative braking efficiencies

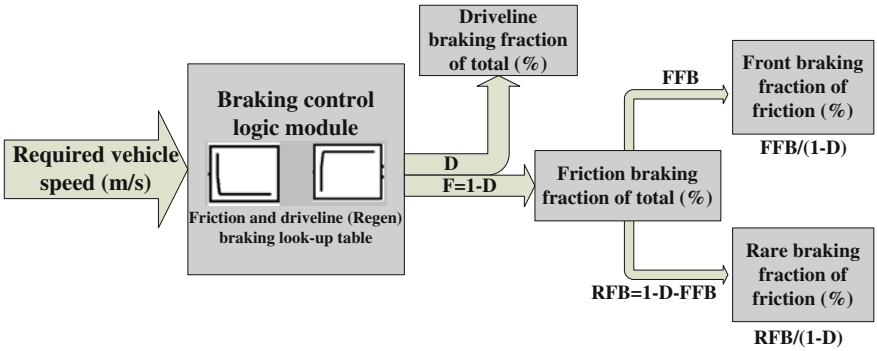

Fig. 4.10 Diagram of braking control logic

of regenerative braking control look-up table increases the percentage of regenerative braking usage. A cumulative amount of 20 % increment was observed compared to the original case. For the fuzzy efficiency control strategy, due to the preset ZEV condition, the regenerative braking efficiency does not increase. The compromise between regenerative braking efficiency and motor-controller efficiency is made by sacrificing regenerative braking efficiency. This is done principally because in the fuzzy efficiency mode, the motor-controller efficiency has greater priority compared to regenerative braking efficiency, as explained in the previous section.

Moreover, it is clear that the fuzzy efficiency mode is better at using electric traction and regenerative braking than the electric assist control strategy. In addition, high regenerative efficiency does not necessarily mean desirable overall drive train efficiency.

4.5 Overall Electric Drive Train Efficiency Analysis

The ultimate purpose of control strategy optimization is to improve the overall drive train efficiency by enhancing motor-controller efficiency. Also, as a key contributor to the overall drive train efficiency, regenerative braking efficiency is also appropriately optimized. Fig. 4.11 shows the comparative overall electric drive train efficiencies over the 4 different control strategies. As is evident, the improvement is approximately 2 times greater than the untreated strategies, which justifies the suitable arrangement and correct proportion of efficiency improvement between the motor-controller efficiency and regenerative braking efficiency.

In general, the fuel economy is proportional to the overall drive train efficiency. However, it is important to note that the rates of increase of fuel economy for the 2 proposed control strategies are slightly different. Consequently, it is easy to see from Fig. 4.12 that the fuel economy increasing rate, when using electric assist

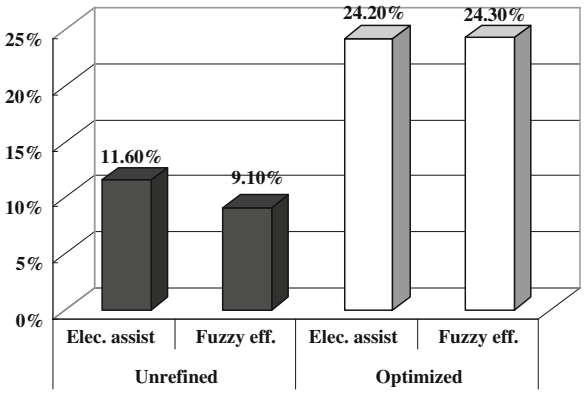

Fig. 4.11 Comparative overall electric drive train efficiencies

control strategy, is larger than that when using the fuzzy efficiency mode. By retrieving the simulation data from the fuel converter and motor-controller, it is straightforward to explain the above-mentioned ambiguity. Since the driving patterns for the 2 control strategies are same, the energy used during the simulated 5 driving cycles is equal as well. However, the employment of electric traction and the effectiveness of regenerative braking are different from each other. Based on the previous analyses, the regenerative braking efficiency, when using the optimized electric assist control strategy, is found to be much higher than when using the fuzzy efficiency mode. Nearly 6 to 7 % of total fuel consumption is saved due to regenerative braking in the case of electric assist control strategy compared to when using fuzzy efficiency mode.

Fig. 4.13 summarizes the efficiency improvement in terms of motor-controller efficiency, in both powering mode as well as regenerative braking mode. Fig. 4.13 also depicts the respective regenerative braking efficiency, overall drive train efficiency, and fuel economy improvements. There are only 2 negative increments, motor-controller efficiency in regenerative mode and the regenerative braking

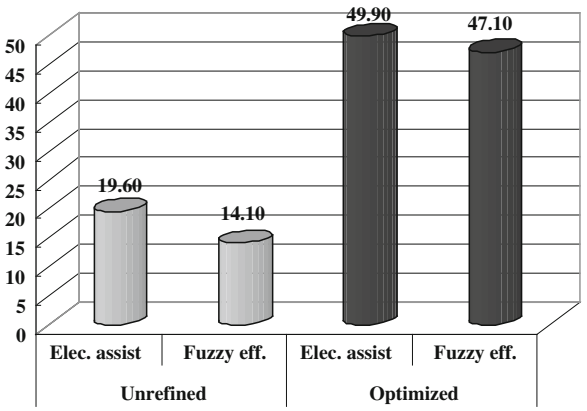

Fig. 4.12 Comparative fuel economies over 4 proposed control strategeis

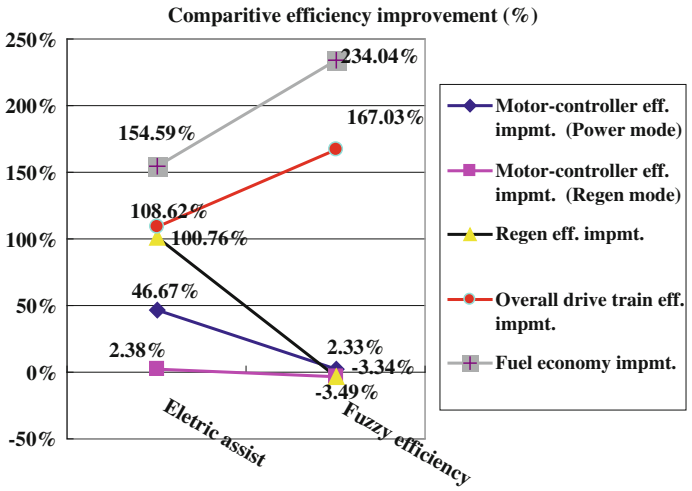

Fig. 4.13 Comparative efficiency improvment

efficiency in fuzzy efficiency mode, which are mainly restricted by the ZEV setting in powering mode, as explained in the previous section. Nevertheless, the increment of overall drive train efficiency and fuel economy, respectively, is more than 100 % higher, which justifies that the decrease is correct and proves to be a necessary trade-off.

4.6 Fuel Cell HEV: Modelling and Control

4.6.1 Modeling Environment

The baseline vehicle and control strategy is modeled and analyzed in the Advanced Vehicle Simulator (ADVISOR) software, which is developed in the MATLAB/Simulink environment [17]. ADVISOR is composed of a group of models, experimentally verified data, and script files. It not only allows the designer to obtain a quick analysis of the performance and fuel economy of conventional, electric, hybrid electric, and fuel cell vehicles, but it also provides detailed simulations and analysis of user-defined power train components, by taking advantage of the modeling flexibility of Simulink and the analytical power of Matlab [18].

ADVISOR uses 3 primary graphical user interface (GUI) screens to guide the user through the simulation process. The GUI facilitates interaction with the raw input and output data that is present in the MATLAB workspace. The vehicle model is depicted graphically using Simulink block diagrams, to define the connections between components, as shown in Fig. 4.14. The component models can

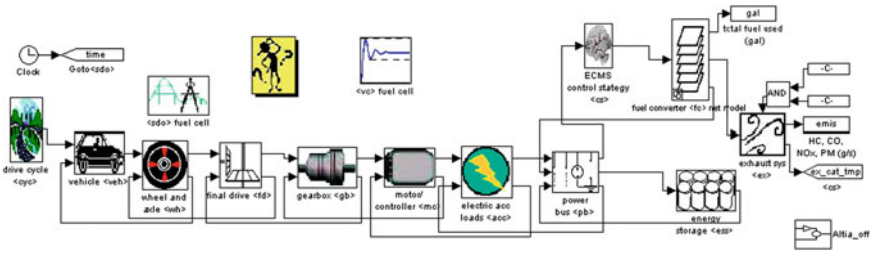

Fig. 4.14 Overall vehicle Simulink diagram in ADVISOR

be inserted into a vehicle model and then connected to define the flow of torque or speed and power from one component to the next. The arrows entering the top input of a component block in the fuel cell vehicle model, shown in Fig. 4.14, represent a torque and speed or a power demand from one component to the next upstream component. The power demand is based on the vehicle speed requirements and the losses of each component. Arrows entering the bottom input port of each block represent what the upstream component is able to achieve.

In general, individual component models are a combination of algorithms programmed in Simulink and data files that store various tuning parameters for the algorithms. By incorporating various vehicle performance and control information into a modular environment within Matlab and Simulink, ADVISOR allows the user to interchange and design a variety of components, vehicle configurations, and control strategies. It also allows quick analysis of the vehicle performance, emissions, and fuel economy of conventional, electric, and hybrid electric vehicles.

4.6.2 Modeling and Selection of Power Components

In this section, the sizing and modeling of the Fuel Cell-Hybrid Electric Vehicle (FC-HEV) power train system are introduced. The power components mainly include the fuel cell system, battery system, and the motor-controller system.

4.6.3 Fuel Cell System

As aforementioned, fuel cells are electrochemical devices that convert the energy of a chemical reaction between hydrogen and oxygen directly into electrical energy. Various types of fuel cells exist, but as stated in Chap. 1, the PEM fuel cell is regarded as the most promising option for automotive application, due to its high power density, low operating temperature of about 80 °C, and high overall efficiency [19].

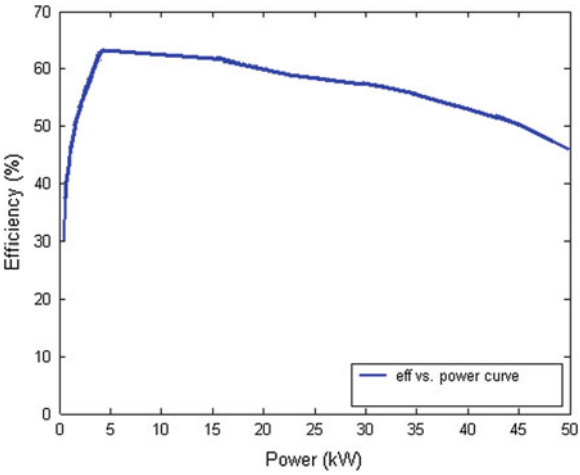

Fig. 4.15 Net power versus efficiency map for a 50 kW fuel cell system model

ADVISOR includes 2 options for modeling the fuel cell. The first one is based on look-up tables, indexed to the polarization curves, which characterize the fuel cell stack performance. The key assumption is that the system can provide a specific net power, while consuming a set amount of fuel, regardless of how complex the system may be [18]. A used net power vs. efficiency data for PEM fuel cell stack built in ADVISOR is shown in Fig. 4.15.

The performance of the auxiliary systems, such as air compressor and fuel pump, can be also characterized with polarization curves, from experimental data in ADVISOR. The power delivered by the fuel cell system is the difference between the power produced by the fuel cell stack and the power consumed by the auxiliary system. The second option is to model a fuel cell stack in a much more complete manner through a co-simulation link between ADVISOR and General Computational Toolkit (GCtool). In such a case, the electrochemistry, thermal characteristics, and mass transfer characteristics can also be incorporated. It must be pointed out, though, that such a detailed model is not necessary for overall vehicle system-level performance analysis.

4.6.4 Battery System

A suitable energy storage system (ESS) is required to assist the fuel cell system, to meet the power demand from the drive train. Currently, lead-acid batteries are employed in conventional cars, because of their low price and rugged structure. On the other hand, for recent HEV applications, nickel metal-hydride (Ni-MH) batteries are commercially used in the market. Compared to lead-acid batteries, Ni-MH batteries generally have much longer lifespan, higher power output, and increased charge and discharge efficiency. Besides, they are also safely recyclable [20].

Ni-MH batteries have been employed successfully in vehicles in the state of California, and demonstrated promise to meet the power and endurance requirements for electric vehicle (EV) propulsion. Meanwhile, Lithium-ion (Li-ion) batteries are likely to become serious competition for Ni-MH in EV/HV applications, but their operating life is still limited. In addition, ultra-capacitors are also currently under investigation in several research programs, but their energy density is much lower than those of batteries. The main advantage of ultra-capacitors is their high power density, which make them great options for hybridizing with battery systems, for supplying short bursts of power during acceleration, or receiving short bursts of regenerative currents, during quick decelerations. Fig. 4.16 shows the energy and power densities comparison of common energy sources [20].

The battery model type used for the FC-HEV under study is the *Ovonic* 45Ah Ni-MH battery. The main performance characteristics of this battery are summarized in Table 4.4. The battery is modeled in ADVISOR based on the internal resistance model, as shown in Fig. 4.17. The circuit determines the output voltage and current based on the load, while estimating the rate at which this power level depletes the resistor through the internal model calculation.

Due to the non-linear behavior of batteries, the parameters of the simulation circuit are determined from experimental data collected by the Battery Thermal Management Laboratory, manufacturer data sheets, as well as lab tests [21]. At each time step, the net battery current is then used to estimate the change in State of Charge (SOC) of the battery. Fig. 4.18 shows the internal resistance of the battery at 40 °C.

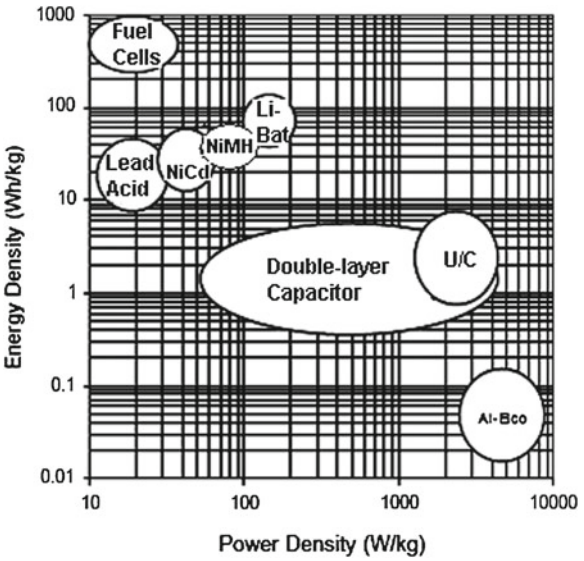

Fig. 4.16 Energy and power densities of various energy storage components [20]

Table 4.4 Ni-MH Battery parameters

Nominal Voltage	12 V
Nominal capacity (C/3)	45 Ah
Nominal energy (C/3)	598 Wh
Peak power (10 s pulse @ 50 %DOD @ 35 deg. C)	3.3 kW
Weight	8 kg
Volume (modules only)	3.2 L

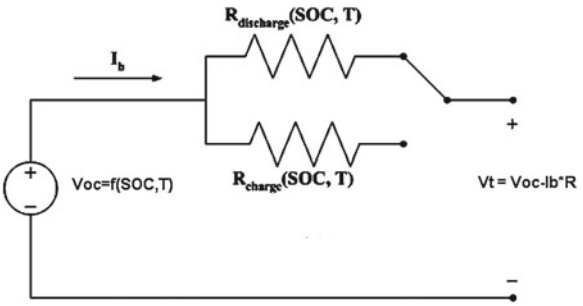

Fig. 4.17 Internal resistance battery model electrical schematic

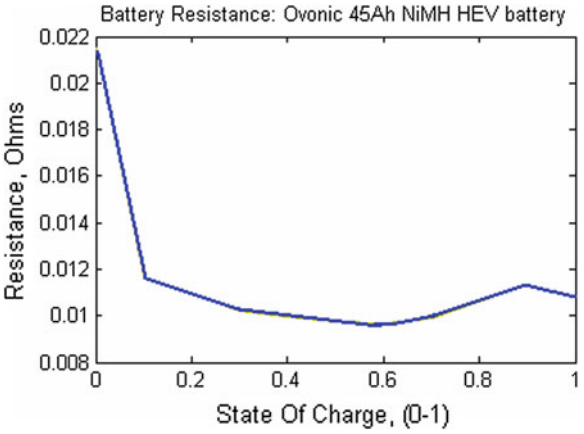

Fig. 4.18 Resistance of the Ni-MH battery at 40 deg. C in ADVISOR

4.6.5 Motor-Controller System

The electric traction motor system plays an important role in the performance of a FC-HEV. The main requirements for motor selection include: high torque density and power density; wide speed range, including constant torque and constant power operations; high efficiency over wide speed range, high reliability, and

robustness; a reasonable cost [22]. There are 3 motor types suitable for HEV applications: permanent magnet motors, induction motors, and switched reluctance motors. The permanent magnet machines possess high efficiency, high torque, and high power density. However, they inherently have a short constant power range, due to limited field weakening capability. In addition, the back EMF can also be a problem at high speeds, because the inverter must be able to withstand the maximum back EMF generated by the stator winding. The switched reluctance motor (SRM) is a promising candidate for HEVs, due to of its simple construction, simple control, and good extended speed performance. However, since the SRM is not yet widely produced as a standard motor in the market, the overall electric propulsion system cost may be higher than other motor options.

Thus, the popular induction motor (IM) is selected for FC-HEV modeling in the thesis due to its simplicity, robustness, and adequate extended speed range. Also, IMs do not have back EMF to deal with, at high speeds [22]. Field-oriented control makes an IM behave like a simple DC machine. In ADVISOR, the entire motor system is modeled based on motor efficiency maps, where the motor efficiency is determined as a function of toque and speed. Fig. 4.19 shows the efficiency map of the *Westinghouse* 75 kW IM. The bold lines represent the maximum torques, according to the speed of the motor.

Corresponding to the backward-facing vehicle modeling approach, the desired speed and torque requests, propagated from the transmission, are translated by the motor model into a power request through a series of mathematical equations.

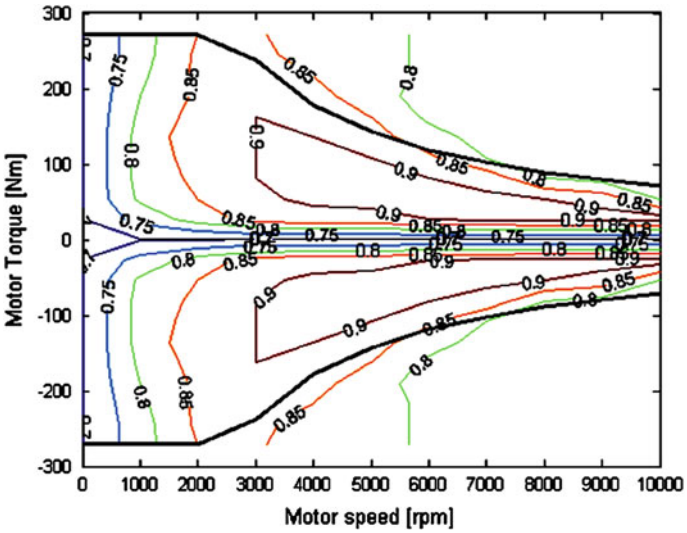

Fig. 4.19 Efficiency map of a *Westinghouse* 75 kW AC induction motor [17]

4.6.6 Baseline Vehicle

The vehicle dynamic model is described by the typical force balance equation as shown in 4.2, from which the total driving force is computed as the sum of rolling resistance force, aerodynamic resistance force, acceleration force, and climbing resistance force. The model first calculates the required driving force, according to the required acceleration. Thereafter, the achievable acceleration is calculated, based on the output driving force. The vehicle speed is determined by the driving cycle, transmission gear ratio, and the wheel radius. In this thesis, we assume that the vehicle has a one-speed transmission.

$$\text{Ftotal} = \text{Frolling} + \text{Faero} + \text{Facc} + \text{Fclimb} \tag{4.2}$$

The vehicle characteristics are assumed to be based on current production of baseline conventional vehicles. The vehicle parameters are selected based on 2 types of vehicles: the mid-size family sedan and mid-size SUV. Table 2.2 outlines the vehicle modeling assumptions (Table 4.5).

4.6.7 Summary

This chapter summarized the sizing and modeling aspects of the vehicle and its main power components. The ADVISOR software as a modeling and simulation environment was introduced. The complete modeled block diagram of the FC-HEV is shown in Fig. 4.20.

As mentioned earlier, the PEM fuel cell is used due to its high power density, low operating temperature, and high efficiency. For system level performance analysis, the fuel cell system is modeled by look-up tables, indexed to the polarization curves, which characterize the fuel cell stack performance. The nickel metal-hydride (Ni-MH) battery is used as the ESS, because of its high energy density and reasonable cost. The battery is modeled based on the internal resistance model and experimental data. The motor system used is an AC induction motor, which is modeled based on its efficiency map. The baseline vehicle parameters are selected based on current production of conventional vehicles. In the analyses performed in the ensuing chapters, 2 types of baseline vehicles are

Table 4.5 Vehicle specifications

Vehicle type	Mid-size SUV	Mid-size Sedan
HEV glider mass	1,179 kg	636 kg
Cargo mass	136 kg	136 kg
Fuel cell vehicle goss mass	2,095 kg	1,300 kg
Rolling resistance	0.012	0.012
Frontal area	2.66 m^2	2.0 m^2
Coefficient of drag	0.44	0.35

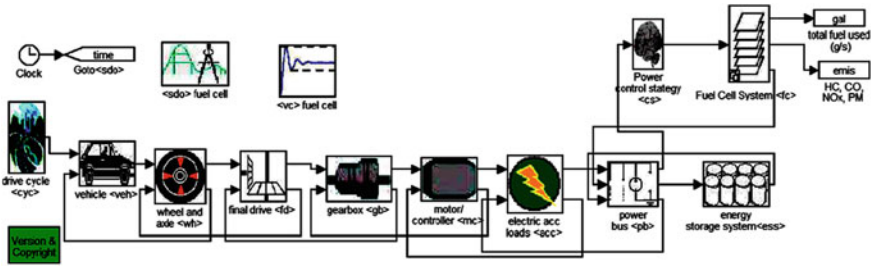

Fig. 4.20 Block diagram of the modeled FC-HEV drive train

considered; they include a mid-size family sedan and a mid-size sports utility vehicle (SUV).

4.6.8 Control Fuel Cell HEV

4.6.8.1 Introduction

A typical drive train layout of a FC-HEV with control information flow and power flow is shown in Fig. 4.21. The FC-HEV utilizes the fuel cell system as the main

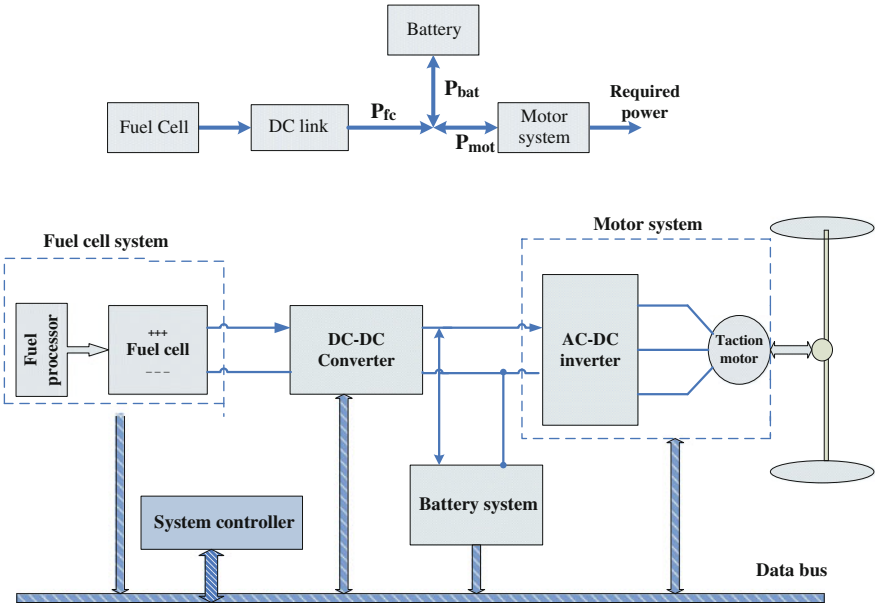

Fig. 4.21 Main schematic of the overall system

power source to provide electricity and uses a reversible energy storage accumulator, such as a battery or an ultra capacitor, as a supplementary power source. This hybridization not only downsizes the fuel cell and fulfills transient power demand fluctuation, but also leads to significant energy savings through regenerative braking energy recovery [23].

As is the case with regular hybrid electric vehicles (HEVs), a good system level power control strategy is essentially required to solve the problem of managing the power sharing between the fuel cell and the battery. An optimal control strategy design helps achieve maximum fuel economy, system efficiency, and maximize ESS life span, while maintaining required vehicle dynamic performance. In addition, simplicity, feasibility, and robustness are also important factors to evaluate different power control strategies. Various types of power control strategies have been proposed for HEVs, which could be extended to FC-HEV applications [24–32].

Some of the popular FC-HEV power control strategies are reviewed in the ensuing sections. Thereafter, optimized design, modeling, and in-depth analysis are performed on 2 types of control strategies, namely the load follower control scheme and the equivalent consumption minimization strategy (ECMS). In order to investigate their control performance, and to further optimize their respective designs, detailed comparisons and analyses based on simulation tests, are also presented in this chapter.

4.6.8.2 Review of FC-HEV Power Control Strategies

The general goal of the power control strategy for a typical FC-HEV drive train is to maximize the vehicle system efficiency and enhance fuel economy, while maintaining the required vehicle performance. There are several global optimization algorithms, such as dynamic programming (DP), developed for HEVs, to find the optimal solution of power distribution [31]. The DP method is a cost function based dynamic optimization tool, which can guarantee global optimal solution up to the grid accuracy of the states. However, these kinds of strategies are based on a prior knowledge of future driving conditions. Therefore, they are not suitable for real-time control, but they can best serve as a benchmark for improving other control strategies.

Rule-based control strategies are popular for FC-HEV power management, due to their simplicity and feasible implementation. These types mainly include the thermostat scheme, load follower scheme [17, 24], and fuzzy logic scheme [26–28]. The thermostat scheme features simplicity and robustness. Under this scheme, the fuel cell will turn on and off based on the battery SOC. The fuel cell turns on when the SOC reaches the low limit and turns off when the SOC reaches the high limit. When the fuel cell is on, it will always operate at the most efficient power level, as shown in Fig. 4.22, which compares the fuel cell operating point of the thermostat scheme with load follower scheme. Although this strategy is simple and easy to control, it has some disadvantages; firstly, it cannot satisfy vehicle driving

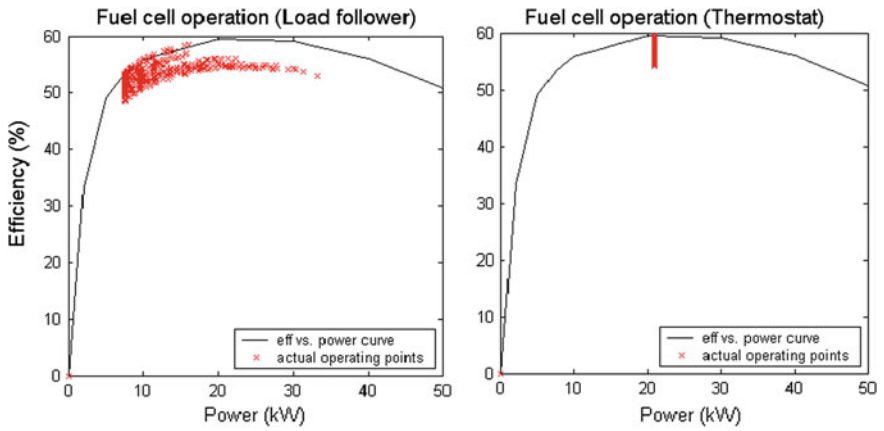

Fig. 4.22 Fuel cell operating points with the load follower and the thermostat scheme

requirements, especially during acceleration or high power command. Moreover, this strategy leads to frequent charging/discharging of the battery, which is unfavorable.

The load follower scheme, to a large extent, can solve the problems occurring in the thermostat scheme. The basis of the power follower scheme is to determine the operation state of the fuel cell, according to the power demand from the vehicle and the battery state of charge (SOC). The fuel cell output is never to be a constant value, but tends to change, following the transient power requirements in a reasonable region. A minimum and a maximum output power level (Pfc_min, Pfc_max) should be determined to avoid the fuel cell system operating in low efficiency. Meanwhile, the battery SOC should be controlled within a range where regenerative braking energy can be effectively absorbed, while ensuring battery life. In this thesis, this control strategy is selected for the purpose of optimal design and simulation test based analyses in the ensuing sections, because it can achieve better control performance compared to thermostat, and it is easy to create an acceptable design within a short time.

More recently, fuzzy logic is becoming increasingly popular in hybrid vehicle control, because it enables the development of dynamic rule-based behavior. It solves the problem that exists in static control approaches, where the parameters are normally optimal for a specific vehicle type and a specific driving condition, while becoming sub-optimal in other conditions. The main advantage of fuzzy logic control schemes is that they can be tuned and adapted to the specific driving conditions and plant dynamics, thus enhancing the degree of freedom of control [28]. Another benefit is that it does not depend on accurate mathematical modeling, which is hard to obtain for complex systems, such as FC-HEVs.

In a fuzzy logic controller, the knowledge of an expert can be coded in the form a rule-base, and can be used in decision making. A basic type of fuzzy logic based power control scheme is illustrated in Fig. 4.23 [26]. As is clear, the inputs of the

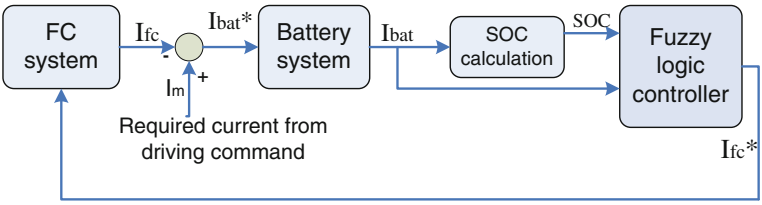

Fig. 4.23 Fuzzy logic based power control scheme

fuzzy controller are battery SOC and battery current, and the fuzzy output is the required current for the fuel cell. Fig. 4.24 shows the basic analysis method for fuzzy logic control. The fuzzifier converts the crisp input value into a fuzzy value, with degrees of membership functions.

The inference engine combines the fuzzy rules into a definite map, from a fuzzy set of inputs to the output, based on fuzzy logic principles. The defuzzifier then reconverts the resulting fuzzy value into a specific crisp value, as a reference variable. The heart of a fuzzy system is a set of knowledge-based IF–THEN fuzzy rules. However, the main limitation of a fuzzy logic control strategy is its complexity, which limits implementation flexibility.

To develop a cost function based optimal algorithm, which is real-time applicable, some improved strategies have been proposed. The Stochastic Dynamic Programming (SDP) has been proposed to solve the power management as a stochastic problem [32]. The basic principle of SDP problem formulation is to model the power command as a stochastic process, and an optimal controller based on the stochastic model can be designed, in order to find an optimal control policy that maps the control decision against the vehicle operation states. At the same time, the disadvantage is that it is computationally expensive to build cost tables and corresponding optimal control for complex dynamic systems. Another popular cost function based control strategy is the equivalent consumption minimization strategy (ECMS) [29], which is developed for parallel HEVs. The ECMS replaces the global cost function to a local one, which adjusts the instantaneous power split by calculating an equivalent fuel cost function for an array of power splits between 2 energy sources, and selects the split with the lowest fuel cost. This type of control strategy can often reach a nearly optimal operation set point. The ECMS strategy, as a representative of cost-function based control strategies, is selected for optimized design and simulation-based study in the ensuing sections.

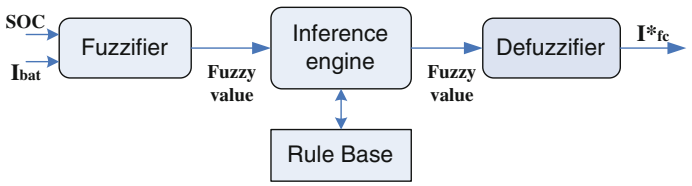

Fig. 4.24 Structure of fuzzy logic controller

4.7 Power Electronics Interface of Fuel Cell and Traction System

4.7.1 Introduction

This section will present the low level power circuit design and control of the power train system for a FC-HEV. As illustrated in Fig. 4.25 of the proposed power train system configuration, the power conditioner between the fuel cell and the battery system plays a crucial role, in order to provide protection of power components and matching the voltage levels of different power sources to the main DC bus. Meanwhile, it will also provides control of the demanded power according to the reference power value (usually transfer to reference current) from the system supervisory controller, as discussed in last chapter.

In the ensuing sections, the power train topology selection based on the component characteristics and power requirements will be discussed. Two popular topologies are considered based on 2 options of hybridization degree selection. Thereafter, the circuit modeling of power components in PSIM software as well as the power converter design will be introduced. Finally, the control scheme design and simulation-based analysis will be presented.

4.7.2 Power Train Configuration

An ideal topology for FC-HEV is that both the fuel cell system and the ESS are directly connected to the propulsion motor. This seems to be most efficient and economical configuration. However, this configuration is applicable only if both

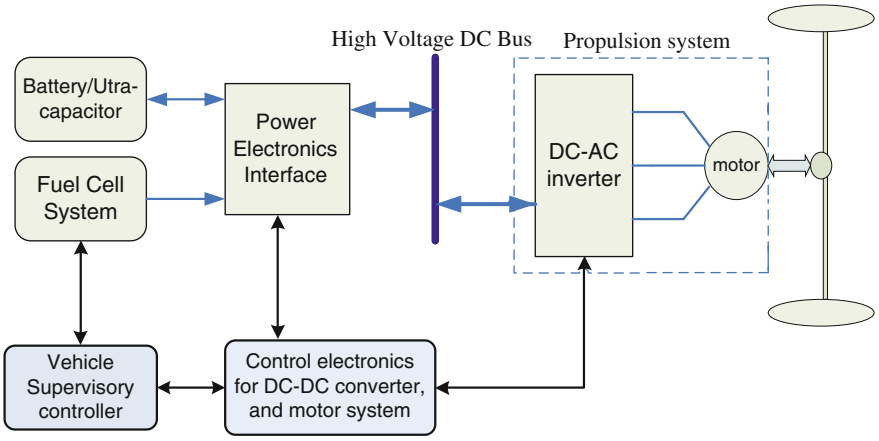

Fig. 4.25 Power train control system of a FCHEV

the fuel cell and ESS output voltages match the voltage level of the DC bus, which in turn, needs be set to a level suitable for usage with the motor system. The fact is that fuel cell output is usually lower than the DC bus requirement, and tends to depict a wide variation during operation, or the voltage between the fuel cell and battery does not match [33]. This leads to low efficiency and reliability, and proves to be extremely complicated when providing power distribution control in a hybrid configuration.

Therefore, a DC/DC converter is necessary for power conditioning between the 2 power sources and the DC voltage bus, which is in turn connected to the propulsion system. In general, there are 2 options of power train structures, based on the position of the DC/DC converter, as shown in Fig. 4.26. In topology-A, the fuel cell is connected to the high voltage DC bus through a unidirectional DC/DC converter, while the battery is directly connected to the DC bus. In this condition, the fuel cell output can be directly controlled, while the battery output voltage needs to match the DC bus voltage level. In topology-B, the fuel cell is directly connected to the DC bus, while the battery is connected to the DC bus through a bi-directional DC/DC converter.

The utilization of a bi-directional converter between the battery and DC bus allows more flexibility to the battery, because such an arrangement not only reduces the voltage requirement of the battery, but also provides the freedom to control its state of charge (SOC). Since the fuel cell is directly connect to the high

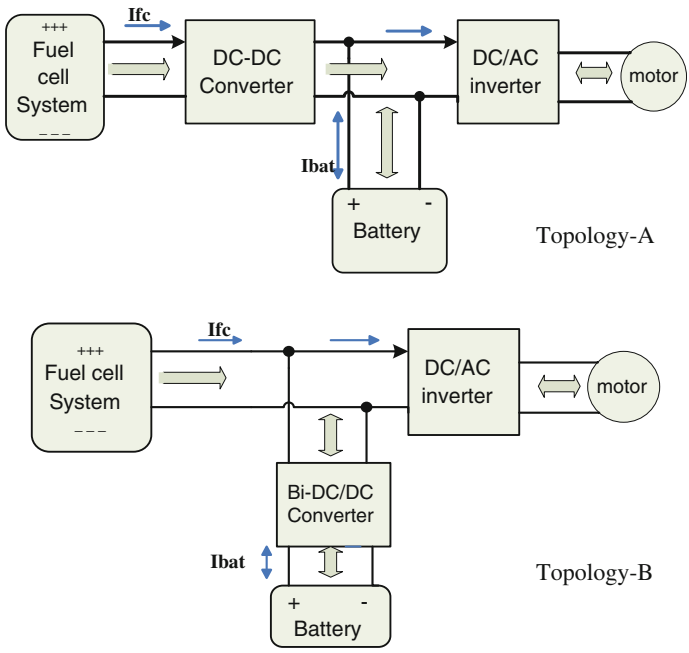

Fig. 4.26 Power train topological options for FC-HEVs

Table 4.6 Two cases of hybridization for a mid-size SUV

	Fuel cell size (PEM) (kW)	Battery size (Ni-MH)	Power train type
Case-1	60	25 modules	Topology-A
Case-2	80	20 modules	Topology-B

voltage DC bus, a large sized stack or voltage level is required, and the control of fuel cell power can only be achieved indirectly, by controlling the battery output, or through internal fuel control. The use of 2 high power converters for both battery and fuel cell generally is not economical from the point of view of cost and size consideration.

In this section, the topology selection is considered according to the hybridization degree. The hybridization degree here is defined as the ratio between the fuel cell rated power and the peak power of the traction motor. A higher hybridization degrees leads to better fuel economy, but requires a large sized fuel cell, which in turn leads to high cost. Here, the sizing of a mid-size SUV type vehicle is considered for study, since SUVs are one of the most popular and fuel inefficient vehicle type. Moreover, SUVs provide more potential to arrange the power component size, since they have large space. Two specific cases of hybridization degrees are selected based on the peak/average power requirement of a mid-size SUV (140 kW/50 kW, in this case), as described in Table 4.6.

For case-1, power train topology-A is chosen, because the fuel cell size is relatively small and the voltage level for a 60 kW PEM fuel cell (200–300 V) does not match the DC bus voltage (300–450 V). Therefore, the DC/DC converter allows a downsized fuel cell and can allow complete control. At the same time the rated voltage of the 25 battery pack cells can be set to be around 400 V, which represents the DC bus voltage level. For case-2, which has a larger fuel cell and smaller battery pack, the 80 kW fuel cell (300–400 V) can be directly connected to the DC bus, while a bi-directional DC/DC converter is needed for the battery, to match the voltage level as well as to control the battery charging and discharging performance.

4.7.3 Power Component Modeling

4.7.3.1 Fuel Cell System

To obtain the electrical characteristics of the fuel cell, its circuit model is represented by a look-up table and controlled voltage source, which provides the fuel cell voltage corresponding to the current drawn from the fuel cell, as shown in Fig. 4.27. The diode at the fuel cell output is to prevent the negative current going back into the stack, and an on–off controller is added, to ensure that the fuel cell operates in an acceptable area.

Fig. 4.27 Fuel cell model

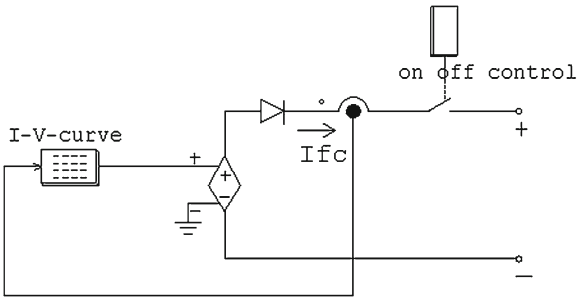

The fuel cell V–I characteristic is normally portrayed in the form of a polarization curve, which is determined by the relation between cell voltage and current density, as described in Chap. 1. Figure 4.28 illustrates the V–I curve of a 60 kW fuel cell. The stack temperature and membrane water content affect the fuel cell voltage. The voltage decreases as higher current is drawn from the fuel cell, due to the fuel cell electrical resistance, inefficient reactant gas transport, and low reaction rate [34]. Lower voltage indicates lower efficiency of the fuel cell, and the maximum current drawn from the fuel cell is defined as the current at which the maximum output power is achieved. Many cells are typically combined in a stack, to satisfy the power requirement of the target application.

4.7.3.2 Battery System

The battery system is modeled based on a typical RC model, as described in Chap. 2. This model consists of a voltage controlled voltage source in series with

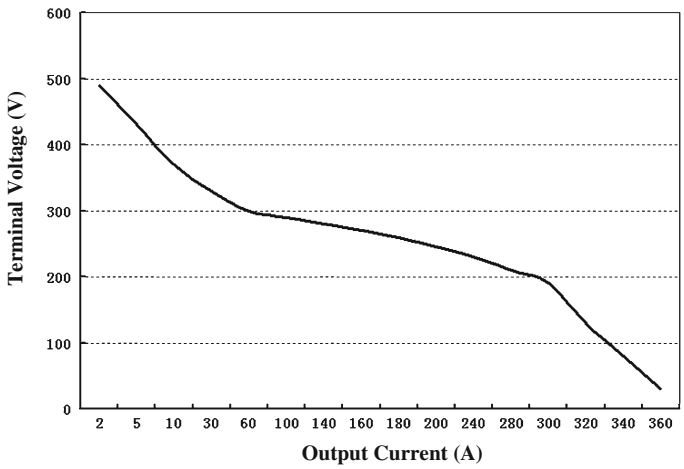

Fig. 4.28 V-I polarization curve of a 60 kW PEM fuel cell stack

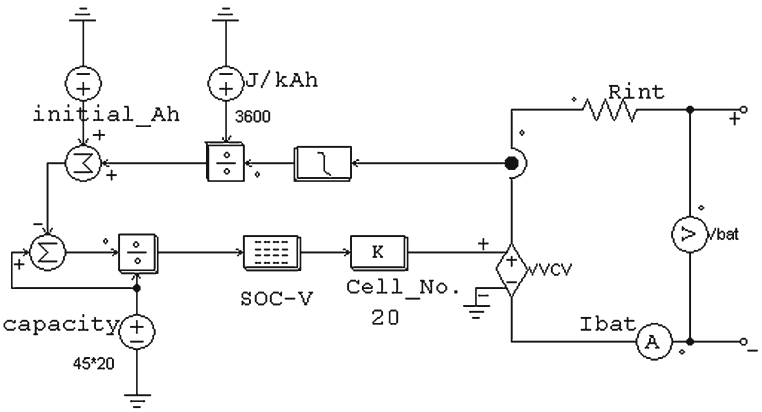

Fig. 4.29 Battery model

an internal resistor, as shown in Fig. 4.29. The battery output voltage is determined by the battery SOC, through a look-up table. The relation between battery cell-voltage and SOC is obtained from validated experimental data, as shown in Fig. 4.30. The battery SOC is calculated as the energy present in the battery divided by the maximum energy capacity (Ah) of the battery pack, as given in 4.3.

$$SOC = \frac{Capacity_{\max}(Ah) - Ah\_used}{Capacity_{\max}(Ah)} \tag{4.3}$$

4.7.3.3 Propulsion System

An active load is used to model the demanded power from the propulsion system, which avoids the complicated modeling of motor and motor controller. The propulsion system is modeled as a controlled current source, drawing current from the

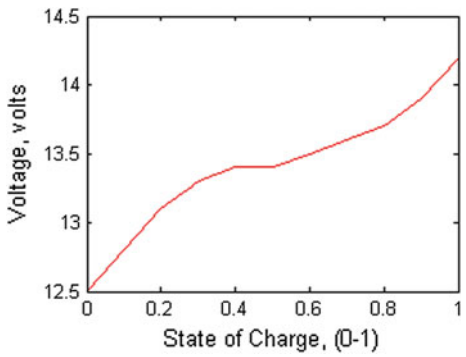

Fig. 4.30 SOC versus terminal voltage curve for Ni-MH battery cell

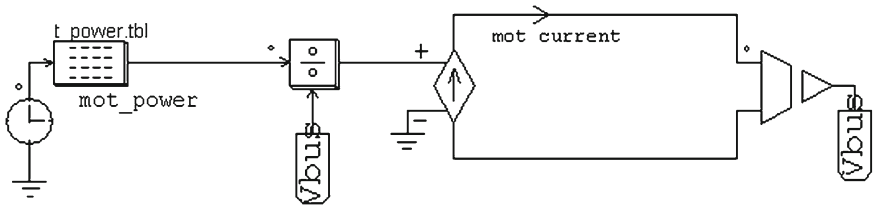

Fig. 4.31 Propulsion system model

system, as shown in Fig. 4.31. Various driving scenarios are translated to corresponding power requirements through a look-up table with respect to time. This relation data can be obtained from the vehicle system level simulations. The motor required current can thereby be obtained after divided by the DC bus voltage.

4.8 Concept of Fuel Cell Plug-in HEV (FC-PHEV)

4.8.1 Fuel Cell-Hybrid Electric Vehicle Architecture

In the long term scenario, fuel cells represent one of the most appealing technologies for vehicle propulsion to further achieve high fuel efficiency, zero emissions, and low noise. Fuel cells are considered among the most promising alternative power sources, which can replace the conventional internal combustion engine (ICE). Compared to battery-powered electric vehicles (EVs), fuel cell vehicles (FCVs) have the advantage of longer driving range without a long battery charging time. In addition, compared to ICE vehicles, FCVs also depict comparatively higher energy efficiency and much lower emissions, due to direct conversion of free energy from the fuel into electric energy, without undergoing combustion. However, to fully achieve the potential energy savings of a fuel cell vehicle, it is important to recover the braking energy and ensure the operation of the FC system at maximum efficiency over the entire range of driving conditions encountered. This can be reached by a hybridization approach similar to gasoline-engine powered HEV. Furthermore, FC-HEVs present the advantages of cleaner and more efficient energy source, combined with the energy savings typical of EVs.

A typical power train of a fuel cell vehicle is as shown in Fig. 4.32. While most major automotive companies are investing in fuel cell vehicles, many challenges remain in getting fuel cell vehicles in the market. The major challenges include increasing fuel cell reliability, developing hydrogen infrastructure, improving on-board hydrogen storage capabilities, and overall cost reduction. One of the main research focuses is to develop a power control strategy and a power management

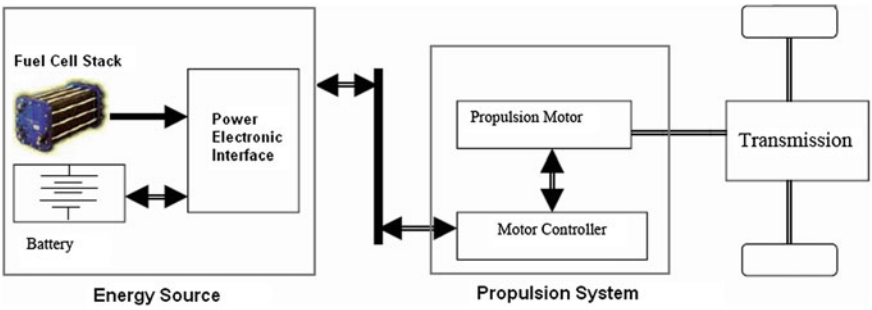

Fig. 4.32 Typical power train layout of FCHEV

system, which includes a fuel cell system, an energy storage system (ESS), and a suitable power electronic interface.

References

1. M. Ehsani, Y. Gao, S. E. Gay, A. *Emadi, Modern Electric, Hybrid Electric, and Fuel Cell Vehicles: Fundamentals, Theory and Design*, 1st edn. (CRC Press, New York, 2004)
2. W.D. Jones, Putting electricity where the rubber meets the road. IEEE Spectr. **44**(7), 18–20 (2007)
3. S. Williamson, M. Lukic, A. Emadi, Comprehensive drive train efficiency analysis of hybrid electric and fuel cell vehicles based on motor-controller efficiency modeling. IEEE Trans. Power Electron. **21**(3), 730–740 (2006)
4. S. Imai, N. Takeda, Y. Horii, Total efficiency of a hybrid electric vehicle, in *Proceedings of IEEE Power Conversion Conference*, Nagaoka, Japan, Aug 1997, pp. 947–950
5. G. Maggetto, J. Van Mierlo, *Electric and Hybrid Electric Vehicle: A Survey, IEE Seminar on Electric, Hybrid Electric, and Fuel Cell Vehicles* (Durham, UK, 2005), pp. 1–11
6. S.S. Williamson A. Emadi, Comparative assessment of hybrid electric and fuel cell vehicles based on comprehensive well-to-wheels efficiency analysis. IEEE **54**(3), 856–862 (2005)
7. F. An, D. Santini, Assessing tank-to-wheel efficiencies of advanced technology vehicles, in *Proceedings SAE World Congress*, Detroit, MI, March 2003
8. L. Eudy, J. Zuboy, Overview of advanced technology transportation, 2004 update, *Technical Report on Advanced Vehicle Testing Activity*, Energy Efficiency and Renewable Energy, U.S. Department of Energy, DOE/GO-102004-1849, Aug 2004
9. A. Burk, *Present Status and Marketing Prospects of the Emerging Hybrid-Electric and Diesel Technologies to Reduce CO2 Emissions of New Light-Duty Vehicles in California* (Institute of Transportation Studies, University of California, Davis) [Online]. Available: http://repositories.cdlib.org/itsdavis/UCD-ITS-RR-07-2
10. J. Burns, T. Cors, B. Knight, B. Thelen, Evaluating advanced automotive energy technologies: a multivariate mobility contribution metric. Int. J. Energy Techn. Policy **2**(3), 262–271 (2004)
11. S.S. Williamson, A. Emadi, Fuel cell vehicles: opportunities and challenges, in *Proceedings of IEEE Power Engineering Society (PES) General Meeting*, vol. 2, Denver, CO, June 2004, pp. 1640–1645

12. X. Li, S.S. Williamson, Comparative investigation of series and parallel hybrid electric vehicle (HEV) efficiencies based on comprehensive parametric analysis, in *Proceedings of IEEE Vehicle Power and Propulsion Conference*, Arlington, TX, Sept 2007
13. G. Rizzoni, L. Guzzella, B.M. Baumann, Unified modeling of hybrid electric vehicle drivetrains, AAAS **4**(3), 246–257 (1999)
14. M. Amrhein, S. Member, P.T. Krein, Dynamic simulation for analysis of hybrid electric vehicle system and subsystem interactions, including power electronics. IEEE Trans. Veh. Technol. **54**(3), 825–836 (2005)
15. J. Wu, A. Emadi, M.J. Duoba, T.P. Bohn, Plug-in hybrid electric vehicles: testing, simulations and analysis, in *Proceedings of IEEE Vehicle Power and Propulsion Conf*erence, Arlington, TX, Sept 2007
16. F. Stodolsky, L. Gaines, C.L. Marshall, F. An, J.J. Eberhardt, Total Fuel Cycle Impacts of Advanced Vehicles, SAE Technical Paper Series, no. 724, 1999
17. N.R.E.L. NREL, Advanced Vehicle Simulator (ADVISOR) Documentation, http://www.ctts.nrel.gov/analysis/advisor_doc
18. T. Markel, A. Brooker, T. Hendricks, V. Johnson, K. Kelly, B. Kramer, M. O'Keefe, S. Sprik, K. Wipke, ADVISOR: a systems analysis tool for advanced vehicle modeling. J. Power Sources **110**(2), 255–266 (2002)
19. D. Boettner, M. Moran, Proton exchange membrane (PEM) fuel cell-powered vehicle performance using direct-hydrogen fueling and on-board methanol reforming. Energy **29**(12–15), 2317–2330 (2004)
20. J. Park, B. Raju, A. Emadi, Effects of An ultra-capacitor and battery energy storage system in a hybrid electric vehicle, Society of Automotive Engineers (SAE) Journal, Paper No. 2005-01-3452, 2005; and, in *Proceedings of SAE 2005 Future Transportation Technology Conference*, Chicago, IL, Sept 2005
21. V.H. Johnson, Battery performance models in ADVISOR. J. Power Sources **110**(2), 321–329 (2002)
22. C.C. Chan, The State of the Art of Electric, Hybrid, and Fuel Cell Vehicles. proc. IEEE **95**(4), 704–718 (2007)
23. A.P. Roussean, R. Ahluwalia, Q. Zhang, Energy storage requirements for fuel cell vehicles, in *Proceeding of SAE World Congress*, Detroit, MI, March 2004, Paper No. 2004-01-1302
24. H.Y. Cho, W. Gao, H. Ginn, A new power control strategy for hybrid fuel cell vehicles, in *Proceedings of IEEE Workshop on Power Electronics in Transportation*, Detroit, MI, Oct 2004, pp. 159–166
25. C. Liang, W. Qingnian, Energy management strategy and parametric design for fuel cell family sedan, in *Proceedings of SAE Future Transportation Technology Conference and Exposition.*, Costa Mesa, CA, Aug 2001, Paper No. 2001-01-2506
26. H.S. Ahn, N.S. Lee, Power distribution control law for FCHEV-A fuzzy logic-based approach, in *Proceedings of IEEE International Conference on Control and Automation*, Budapest, Hungary, June 2005, pp. 486–0490
27. N.S. Lee, G.M. Jeong, H.S. Ahn, Improvement of fuel economy using fuzzy logic-based power distribution control strategy for a FCHEV, in *Proceedings of IEEE International Conference on Computational Intelligence and Security*, vol. 1, Guangzhou, China, 2006, pp. 891–894
28. J.S. Lai, D.J. Nelson, Energy management power converters in hybrid electric and fuel cell vehicles,in *Proceedings of the IEEE*, vol. 95, April 2007, pp. 766–777
29. G. Paganelli, Y. Guezennec, G. Rizzoni, Optimizing control strategy for hybrid fuel cell vehicles, in *Proceedings of SAE International Congress*, Detroit, MI, March 2002, Paper No. 2002-01-0102
30. P. Rodatz, G. Paganelli, A. Sciarretta, L. Guzzella, Optimal power management of an experimental fuel cell/supercapacitor-powered hybrid vehicle. Control Eng. Practice **13**(1), 41–53 (2005)
31. J. Liu, H. Peng, Control optimization for a power-split hybrid vehicle, in *Proceedings of IEEE American Control Conference*, Minneapolis, MN, June 2006, pp. 14–16

32. A. Schell, H. Peng, D. Tran, E. Stamos, C.C. Lin, Modeling and control strategy development for fuel cell electric vehicles. Annual Reviews Control **29**, 159–168 (2005)
33. K. Rajashekara, Power conversion and control strategies for fuel cell vehicles, in *Proceedings of 29th Annual Conference of the IEEE Industrial Electronics Society*, vol. 3, Roanoke, VA, Nov 2003, pp. 2865–2870
34. J.H. Hirschenhofer, D.B. Stauffer, R.R. Engleman, M.G. Klett, *Fuel Cell Handbook*, 4th edn. (Department of Energy, Federal Energy Technology Center, USA, 1998) DOE/FETC-99/1076

Chapter 5
EV and PHEV Battery Technologies

5.1 Energy Storage Issues of PHEVs and EVs

It is well-known today that batteries are indeed the main stumbling block to driving electric vehicles. In fact, the common issues related to lithium rechargeable cells can be summed up by one simple topic: cell equalization. Typically, a battery of a HEV consists of a long string of cells (typically 100 cells, providing a total of about 360 V), where each cell is not exactly equal to the others, in terms of capacity and internal resistance, because of normal dispersion during manufacturing. However, the most viable solution for this problem might not originate from mere changes in battery properties. The aim of this chapter is, first, to explain the role of power electronics based battery cell voltage equalizers and their role in improving cycle life, calendar life, power, and overall safety of EV/HEV battery energy storage systems.

It is imperative that most studies related to energy storage systems (ESS) for HEV applications must follow a cost-conscious approach. For instance, taking into account that typical lithium batteries cost about $500/kWh [1] (or $250/kWh [2, 3], if manufactured in high volumes), a typical 16 kWh battery, which provides about 80 km (50 miles) autonomy to a small vehicle (simulated and tested under the Federal Test Procedure, FTP driving pattern). This amounts to a surcharge of about $5,000 over the price of a standard vehicle, exceeding the reasonable budget for an medium consumer.

Moreover, issues related to cycle life and the calendar life issues cannot be ignored. Depending on the intensity of usage, an average cobalt or manganese cathode Li-ion battery holds about 500 cycles of 80 % the capacity, before losing 20 % of its initial capacity [4]. If the battery is replaced at that point and the cost of electricity is added, the expenses rise to $0.1/km. Consequently, the existing scheme makes the EV option more expensive than the traditional gasoline based vehicle. Considering newer batteries based on lithium iron phosphate ($LiFePO_4$) chemistries, these numbers are slightly better, withstanding 1,000 cycles on current

S. S. Williamson, *Energy Management Strategies for Electric and Plug-in Hybrid Electric Vehicles*, DOI: 10.1007/978-1-4614-7711-2_5,

technology, and expecting (but still not proven) 6,000–7,000 cycles for future PHEV applications. On the other hand, the $LiFePO_4$ chemistry depicts slightly lower energy density (100 Wh/kg) [5, 6]. Although $LiFePO_4$ seems to be the best fit for EVs, the long term cycle life and volume costs have to be considered seriously. As a reference, current price per unit of $LiFePO_4$ ranges from $1.90 to $2.40/Wh, compared to $0.86/Wh, for typical manganese based Li-ion batteries [1–3, 5, 6]. Extrapolating the current unit price relationship to high volume applications, the battery pack for a typical medium-sized car would cost in the range of $7,000–10,000 for a 16 kWh pack.

Another critical issue to be considered is overall safety. The key factors that play a vital role in maintaining safety include, usage of high quality materials and safety monitoring at the development process. In addition, continuous monitoring of cell current, cell voltage, temperature, and taking eventual corrective measures, also helps in critically improving the safety of the system.

However, the most viable solution for today's problem might not be originated merely from changes in the battery chemistry. In fact, a much smarter solution relies on a power electronic battery cell equalizer, which can improve not only the cycle life (the quantity of charge–discharge cycles before the end of life) of batteries, but also their calendar life (the time, fully charged and no cycling, to end of life), power, and safety. In the following chapters the impact of the utilization of a battery cell equalizer is going to be analyzed, in terms of economical as well as safety advantages.

5.1.1 Battery Chemistries

5.1.1.1 Battery Parameters

To design an efficient, precise, reliable, and safe charger, parameters of the battery pack should be determined. A brief definition of battery parameters are mentioned here which will be used later.

Battery Capacity

Measured in Ampere-Hour (Ah), battery capacity indicates the amount of charge that can be drawn from a fully charged battery until it gets fully discharged. An important effect in batteries is that the higher amount of current drawn from a battery, the lower capacity the battery will have. Hence, theoretically, battery capacity is defined as the amount of current drawn from a battery that completely discharges it in 1 h. However, in practice battery manufacturers specify a table showing the amount of time the battery runs with different constant current loads and different constant power loads. In practice, this table provides more practical information rather standard definitions, because, after production different loads with different characteristics may be connected to the battery.

C Rate

This parameter is used to show the amount of current used for charging the battery. For example, for a 10 Ah battery, when it is mentioned to terminate the charging process while the charging current falls below C/10 rate (10 h rate), it means the charging should be stopped when current becomes less than the amount of current with which the battery is discharged after 10 h, or specifically 10 Ah/10 h = 1 A

State of Charge

State of Charge (SoC) is the percentage of charge available from a battery to the whole capacity of the battery. SoC is difficult to measure directly and usually some methods are used to estimate it indirectly. Besides, according to aging the rated capacity of the battery reduces over time, hence, for determining accurate SoC, the rated capacity should be measured or calculated regularly.

Depth of Discharge

Depth of Discharge (DoD) is defined as (100-SoC) in percentage, i.e., the percentage of total charge of the battery which has been utilized. This parameter is usually used in discharge patterns recommendations. For example, the battery manufacturer may recommend the user not to go over 70 % DoD according to lifetime issues.

Energy Density

Energy density can be defined based on volume or weight, i.e., Wh/L or Wh/kg. The "Volumetric Energy Density," which is defined as the amount of available energy from a fully charged battery per unit volume (Wh/L). As we know Liter is used for measuring the volume of liquids, however, even for solid electrolytes such as Lithium Polymer batteries, the same unit is usually used. The other way of defining the Energy Density is "Gravimetric Energy Density" which is also referred as "Specific Energy" and defined as the available energy from a fully charged battery per unit weight (Wh/kg). Based on application and based on the importance of the volume or weight, either definition can be used. In the case of EVs/PHEVs usually weight is a more important factor than volume, so, mostly Specific Energy used.

Charging Efficiency

The chemical reactions inside the battery during charge and discharge are not ideal and there are always losses involved. Therefore, not all the energy used to charge

the battery, is available during discharge. Some of this energy is wasted as heat dissipation. The charging efficiency can be defined as the ratio of available energy from the battery in a complete discharge to the amount of energy needed to completely charge the battery. This parameter may be mentioned by other names such "Coulombic Efficiency" or "Charge Acceptance". In general, the coulombic efficiency for a new battery is high, however, reducing as the battery ages.

Next section discusses some aspects of different battery types used in EVs and PHEVs regarding charging. This will help in designing more efficient and flexible chargers based on battery behaviors which will finally lead to improvement of battery packs lifetime.

5.1.1.2 Main Characteristics of Commonly Used Batteries in EV/PHEV Battery Packs

Knowledge of characteristics of different battery chemistries is necessary for designing a reliable and efficient charger. There are hundred types of batteries described in reference books [7] and technical literature. Most of them are demonstration prototypes, working under laboratory conditions and still under investigation, not commercialized maybe because of costs, non-mature technology, low energy density, safety, toxic components, and so on. The most widely available batteries are Pb-Acid, Ni–Cd, Ni–MH, Li-ion, and Li-Polymer which are described below:

Lead-Acid (Pb-Acid)

For over one century, lead-acid batteries have been utilized for various applications including traction. Their well-improved structure has led to Valve Regulated Lead Acid (VRLA) batteries which can be considered as maintenance free batteries, which is a desirable characteristic for PHEVs. In terms of charge efficiency they have a high efficiency in the range of 95–99 %. The main disadvantage of Lead-acid batteries is their weight, in other words, they have a low specific energy (30–40 Wh/kg) compared to their counterparts.

Nickel Cadmium (Ni–Cd)

Considering low power applications Nickel Cadmium (Ni–Cd) batteries also benefit from a mature technology but considering traction applications their specific energy is low as well. The typical specific energy for this type is 45–60 Wh/Kg. The main applications are in portable devices, but they are also recommended when high instantaneous currents must be provided. They are typically used when long life and reasonable costs are desired. However, they have environmental concerns for recycling because they contain toxic metals [8].

Nickel-Metal Hydride (Ni–MH)

Comparing to previous types they have higher specific energy at the expense of lower cycle life. In general, for the same size batteries, NiMH batteries can have up to two or three times more energy than a Ni–Cd type. The typical value for the specific energy of the present technology NiMH batteries is in the range of 75–100 Wh/Kg. This type is widely used in EV and PHEV applications.

Lithium-Ion (Li-Ion)

This type has noticeably high specific energy, specific power, and great potential for technological improvements providing EVs and PHEVs with perfect performance characteristics such as acceleration performance. Their specific energy is in the range of 100–250 Wh/kg. Because of their nature, Li-ion batteries can be charged and discharged faster than Pb-Acid and Ni–MH batteries, making them a good candidate for EV and PHEV applications. Besides all, Li-ion batteries have an outstanding potential for long life if managed in proper conditions, otherwise, their life can be a disadvantage. One of the main reasons is almost the absence of memory effect in Li-based batteries. A weak point of Li-based batteries is safety since they are highly potential for explosion due to overheating caused by overcharging. They can almost easily absorb extra charge and get exploded. The use of advanced battery management systems (BMS) can ensure reliable range of operation of Li-ion batteries even in cases of accidents. Another advantage is that Li-ion batteries have environmental friendly materials when compared with Nickel-based batteries.

Lithium Polymer (Li-Po)

Li-Po batteries have the same energy density as the Li-ion batteries but with lower cost. This specific chemistry is one of the most potential choices for applications in EVs and PHEVs. There have been significant improvements in this technology. Formerly, the maximum discharge current of Li-Po batteries was limited to about 1C rate; however, recent enhancements have led to maximum discharge rates of almost 30 times the 1C rate, which greatly improves and simplifies the storage part of the EVs and PHEVs in terms of power density, since this can even eliminate the need of ultra-capacitors. Besides, there have been outstanding improvements in charging times. Recent advances in this technology have led to some types which can reach over 90 % SoC in a couple of minutes which can significantly increase the attraction toward EVs and PHEVs because of noticeable reduction of charging time. Because this type is a solid state battery, having solid electrolyte, the materials would not leak out even in the case of accidents. One of the other advantages of this type is that it can be produced in any size or shape which offers flexibility to vehicle manufacturers.

5.1.2 Battery Modeling and Simulation

5.1.2.1 Battery Models

Electrochemical nature of batteries has led to their highly nonlinear behavior dependent on many factors and has made it difficult to predict their characteristics such as V–I characteristic, state of charge, state of health, runtime, etc. Estimating their characteristics needs appropriate and accurate models. There are numerous battery modeling approaches and techniques in literature, each of which is more appropriate for some specific design aspects and highlighting specific effects. In general, there are many factors such as temperature, discharge current rate, age, etc. affecting the behavior of batteries. The question that arises is that for designing a transportation system or charger system "Should all these features be taken into consideration?" and if not "Which ones should be considered?" and "How much precision is required?" Numerous researches have been done about modeling of batteries for low power and very low power applications such as laptops, cell phones, battery powered digital processors, sensors, etc. In general, these studies mainly deal with behaviors of single cells or small number of cells. However, in the case of EVs/PHEVs including high power battery packs containing hundreds of cells some phenomena are exaggerated or even some can be observed only in battery packs and not in single cells, like electrical characteristics unbalance in series strings or thermal unbalance through battery pack. This shows that modeling battery packs of EVs/PHEVs needs special considerations. Unfortunately, because of their non-mature and expensive technology, not many data and experimental results are available. Hence, there seems a gap between experimentally confirmed battery models available for single cells which can be cheaply verified in any lab on one side and models of expensive battery packs of hundreds of cells with cell equalization circuits, complex controllers, protection circuits, and data acquisition systems which need to be under test for months or years on the other side. Here we first summarize and categorize different models available in the literature with specific focus on vehicular applications and finally will introduce a model which has sufficient precision and is suitable for charger application.

5.1.2.2 Electrochemical Models

Electrochemical models are based on chemical reactions occurring inside the battery cells. As a result, they are the most accurate models, since they simulate the cells at the microscopic scale. They are mostly consisted of six coupled, nonlinear differential equations. Hence, the simulations may need hours or even days of time which makes them not a good candidate for vehicular applications, since, the control systems usually need real-time data.

5.1.2.3 Stochastic Models

Stochastic models are less descriptive but more intuitive compared to the electrochemical models. They are mainly based on discrete-time Markov chains. In its simplest form, the net charge inside the battery is divided into equal charge units, each of which represents the required amount of energy for a unit to be transferred into or out of the cell.

5.1.2.4 Analytical Models

The analytical models generally use some heuristic techniques or empirical formulas to model specific characteristics of batteries. One of the simplest and oldest analytical methods is the Peukert's equation ($C = K/(I^a)$) which shows the dependence of battery capacity on the discharge rate of the battery. Some modifications can be implemented to Peukert's equation to improve it such as integrating the current. However, because of other nonlinear effects like recovery effect this equation can still have high errors in practice. An experimental setup showing the discharge effect of a Lithium-Ion battery for constant power load can be found in [9]. Another example is the Kinetic Battery Model (KiBaM). Batteries can be physically modeled as a combination of two connected reservoirs of water [10] resembling the charge of the battery as shown in Fig. 5.1 Kinetic Battery Model (KiBaM). This model evidently illustrates the relaxation effect in the batteries. Another analytical model known as Rakhmatov and Vrudhula's diffusion model [11] uses the concentration of active materials in the electrolyte as a key point in modeling process. This model shows the unavailable charge inside the

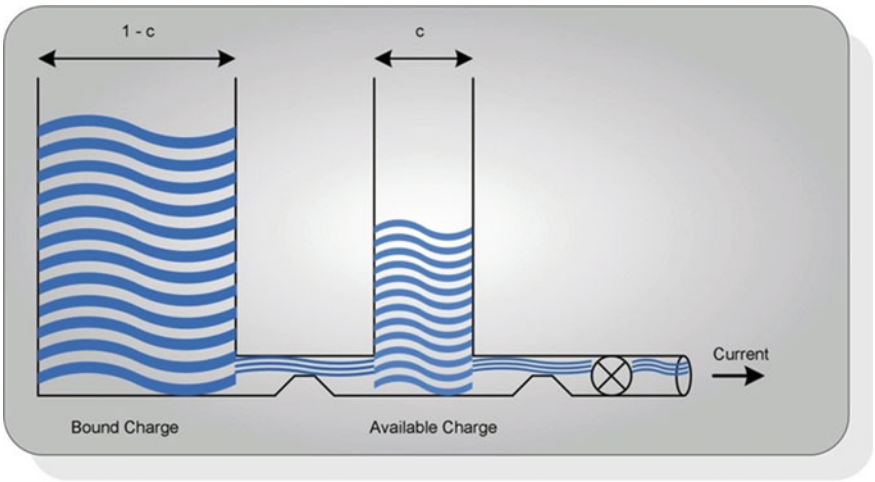

Fig. 5.1 Kinetic battery model (KiBaM)

battery and predicts the runtime of the battery. It can be proved that the diffusion model is in fact a continuous version of the KiBaM [12].

5.1.2.5 Electrical Circuit Models

The electrical circuit models generally use electrical components to model the behavior of a battery. These are the most suitable models for electrical engineering simulation purposes because of their electrical nature which makes them possible to get connected directly to the electrical network. Batteries may be modeled with a constant voltage source or a constant voltage source in series with a resistance in its simplest form, a controlled voltage source or a very large capacity capacitor. Other effects can be modeled by adding more components to the capacitor. For example, the discharge rate capacity can be modeled by adding a controlled voltage source in series with the capacitor with reverse voltage polarity and the coefficients related to different current rates can be stored in a look-up table. The above-mentioned types of battery models are oversimplified and are mainly for investigating the performance of the circuit connected to them rather than evaluating themselves. For instance, the validity of voltage source in series with a resistor is valid for limited purposes such as steady-state DC conditions and short amounts of time, since this model cannot consider the discharge of the battery. Other models, although considering more effects, still are unable to describe dynamic or transient behavior of short time constant load profiles such as pulse discharge. In general, the electrical circuit models can be mainly classified to three main categories [13]: (a) Thevenin-based models, (b) Impedance-based models, and (c) runtime-based models. The above-mentioned electrical circuit models are shown in their simple form in Fig. 5.2. More complicated ones can be found in literature.

The impedance-based models constitute a very important category and are still under investigation and need more research. They can describe the dynamic behavior of the batteries accurately and this is a very important point for battery management systems, hence, we describe them more deeply here. This model category utilizes the fact that impedance characteristics of batteries provide some information about the state of the batteries in general. This information is dependent on different factors such as SOC, temperature, life cycle and charge/discharge current, etc. The method which is used for measuring the impedance spectra is called “Electrochemical Impedance Spectroscopy (EIS)” which can be used for any electrochemical system such as fuel cells, electrochemical capacitors, ultra-capacitors, batteries, etc. This is mainly implemented by applying a small amplitude sinusoidal current or voltage signal to the system and monitoring the response for different frequencies. The reason of choosing small amplitude is to keep the system in the linear region; hence, the response will have the same wave shape with probably different amplitude and phase angle. Using the input signal and response signal, the impedance can be calculated and plotted for different frequencies. In general, there are different chemical reactions happening and

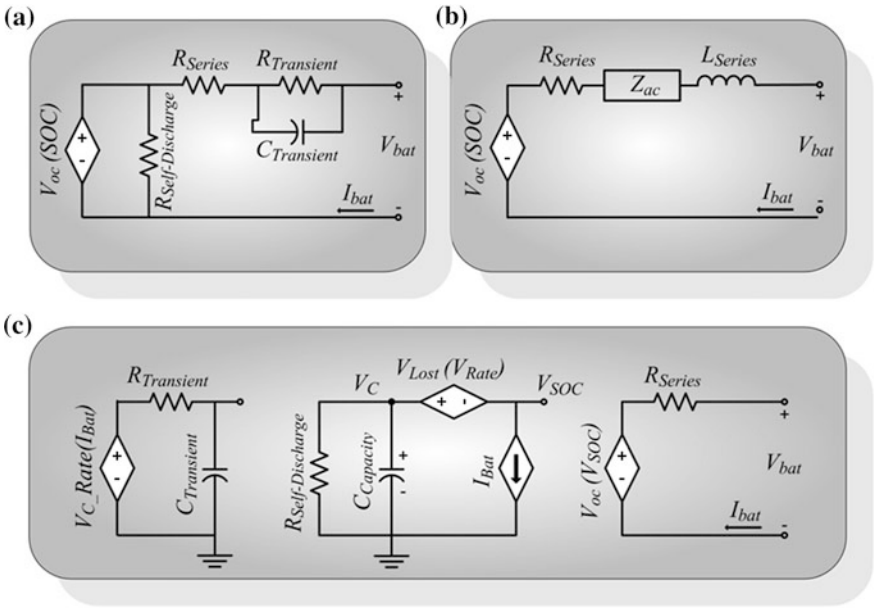

Fig. 5.2 **a** Thevenin-based, **b** impedance-based, **c** runtime-based battery models

different elements inside a battery such as solution resistance, diffusion layer, electrode double layer capacitance, electrode kinetics, etc. By applying different frequencies, some reactions keep happening and others will have lower effect and attenuate for some frequency ranges. This provides the opportunity of modeling different reactions and parameters inside the battery with different electrical components in the electrical circuit model. Despite this, still the response will be a combination of different effects and this makes the EIS analysis somewhat difficult [14]. There are different approaches for analyzing the EIS, however, the most conventional and suitable one is interpreting the results in circuit language. The complete electrochemical equivalent circuit model for Lithium-ion batteries is shown in Fig. 5.3. Other chemistries such as lead-acid may also be presented with the same configuration. Each of the elements is modeling a phenomena or element

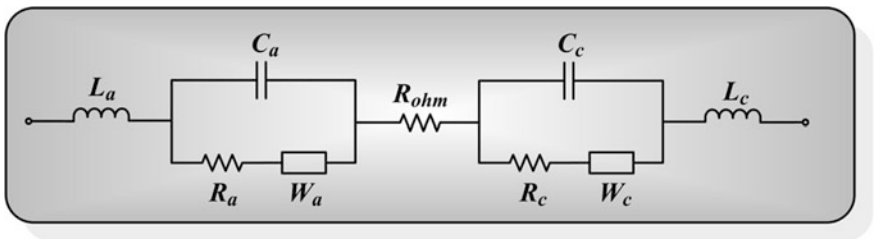

Fig. 5.3 Electrochemical equivalent circuit model

inside the battery. For example, the electrodes of the battery are porous. At high frequencies, this causes the electrodes to show an inductive behavior. The inductors L_a and L_c are modeling this behavior. The letter "a" stands for anode and "c" stands for cathode. The interpretation of other elements can be found in [15]. Other configurations are also possible, such as ladder circuit representation [16].

Choosing the circuit model configuration is the first step. The second step is to determine the values of parameters depending on the battery chemistry, Ampere-hour capacitance, SoC, type of electrodes and electrolyte, load profile, etc., in other word, system identification. There are different approaches available in the literature, one of which proposed in [16] is a universal parameterization technique which can be applied to different chemistries with different capacitance and charge/discharge ratings. Despite the effectiveness of these configurations and approaches for design purposes, sometimes they are too complex and time consuming for real-time control applications. This problem is discussed in [17] and a simplified model and identification technique suitable for real time applications is proposed, which is the case for battery management systems in EVs/PHEVs.

Another modeling approach is based on modeling the ohmic resistance of batteries. In general the internal resistance of batteries can be divided into two main parts: ohmic resistance and polarization resistance. The ohmic resistance mainly consists of electrode resistance, electrolyte resistance, separator resistance, and contact resistance. On the other side, polarization resistance is dependent on chemical polarization and electrolyte concentration. These two types of resistances are illustrated in Fig. 5.4, which is the result of applying a pulse discharge current to the battery and monitoring the voltage profile.

The immediate vertical voltage drop is due to the ohmic resistance "R_{ohm}", while the exponential voltage drop is due to the polarization resistance "R_{pol}" which happens slowly. Ohmic resistance has some information about state of the battery. For instance, higher battery ohmic resistance will cause lower battery voltage, more ohmic loss, shorter discharge time, and lower power available from the battery. Hence, modeling the ohmic resistance of a battery provides some valuable input to

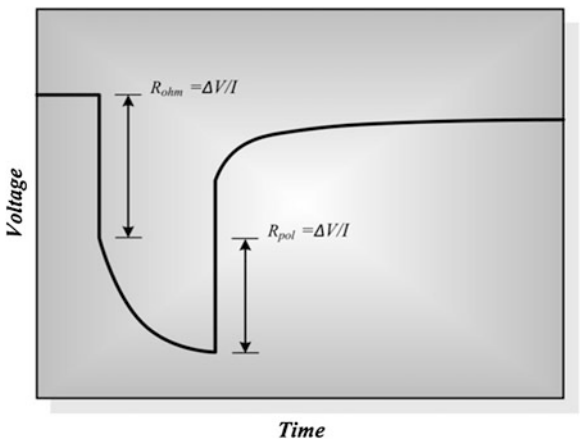

Fig. 5.4 Typical voltage response of Li-ion battery discharged by a pulse discharge current

the battery management system for better utilization of cells inside the pack which will eventually lead to better life cycle. Reference [18] investigates the relation of ohmic resistance with life cycle, discharge rate, depth of discharge, temperature, SoC, and finally comes up with a model which can be used in lifetime evaluation of batteries. Similarly [19], proposes a nonlinear resistance dependent on SoC which can add to the accuracy of the battery model while used.

5.1.2.6 Thermal Models

Another significant factor affecting battery packs performance and life cycle is temperature. Experimental results show that each 10 °C increase in the operating temperature compared to the nominal temperature of the designed battery pack will reduce the life cycle of the batteries approximately to half of the nominal life cycle. This simply shows the importance of the temperature factor. As mentioned before, there are some affects that are only observed in the battery packs and not in single cells. One of these effects is the temperature difference through a battery pack. For example, cells which are in the middle of the battery pack have higher temperature compared to those at the edges of the pack because of less ventilation. Since battery parameters change with temperature variation, different cells inside a pack will have different characteristics. This cell mismatch will significantly reduce the life cycle of the whole pack. This effect and other effects contributing to the life cycle of battery packs are investigated in [20]. This shows the need of thermal models of the battery packs which helps designing a more effective battery management system. These thermal effects are being investigated in laboratories like National Renewable Energy Laboratory (NREL) and results can be found in their reports [21, 22, 23].

The importance of temperature effects is not only for improving performance. Safety issues for Lithium-based batteries are highly dependent on temperature. Thermal runaway of Lithium-ion batteries is a very important safety point and must be considered in the battery management systems. This involves the availability of accurate thermal models of battery packs. It is worth mentioning some of the models available in the simulation softwares used for vehicular applications. One of the well-known simulators is ADVISOR by the National Renewable Energy Laboratory written in Matlab/Simulink environment. The models which have been used by this software are: (i) internal resistance model, (ii) resistance–capacitance (RC) model, (iii) PNGV capacitance model, (iv) neural network lead-acid model. Detailed description of these models and their accuracy can be found in [24].

5.1.2.7 Other Models

Battery models can be categorized based on different approaches they are driven. However, there are other important factors that battery models can be classified based on. Some of them can be mentioned as [25]: (i) the types of load profiles

supported (e.g., constant current vs. variable current or constant power vs. variable power), (ii) supported battery chemistries (Lithium-ion, Pb-Acid, etc.), (iii) battery effects that are modeled (e.g., relaxation effect, current rate capacity effect, thermal effect, etc.), (iv) computational efficiency (being fast enough for real-time control purposes), and (v) degree of precision in predicting real-life behavior of the batteries. In addition to the above-mentioned models, there are more advanced modeling techniques such as Extended Kalman Filter (EKF) for estimating the parameters of a battery model which increases accuracy especially in the case of variable current load profile which is the case for vehicular applications [26]. It is noted that Kalman filtering is a least-squares optimal estimation algorithm for linear dynamic systems where modeling and measurement errors are assumed as Gaussian white noises [27]. The algorithm recursively improves the state estimate such that the variance of the estimation error at any iteration is minimized. First, the previous state estimate and its error covariance are updated using the state-space model. Then, the updated estimate is corrected based on the latest output measurement in an optimal fashion. On the other hand, EKF is the extended form of this estimation algorithm to nonlinear dynamic systems. While the nonlinear state-space model is directly employed for the state estimate update, the other operations are done using the linearized model. Modeling the transient behavior or relaxation effect of batteries can be modeled by parallel-connected RC circuits putting in series with the battery model. By increasing the number of these brunches the accuracy of the model increases, however it causes the increased complexity and simulation time as mentioned before. In [28] it is shown that the selection of an appropriate battery model for a certain PHEV application can be formulated as a multi-objective optimization problem balancing between the model accuracy and the computational complexity. This multi-objective optimization problem is mapped into a weighted optimization problem to solve. Genetic Algorithm has also been used for battery modeling purposes. Sometimes it is very useful to derive a model based on data sheets available from manufacturers. In [29] the charge and discharge characteristics of the battery supplied by the original equipment manufacturers (OEMs) are used to find the parameters of an equivalent circuit model (ECM) for a battery. A multi-objective optimization genetic algorithm (MOOGA) is proposed to find the model parameters. This reduces the time of parameter extraction and also eliminates the need of extensive experimentation in the early phases of design. A genetic algorithm (GA), a sub-class of the larger class of evolutionary computation techniques, is a randomized search method for finding the global solution to an optimization problem, based on the principles of natural evolution, such as inheritance, mutation, selection, and so on [30]. In this method, an initial population of solution candidates evolves toward an improved generation. In each generation, the fitness of any candidate solution is evaluated to form a new population of solutions. This iteration is continued till a specific number of generations is produced and/or a satisfactory fitness level is generated [31].

5.1.2.8 Utilized Battery Model

First of all, it is important to note that every battery model is suitable for a specific application and design purpose. Having a very detailed and accurate model is not necessarily an advantage for any kind of application. The accuracy and complexity of a model should be justified for any specific application to avoid unnecessary calculations and complexity. Since our application is a battery pack charger and charging process happens during hours of time, the battery pack is a very slow dynamic system with a very big time constant compared to power electronics circuits connected to it which have time constants of time scales of milliseconds or even microseconds. This fact will be reminded during the battery modeling process. In addition, considering all the details and effects in EV/PHEV battery packs such as cell equalization circuits, sensors, controllers, thermal effects, relaxation effect, and so on is not practical since they add extra complexity to the system without any valuable advantage for designing a battery charger. This is a realistic consideration in simulation packages as well. For example, the battery model [32] used in Matlab/Simulink which we will also use for verification of our model has some limitations and assumptions such as constant internal resistance, neglecting Peukert's effect, temperature, self-discharge, and memory effect. Despite all of these limitations, this model gives very accurate results compared to practical data and manufacturer datasheets. Neglecting small differences in single cells characteristics, we can assume the battery pack with all of its components and effects as a very big single battery cell. For our simulation purposes, we have chosen the battery pack of commercialized Chevy Volt as an example which has been introduced to the market recently as a successful PHEV with a noticeable sale in North America, Europe, and Asia with lots of awards from different organizations. The specifications of this battery pack can be summarized as a 16 kWh, 45 Ah Lithium-Ion battery pack, 10.4 kWh of which is allowed to be used according to the battery management system for life cycle assurance. It consists of 288 individual cells arranged into nine modules with nominal voltage of 355 V. A typical voltage characteristic and SoC versus time is depicted in Fig. 5.5 which is obtained using Matlab/Simulink battery model with the specifications of Chevy Volt battery pack by connecting a 15 A DC current source to the battery.

For prolonging life cycle of battery packs battery management systems are usually set to operate the battery packs over 30 % and less than 90 % of SoC. This is valid also for Chevy Volt which allows the battery pack to operate only in a 60 % SoC window. If Fig. 5.5 is shown just for SoC range of 30–90 % Fig. 5.6 will be obtained.

As it can be seen from Fig. 5.6 the voltage characteristic of Li-ion battery is fairly linear with an almost constant slope for the range of 30–90 % SoC which is our SoC range of interest. This reminds of a big capacitor in parallel with a resistor getting charged by a constant current source. So we use the model shown in Fig. 5.7 as our battery model.

To find the proper value of capacitor, according to the equation $i_c = C\ \mathrm{d}V/\mathrm{d}t$ and constant current value, if the derivative of voltage is known the C value can

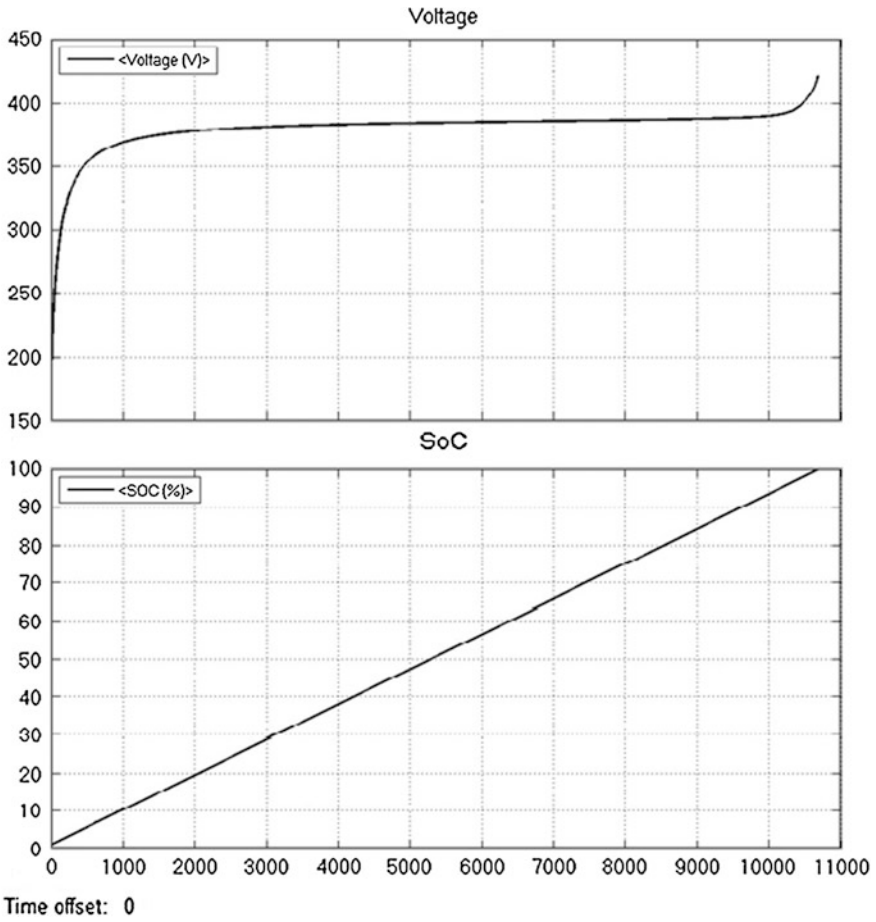

Fig. 5.5 Voltage characteristic of 45 Ah Li-ion battery

be calculated. Fig. 5.8 shows voltage derivative along with voltage and SoC. As visible in Fig. 5.8 the voltage derivative of the battery pack is around 10^{-3} (V/s) which results in a capacitor value of 15,000 F. The resistor in parallel with the capacitor may seem unnecessary; however, considering it has some advantages. First of all it can model the self-discharge of the battery pack. In addition, since most of the available power converter models assume a resistor in parallel with a filter capacitor as a load this approach is compatible with existing power converter models and minimizes the probable required modifications while connecting the battery model to the power converter which highly simplifies the modeling procedure of the overall system. The value of this resistor can be calculated based on the self-discharge rate of the battery which is dependent on the temperature and is variable for different chemistries. For Lithium-ion batteries the self-discharge rate

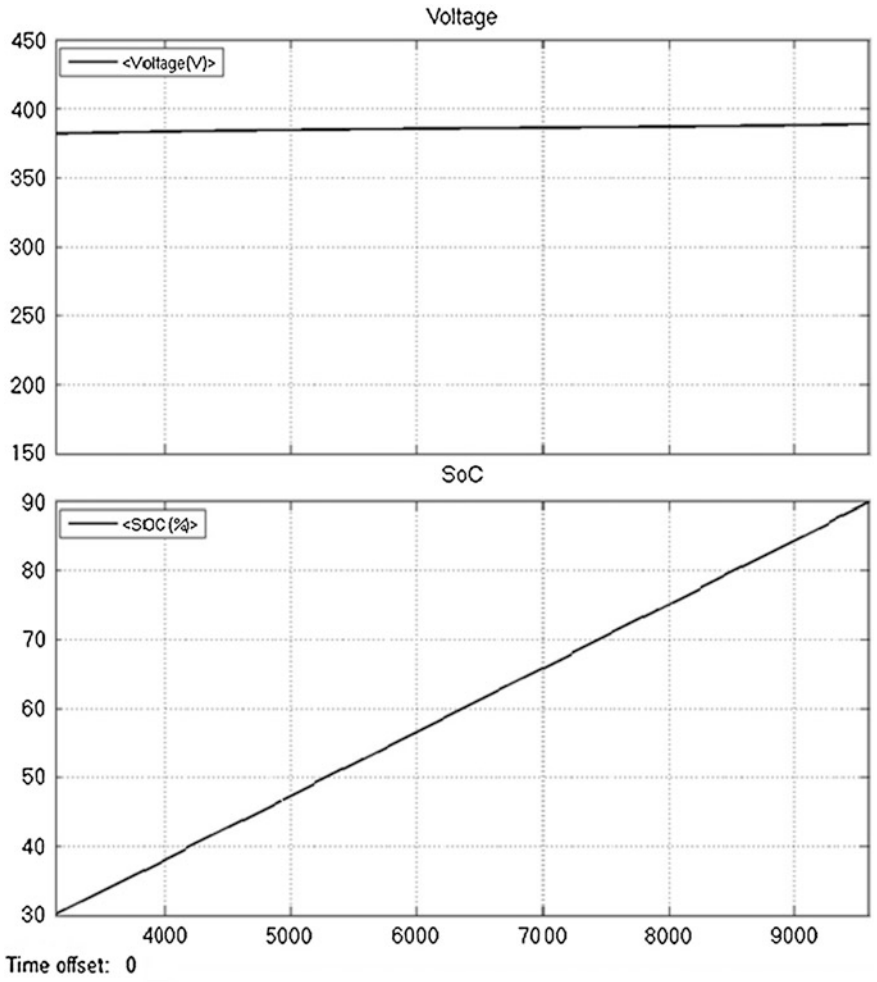

Fig. 5.6 Voltage characteristic of 45 Ah Li-ion battery from 30 to 90 % SoC

per month is 8 % at 21 °C, 15 % at 40 °C, and 31 % at 60 °C [33]. Since battery packs warm up during charging process because of generated heat and they are enclosed in a package, we assume 40 °C for our calculations as a reasonable average temperature.

During self-discharge according to the battery model, the capacitor is discharging through the parallel resistor, so a simple KCL equation results in $dV/dt = V/(R \times C)$. Since the charge in a capacitor is linearly dependent to the voltage of the capacitor ($q = C \times V$), self-discharge can be measured using the voltage. According to Fig. 5.7 voltage of the battery pack at 90 % SoC is around 390 V. According to 15 % per month rate of discharge, the battery pack voltage will

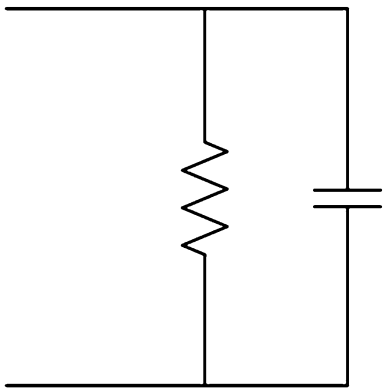

Fig. 5.7 Parallel RC battery model

decrease around 0.15 × 390 V = 58.5 V per month. Using the KCL equation mentioned above (58.5/(30×24×60×60) = 390/(R×15,000)) the resistor value will be calculated as around 1,150 Ω.

To verify the validity of the derived model with the parameter values calculated above, the results from the battery model in Matlab along with the results from the parallel RC model are shown on the same plot as in Fig. 5.9. The continuous black line shows the results from Matlab battery model and the dashed magenta line shows the data from parallel RC model with calculated parameter values. First row of Fig. 5.9 shows the voltage of the battery, second row shows the SoC change, third row represents the voltage derivative versus time and forth row explains the voltage error between two models. There may seem a big difference between voltages and voltage derivatives and huge voltage error, however, if we consider only from 30 to 90 % SoC **Fig.** 5.10 will be obtained which shows very good match between two models. As visible from **Fig.** 5.10 the voltage error between two models is less than one volt which means less than 0.3 % error which is a great match.

5.1.2.9 Summary

In this chapter, battery parameters such as capacity, C rate, SoC, DoD, etc. which are used to characterize batteries were introduced. Characteristics of commonly used batteries in vehicular applications such as Lead-Acid, Nickel Cadmium, Nickel-Metal Hydride, Lithium-Ion, and Lithium Polymer were studied. Different chemistries may need different charging methods. Various charging schemes such as constant voltage charging, constant current charging, taper current charging, pulse charging, reflex charging, and float charging were mentioned. It is very important to terminate the charging process on time in order to avoid damaging expensive battery packs. Several termination methods were reviewed including time, voltage, voltage drop, current, and temperature.

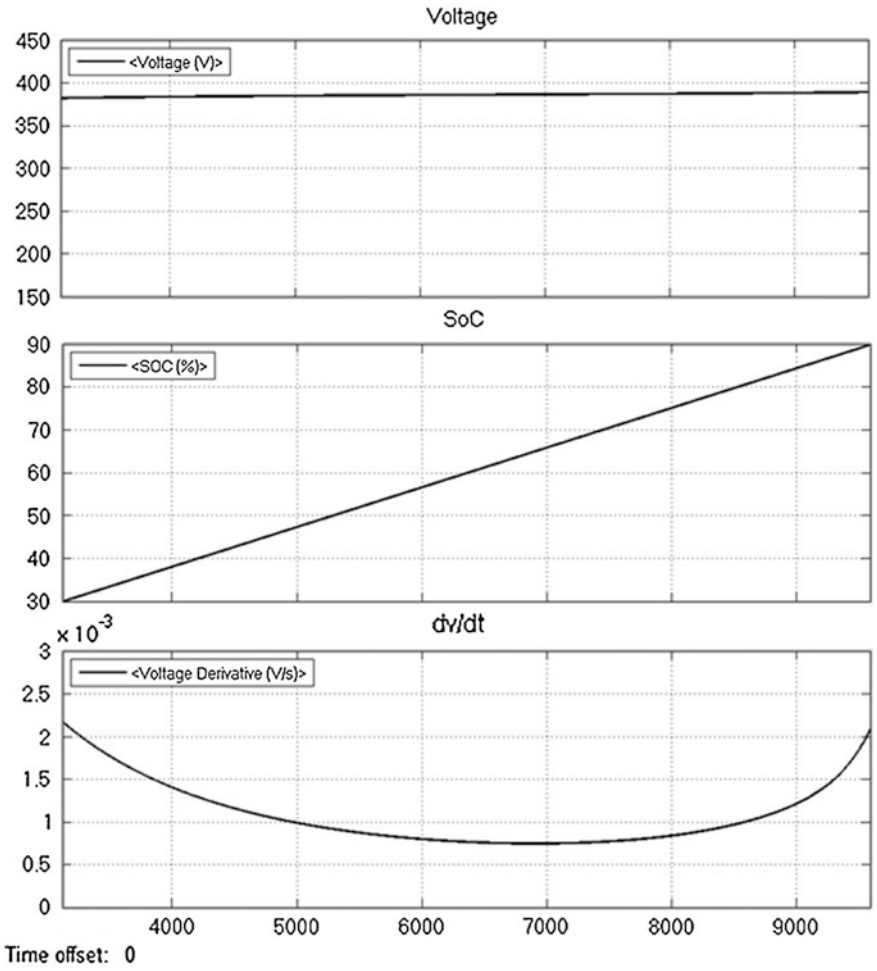

Fig. 5.8 Voltage characteristic and derivative of 45 Ah Li-ion battery from 30 to 95 % SoC

Cell balancing which is a very important issue in extending the life time of battery packs was described and its effects were investigated. Different cell balancing techniques such as charging, passive, and active were studied. Importance of SoC estimation in the performance of battery charger was mentioned and different SoC estimation techniques such as complete discharge, ampere-hour counting, measurement of physical characteristics, open circuit voltage, and soft computation techniques were investigated. Charging algorithm was defined and a typical charging algorithm for Lead-Acid batteries were mentioned.

Not only the performance and accuracy of the battery charger highly depends on the battery model, for designing any type of system the model of the load

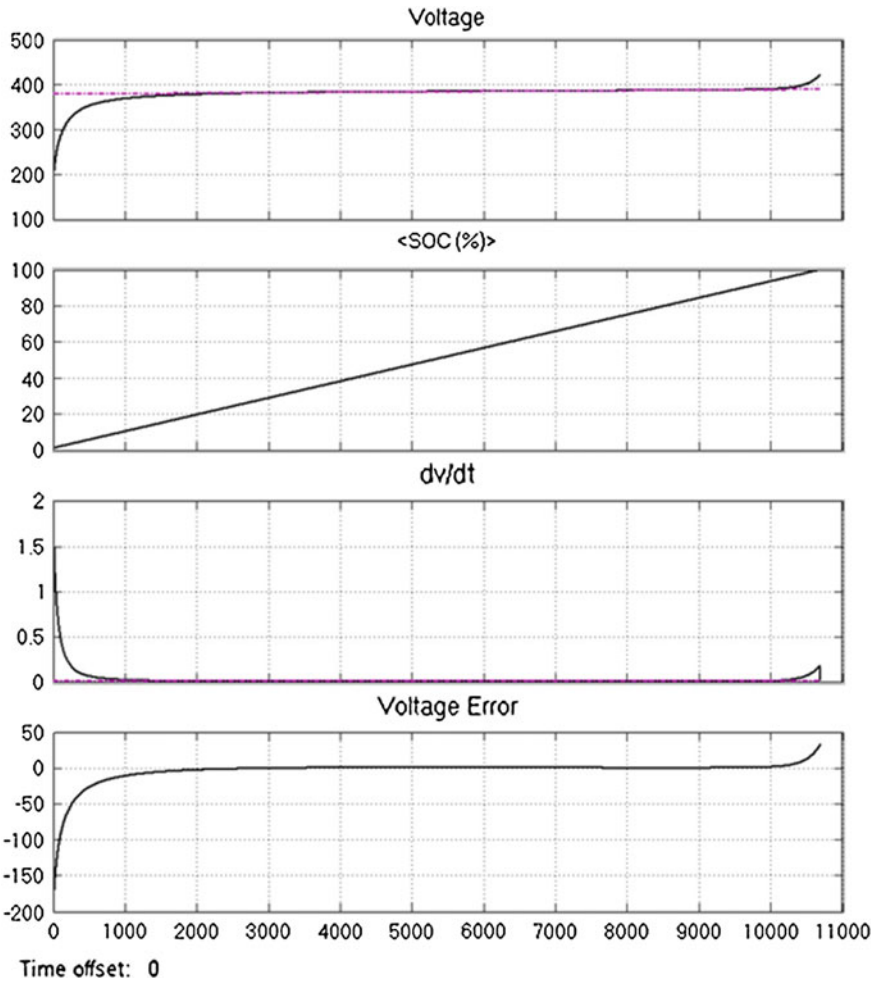

Fig. 5.9 Simulation results for matlab battery model and parallel RC model for 100 % SoC window

should be appropriately selected to ensure reliable and efficient performance of the system. Various types of battery models such as electrochemical models, stochastic models, analytical models, electrical circuit models, thermal models, etc., have been comprehensively investigated in this chapter. According to our application and the required accuracy a simplified battery model has been utilized which shows acceptable accuracy.

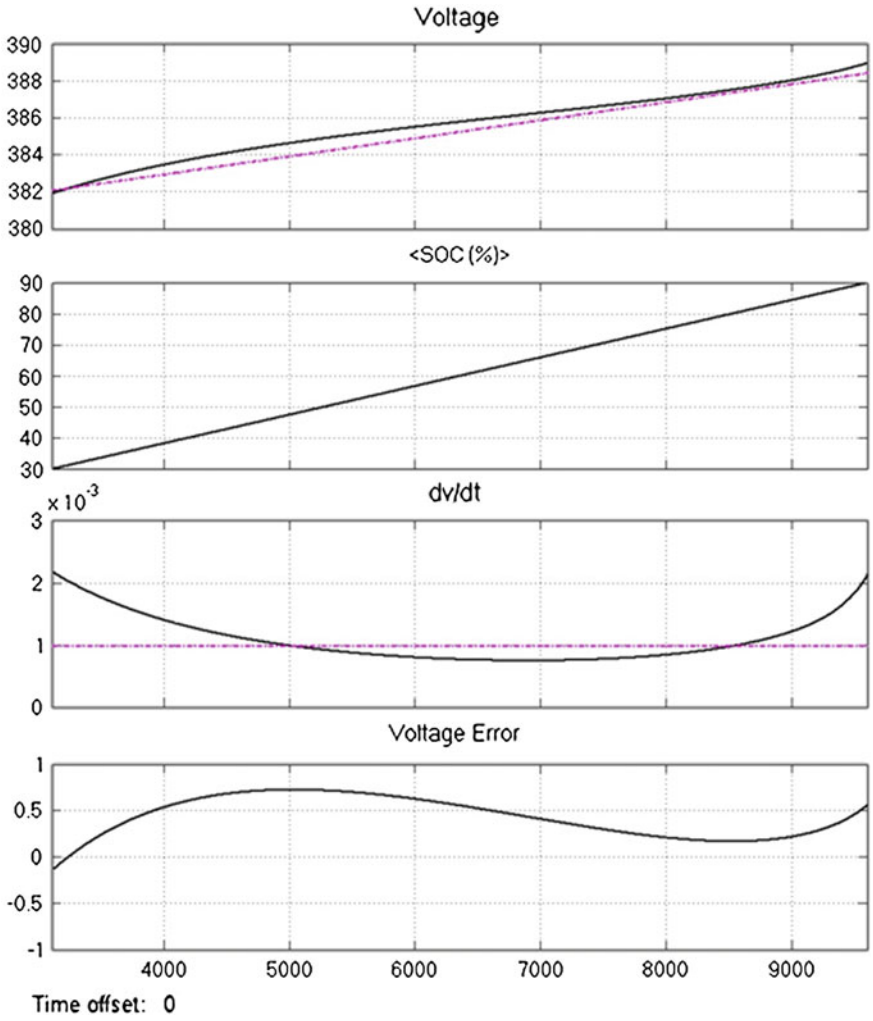

Fig. 5.10 Simulation results for matlab battery model and parallel RC model for 60 % SoC window

5.1.3 Lithium-Ion Batteries

5.1.3.1 Introduction to Lithium Batteries

Lithium rechargeable battery technologies, although not mature enough to be used in EV/PHEVs, prove to be the best solution for PHEV applications today. For instance, a 20 kWh lithium-ion battery weighs about 160 kg (100–140 kWh/kg), which is acceptable for PHEV applications. In contrast, current HEV Nickel-Metal Hydride (Ni–MH) batteries weigh between 275 and 300 kg, for the same

application. Moreover, Li-ion batteries also depict excellent power densities (400–800 W/kg) [3], allowing more than 2C discharge rate. "C" represents the discharge of full capacity in 1 h (at the rate of 40–80 kW peak power, in a 20 kWh pack), and up to 10 C for some chemistries [5, 6]. However, they also suffer from many drawbacks. One of them is the cost (projected at about $250–$300/kWh; $600/kWh for the $LiFePO_4$ chemistry), which is the most expensive of all chemistries [1, 3]. The second drawback is that lithium is a very flammable element, whereby its flame cannot be put off with a normal ABC extinguisher [34]. Finally, Li-ion batteries have a cycle life between 400 and 700 cycles, which does not satisfy HEV expectations [3]. Therefore, finding a solution to these issues is extremely crucial.

In order to resolve safety issues, few manufacturers have modified the chemistry of the battery [5, 6]. This is currently the case for Lithium iron phosphate ($LiFePO_4$) batteries, which seem to have handled few issues related to EV applications, such us reducing flammability and obtaining higher cycle life (1,000 cycles or more) [5, 6], but the higher cost and equalization issues are still pending to be resolved.

With reference to cycle life, the battery can suffer significant degradation in its capacity, depending on its usage. Furthermore, the internal resistance also increases with each charge cycle. Also, according to the chemistry and the quality of the cells, a battery typically loses about 20 % of its initial capacity after about 200–2,000 full cycles, also known as the 100 % SOC cycles. The cycle life can be greatly increased by reducing SOC, by avoiding complete discharges of the pack between recharging or full charging. Consequently, a significant increase is obtained in the total energy delivered, whereby the battery lasts longer. In addition, over-charging or over-discharging the pack also drastically reduces the battery lifetime [35–42].

5.1.4 Characteristics of Lithium-Ion Batteries

Lithium-ion batteries have noticeably high specific energy, specific power, and great potential for technological improvements providing EVs and PHEVs with perfect performance characteristics such as acceleration performance. Their specific energy is in the range of 100–250 Wh/kg. Because of their nature, Li-ion batteries can be charged and discharged faster than Pb-Acid and Ni–MH batteries, making them a good candidate for EV and PHEV applications. Besides all, Li-ion batteries have an outstanding potential for long life if managed in proper conditions, otherwise, their life can be a disadvantage. One of the main reasons is almost the absence of memory effect in Li-based batteries. A weak point of Li-based batteries is safety since they are highly potential for explosion due to overheating caused by overcharging. They can almost easily absorb extra charge and get exploded. The use of advanced battery management systems (BMS) can ensure reliable range of operation of Li-ion batteries even in cases of accidents. Another advantage is that Li-ion batteries have environmental friendly materials when compared with Nickel-based batteries.

5.1.5 Cycle Life Versus State of Charge

5.1.5.1 Cycle Life versus SOC

In the context of this section, 100 % SOC is the state of a cell after being fully charged at 4.2 V per cell, and 0 % SOC corresponds to the state of a fully discharged cell (3 V per cell). The initial Capacity (C) is the capacity during the first few cycles that go from 100 to 0 % SOC, and the cycle life is the amount of cycles after the cell loses 20 % of its initial capacity.

If the battery is initially not fully charged, and not fully discharged during the discharge period and before charging again, then the full capacity is not used. Contrary to the Ni–Cd batteries, in lithium batteries this is actually beneficial to the cell. In fact, the cycle life is greatly increased.

In Fig. 5.11a, the cycle life of several available cells in the market are shown, under different SOC during the cycle. It can be appreciated how cycle life increases as SOC utilization is reduced. In this case, SOC utilization is considered to be centered around 50 % SOC, or half charge. This is also confirmed by Fig. 5.11b, where the total energy delivered during the cell lifetime is also higher when SOC reduces. The latter is expressed in C units (initial capacity under 100 % SOC).

The trend curves are critical for economical analysis. They are estimated based on the tests performed by [35–43]. Each point represents the value during a test performed on multiple reference sources, and the dotted line is the calculated trend of all those values. The plots of Figs. 1–4 can also be the subject matter for further analyses. For example, in 360 V HEV batteries, a string of 100 cells is used. In this simulation, a 5 % initial dispersion (σ) in the capacity of the cells is considered, charging the pack at 4.1 V per cell (86 % SOC), and discharging at 72 % of the total capacity (up to 14 % SOC). An interesting trend can be observed. The smaller capacity cells swing initially from about 92–8 % SOC, which is 84 % of the total capacity, instead of the average 72 %. This higher SOC swing can be translated into less cycle life (282 cycles, instead of 600), which is a deeper degradation for the smallest capacity cells.

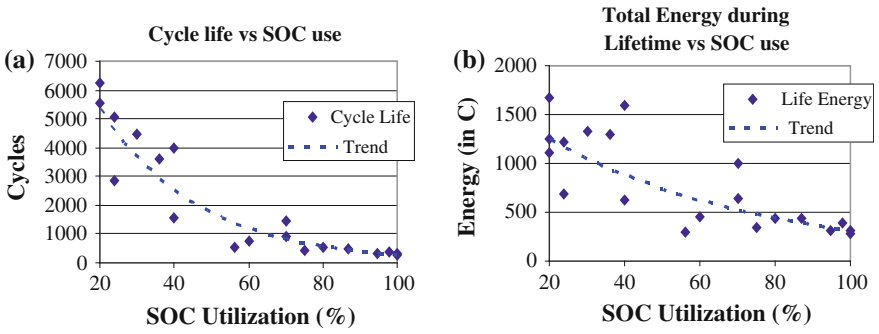

Fig. 5.11 **a** Cell cycle life versus SOC utilization; **b** cell total energy delivered during total lifetime versus SOC utilization

This effect deepens during successive cycles, producing a premature degradation of smallest capacity cells, which brings the whole pack into a premature "out of service." Figure 5.12a shows the distribution of SOC (quantity of cells vs. SOC) at the end of discharge, in steps of 47 cycles. Figure 5.12b shows the distribution of SOC (quantity of cells versus SOC) at the beginning of discharge, in steps of 47 cycles. The gradually increasing SOC span is an indication of the reduced capacity.

From Fig. 5.12, it is clear that the end of life arrives faster, because of the initial dispersion in capacity. Another critical inference that can be drawn is that the dispersion increases with cycle life. In this case, 282 operation cycles causes the smallest capacity cell to completely discharge, even if the demanded capacity is 72 % of the nominal capacity. The average capacity cell, on the other hand, withstands 602 cycles of 72 % nominal capacity, before overcharging or over-discharging. Although, this cycle life is better, it is still not enough from the point of view of PHEV energy storage applications.

Throughout this chapter, several issues related to lithium batteries, for EV/HEV/PHEV applications, have been exposed, particularly the unbalance in SOC among cells. It is clear that there can be considerable improvements in lifetime of a battery pack, if all cell capacities are suitably matched. A practical solution to obtain cell equalization exists in the form of an electronic cell equalizer. In Chap. 6, the most common equalizer topologies are reviewed.

5.1.6 Solutions to Keys Issues

An alternative way to solve the above-mentioned problems, which are essentially common to the all lithium rechargeable batteries, is using electronic control, in the form of cell voltage equalizers. Few of the control rationales are briefly listed below.

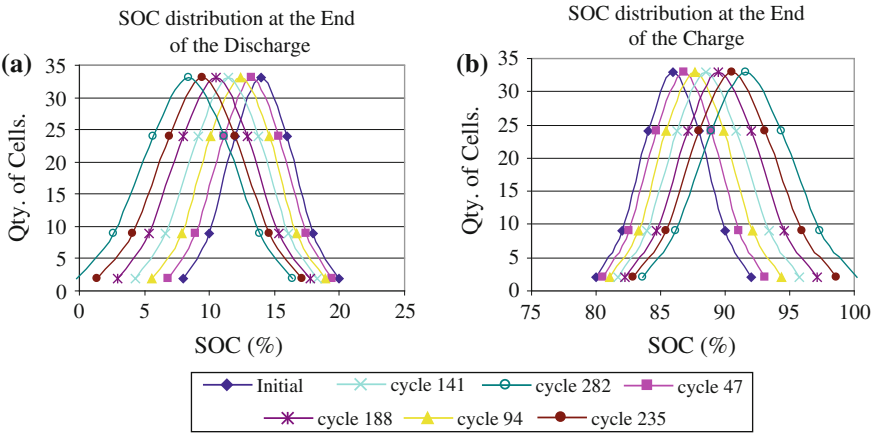

Fig. 5.12 **a** Cell distribution of SOC in a pack, with initial $\sigma = 5$ %, at the end of discharge; **b** cell distribution of SOC in a pack, with initial $\sigma = 5$ %, at the end of charge

5.1.6.1 Over-Voltage Protection

This functionality cuts charging current when the total voltage is more than 4.3 V per cell. This is because, at higher voltages, metallic lithium is formed inside the cell [35], which is highly flammable, as explained earlier [34]. For the sake of simplicity, this protection is sometimes applied to the whole pack of cells, instead of measuring the voltage of each cell.

5.1.6.2 Under-Voltage Protection

This functionality cuts discharging current when voltage is under 2.5 V per cell. Under this voltage, some capacity fades, and a specific quantity of unwanted copper plating is formed inside the cell [36]. This unwanted copper may generate internal short circuits. Also in this case, for the sake of simplicity, the total voltage might be measured, instead of verifying the voltage of each cell.

5.1.6.3 Short Circuit or Over-current Protection

This protection scheme disconnects the charging/discharging current if it is over a certain limit (2–50 ℃, depending on the cell technology) [43].

5.1.6.4 Overheating Protection

There are two reasons as to why it is recommended to avoid working at high temperature: First is safety, because of the lithium flammability [34]. The second is degradation of the capacity increases with higher cell temperature. In this case, current stops flowing, if pack temperature rises over a certain value (about 60 °C) [43].

5.1.6.5 Cell Voltage Equalizing

Using a simple cell voltage equalizer, based on heat dissipation (using a resistor), some of the excessive power from the higher voltage cell can be successfully purged. Due to heating problems that this method may involve, the discharging current must be relatively small (about 300 mA, depending on the capacity of the pack).

Although these protection functionalities are useful, they prove to be highly insufficient. In fact, the differences in capacity and internal resistance from cell-to-cell, within the same pack, may result in unwanted voltage peaks, especially during the final stages of charge and discharge. For example, during the charge of a battery pack, due to differences among the cells, a smaller capacity cell will

finish with a voltage higher than the average. Depending on the protection circuitry, usually controlled by the total pack voltage, this situation may not be detected, and even if detected, the protection will simply cut the charger, reducing the battery capacity and not solving the issue at hand. A resistive equalizer will only reduce the voltage of the overcharged cell gradually, but it will not be able to avoid degradation of the cell.

A similar situation occurs during discharge. The lower capacity cell suffers from over-discharge, which is not detected by the protection circuit. Furthermore, the reduced capacity cell goes into overcharge and over-discharge. Thus, it suffers from additional capacity reduction and the cell rapidly deteriorates, which downgrades the overall capacity of the pack.

References

1. AA Portable Power Corp., Li-ion 18650, quantities of 50,000, Jan. 2009
2. T. Markel, A. Simpson, Energy storage systems considerations for grid-charged hybrid electric vehicles, in *Proceedings of IEEE Vehicle Power and Propulsion Conference*, Chicago, 2005, pp. 344–349
3. M. Anderman, F. Kalhammer, D. MacArthur, Advanced batteries for electric vehicles: an assessment of performance, cost, and availability, *Technical Report for the State of California Air Resources Board*, June 2000
4. U.S. DOE, *Retail Gasoline Historical Prices.* June 2009
5. A123 systems, Inc.; see company website: http://www.a123systems.com
6. LiFeBATT, Inc.; see company website: http://www.lifebatt.com
7. T.R.Crompton, *Battery Reference Book*, 3rd edn (Newnes, Oxford, 2000)
8. I. Buchmann, *Batteries in a Portable World: A Handbook on Rechargeable Batteries for Non-Engineers*, 2nd edn (Cadex Electronics Inc, Richmond, 2001)
9. S. Park, A. Savvides, M.B. Srivastava, in *ISLPED '01 Proceedings of the 2001 International Symposium on Low Power Electronics and Design.* Battery capacity measurement and analysis using lithium coin cell battery, California, USA, 2001
10. J.F. Manwell, J.G. McGowan, Lead acid battery storage model for hybrid energy systems. Elsevier J. Sol. Energy **50**(5), 399–405 (1993)
11. D. Rakhmatov, S. Vrudhula, D.A. Wallach, A model for battery lifetime analysis for organizing applications on a pocket computer. IEEE Trans. VLSI Syst. **11**(6), 1019–1030 (2003)
12. M.R. Jongerden, B.R. Haverkort, Which battery model to use? IET Softw. **3**(6), 445–457 (2009)
13. M. Chen, G.A. Rincon-Mora, Accurate electrical battery model capable of predicting runtime and I-V performance. IEEE Trans. Energy Convers. **21**(2) 504– 511 (2006)
14. Gamry instruments. Application note: basics of electrochemical impedance spectroscopy (2007), www.gamry.com
15. A. Ramamurthy, S. Notani, S. Bhattacharya, Advanced lithium ion battery modeling and power stage integration technique, in *2010 IEEE Energy Conversion Congress and Exposition (ECCE)*, pp. 1485–1492, 12–16 September 2010
16. E. Barsoukov, J.H. Kim, C.O. Yoon, H. Lee, Universal battery parameterization to yield a nonlinear equivalent circuit valid for battery simulation at arbitrary load. J. Power Sour. **83** (1–2), 61–70 (1999)

17. J. Lee, J. Lee, O. Nam, J. Kim, B.H. Cho, H-S. Yun; S-S. Choi, K. Kim, J.H.Kim, S. Jun, Modeling and real time estimation of lumped equivalent circuit model of a lithium ion battery, in *12th International Power Electronics and Motion Control Conference, 2006. EPE-PEMC 2006*, pp. 1536–1540, 2006
18. X. Wei, B. Zhu, W. Xu, Internal resistance identification in vehicle power lithium-ion battery and application in lifetime evaluation. International conference on measuring technology and mechatronics automation, icmtma, vol. 3, pp. 388–392, 2009
19. L.W. Yao, J.A. Aziz, Modeling of lithium ion battery with nonlinear transfer resistance. IEEE applied power electronics colloquium (Iapec), pp. 104–109, 18–19 April 2011
20. A. Shafiei, S.S. Williamson, Plug-in hybrid electric vehicle charging: current issues and future challenges. IEEE vehicle power and propulsion conference (VPPC), pp.1–8, 1–3 September 2010
21. A. Pesaran, V. Johnson, Battery thermal models for hybrid vehicle simulations. J. Power Sour. **110**, 377–382 (2002)
22. D. Bharathan, A. Pesaran, A. Vlahinos, G.-H. Kim, Improving battery design with electro-thermal modeling. IEEE conference on vehicle power and propulsion, p. 8, 7–9 September 2005
23. X. Hu, S. Lin, S. Stanton, W. Lian, A foster network thermal model for HEV/EV battery modeling. IEEE Trans. Ind. Appl. **47**(4) 1692–1699 (2011)
24. V.H. Johnson, Battery performance models in advisor. Elsevier J. Pow. Sour. **110(**2), 321–329 (2002)
25. Lahiri, K.; Raghunathan, A.; Dey, S.; Panigrahi, D, Battery-driven system design: a new frontier in low power design, in *Design Automation Conference Proceedings of ASP-DAC 2002. 7th Asia and South Pacific and the 15th International Conference on VLSI Design*, pp. 261–267, 2002
26. M. Knauff, C. Dafis, D. Niebur, A new battery model for use with an extended kalman filter state of charge estimator. American control conference (ACC), pp. 1991–1996, 2010
27. B.O. Anderson, J.B. Moore, *Optimal Filtering* (Prentice-Hall, Englewood Cliffs, 1979)
28. H. Zhang, M-Y. Chow, Comprehensive dynamic battery modeling for PHEV applications. IEEE power and energy society general meeting, pp. 1–6, 25–29 July 2010
29. P. Kumar, P. Bauer, Parameter extraction of battery models using multi objective optimization genetic algorithms. 14th international conference on power electronics and motion control (EPE/PEMC), pp. T9-106-T9-110, 6–8 September 2010
30. W. Banzhaf, P. Nordin, R. Keller, F. Francone, *Genetic Programming, an Introduction* (Morgan Kaufmann Publishers, San Francisco, 1998)
31. D.E. Goldberg, *Genetic Algorithms in Search, Optimization, and Machine Learning*. (Addison-Wesley, Reading, l989)
32. O. Tremblay, L.-A. Dessaint, Experimental validation of a battery dynamic model for ev applications. World Electr. Veh. J. **3**. ISSN 2032-6653 - 2009 AVERE, EVS24 Stavanger, Norway, 13–16 May 2009
33. H. Abea, T. Muraia, K. Zaghibb. Vapor-grown carbon fiber anode for cylindrical lithium ion rechargeable batteries. J. Power Sour. **77(**2), 110–115 (1999)
34. H. Webster, Flammability assessment of bulk-packed, rechargeable lithium-ion cells in transport category aircraft. Office of aviation research and development, September 2006
35. P. Ramadass, B. Haran, R. White, B. Popov, Performance study of commercial $LiCoO_2$ and spinel-based Li-ion cells. J. Power Sour. **111**(2), 210–220 (2002)
36. H. Maleki, J. Howard, Effects of overdischarge on performance and thermal stability of a Li-ion cell. J. Power Sour. **160**(2), 1395–1402 (2006)
37. J.W. Lee, Y.K. Anguchamy, B.N. Popov, Simulation of charge-discharge cycling of lithium-ion batteries under low-earth-orbit conditions. J. Power Sour. **162**(2), 1395–1400 (2006)
38. G. Ning, B. Haran, R. White, B. Popov, Cycle life evaluation of pouch lithium-ion battery, in *Proceedings 204th Meeting of the Electrochemical Society,* Orlando. Abstract No. 414, October 2003

39. P. Liu, K. Kirby, E. Sherman, Failure Mechanism Diagnosis of Lithium-Ion Batteries, in *Proceedings of 206th Meeting of the Electrochemical Society,* Honolulu, Hawaii, Abstract No. 387, October 2004
40. K.A. Striebel, J. Shim, R. Kostecki, T.J. Richardson, P.N. Ross, X. Song, G.V. Zhuang, *Characterization of High-Power Lithium-Ion Cells—Performance and Diagnostic Analysis*. (Lawrence Berkeley National Laboratory, Berkeley, 2003). Paper LBNL-54097
41. H. Croft, B. Staniewicz, M.C. Smart, B.V. Ratnakumar, Cycling and Low Temperature Performance of Lithium-Ion Cells, in *Proceedings of IEEE 35th Intersociety Energy Conversion Engineering Conference and Exhibit,* vol. 1 (Las Vegas, Nevada, 2000), pp. 646–650
42. M.C. Smart, B.V. Ratnakumar, L. Whitcanack, S. Surampudi, J. Byers, R. Marsh, Performance characteristics of lithium-ion cells for NASA's Mars 2001 Lander application. IEEE Aerosp. Electron. Syst. Mag. **14**(11), 36–42 (1999)
43. Texas Instruments, *Bq27500-System Side Impedance Track Fuel Gauge*, September 2007
44. U.S. DOE, *Annual Energy Review 2008*. June 2009, p. 34
45. U.S. DOE, *International Petroleum Monthly, World Oil Balance 2004–2008.* June 2009
46. U.S. DOE, *Annual Energy Review 2008.* June 2009, p. 24

Chapter 6
On-Board Power Electronic Battery Management

6.1 Battery Cell Voltage Equalization Problem

6.1.1 Introduction

A battery cell voltage equalizer is essentially a power electronic controller, which takes active measures to equalize the voltage in each cell. Furthermore, by few additional methods, such as measuring the actual capacity and internal resistance of each cell (followed by instantaneous SOC computation), it is capable of equalizing the SOC of each cell. As a result, each of the cells will have the same SOC during charging and discharging, even in conditions of high dispersion in capacity and internal resistance. If all the cells have the same SOC utilization, they will degrade equally, at the average degradation of the pack. If this condition is accomplished, then all the cells will have the same capacity during the whole lifetime of the battery pack, avoiding premature end of life (EOL), due to the EOL of only one cell. If after SOC equalization, there still exists a case of faster degradation in some cells, the equalizer will further reduce the current demand on those cells, thus reducing the demand and degradation. In the example presented in Sect. 1.3.3, in Fig. 1.5, instead of 282 cycles, the pack would last 602 cycles. For the same application, the requirement of current though the equalizer is 5 Amps of equalizing current from any one cell to another, as will be explored later in Sect. 4.2.

In principle, there exist three basic groups of equalizers; resistive, capacitive, and inductive. In the next section, their main characteristics are explored.

S. S. Williamson, *Energy Management Strategies for Electric and Plug-in Hybrid Electric Vehicles*, DOI: 10.1007/978-1-4614-7711-2_6,

6.2 Introduction to Classic and Advanced Battery Cell Voltage Equalizers

6.2.1 Resistive Equalizers

Resistive equalizers simply burn the excess power in higher voltage cells, as depicted in Fig. 6.1. Consequently, they represent the cheapest option, and are widely utilized for laptop batteries.

Obviously, due to inherent heating problems, resistive equalizers tend to have low equalizing currents in the range of 300–500 mA, and work only in the final stages of charging and flotation. Due to the virtual nonexistence of energy recovery, the efficiency is 0 %. Also, because the battery should avoid working at high temperatures (Chap. 5), and because in this configuration, all the equalizing current is transformed into heat, this equalizer configuration is not recommended for high reliability battery packs [1].

6.2.2 Capacitive Equalizers

Capacitive-based equalizers use switched capacitors, as shown in Fig. 6.2, in order to transfer the energy from the higher voltage cell to the lower voltage cell. It switches the capacitor from cell-to-cell, allowing each cell to physically have the same voltage. Besides, it also depicts higher current capabilities than a resistive equalizer.

In addition, capacitive equalizers are also quite simple to implement, without any control issues [1, 2]. At the same time, the main drawback of capacitive equalizers is the fact that they cannot control inrush currents, in the case of big

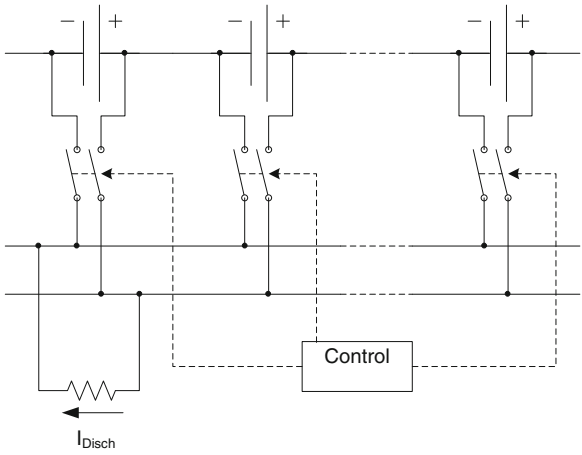

Fig. 6.1 Schematic representation of a typical resistive equalizer

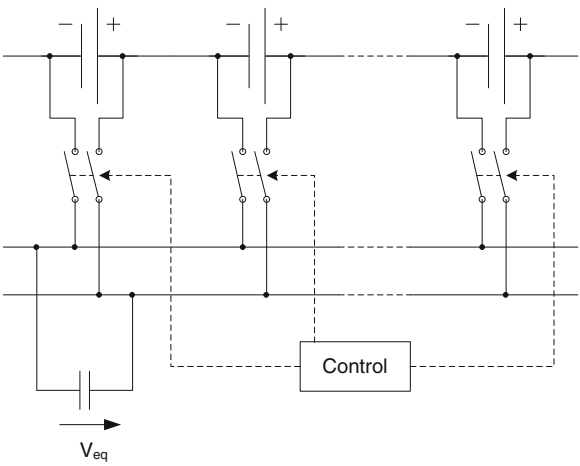

Fig. 6.2 Schematic representation of a typical capacitive equalizer

differences in cell voltages, leading to potentially devastating current ripples flowing into the cells. Furthermore, they do not allow any desired voltage difference, which are especially critical in equalizing SOC.

6.2.3 Inductive Equalizers

Inductive or transformer-based equalizers use an inductor to transfer energy from the higher voltage cell to the lower voltage cell. In fact, this is the most popular family of high-end equalizers. Due to its capability to fulfill most of the needs for vehicular energy storage: high equalizing current, high efficiency, and in some configurations, controllability, it is explored in detail in forthcoming sections of this chapter.

6.2.3.1 Basic Inductive Equalizer

A basic inductive equalizer is shown in Fig. 6.3. These equalizers are relatively straightforward and can transport a large amount of energy. At the same time, they are also capable of handling more complex control schemes, such as current limitation and voltage difference control [3].

This allows the controller to compensate for the internal resistance of the cells, and increase equalization current, independent of the cell voltage. On the other hand, it takes some additional components to avoid current ripples from getting into the cell. Typically, this configuration requires two switches (plus drivers and controls) per cell. Also, due to switching losses, the distribution of current tends to be highly concentrated in adjacent cells. Hence, a high-voltage cell will distribute

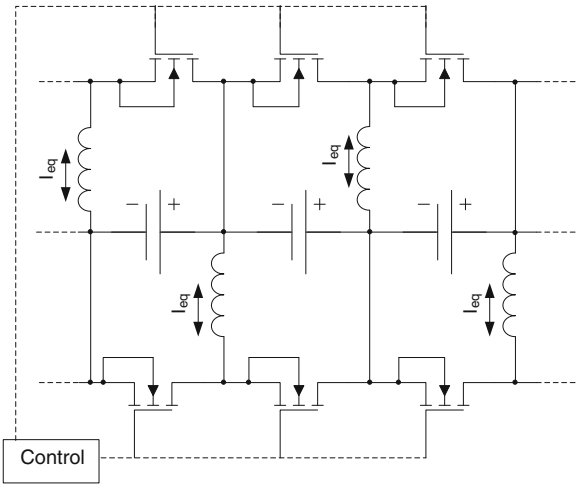

Fig. 6.3 Schematic representation of a typical inductive equalizer

the current largely among the adjacent cells, instead of doing it equally in all the cells along the string. In this case, the typical 50 % duty cycle switching scheme could be replaced by a more global scheme, with a slight additional cost of more processing power.

6.2.4 Cuk Equalizer

As the name indicates, this is an inductive-capacitive type of equalizer, primarily based on the *Cuk* converter topology. It shares almost all the positive characteristics of inductive equalizers, plus a very small cell current ripple. However, it suffers in terms of additional cost of power capacitors and double rated switches (higher voltage and current handling) [4–6]. The schematic representation of a typical *Cuk* equalizer is shown in Fig. 6.4.

The *Cuk* equalizer does incur additional losses due to the series capacitor, having slightly less efficiency than typical inductive equalizers. Similar to

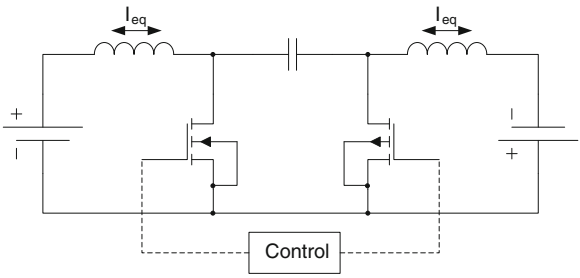

Fig. 6.4 Schematic representation of a typical *Cuk* equalizer

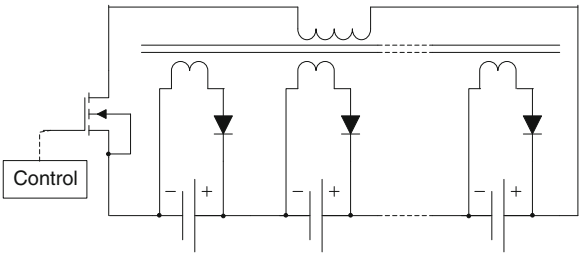

Fig. 6.5 Schematic representation of a multiwinding transformer equalizer

inductive equalizer, the *Cuk* equalizer also presents some issues while distributing equalizing current among all the cells in the string. This equalizer also possesses high current and complex control capability, at the expense of additional processing power.

6.2.5 Transformer-Based Equalizers

The solutions provided by transformer-based equalizers theoretically permit the right current distribution along all cells, without any additional losses or control issues. One such popular arrangement is depicted in Fig. 6.5 [1].

Such a topology poses an additional problem of using a very complex multisecondary transformer. This transformer is very difficult to mass produce, because all the secondary windings must have exactly the same voltage and resistance. If not, the differences will be translated into cell voltage difference, failing to perform the equalization accurately. Hence, this option is not a practical solution for high-count HEV cell packs. Moreover, this option also lacks the capability of handling complex control algorithms, such as current and voltage control. An alternative solution is presented in Fig. 6.6, using separate transformers for each cell.

This solution is modified here, in order to use 1:1 transformers, which are less difficult to mass produce [1]. Although this topology represents a substantial improvement with respect to multisecondary transformers, in terms of manufacturability and cost, only a very small dispersion can be accepted in the transformer

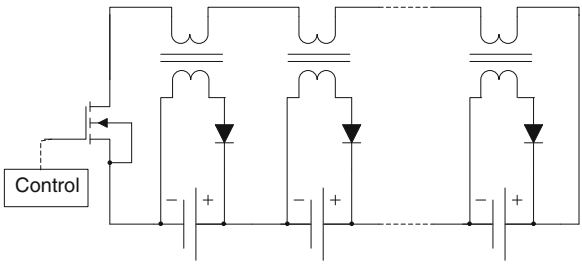

Fig. 6.6 Schematic representation of a multiple transformer equalizer

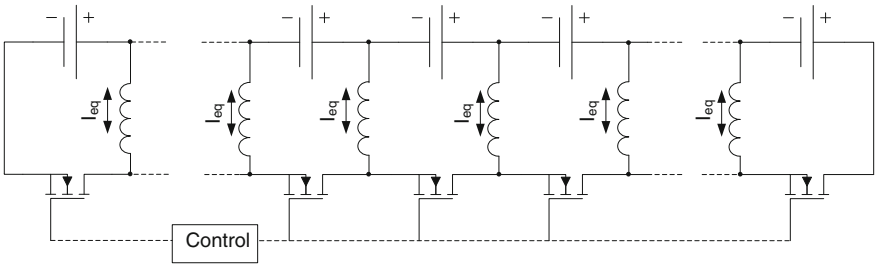

Fig. 6.7 Schematic representation of the proposed cell equalizer

primary inductance. This is still very difficult to obtain in commercial inductors, with the risk of experiencing current and voltage imbalance.

6.2.6 Novel Cell Voltage Equalizer

Keeping the various drawbacks of classic cell equalizers in mind, a novel design of a multicell equalizer, more specific for PHEV/EV energy storage applications, is presented in this chapter. A simplified block diagram representation, that primarily highlights the basic principle of operation of a multicell equalizer topology, is shown in Fig. 6.7.

The proposed novel equalizer circuit has several advantages:

(a) Standard manufacturing requirements: the overall manufacturing process is simple, using low-cost commercial components, no calibration required.
(b) Low component count: it only uses one MOSFET per equalized cell (instead of 2, in the typical and *Cuk* configurations), which reduces the component count, and therefore, the cost, as seen later in Table 6.3.
(c) Equal current distribution: It is capable of sharing the equalizing current more efficiently than other popular equalizers, except transformer-based equalizers.
(d) Low cell current ripple: The inductors work in continuous conduction mode, thus obtaining minimal current ripple flowing through the cells.
(e) Independent current control: The proposed equalizer is capable of controlling the equalizing current independent of the cell voltage. Thus, it can achieve high equalizing currents independent of both the cell voltage as well as resistance.

The proposed equalizer topology also possesses a few drawbacks:

(a) Need for additional processing power: The current control in this circuit is based on the MOSFET's trigger timing calculation, a process which is highly multifaceted, which has to be implemented in the on-board microcontroller. If SOC equalizing is desired (instead of cell voltage equalizing), additional

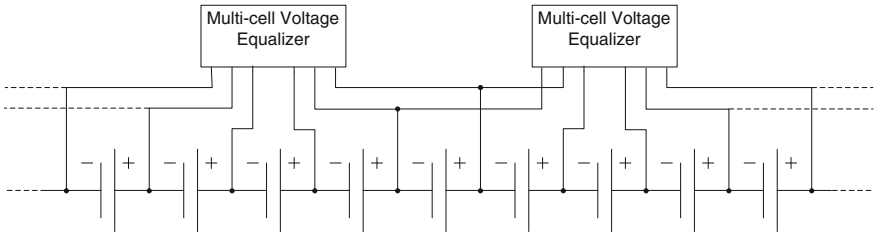

Fig. 6.8 Schematic representation of the proposed cell equalizer chaining method

processing power is invariably required. On the other hand, the necessary processing power can be easily allocated within the same on-board microcontroller, actually used for monitoring purposes. It is worth mentioning here that current available microcontroller technology allows performing such calculations without much additional cost.

(b) Chain length limitations: Because each MOSFET withstands the total voltage, and very low internal resistance MOSFETs (RdsOn) have usually low voltage (in the order of 30–60 V) [7], the amount of cells that the equalizer can handle is limited (from 4 to 10 cells). Furthermore, the timing calculation complexity grows exponentially with the amount of cells. Keeping these issues in mind, this thesis explores four and five cell equalizers, without being necessarily limited to these numbers. In order to overcome this limitation, the cell equalizers can be chain connected, as shown in Fig. 6.8.

6.2.7 Summary

Table 6.1 summarizes the capabilities of each type of equalizer. They are classified in relation with the main characteristics of each type of equalizer, as previously reviewed. The ranking scheme considers the positive or negative effect over

Table 6.1 Comparison of cell equalizer characteristics [1–6]

Equalizer type	Equalizing current	Current distribution	Current control	Current ripple	Manufacture	Cost	Control
Resistive	–	N.A.	+	+++	+++	+++	+++
Capacitive	–	+	–	–	++	++	++
Basic inductive	++	+	+	++	+	–	–
Cuk	++	+	+	+++	–	–	–
Transformer	+	+++	–	–	–	–	++
Novel equalizer	++	++	++	++	+	+	–

the equalizer, i.e., higher equalizer current is positive, while higher cost is negative.

It can be appreciated, that in general, none of the equalizer configurations is a perfect fit for a particular set of applications. For example, in very low cost, low-current applications, such as laptop batteries, the resistive equalizer is practical. For intermediate size batteries, where current or battery string length is limited, the capacitive or transformer based equalizers can be envisaged. In high-current applications, especially with high count battery strings, the options are less obvious. In this high-current range, the proposed novel cell equalizer configuration outperforms the various other options in terms of average performance, demonstrating positive performance in all characteristics, except in control complexity. The control aspect, though, as described before, does not necessarily imply a higher cost.

In conclusion, the high-current carrying capability and the possibility of advanced control, based on instantaneous battery SOC estimation, combined with low cost and simplified manufacturing, makes the novel equalizer configuration a highly attractive and practical option for EV/HEV/PHEV energy storage applications. In the next chapter, the economic feasibility of using a cell equalizer is explored, in general. In particular, the cost impact of the novel cell equalizer is thoroughly reviewed.

6.3 Economic Significance of Battery Cell Voltage Equalization

6.3.1 Introduction

In order to evaluate the economic feasibility of battery cell equalizers, more specifically, the novel cell equalizer configuration presented in this thesis, several critical factors need to be taken into account. Considering the high initial investment of a battery for PHEV applications ($5–10 K), and the unimpressive cycle life of 500–2000 cycles in typical usage (Sect. 1.3.2), at a first glance, the lithium rechargeable battery does not seem to be apt for EV/PHEV applications. Furthermore, certain concerns have been raised about the safety of using lithium rechargeable batteries in mobile applications.

Through the work presented in this chapter, it can be observed that a cell voltage equalizer with certain characteristics can seriously improve the cycle life and safety of lithium batteries. Later, the equalizer cost will also be determined. Finally, the conditions for the economic feasibility of PHEVs will be weighed against the size of the battery pack and the use of a cell equalizer arrangement. Parameters such as rising price of the gas, capital interests, and calendar lifetime of the cell will also be taken into account.

The characteristics of lithium batteries, particularly its cycle life, have been analyzed in Sect. 1.3.3 "Cycle life versus SOC." It was concluded that deeper discharges as well as a higher charges drastically reduce the cycle life of a cell. In addition, the continuously degrading effect in cell capacity, followed by charge–discharge cycles on a multiple cell string, with initial small dispersion, was also demonstrated. In the next section, the benefits of the use of the battery cell equalizers will be highlighted.

6.3.2 Importance of Battery Cell Equalizers

The primary characteristic of a battery cell equalizer is that it has the capacity to take energy from a higher SOC cell to a lower SOC cell. Several configurations have been explored in [1–6], and in Sect. 6.2 of this chapter. It is worth mentioning here that only a few of them are capable of meeting cost targets and power/efficiency requirements of EVs and PHEVs.

Simulations performed on a battery string composed of 100 cells (360 V), with an initial capacity dispersion (σ) of 5 %, have proven that an equalizer used in a typical PHEV application must be capable of driving more than 5 A from the high voltage cell to the low voltage cell, in order to balance the SOC utilization of each cell, independent of individual cell capacities. In addition, this process should cost a small fraction of the overall battery price. The equalizer cost will be considered as $400, as analyzed later in Table 6.3.

Due to the equalizing characteristics of cell voltage equalizers, the SOC would tend to be equal in all cells; thus, the equalized battery pack will exhibit the cycle life of an average capacity cell, and not the one of the lower capacity cell. As a result, the whole battery pack will withhold 600 cycles, like the average cell, instead of 280 cycles, using 80 % of the capacity. In addition, a higher cycle life is obtained using a smaller fraction of the total capacity. Consequently, the battery pack gains cycle life from 50 to 100 %, compared to nonequalized battery packs, as seen on Chap. 5. The financial impact of this fact will also be analyzed later in this section.

As aforementioned, the microcontroller located in each equalizer board performs voltage and temperature monitoring of each cell, in order to maintain safety and health monitoring of the pack. These microcontrollers report the status to a central processor, which assures environmental conditions, such as maximum current and temperature control, and will perform failure detection and prediction. Microcontrollers are also responsible for MOSFET gate timing calculations for their own equalizer, located in the same board.

For comparative purposes, the cost of a typical cell voltage equalizer and the proposed novel cell equalizer, both capable of complying with the aforementioned specifications, will be analyzed in the next section. The transformer-based equalizer and the *Cuk* equalizer will not be considered here; the first, because of impractical manufacturing issues, and the latter due to higher costs.

6.3.3 PHEV/EV Cell Equalizers

The typical cell voltage equalizer, as shown in Fig. 6.9, proposed in [3], is a very simple, yet powerful example of an equalizer. It has a high-current capacity and common components. In order to meet safety requirements, both temperature as well as voltage monitoring, have been added to the proposed system.

Although fundamental benefits exist for the typical configuration, it also presents some weaknesses, i.e., higher cost, due to the double switch per cell and poor current distribution, which includes capability of distributing current equally among all cells. Conversely, the proposed novel cell voltage equalizer, shown in Fig. 6.10, also has the ability to drive high currents, while achieving high efficiency at the same time. Besides, it may also cost less than the typical equalizer, mainly due to the use of only 1 MOSFET (and its driver) per cell, as shown in Table 6.2. Although the control core is more complex than the typical equalizer, a simple implementation is presented in Chap. 5, and it may be implemented in the same microcontroller that performs safety monitoring, with only a small increase in RAM memory (1 kB) and calculation time (2 ms every sampled second). The additional cost of these requirements is evaluated in Table 6.2.

It must be pointed out here that both the equalizer arrangements have the potential to comply with the specifications needed for a PHEV application. In the next section, their cost implications will be studied in detail.

6.3.4 Cost Analyses of Cell Equalizers

One of the key reasons for using a cell voltage equalizer is to increase lifetime and reduce overall cost of energy storage. Considering the fact that the main benefits of a cell equalizer is to extend lifetime of a battery pack, it is clear that it should not

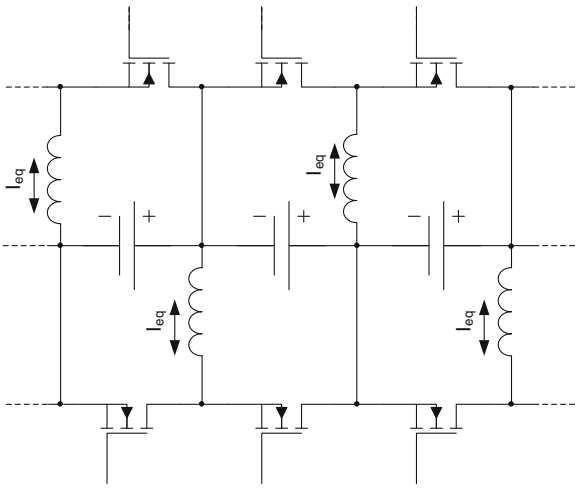

Fig. 6.9 Typical cell voltage equalizer

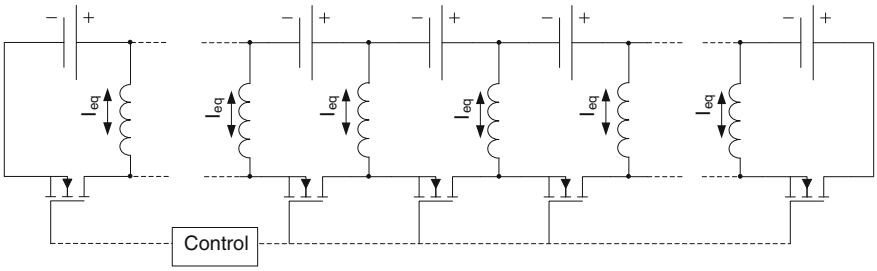

Fig. 6.10 Proposed novel cell voltage equalizer

cost more than a small fraction of the battery pack itself. In this cost analysis, factors such as timing calculation, safety-monitoring, and inter-communication will be considered. These tasks will be performed by a microcontroller. Due to factual limitations, such as quantity of Analog-to-Digital inputs as well as PWM output channels, 1 microcontroller per equalizer unit of 5 cells, in the proposed topology, can perform the job satisfactorily. In case of the typical equalizer configuration, 1 microcontroller is dedicated to every three equalizer units (6 MOSFETs). This is due to the limitation in the number of PWM output channels, which ranges between 4 and 8 outputs per microcontroller. The constructed prototype uses a 6 PWM channel microcontroller, which provides an excellent balance between functionality and cost.

Even if the voltage ratings of the MOSFETs in the typical and novel equalizer are different, they in fact use the same MOSFETs. This is due to the fact that the novel equalizer uses 30 V MOSFETs, which is considered to be the lowest MOSFET voltage. The typical equalizer would be able to use lower voltage rating (20 V). However, in reality, those MOSFETs are simply not commercially available.

Table 6.2 Cost breakdown of the mounted equalizer board

Equalizer Board items	Quantity per board		Cost per unit ($)
	New Equalizer	Typ. equalizer	
Equalizer units	1	3	
Equalized cells	4	3	
MOSFETs	5	6	0.4
MOSFET drivers	5	6	0.6
Inductors	4	3	0.8
Microcontroller	1	1	3
Capacitors	5	4	0.2
Optocouplers	2	2	0.1
Other components	1	1	0.5
PCB	1	1	1.6
Component mounting	40	40	0.03

Table 6.3 Equalizer total cost estimation

Eq. type	$/board	Cells/board	$/Cell	Boards/pack	$/pack
New equalizer	15.84	4	3.96	25	396
Typical equalizer	15.81	3	5.27	34	537.5

Table 6.2 shows the cost breakdown (the cost of the parts and the assembly) for both the novel as well as typical equalizer. The prices are based in quantities of 10 K [7], which is a rather small quantity, given the fact that an equalizer for a battery pack would need close to 100–120 MOSFETs. In fact, it is safe to assume improvements in price with higher production volumes.

Consider a 20 kWh battery pack, consisting of 100 cells, costing a total of nearly $6,000. The expected aim is for the equalizer not to cost more than 10 % of the battery pack. This pushes the equalizer price to $6 per cell and a total of $600 per battery pack. Table 6.3 summarizes the estimated total cost for each equalizer.

Table 6.3 proves that in both cases, the cost target was met, and that the proposed novel equalizer outperforms the typical equalizer cost by 37 %. Moreover, Table 3.2 also proves that the cost target is not only met, but is also improved by 40 %. In the next section, the economic feasibility of PHEVs will be analyzed.

6.3.5 PHEV Economic and Financial Analysis

It is obvious that there is an economic impetus in switching from conventional gas-based vehicles to advanced EVs/HEVs/PHEVs. Thus, an in-depth economic and financial analysis is mandatory, based on the following critical factors:

(a) Cost of gas: Even considering the fall of gas prices after Sept. 2008, statistically, gas prices have elevated to an average of 15 % per year in the last 5 years [1]. Several scenarios will be considered (10, 15, and 20 % per year), based on 0.6 USD per liter, at the end of 2008, which is a very conservative estimation, considering the latest rise in gas prices (since May 2009). Gas savings, based on this calculation, will be used to pay the surplus of a PHEV system, if possible.
(b) Interest on capital will be estimated as 5 %.
(c) Rise in electricity price will be considered as 5 %, starting from $0.1/kWh (2008) [8].
(d) The calculations performed in this chapter are for an average small vehicle (family sedan), considering all-electric driving of 16,000 km (10,000 miles) per year, with one charge per day. Additional mileage, based on gas, is to be considered.

(e) Autonomy of 50 km (30 miles) is considered, which fairly represents the daily driving average. This is equivalent to 7.5 kWh per charge, based on simulations performed in the ADVISOR software, under the UDDS test procedure [9].
(f) The overall cost of the equalizer was demonstrated before, and is considered here as $600.
(g) The influence of the cost of a lithium battery will also be evaluated, using three types of batteries: low, average, and full performance.
(h) Low-cost batteries are represented by the typical Li-ion chemistry, like the one used in laptops, costing about $300/kWh. The cycle life is shown in Fig. 6.11. The annual degradation, which is independent of cycle degradation, amounts to 3 % per year [10, 11].
(i) Full-performance batteries are essentially top-of-the-line cells, with LiFePO4 chemistry. Although it is a new technology, and complete data is not yet available, it is possible to consider the volume price as $600/kWh. In addition, the cycle life is about 3 times better than typical Li-ion batteries (1000 cycles at 100 % SOC [12]), with an annual degradation of 1 % [12, 13].
(j) Average batteries, represented by good quality Li-ion, or some alternate Lithium chemistry, cost about $400/kWh, with cycle life two times better than those depicted by low-cost cells, with an annual degradation of 2 %.
(k) A fixed cost of $3,000 will be added to the PHEV, to account for additional costs, for all-electric propulsion.
(l) The remaining value of the battery at the end of its lifetime will not be considered, although a battery with half its original capacity would still be useful for other applications, such us UPS systems [11].

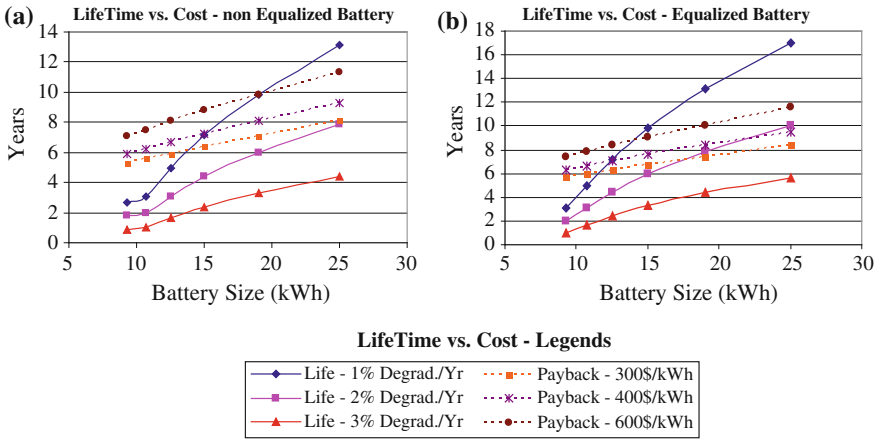

Fig. 6.11 Battery lifetime versus electric system payback time, **a** nonequalized system; **b** equalized system

In the next few sections, several combinations of battery capacities will be analyzed in order to obtain 50 km (30 miles) autonomy in a PHEV. Using larger batteries for similar requirements will allow smaller discharges with respect to full capacity, and will make cycle life longer, as was seen in the Chap. 1. On the other hand, larger batteries point toward higher initial costs, and will affect the payback time, and hence, the Return on Investment (ROI). The ROI will be calculated using the estimated gas saved during the battery utilization, minus the electricity expenses, considered as down-payment per year, leaving the remaining capital exposed to annual interests.

Figure 6.11a presents a comparison of the battery lifetime and the system payback time as a function of the battery size. Also, the lifetime is expressed as a function of annual degradation (1, 2, and 3 %), and payback time is expressed as a function of the initial battery cost ($300, $400, and $600/kWh). Figure 6.11b represents the same comparison, for a system with a cell equalizer.

From Fig. 6.11a, it can be appreciated that a nonequalized system is almost never or marginally paid back. The investment only returns under strict conditions, such as over-sizing the battery to 25 kWh, and having a long life battery with 1 % degradation per year. On the other hand, Fig. 6.11b demonstrates that returns are significant for a system with a suitable cell equalizer. Hence, it can be safely concluded that any battery, lasting more than 10 years, will more than pay back for itself. Not surprisingly, some hybrid manufacturers warrant their hybrid components up to 8 years or 160,000 km.

Figure 6.12a, b, and c depict a comparison of net gains using a PHEV system, compared to a conventional gas vehicle, at the end of the lifetime. This scenario is considered for an equalized system, using the following combinations: a battery with 1 % degradation per year and $600/kWh, 2 % and $400, and 3 % and $500. The plots show the returns on PHEV surcharge investment against the gas costs saved at the end of the life of the battery (ROI), as a function of battery size. Figure 6.12a depicts the returns, considering the rise in gas prices, at an average of 10 % per year, Fig. 6.12b shows this value to be 15 % per year, and Fig. 6.12c shows it to be 20 % per year. Figure 6.12d again, considers a 15 % gas price increase per year, but starting in 2010, at $0.7/liter, which is the calculated value, using the 5-year tendency in gas price fluctuation trend.

It is clear that the higher the rise in gas prices, the greater the savings, and thus, higher the benefit of using a PHEV system. The 10 % average annual increase of gas price is not likely to happen, considering that gas at the pump station has risen at an average of 15 % per year, in the last 5 years. This rate was about 25 % in 2007–2008, and it currently seems to be recovering from the price fall from Sept 2008 to May 2009. It must be noted that these projections have not considered any artificial event, such as political instability or speculation, which will make the PHEV option even more interesting. In any case, the ROI is higher in all scenarios, for batteries that last more than 10 years. Although the ROI for a 25kWh battery

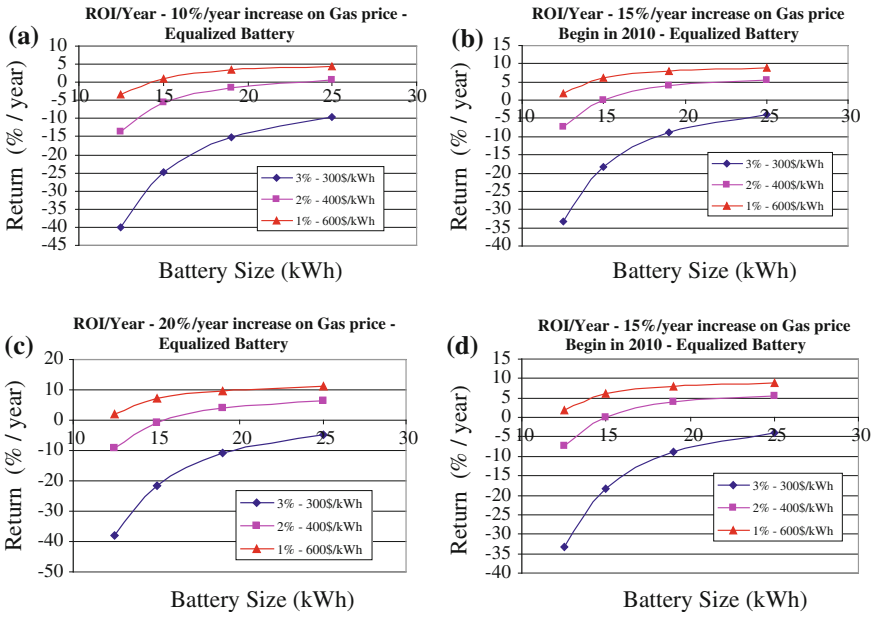

Fig. 6.12 Battery ROI/year for a PHEV system investment, at the end of battery lifetime **a** considering 10 % gas price increase/year; **b** considering 15 % gas price increase/year; **c** considering 20 % gas price increase/year; **d** considering 15 % gas price increase/year, starting in 2010

pack (30 % SOC discharge) is slightly higher, the difference may not be worth the increase in the initial investment and weight. Furthermore, the predicted returns starting next year (2010) are much more notable.

It is interesting to note that a slight gain in the ROI is experienced by reducing the annual degradation, instead of lowering the cost of the battery. Using a battery with 1 % degradation per year and paying 20 % more on battery cost makes 1.5 % more return per year, in all cases. In other words, it pays more to extend the battery life, rather than producing it slightly cheaper. Also, the impact on the ROI by using different battery technologies is smaller than that when using a suitable cell equalizer. Thus, it is obvious that future research directions and discussions, specifically related to battery lifetime, should be duly channeled toward critical issues, such as cell equalization, monitoring, and sizing, rather than being focused solely on mere battery chemistries.

There are other benefits of using an EV/PHEV system, not considered in this analysis, like government subsidies to green vehicles, tax rebates, carbon taxes, and protection against gas price spikes. They have not been considered here, because the objective of this chapter is to prove the economical feasibility of an equalized PHEV energy storage system, independent of artificial conditions, which in any event, will eventually become additional net gains.

6.3.6 Summary

In conclusion, it is safe to say that PHEVs are indeed economically viable today, even in a medium-priced oil market, given the following conditions:

(a) The battery should be oversized in order to last longer, and it should never be fully discharged nor fully charged. These conditions are enforced by the on-board hybrid management system (not part of the equalization system), which turns off the utilization of the battery, if the SOC (or the voltage) is outside limits. Of course, this fact will raise the initial investment.
(b) The use of a cell equalizer and monitor is mandatory. Longer lifetime of the battery pack at a very low cost makes a huge difference in the ROI. On the other hand, the cell equalizer has to comply with low-cost, high-current, and high-efficiency requirements. A novel cell voltage equalizer, capable of accomplishing these expectations, is described in the next chapter.
(c) Battery annual degradation and cycle life are imperative parameters. Currently, the $LiFePO_4$ chemistry seems to comply with these requirements. Nevertheless, the useof battery equalizers double the profits obtained with high-quality batteries, with lower annual degradation.

In summary, in Fig. 6.11, it can be appreciated that any battery lasting more than 10 years is paid-off, and preferably more than 12 years, in order to have interesting returns. This is possible under the aforementioned conditions, with the best battery technology available today. Not surprisingly, current proposed PHEV architectures consider using the smallest battery that would last about 10 years. In this scenario, considering an initial cost of about $10,000, the ROI is expected to be about 10 years.

In addition, there would be much more profits of using PHEVs in the next 2–3 years, due to the continuously rising price of oil. For example, a PHEV produced in 2010 could increase the ROI from 6.5 to 8 % per year. Moreover, the work presented in this chapter has not considered surcharges, which may be due to political instability, disruptions in oil production (for natural or artificial causes), speculation in prices, and peak oil theories; all of the events that are highly likely to occur.

Given these conditions, the high initial investment will be fully compensated by savings in gas in the ensuing years. Also, the high returns will most definitely invite investors to support initial costs. As future work, additional experimental verification will be necessary to add more mathematical precision to the battery cycle life model.

In conclusion, appropriately designed cell equalizers and improved battery dimensioning models will most definitely pave the way toward wider utilization of EVs/PHEVs. A novel cell voltage equalizer is discussed in detail in the next chapter, which is capable of accomplishing the low cost, high current, and high efficiency.

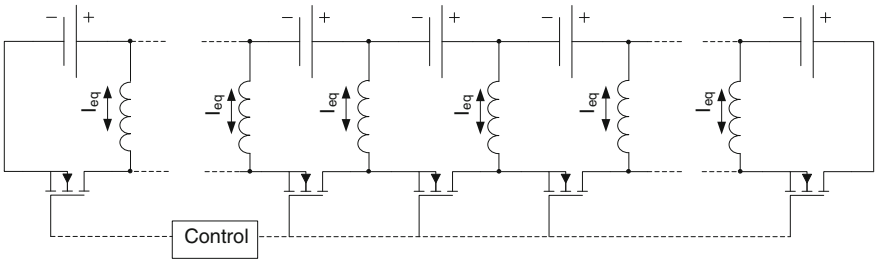

Fig. 6.13 Schematic representation of the proposed cell equalizer

6.4 Design and Performance of a Novel Power Electronic Cell Equalizer

6.4.1 Introduction

It has been proven in the previous chapters that an equalizer to be used in a typical PHEV/EV application should be capable of driving more than 6 A from a high-voltage cell to a low-voltage cell, and must cost a small fraction of the battery price (less than 10 %). An equalizer, which satisfies these conditions, drastically improves the life cycle of an EV battery, increasing the chances of positive ROI.

In this chapter, the proposed novel battery cell equalizer, as presented in Sect. 6.2.6, is thoroughly evaluated. A schematic representation of the proposed cell equalizer is shown in Fig. 6.13. Thereafter, the common specifications of an equalizer for EV/PHEV ESS applications are evaluated. The capabilities as well as cost issues of the proposed equalizer topology will also be analyzed in detail in this chapter. Finally, a comprehensive comparison between the mathematical model of the novel equalizer, a typical inductive equalizer (as presented in Sect. 6.2.3), and the experimental prototype (Fig. 6.14) of the novel equalizer, is also included.

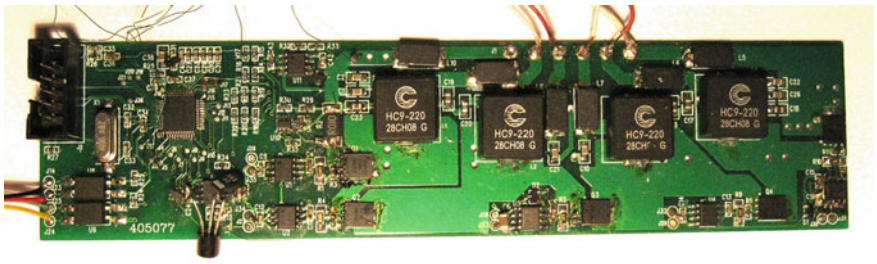

Fig. 6.14 Experimental prototype of the novel cell equalizer

6.4.2 Design Specifications

Considering that the main goal of an equalizer is maintaining the same SOC at all times, there are several issues to consider for an equalizer design. First, the equalizer must be capable of transferring the necessary amount of power to maintain the battery cells balanced, not necessarily during high power peak demands, but during the full discharge or charge cycles. A common EV/PHEV battery consists of a string of around 100 cells. Because of normal dispersion, not all cells have the same capacity. In fact, measurements performed in the laboratory and by [6] demonstrated a dispersion of up to 5 % in the capacity of cells. It was determined in the previous chapter that an EV/PHEV battery has to possess energy between 15 and 30 kWh, in order to be paid off. This means that each cell of the battery pack has a capacity ranging between 50 and 100 Ah. Furthermore, discharging larger batteries by 50 %, in 30 min, will lead to an average consumption of 100 A. In order to compensate for 5 % dispersion in the cell capacities, the equalizer should transfer up to 5 A from any one of the cells to another.

Second, the equalizer has to depict a good efficiency during energy transfer. As a reference, the obtained efficiency from previous literature, starts as low as 60 %, using hard switching [5, 6], to 80–83 %, using soft switching [6, 14]. In addition, as will be analyzed in Sect. 4.4.3, the typical equalizer obtains an average of 70 % power transfer efficiency. Although the equalizer presented in this thesis uses hard switching, an improvement in the efficiency is expected, and an initial objective of 75 % efficiency will be set.

Third, any equalizer should have a certain precision in the equalization balance. The SOC estimation, used in [15–17], obtained about 0.1 % precision in V_{OC} estimation. Because the equalizer presented in this chapter equalizes V_{OC}, this difference will be considered as the accepted unbalance in the cells.

Furthermore, as was analyzed in Chap. 3, the equalizer should cost a small fraction of the cost of the battery (less than 10 % of the total cost, about $6.00/cell), in order to allow the EV/PHEV system to be paid off. The equalizer presented in this thesis easily meets this criterion, as demonstrated in Sect. 6.3.

Finally, an equalizer has to be capable of reporting status and alarms of the battery condition to a central processor. Table 6.4 summarizes the design specifications of an equalizer for EV/PHEV applications.

Table 6.4 Design specifications of an equalizer for EV/PHEV applications

Equalizer specifications	Cost per unit ($)
Peak equalizing current	>5 A
Efficiency	>75 %
V_{OC} error between cells	>0.1 %
V_{OC} cell average error	>0.1 %
Cost	>$6.00/cell

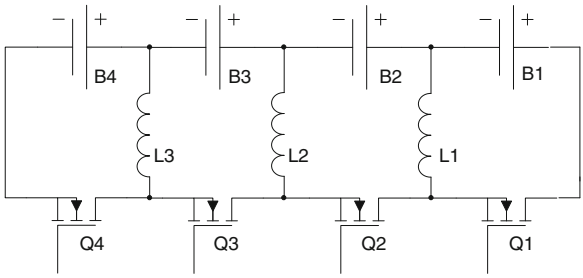

Fig. 6.15 Topological layout of a 4-cell voltage equalizer

6.4.3 Circuit Analysis of the Proposed Cell Voltage Equalizer

6.4.3.1 The Proposed Cell Voltage Equalizer

In this example, a 4-cell equalizer will be analyzed in detail, as shown in Fig. 6.15. This analysis may be extended to any *N*-cell equalizer. Figure 4.3 shows the MOSFET firing sequence.

Figure 6.16 shows that all MOSFETs are triggered together, except one, at all times. In this example, each mode has equal operating time, *T* (total time), over *N* number of cells, and is represented by one of the MOSFETs turned off. For example, in a 4-cell equalizer, each MOSFET will be off for about one-fourth of the time, plus or minus an adjusting time (dt_n). The duty cycle of each mode will be defined as τ_n, where *n* is the mode number.

Among the various tasks to be performed by the equalizer, it also sometimes needs to shift current with very little or no voltage difference. At the same time, high current is always desirable, which means that very small parasitic resistances, copper traces, as well as the internal resistance of MOSFETs (R_{dsOn}) may have a strong influence on overall current distribution. In order to correct this effect, small modifications can be made in trigger timing, allowing production of desired distribution of current. The main objective of the small dead-time between modes, as shown in Fig. 6.16 (*DT*), is to avoid a current shoot through in the MOSFETs. This is not considered as an operation mode, due to its trivial influence on the overall operational characteristics.

The different modes of operation of the 4-cell equalizer are displayed in Fig. 6.16. Each mode is defined by one of the MOSFETs not in conduction.

The voltages and currents in the circuit are shown in Figs. 6.17 and 6.18. For demonstration purposes, in this example, the circuit is performing a current transfer from the first cell to the second cell, with all the cells having the same voltage, equal to one-fourth of the total voltage (V_t). The duty cycle of each mode (τ_n) has been adjusted, in order to force the current transfer in the desired manner. The timing calculation is described in the next section.

The minimum τ_n will be set to 0.5 times the typical time, and the maximum τ_n is set to 1.5 times the typical time. This is set to avoid overly fast switching and the possibility of one mode disappearing. The dead time between modes is very small,

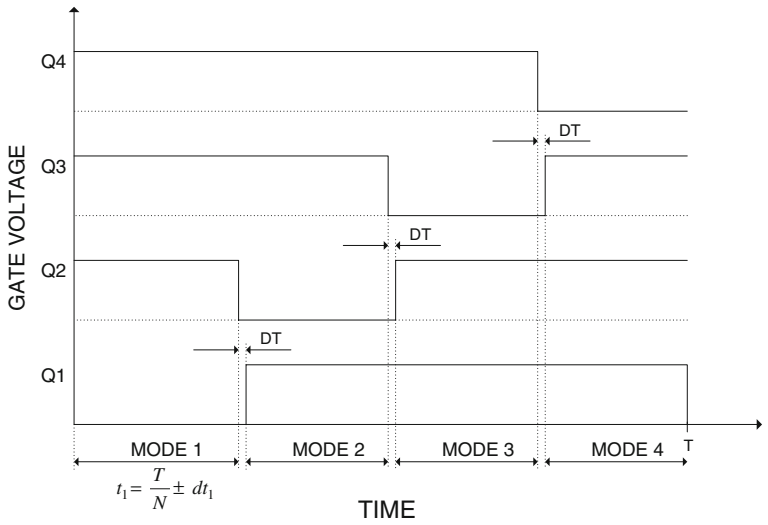

Fig. 6.16 MOSFET firing sequence for the 4-cell topology

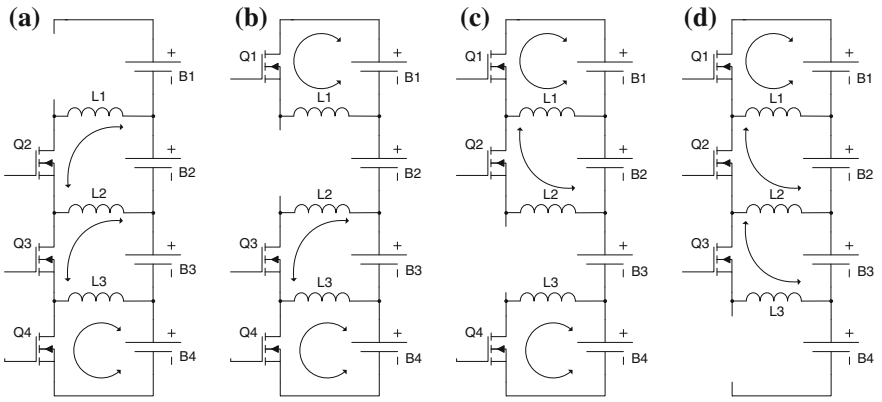

Fig. 6.17 Modes of operation: **a** Q1 off, **b** Q2 off, **c** Q3 off, and **d** Q4 off

compared to τ_n (around 50 ns, vs. 2 μs, in the equalizer used in this thesis), and it can be safely ignored from the mathematical model.

The MOSFETs have to be selected to withstand V_t as maximum voltage, plus ringing due to parasitic inductances of the PCB traces. In this prototype, 30 V MOSFETs were selected, for a maximum working voltage of 21 V, which is the minimum voltage found in commercial MOSFETs. The maximum MOSFET current is the maximum inductor current plus headroom to avoid malfunction in

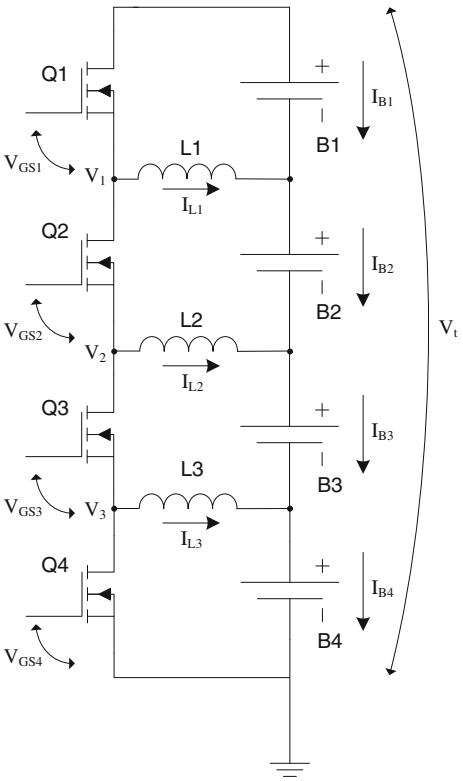

Fig. 6.18 Equalizer voltages and currents

the case of short circuit in the outputs. Another important parameter is the Rds_{ON} versus the C_{GS} as well as cost. For example, the use of a MOSFET with an Rds_{ON} of 3 mΩ, instead of 7 mΩ, leads to an increase of 5 % in the efficiency at high power. However, a 10 % higher cost per cell is incurred, and idle losses are doubled, due to a higher C_{GS}. Actually, both types of MOSFETs are good for this application, depending on the trade-off between power and cost.

The inductor sizes are computed so as to operate in CCM in most cases, as seen in Fig. 6.19 (I_{L1} and I_{L2}). Lower inductance values will increase the current ripple, thus increasing idle losses. The results of this current ripple on the inductors can be observed later, in Sect. 6.4.6. On the other hand, higher inductance values increase the cost and the size of the equalizer. Higher switching frequency will reduce the current ripple (and the idle losses). However, this will increase the switching losses, reducing the efficiency at higher power transfer. A successful design should balance switching frequency, inductor size, cost, and efficiency, to find the optimal combination for each application. The equalizer designed in this thesis was optimized to work efficiently between 1 and 5 Amps of current transfer.

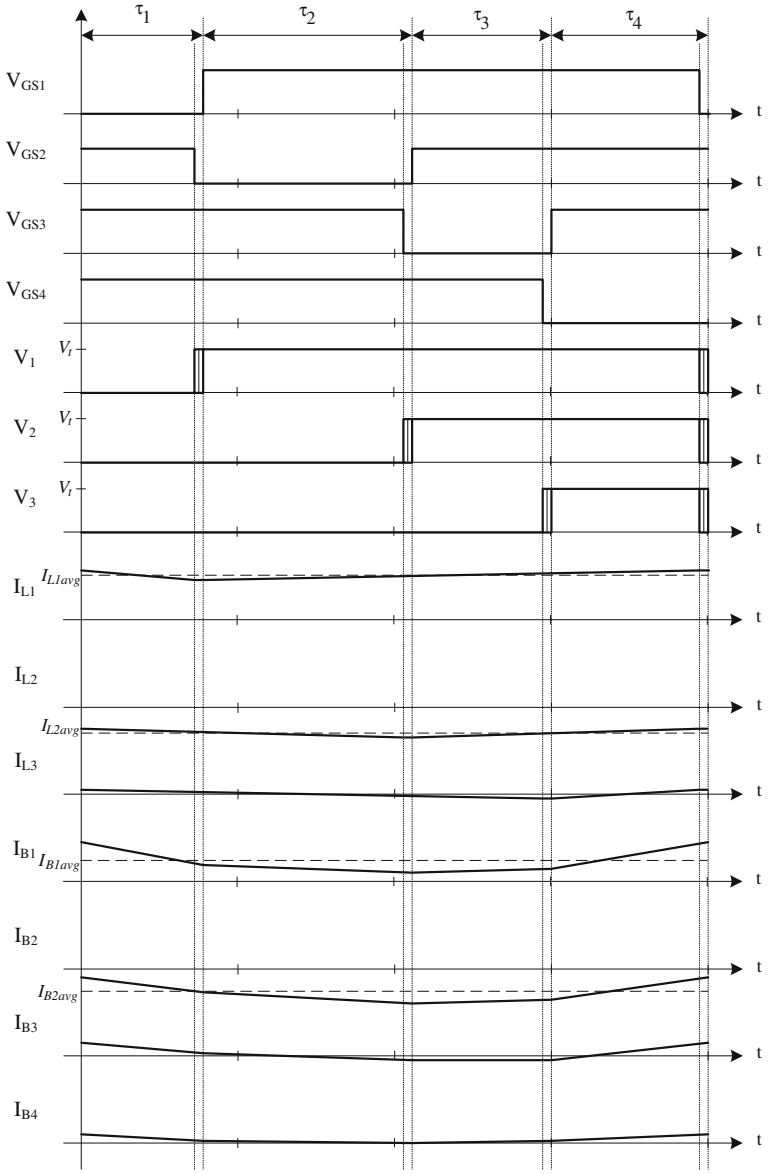

Fig. 6.19 Equalizer voltages and currents

Furthermore, as can be appreciated in Fig. 6.19, current is transferred as desired, from cell 1 to cell 2. There is also an undesired current ripple over the cells, which should be filtered, to avoid additional losses in the internal resistances of the cells.

6.4.4 Mathematical Model of the Proposed Cell Voltage Equalizer

In this section, two possible mathematical models of the 4-cell equalizer will be analyzed and compared to simulations performed in a "closest-to-real" situation. The "first" mathematical model was simplified, in order to fit in the reduced processing power of a microcontroller. Thereafter, a second order model was deduced, in order to validate the modeling technique. Moreover, it is possible to extend the model to 5 or more cells per system.

Defining the currents and voltages in the equalizer, as shown in Fig. 6.20, the current through the inductors (I_{Ln}) is considered constant (as seen in Fig. 6.19). I_{Ln} can be computed as the average voltage applied over the inductors (in all modes) divided by the inductor internal resistance (R_{Ln}). Taking into account the voltage lost in the MOSFET resistance (R_{ds}), which depends on the inductor currents and the timings, and taking into consideration cell voltage (V_{bn}), which is sum of V_{OC} and voltage drop across the internal resistance, and total battery pack voltage (V_t), as well as the duty cycle of each mode τ_n, the Eqs. 6.1, 6.2, and 6.3 describe the voltages and currents in the first, second, and third mode:

$$-Vb_1 + \tau_1 \cdot Vt = \begin{pmatrix} I_{L1} & I_{L2} & I_{L3} \end{pmatrix} \cdot \left[\begin{pmatrix} 3 & 1 & 1 & 1 \\ 2 & 0 & 1 & 1 \\ 1 & 0 & 0 & 1 \end{pmatrix} \cdot \begin{pmatrix} \tau_1 \\ \tau_2 \\ \tau_3 \\ 1 - \tau_1 - \tau_2 - \tau_3 \end{pmatrix} \cdot R_{ds} + \begin{pmatrix} R_L \\ 0 \\ 0 \end{pmatrix} \right] \tag{6.1}$$

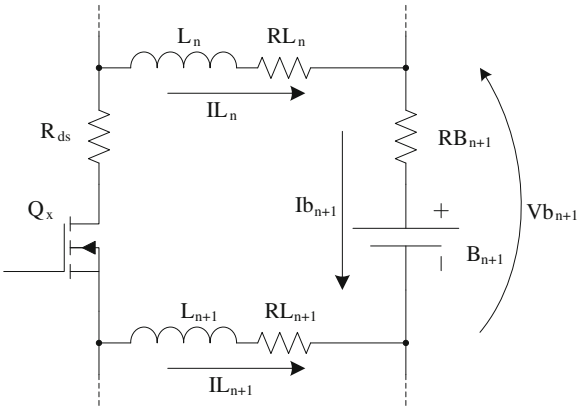

Fig. 6.20 Equalizer currents and voltages

$$-Vb_1 - Vb_2 + \tau_1 \cdot Vt + \tau_2 \cdot Vt = \begin{pmatrix} I_{L1} & I_{L2} & I_{L3} \end{pmatrix} \cdot \left[\begin{pmatrix} 2 & 0 & 1 & 1 \\ 2 & 2 & 2 & \\ 1 & 1 & 0 & 2 \end{pmatrix} \cdot \begin{pmatrix} \tau_1 \\ \tau_2 \\ \tau_3 \\ 1 - \tau_1 - \tau_2 - \tau_3 \end{pmatrix} \cdot R_{ds} + \begin{pmatrix} 0 \\ R_L \\ 0 \end{pmatrix} \right] \tag{6.2}$$

$$\begin{aligned} &-Vb_1 - Vb_2 - Vb_3 + \tau_1 \cdot Vt + \tau_2 \cdot Vt + \tau_3 \cdot Vt \\ &= \begin{pmatrix} I_{L1} & I_{L2} & I_{L3} \end{pmatrix} \\ &\cdot \left[\begin{pmatrix} 1 & 0 & 0 & 1 \\ 1 & 1 & 0 & 2 \\ 1 & 1 & 1 & 3 \end{pmatrix} \cdot \begin{pmatrix} \tau_1 \\ \tau_2 \\ \tau_3 \\ 1 - \tau_1 - \tau_2 - \tau_3 \end{pmatrix} \cdot R_{ds} + \begin{pmatrix} 0 \\ 0 \\ R_L \end{pmatrix} \right] \end{aligned} \tag{6.3}$$

The average current through each cell, I_{Bx}, is related not only to I_{Lx}, but also to the timing of each mode. Hence, the equation for the cell currents is:

$$\begin{bmatrix} -(\tau_2 + \tau_3 + \tau_4) & -(\tau_3 + \tau_4) & -\tau_4 \\ \tau_1 & -(\tau_3 + \tau_4) & -\tau_4 \\ \tau_1 & \tau_1 + \tau_2 & -\tau_4 \\ \tau_1 & \tau_1 + \tau_2 & \tau_1 + \tau_2 + \tau_3 \end{bmatrix} \cdot \begin{pmatrix} I_{L1} \\ I_{L2} \\ I_{L3} \end{pmatrix} = \begin{pmatrix} Ib_1 \\ Ib_2 \\ Ib_3 \\ Ib_4 \end{pmatrix} \tag{6.4}$$

In order to reduce the complexity of the above equations, the MOSFETs could be considered as ideal switches ($R_{ds} = 0\ \Omega$). Under these conditions, Eqs. 6.1–6.4 can be simplified and combined to form Eq. 6.5; it depicts the equation of the cell currents as a function of the cell voltages and the timing. In the context of this thesis, this equation will be referred to as the "First Mathematical Model".

$$\begin{aligned} &\begin{bmatrix} -(\tau_2 + \tau_3 + \tau_4) & -(\tau_3 + \tau_4) & -\tau_4 \\ \tau_1 & -(\tau_3 + \tau_4) & -\tau_4 \\ \tau_1 & \tau_1 + \tau_2 & -\tau_4 \\ \tau_1 & \tau_1 + \tau_2 & \tau_1 + \tau_2 + \tau_3 \end{bmatrix} \\ &\cdot \begin{bmatrix} -(\tau_2 + \tau_3 + \tau_4) & \tau_1 & \tau_1 & \tau_1 \\ -(\tau_3 + \tau_4) & -(\tau_3 + \tau_4) & \tau_1 + \tau_2 & \tau_1 + \tau_2 \\ -\tau_4 & -\tau_4 & -\tau_4 & \tau_1 + \tau_2 + \tau_3 \end{bmatrix} \cdot \begin{pmatrix} Vb_1 \\ Vb_2 \\ Vb_3 \\ Vb_4 \end{pmatrix} \cdot \frac{1}{R_L} \\ &= \begin{pmatrix} Ib_1 \\ Ib_2 \\ Ib_3 \\ Ib_4 \end{pmatrix} \end{aligned} \tag{6.5}$$

Combining Eqs. 6.1, 6.2, and 6.3 leads to Eq. 6.6, which expresses the inductor currents versus cell voltage and timing.

$$\begin{bmatrix} -(\tau_2+\tau_3+\tau_4) & \tau_1 & \tau_1 & \tau_1 \\ -(\tau_3+\tau_4) & -(\tau_3+\tau_4) & \tau_1+\tau_2 & \tau_1+\tau_2 \\ -\tau_4 & -\tau_4 & -\tau_4 & \tau_1+\tau_2+\tau_3 \end{bmatrix} \cdot \begin{pmatrix} Vb_1 \\ Vb_2 \\ Vb_3 \\ Vb_4 \end{pmatrix} \cdot \frac{1}{R_L} = \begin{pmatrix} I_{L1} \\ I_{L2} \\ I_{L3} \end{pmatrix} \tag{6.6}$$

Also, the inductor currents can be deduced as:

$$\begin{pmatrix} I_{L1} \\ I_{L2} \\ I_{L3} \end{pmatrix} = \begin{pmatrix} Ib_1 - Ib_2 \\ Ib_2 - Ib_3 \\ Ib_3 - Ib_4 \end{pmatrix} \tag{6.7}$$

Then, consider the following relationships:

$$\tau_4 = 1 - \tau_1 - \tau_2 - \tau_3 \tag{6.8}$$

$$Vt = Vb_1 + Vb_2 + Vb_3 + Vb_4 \tag{6.9}$$

Substituting Eqs. 4.8 and 4.9 into 4.6, and upon inverting the resulting equation, the timing as a function of the cell voltages and inductor currents is obtained (Eq. 4.10). When used in a microcontroller, the inverted equation can help calculate the timing of the MOSFETs. Chapter 5 (Sect. 5.3) proposes a control system to calculate the inductor currents in closed loop.

$$\begin{pmatrix} \tau_1 \\ \tau_2 \\ \tau_3 \end{pmatrix} = \frac{1}{Vt^3} \cdot \begin{pmatrix} Vt^2 & 0 & 0 \\ -Vt^2 & Vt^2 & 0 \\ 0 & -Vt^2 & Vt^2 \end{pmatrix} \cdot \left(\begin{pmatrix} I_{L1} \\ I_{L2} \\ I_{L3} \end{pmatrix} \cdot R_L + \begin{pmatrix} Vb_1 \\ Vb_1 + Vb_2 \\ Vb_1 + Vb_2 + Vb_3 \end{pmatrix} \right) \tag{6.10}$$

Although it is relatively simple, this mathematical model considers that R_{ds} is much smaller than the inductor resistance. In fact, this is not always true, because high power inductors may have very low resistance, sometimes comparable to that of MOSFET resistance (about 5 mΩ). Thus, this supposition makes the "first mathematical model" only an approximate estimation of the real behavior of the equalizer. In fact, this was the case in the equalizer prototype used in this thesis, where the "first mathematical model" was found to have critical differences with the measurements. In order to obtain a better prediction, R_{ds} has to be considered as non-negligible. Consequently, merging Eqs. 6.1, 6.2, and 6.3 results in Eq. 6.11, linking the inductor current, I_{Lx}, timing, t_x, and cell voltage, V_{Bx}. Finally, it can be concluded that Eqs. 6.4 and 6.11 represent the "Second Mathematical Model".

$$\begin{bmatrix} \frac{Vt}{R_{ds}} - 2I_{L1} - I_{L2} & I_{L2} + I_{L3} & I_{L3} \\ \frac{Vt}{R_{ds}} - I_{L1} + I_{L3} & \frac{Vt}{R_{ds}} + I_{L1} + I_{L3} & 2I_{L3} \\ \frac{Vt}{R_{ds}} + I_{L2} + 2I_{L3} & \frac{Vt}{R_{ds}} + I_{L1} + I_{L2} + 2I_{L3} & \frac{Vt}{R_{ds}} + I_{L1} + 2I_{L2} + 2I_{L3} \end{bmatrix} \cdot \begin{pmatrix} \tau_1 \\ \tau_2 \\ \tau_3 \end{pmatrix} = \begin{bmatrix} \frac{Vb_1}{R_{ds}} + I_{L1} + I_{L2} + I_{L3} + I_{L1}\frac{R_L}{R_{ds}} \\ \left(\frac{Vb_1}{R_{ds}} + \frac{Vb_2}{R_{ds}}\right) + I_{L1} + 2I_{L2} + 2I_{L3} + I_{L2}\frac{R_L}{R_{ds}} \\ \left(\frac{Vb_1}{R_{ds}} + \frac{Vb_2}{R_{ds}} + \frac{Vb_3}{R_{ds}}\right) + I_{L1} + 2I_{L2} + 3I_{L3} + I_{L3}\frac{R_L}{R_{ds}} \end{bmatrix} \tag{6.11}$$

Upon analyzing Eq. 6.11, it is clear that the cell current is a complex function of the MOSFETs' gate timing and cell voltages. As aforementioned, this model can be also extended to five cells or more, although the mathematical complexity will grow exponentially. The prototype presented in this thesis uses an implementation of the 5-cell model, in order to calculate timing as a function of cell voltages and desired current.

In the next section, a detailed comparison between the results obtained from the mathematical model, the simulations, and the experimental tests will be presented.

6.4.5 Comparative Study Between Simulations and Experimental Results

6.4.5.1 Prototype Evaluation

A prototype of the cell equalizer has been implemented using low-cost, standard components. A 5-cell instead of a 4-cell equalizer prototype has been built, in order to improve the cost effectiveness. The equalizer under test is connected to a pack of 20, 2.2 Ah, Li-ion cells (size 18650), in a 4-parallel, 5-series arrangement [18]. The complete pack has 18 V, 8.8 Ah, and 500 mΩ equivalent series resistance, including current sensing resistors and cables. The objective of the test is to demonstrate the functionality of the equalizer, as well as measuring the efficiency and maximum current capabilities. The test is performed using a simple cell voltage control, much simpler than the SOC equalization, presented in Sect. 6.5.

The functionality and the efficiency have been tested by creating an imbalance in the pack, discharging cell "2" by 6 A, during 20 min (2 Ah imbalance), and activating the equalizer in cell voltage equalizing mode. During run time, the equalizer will tend to make the voltage over each cell equal. The SOC equalizing mode, which has a better dynamic response, is explored later, in Sect. 6.5. The cell voltages during equalization are shown in Fig. 6.21, and the corresponding cell currents are shown in Fig. 6.22.

Integrating the current in cell #2, it can be appreciated in Fig. 6.22 that the equalized energy is about 2 Ah, exactly the same amount lost during the forced

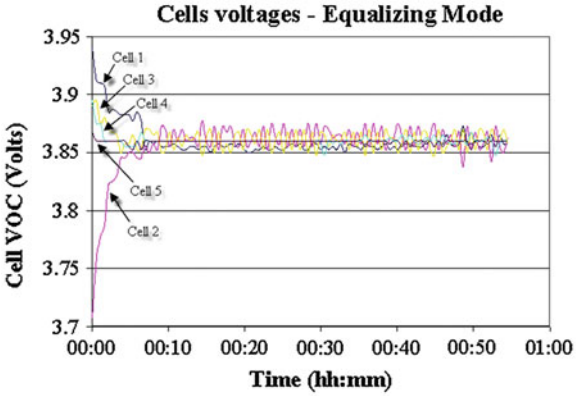

Fig. 6.21 Cell voltages during equalization, with 2 Ah initial imbalance in Cell "2"

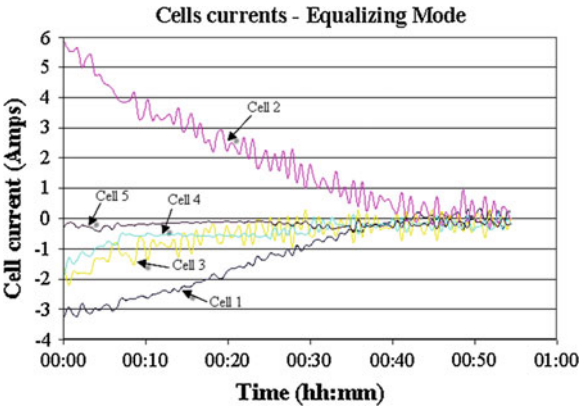

Fig. 6.22 Cell currents during equalization, with 2 Ah initial imbalance in Cell "2"

imbalance. It is also notable that the equalizing current is not constant, but rather depicts a linearly decreasing behavior, taking the equalizing process twice the time to equalize than if the current were constant at 6 A. This is improved later, using SOC equalization, explained in Chap. 5, where the SOC is equalized, instead of cell voltage. Hence, all the cells will tend to have the same voltage, but not necessarily the same SOC. Referring to Fig. 6.21; it can be appreciated that the voltages equalize particularly fast compared to the current in Fig. 6.22 (proportional to the SOC). In order to equalize the SOC as fast as possible, the equalizer should maintain 6 A current for 20 min. This objective is not possible because of controller stability issues, and it will be explored in Chap. 5. The noise in the cell voltage during this test was rather high (about 0.3 %), which is higher than specified (0.1 %). This is improved later, using the SOC equalization method.

6.4.5.2 Mathematical Model and Experimental Comparison

In order to evaluate the effectiveness and limitations of the mathematical model, its results will be compared to a 4-cell system, simulated in PSpice, using the most complete model of a typical low cost MOSFET, incorporating the experimental results at the same time. For this comparison, only the "Second Mathematical Model" will be used (Eqs. 6.4 and 6.11), because, in this prototype, the assumptions considered in "First Mathematical Model" (Eq. 6.10), are not true (i.e., the MOSFETs R_{ds}, plus the trace impedances and capacitors' equivalent resistances, estimated in 20 mΩ, are not much smaller than the inductance equivalent resistance, about 10 mΩ), leading to critical errors in the "First Mathematical Model." The simulation studies also consider a small dead-band time between modes, shown in the previous firing sequence (Fig. 6.4), in order to avoid shoot through in the MOSFETs. The simulations also take in account the dynamic response of the MOSFETs, which, due to high switching frequency (higher than 100 kHz), will exhibit high switching losses. Because these losses are not considered in the mathematical model, some differences between the models and the simulations are expected. The mathematical model and the simulations also take into account the parasitic equivalent series resistances of several other components such as filter capacitors, PCB traces, and cables. Finally, the measurements performed on the prototype will be compared against both calculations.

The average current through the cells is shown in Fig. 6.23, as a function of delta T1 (difference in timing of MOSFET 1, as a percentage of nominal time, corresponding to the time in Mode 1, as shown in Fig. 6.16), considering equal voltage in all cells. The dots represent the measured working points, and the corresponding lines represent the characteristic trend.

Second, the current through the cells is shown in Fig. 6.24 as a function of dt_2 (difference in timing of MOSFET 2, as a percentage of nominal time, corresponding to the time in Mode 2, as shown in Fig. 6.16), considering equal voltage in all cells.

Because of the equalizer symmetry, the results of varying dt_3 and dt_4 (modes III and IV) are similar to dt_2 and dt_1, respectively.

The current through the cells in the prototype matches the mathematical model and the simulations fairly well. In particular, the current prediction of the developed model for a corresponding cell (for example, current through cell #2 by varying dt_2) is very precise, obtaining a mean squared error of less than 5 %. The remaining differences between the *PSpice* simulations and the results from the model can be attributed to the fact that the mathematical model does not take into account the dead-time and the dynamic losses (the losses due to the switching) in the MOSFETs. It also does not take into account variation of MOSFET R_{dt} with temperature. In addition, it can be appreciated that a change in the timings of one MOSFET mainly affects the current over the corresponding cell, and to some extent, the currents over the other cells, in a less significant manner.

Because the equalizer works in closed loop, using the controller described in Chap. 5 eliminates the relatively small difference between the model and the

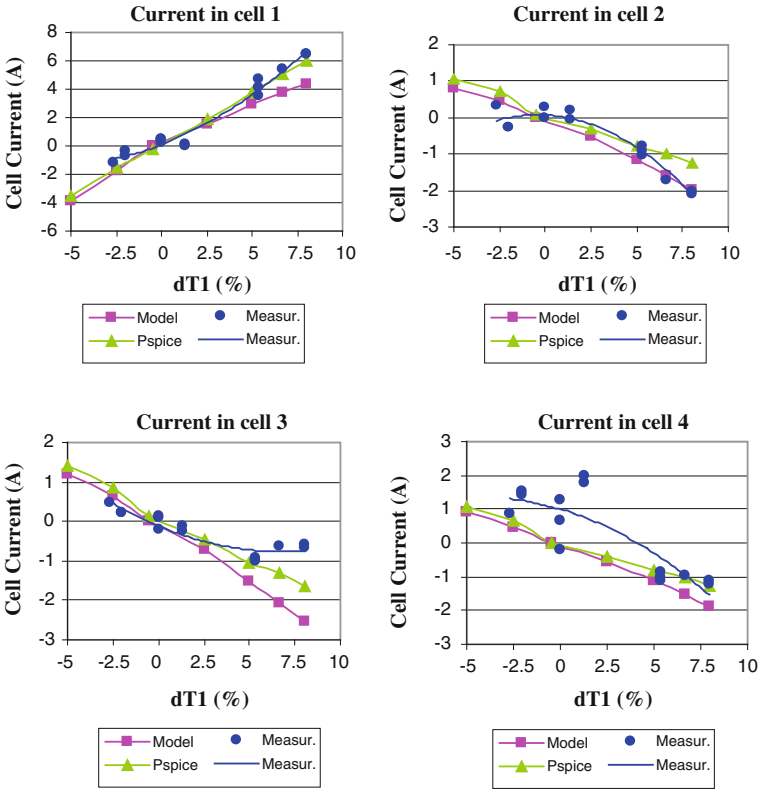

Fig. 6.23 Current through cells, with varying dt_1

prototype. Thus, the final precision of the system remains unaffected. These errors are cancelled by the high open loop gain of the controller.

The total efficiency is also predicted with good precision. Figure 6.25 shows the efficiency, defined as total losses divided by the total transferred power to the cells, as a function of dt_1 and dt_2.

From Fig. 6.25, it can be appreciated again that, for most parts, the mathematical model and the simulations match the measurements on the prototype. Furthermore, it may also be observed that the efficiency drops, when the timing becomes much different from the nominal timing. As determined previously in the design specifications (Sect. 6.4.2), equalizing currents are usually lower than 5 A (dt less than 5 %). Thus, the efficiency is higher than 80 % in this scenario. This is a rather good performance, considering the MOSFETs are working in hard switching. In fact, this performance is very close to the efficiency obtained by other equalizers using soft switching, such as the ones used in [6, 14].

On the other hand, a large performance drop (down to 60 % efficiency) is found near the neutral timing, when low current is transferred. At this working point, the

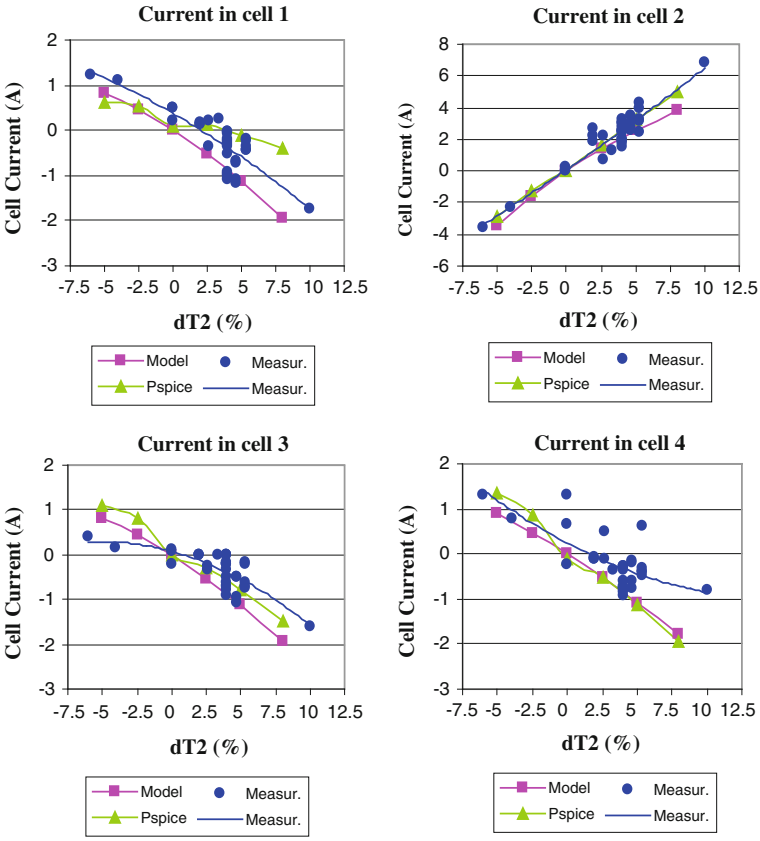

Fig. 6.24 Current through cells, with varying dt_2

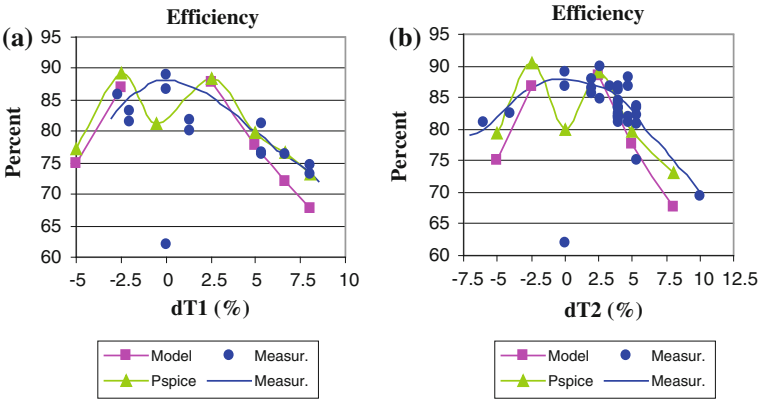

Fig. 6.25 Total efficiency (**a**) with varying dt_1, and (**b**) with varying dt_2

equalizer fails to meet the specifications of 75 % efficiency. This is due to the idle losses generated by the inductor current ripple, as explained in Sect. 6.4.3.1. These losses are around 1 W, which affect the performance of the equalizer when the transferred current is less than 1 A (equivalent to 3.6 W). There are two ways to solve this issue: by increasing the inductance to reduce the current ripple, which increases the cost, size, and weight, or by avoiding operation under 1 A current transfer, at the cost of allowing a small SOC difference between cells. The later method, called "deadband" method, is the solution used in this thesis, stopping the equalization when the difference of V_{OC} between cells is less than 0.1 %, as explained in detail in Sect. 6.5.

6.4.6 *Comparison Between Typical Equalizer And Prototype Experimental Results*

In order to compare the theoretical performance of both equalizers against the experimental measurements performed on the novel equalizer prototype, given the fact that the efficiency depends on the transferred power, several working points have been simulated to emulate a real scenario. Primarily, the simulations have been separated in two groups: transfer current to/from the first cell of the chain, summarized in Fig. 6.26, and to/from the second cell, summarized in Fig. 6.27. These batches of simulations have been discriminated, because they exhibit different performances. These groups of simulations of the novel equalizer have been called "A." The corresponding groups of simulations of the typical equalizer are called "B." Finally, the experimental test results for the proposed equalizer prototype will be called "C".

The "transferred power" is defined as the power provided to one or many cells, and the "total efficiency" is defined as the total equalizer losses over the transferred power from one or many cells (using the same components and switching

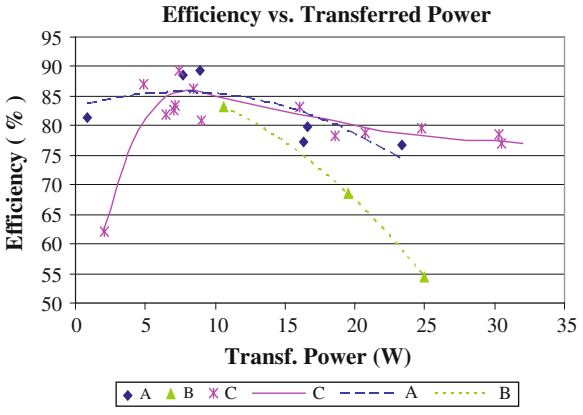

Fig. 6.26 Efficiency versus transferred power on first cell: **a** Simulation novel EQ. **b** Simulation Typ. EQ. **c** Experimental measurements novel EQ

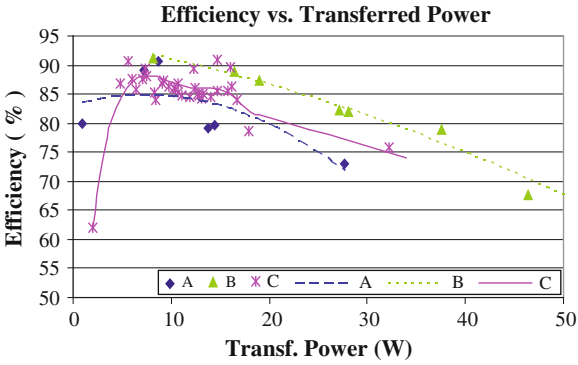

Fig. 6.27 Efficiency versus transferred power on second cell: **a** Simulation novel EQ, **b** Simulation typ. EQ, and **c** Experimental Measurements Novel EQ

frequency). Figures 6.26 and 6.27 summarize the efficiency versus transferred power for the simulations on several working points for both the typical and novel equalizers, as well as the experimental measurements on the novel prototype. Figure 6.26 shows the results with varying dt_1, thus generating power transfer mainly in the first cell, while Fig. 6.27 shows the results with varying dt_2, which creates power transfer mainly in the second cell.

From Fig. 6.26, it can be observed that the best performance is achieved by the novel cell equalizer. Figure 6.26 clearly indicates more than 80 % efficiency for a power transfer of 5–20 W (equivalent to 1.4–5.5 A). It must be noted that there exist only minor differences between the simulation and experimental measurements in this range of power transfer. The only important difference is at low transferred power (less than 3 W), whereby the efficiency falls under the specifications (approximately 60 %). As explained before, this is due to the idle consumption of about 1 W. This phenomenon was observed in the simulations as well as real measurements, due to the inductor current ripple flowing through the system.

In Fig. 6.27, there is a trivial difference in the performance, with the real measurements actually performing better than those predicted in the simulations. It presents the same worst-case performance (60 % efficiency) at low transfer power. Comparing all cases, the worst efficiency (68 %, at 20 W, and 55 %, at 25 W) is observed in the case of the typical cell equalizer, draining from the first cell. In fact, this result was predictable, since the current must traverse more equalizer units to flow from the first cell to the last cell, as shown in the configuration of Fig. 6.3. In general, the new equalizer performs better in extreme-to-extreme cell power transfers, contrary to the typical equalizer, which theoretically performs slightly better in adjacent cell power transfers.

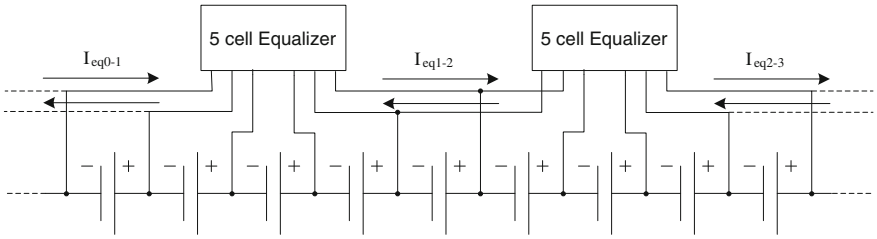

Fig. 6.28 Equalizer chain current transfer

6.4.7 Equalizer Chaining Method

Higher efficiencies of the equalizer in extreme-to-extreme cell power transfer cases are especially interesting for real EV/PHEV applications, where the utilization of long strings of cells is common. The proposed equalizer, using the chaining method introduced in Fig. 6.8, would be able to transfer power efficiently from one equalizer unit to another. This is particularly true, given its properties of higher than 80 % efficiency during power transfers from extreme-to-extreme cells. This is in contrary to the typical cell equalizer, where the average efficiency is 15 % lower than that of the novel equalizer. Thus, the novel equalizer is capable of distributing excess energy among equalizer units in a more efficient manner than the typical equalizer. Figure 6.28 depicts a possible method to extend the equalization to a long chain of cells. Figure 6.28 also shows an example of current transfer between equalizers.

Basically, each equalizer unit is connected to the next one by sharing the last cell. When one equalizer needs to transfer excess power to the other equalizer, first, it sends it to its last cell, after which the next equalizer takes power from its first cell. A possible way to calculate the amount of current transfer includes each equalizer communicating their average cell SOC to a central controller, which decides the amount of current that the equalizers should transfer between each other.

The total system efficiency is dependant on the amount of equalizer units that the energy must traverse, which is totally dependent on the capacity dispersion of the cells. Supposing a 5 % Gaussian distribution in the battery cell capacities, about 20 cells out of 100 cells have more than ± 3 % dispersion. That is about one cell with high capacity dispersion per equalizer unit. Hence, in a typical simulated case, the energy did not have to traverse more than 1 unit. Rather, the energy only traversed partially to the next unit. In this case, depending on the capacity distribution of the cells, the total system efficiency is found to be about 75 %, which satisfies minimum original specifications. This is clearly better than the total system efficiency obtained by the typical equalizer, which is found to be about 68 %.

6.4.8 Summary

Overall, it can be safely inferred that the proposed novel cell equalizer prototype performs as predicted, obtaining a 90 % peak efficiency at 7 W power transfer, and 77 % at 30 W transfer, as shown in Figs. 6.24 and 6.25. There is a good agreement between the efficiencies observed in the model, simulations, and the experimental results. However, as aforementioned, there exists an exception at low power transfer (less than 3 W) where the high losses (about 1 W) caused by the inductor current ripples affect the overall efficiency. This is the only operating point where the efficiency (60 %) is worse than the specifications (75 %). These losses can be eliminated by turning off the equalizer when the transferred power is so small that it does not justify the losses, as described in Sect. 6.5.

It is worthwhile mentioning here that the maximum equalizer current is higher than the specifications (7 A). However, the range of equalizing current, where the efficiency is good, is limited from 1 to 5 A, in accordance with the specifications.

The equalization test performed in Sect. 6.4.3.1 proved not to be up to expectations. This is because the test depicted a long equalizing time (40 min, instead of the ideal 20 min). It also depicted a noise of 0.3 %, instead of 0.1 %. It is worth pointing out that this test used cell voltage equalization instead of SOC equalization. The controller presented in Sect. 6.5 is developed to improve these issues.

The cost targets are met without difficulty, as demonstrated in Sect. 6.3.4. The cost achieved is $4.00/cell, against a maximum of $6.00/cell. This is considered in the economic analysis, in Chap. 3. The equalizer includes the communication capabilities demanded in the specifications.

It can be clearly deduced that the novel cell equalizer outperforms the typical cell equalizer, when the power has to be distributed from the first to the last cell of an equalizer module. This is particularly useful in very long battery cell strings, using the method described in Sect. 6.4.7. The difference in extreme-to-extreme cell performance leads to a major difference in total system efficiency of about 75 % (for the novel equalizer), against 68 % (for the typical equalizer), using a 5 % Gaussian dispersion in the battery cell capacities.

6.5 Controller Design for Developed Cell Equalizer

6.5.1 Introduction

In the previous sections, the topological layout and design of a novel cell equalizer configuration was presented, which is capable of meeting the performance and cost targets for PHEV/EV applications. As aforementioned, the only practical weakness of this configuration is the complex control algorithm, especially if SOC equalizing is desired. The purpose of this chapter is to introduce a new and

simplified control scheme, based on open-circuit voltage estimation, for the novel cell equalizer configuration, fulfilling expectations of low cost, large currents, and high efficiency. Practical issues, such as limitations on maximum and minimum cell voltage, noise, errors in quantization, and modeling, among others, are explored. It is critical to point out that the designed control scheme is not necessarily limited to the novel cell voltage equalizer configuration, but may also be applicable to other equalizer topologies, like those presented in [1–6]. Finally, a comprehensive comparison between theoretical test results and practical equalization test results is presented.

6.5.2 Controller Functions

The on-board controller has several responsibilities, some of them exclusively for the proposed novel cell equalizer configuration, such as:

(a) Real-time measurement of cell voltages: The controller measures the voltage of each cell individually, at a certain sampling frequency. In the prototype used in this thesis, this time is set at 1 s.
(b) Computation of the SOC of each cell: Using a method proposed later in this section, the controller calculates the SOC based on cell voltages.
(c) Calculation of equalizing current: Considering diverse factors, such as equalizer efficiency and maximum cell ratings, the controller estimates the desired equalizing current.
(d) MOSFET timing calculation: Based on the mathematical models, presented in 6.4.4, the controller calculates the MOSFET gate timings, to obtain desired equalizing current.
(e) Current measurement: Alternatively, the cell equalizer unit may include a cell current measurement option, to improve the equalizing and the SOC estimation precision. This can be replaced with single current measurement per battery pack, and the single cell current can be mathematically estimated using the mathematical model presented in Sect. 6.4.4.
(f) Safety monitoring: In addition, the controller monitors each cell individually, including temperature, investigating voltage and internal resistance anomalies, and may also be responsible for state of health (SOH) monitoring [17, 19]. This provides valuable information that leads to warnings, or eventually a system shut down. Safety monitoring, although overviewed, is not covered in the scope of this chapter.
(g) Communication: The controller shares information with all the controllers in each chained equalizer [19] and eventually, with the main controller, in order to allow better current sharing and distribution. The multiple equalizer chain management and current distribution is not part of this thesis, and could be explored as future work.

All the above tasks are performed real-time, in an inexpensive, low-consumption microcontroller through simplified, yet precise methods, as explained in the ensuing sections. These methods include estimating cell open circuit voltage (V_{OC}) and internal resistance. Due to the high interaction between the control block and the battery model, the latter will be explored in detail in the next section.

6.5.3 Lithium-Ion Cell Electrical Model

There exist several equivalent models for batteries, with varying complexities [15–17, 20]. In [15], the V_{OC} error is about 0.1 %, and in [16, 17], the SOC error is about 5 %. All values are consistent with the error obtained by the method described later in this thesis. For the equalizer controller explored in this chapter, the battery cell equivalent electrical model presented in [15] has been chosen, because of its simplicity and high precision in the range of SOC typically used in electric vehicles (from 30 to 80 % SOC) (as highlighted in Sect. 6.3). The equivalent model of a battery cell is shown in Fig. 6.29.

In the equivalent model of Fig. 6.29, R_{int} represents the total steady state cell internal resistance, including connections; R_a, R_b, C_a, and C_b model the dynamic response, in the case tested in this thesis with a time response of 3 s and 50 s; the open circuit voltage (V_{OC}) has a nonlinear relationship with SOC, temperature, and age, and represents chemically stored energy. The internal resistance is also dependent on SOC, temperature, and age. Hence, internal resistance cannot be considered as a constant. I_{Cn} is the cell current, which comprises of I_{Bat} (total battery current) and I_{Eqn} (equalizing current). The battery used in this prototype has 4, 2.2 Ah lithium-ion (Li-ion) cells connected in parallel, five groups of four cells in series, totalling 8.8 Ah, and 18 V nominal voltage. Figure 6.30 shows the voltage in slow discharge of this Li-ion cell, practically equal to the V_{OC}. Figure 6.30 plots the variation of internal resistance as a function of the SOC.

The dynamic response equivalent capacitors and resistors, R_a, R_b, C_a, and C_b, although not constant, remain stable in a good range of SOC, as can be appreciated through measurements performed in [15]. Figure 6.31 also provides an estimate of the SOC-region where the equivalent model is valid (from 100 to 15 % SOC).

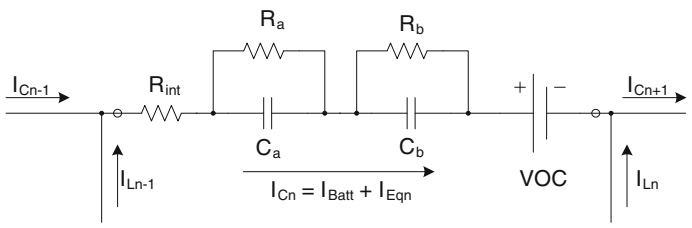

Fig. 6.29 Equivalent electrical model of a battery cell

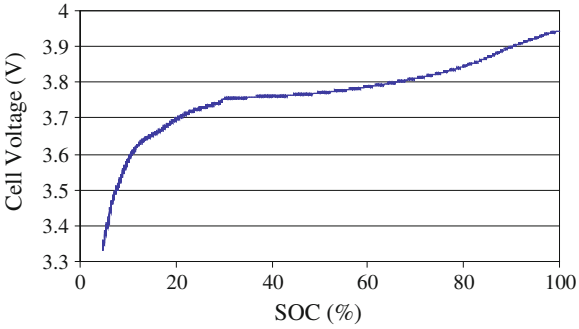

Fig. 6.30 Cell voltage in slow discharge (V_{OC} vs. SOC)

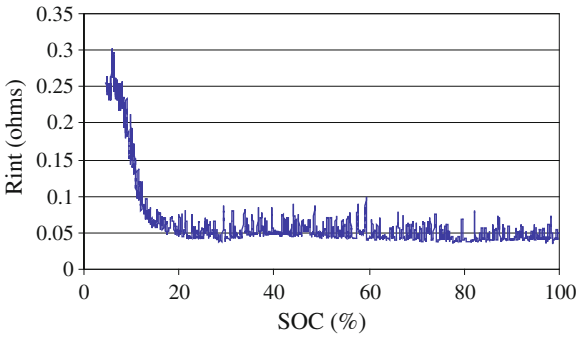

Fig. 6.31 Internal resistance versus SOC

6.5.4 VOC Determination

The most precise technique, yet not practical, to find the V_{OC} of a battery, is to disconnect the current for a long period of time, in order to pass through the transient response time. In fact, the battery will be loaded according to the user demand. The only controllable load is the equalizer: equalizing current can be stopped for short periods of time, in order to estimate the V_{OC}, after which the equalizing process can be resumed. The remaining issue is settling time necessary to achieve the steady state voltage, which is too long for a feasible battery equalizer (from tens of seconds to several minutes), as shown in Fig. 6.32.

To solve this issue, a simple method for estimating the V_{OC}, with only short time periods of no equalizing current, is presented in this chapter. Because of the long settling time of the battery voltage, several seconds are necessary to make an accurate estimation. In this case, only 4 s was enough for the equalizer controller to obtain a V_{OC} estimation error of less than 1 %. In fact, there are several methods to calculate battery model parameters, even without forcing variations in current, like those presented in [16, 17, 20]. However, the computation power required for these tasks is extremely demanding for an inexpensive microcontroller, like the one used in this application. Hence, simplified versions of the methods presented

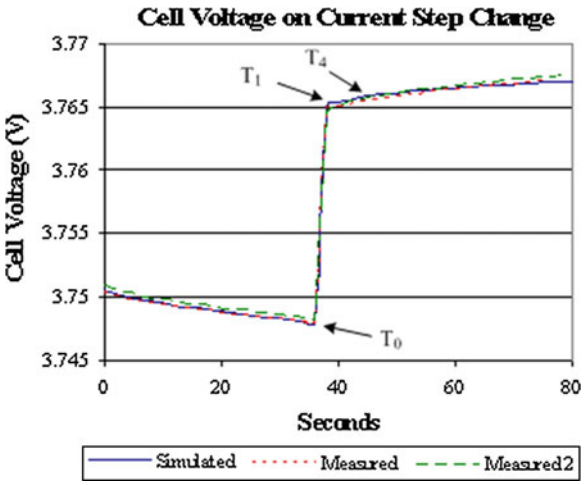

Fig. 6.32 Cell voltage during a step change in current

in [16, 17, 20] must be developed, before they can be utilized for low-cost applications, such as the one presented in this thesis.

6.5.5 VOC Estimation Algorithm

Based on the battery model described in Sect. 6.5.2, it is possible to mathematically calculate the voltage on a battery cell (V_b) during a forced step change of current, such as the one generated when the equalizer turns off, using the following equation:

$$V_b = VOC + R_{\text{int}} \cdot (I_{Bat} + I_{Eq} \cdot \delta_0) + R_a \cdot I_{Eq} \cdot e^{-\frac{t}{T_a}} + R_b \cdot I_{Eq} \cdot e^{-\frac{t}{T_b}} \qquad (6.12)$$

Here, V_b is the instantaneous cell voltage, starting at T_0, I_{Eq} is the equalizing current, active only at T_0 and interrupted after T_1, I_{Bat} is the battery pack current, R_{int} is the static internal resistance, R_a, R_b are the dynamic resistances, and T_a, T_b are the dynamic time constants. R_{int}, R_a, and R_b are considered unknown, while T_a and T_b are constants. R_a and R_b are considered to be related and proportional. For example, in calculations made from real measurements, observed from the battery cells used in this prototype, $R_a/R_b \approx 0.1, T_a = 3$ s, and $T_b = 50$ s. The voltage samples (Fig. 5.4) are observed at T_0, (when I_{Eq} is still active), at T_1 (the first second after $I_{\text{Eq}} = 0$), and at T_4 (the fourth second after $I_{\text{Eq}} = 0$). The cell equalizer current and total battery current are used in the algorithm to determine the estimated V_{OC}. Taking the above points into consideration, V_b can be approximated as:

$$V_b \cong VOC + R_{\text{int}} \cdot (I_{Bat} + I_{Eq} \cdot \delta_0) + R_b \cdot I_{Eq} \cdot k_t \qquad (6.13)$$

$$k_t = \frac{R_a}{R_b} \cdot e^{-\frac{t}{T_a}} + e^{-\frac{t}{T_b}} \tag{6.14}$$

Knowing I_{Bat}, I_{Eq}, V_b, and using the three equations generated from (6.13), by replacing t by T_0, T_1, and T_4, the unknown variables R_b, R_{int} and finally, V_{OC} can be calculated. It must be pointed out that k_t is previously stored in a lookup table, based on values that are specific for a particular type of battery cell. The resulting three system of equations are easy to solve, reducing the computational power demand.

The performance of the V_{OC} estimator has been validated using the following experimental algorithm. The cell is loaded using a known current. Thereafter, the load is interrupted, until the cell voltage reaches a constant value. This value (the actual V_{OC}) is compared with the V_{OC} estimated using the previous method. Figure 6.33 shows the error between the estimated V_{OC} and the measured V_{OC} as a function of the SOC. As the SOC approaches 0 % (discharged cell), the previous assumptions become less accurate.

Figure 6.33 points out an obvious limitation of the method, wherein closer to 10 % of SOC, the error sharply increases, due to a very significant change in the equivalent dynamic resistances and time constants, nearing the full discharge state of the cell. It may be inferred that the method is accurate to 0.1 % in the 20 % to 100 % SOC range. Outside this SOC range, the method becomes ineffective, due to parameter dependency on the SOC. Nevertheless, for PHEV/EV applications, where the longevity of battery operation is important, this is not considered to be a major issue, because the battery is never discharged under 30 % SOC, as explained earlier, in Sect. 6.3.3. On the other hand, an error of 0.1 % in V_{OC} corresponds to an error of 1–3 % in SOC (using Fig. 6.30, V_{OC} vs. SOC), which corresponds with the error obtained by [16, 17]. This error generates undesired differences in cell equalization. For EV/PHEV applications, suitable calibration of the equalizer is necessary during the manufacturing process to avoid additional errors due to voltage measurements (0.1 %) and voltage reference (0.05 %). Without calibration, the absolute overall error could increase to about 0.25 %, corresponding to a maximum error of 7.5 % in SOC, which is very high for this application.

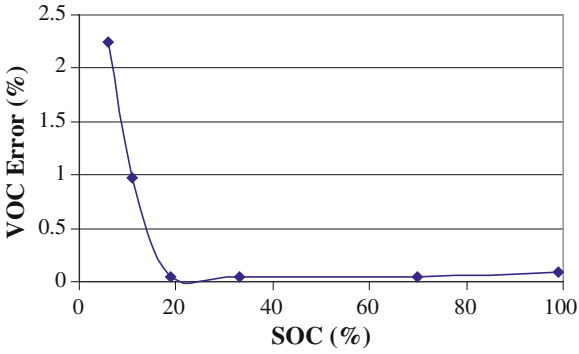

Fig. 6.33 V_{OC} estimation error versus SOC

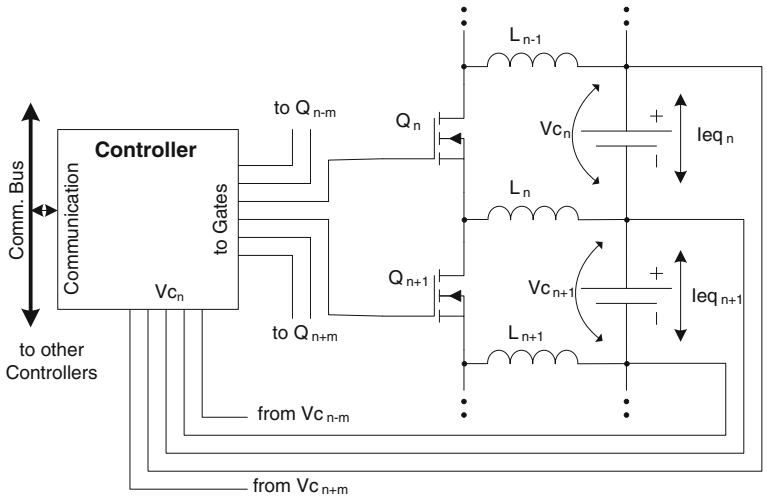

Fig. 6.34 Equalizer controller block diagram

In the next section, the V_{OC} estimation method is applied to the novel battery cell equalizer control system.

6.5.6 *Proposed Cell Equalizer Control Strategy*

The cell equalizer controller is composed of several blocks: cell V_{OC} estimation, overviewed in the previous section; V_{OC} difference calculation, which is used as an error signal; a proportional-integral block (PI), that will affect the error signal; desired cell current calculation, based on the PI output; cell current and voltage limiter; and finally, the timing calculations for the MOSFETs, calculated using Eqs. 6.4 and 6.6. Figure 6.34 shows the equalizer controller block diagram, while Fig. 6.35 shows the equalizer controller details.

As mentioned in the previous section, the V_{OC} estimator needs to interrupt the equalizing current for at least 4 s, in order to record the necessary measurements of

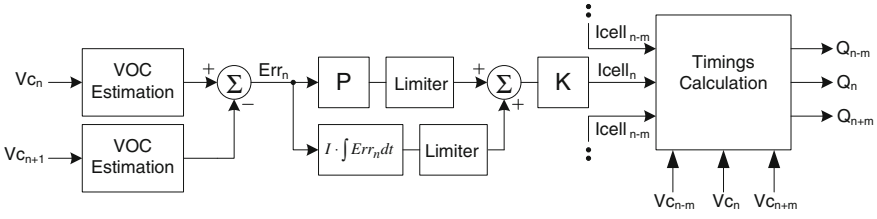

Fig. 6.35 Equalizer controller details

cell voltage. The V_{OC} of each cell is estimated using cell voltage measurements, cell equalizing currents, provided by the equalizer hardware (or from estimations), using the cell voltages and the load current, and finally, using the load current, taken from the system controller. The objective is to equalize the V_{OC} of each cell, so that the difference is used as the error signal, as represented in Eq. 6.15.

$$Err_n = Vc_{n+1} - Vc_n \tag{6.15}$$

Because these errors are sampled at a very slow rate (from 30 s to several minutes), the error signal is passed through a PI block, to avoid stability issues, and to improve the steady state error, as represented in Eq. 6.16. An optional derivative component in the controller is not used here, because of the inherent noise related to V_{OC} estimation, which would be amplified to unacceptable levels.

$$PIerr_n = Err_n \cdot P + I \cdot \int Err_n dt \Big|_{resetable} \tag{6.16}$$

Once the complete equalization is obtained, i.e., the error signals are very close to zero, the equalizer can be turned off, to reduce consumption, and the error integration is reset. This method can be termed as the "Dead-Band" method. Thereafter, the desired cell currents are calculated based on (6.17) and (6.18).

$$Ic_{n+1} - Ic_n = k^* PIerr_n \tag{6.17}$$

$$\sum_n Ic_n = 0 \tag{6.18}$$

Safety is insured by limiting the cell currents to a maximum acceptable level by each cell, and limiting the maximum cell voltage, using the internal resistance obtained from V_{OC} estimation. Additional warnings are issued when the cell voltage is too low or the temperature is too high.

Additional precautions should be taken, such as maximum cell temperature, maximum equalizer current, and balance between equalizing time and efficiency. Figures 6.5, 6.6, 6.7, and 6.8 show the efficiency of the equalizer versus the transferred power (Sect. 6.4.4). It is clear that a medium range of equalizing current (from 5 to 20 W of transferred power, equivalent to 1.5–5 A) is desired, when high efficiency is critical. The average efficiency in this range is about 85 % (Fig. 6.36).

Based on the above considerations, the desired cell current and instantaneous cell voltage values are inserted into Eqs. 6.4 and 6.6, in order to obtain the timings of the MOSFETs. To avoid shoot through in the MOSFET chain, minimum turn-off times (50 % of the typical τ_n time), maximum turn-off times (150 % of the typical τ_n time), and a guard time (of 50 ns) must be enforced in each MOSFET. If the calculated timing violates these limits, then the desired cell currents are reduced, and the timing is recalculated, until an allowed timing scheme is obtained.

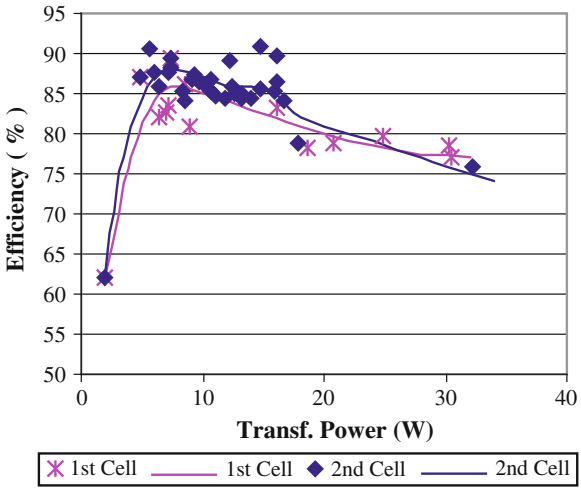

Fig. 6.36 Equalizer efficiency versus transferred power

In the next section, an appropriate controller for the proposed novel equalizer will be modeled and the stability of the system will be evaluated, considering the proportional and integral coefficients and sampling time as major parameters.

6.5.7 Proposed Cell Equalizer Controller Modeling

Several simplifications must be applied in order to evaluate the controllability, reduce the amount of variables, as well as linearize the proposed nonlinear system. These tasks are explained in detail in the ensuing sections.

6.5.8 Cell Equalizer Control System Simplification

The first case of simplification is to consider the fact that the equalizer will transfer energy from only one cell to another. The model is exactly that of a basic inductive equalizer. The system will then be simplified to "one input-one output," as shown in Fig. 6.37.

Considering the duty cycle ($\tau_n = t_n/T$) of each MOSFET, which are complementary to each other ($t_1 + t_2 = T$), the equalizer can be seen as a DC/DC converter, satisfying the operating rules of an ideal transformer. This is shown in Fig. 6.38, where the primary is connected to cell #1 and the secondary is connected to cell #2. Voltage ratio (n) is equal to the duty cycle ratio, τ_1/τ_2, as summarized in Eq. 6.19. Resistor, R, represents the added internal resistance of the cells, cables, PCB traces, and conduction losses in the DC/DC converter.

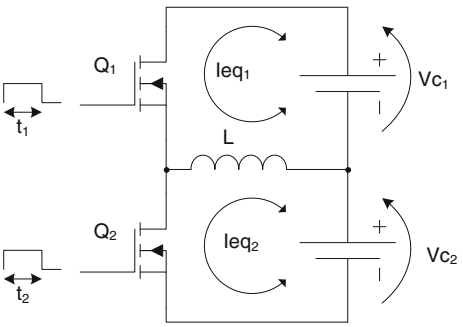

Fig. 6.37 Simplified "one input-one output" equalizer model

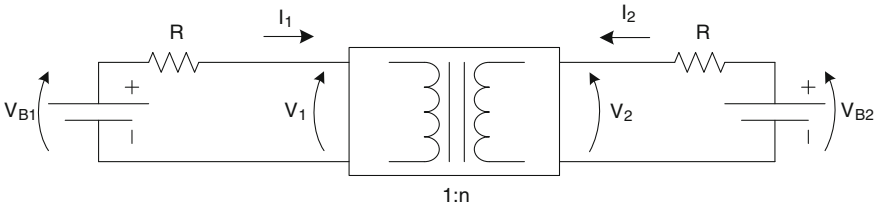

Fig. 6.38 Simplified electrical model of the equalizer

Considering ideal converter efficiency, the current ratio is expressed as shown in Eq. 6.38.

Voltage ratio can be written as:

$$\frac{V_2}{V_1} = \frac{\tau_1}{\tau_2} = \frac{\tau_1}{1-\tau_1} = n \tag{6.19}$$

Current ratio can be written as:

$$\frac{I_2}{I_1} = -\frac{\tau_2}{\tau_1} = \frac{\tau_1 - 1}{\tau_1} = -\frac{1}{n} \tag{6.20}$$

Considering the fact that V_{OC} sampling frequency is about 1 min, and the first time constant is about 3 s, the dynamic model of the cell, as shown in Fig. 6.29, can be reduced to the model of Fig. 6.39. In the reduced model, the first time constant is ignored. The cell V_{OC} can be considered as linear, particularly from 30

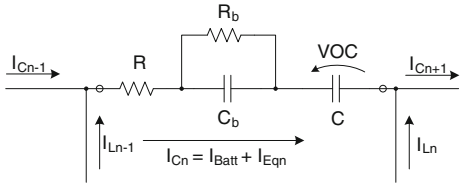

Fig. 6.39 Simplified electrical cell model

to 70 % SOC. R_{int} can be considered as constant, as was depicted in Fig. 6.30. Hence, the battery cell can be modeled as a simple capacitor.

The V_{OC} estimation method, as discussed in section VOC Estimation Algorithm 6.5.5, is theoretically capable of obtaining V_{OC}, independent of the effects caused by R_b and C_b. In fact, there is always a noteworthy V_{OC} estimation error, mainly due to a miscalculation of R_b. This error can be modeled as a capacitor-resistor pair (R_2–C_2), replacing the R_b–C_b pair. Because their time constant (50 s) is too close to the sampling frequency, T_S (30–120 s), it cannot be ignored from the stability analysis.

The controller error signal is obtained from the difference between both the estimated V_{OC} values. Depending on the difference between the R_b–C_b pairs of each cell, two possible electrical models can be analyzed; one case with a remaining V_{OC} estimation error (R_2–C_2) in series with cell #1, as shown in Fig. 6.40, and another case in series with cell #2, as shown in Fig. 6.41.

VB_1 and VB_2 are the instantaneous V_{OC} estimations. The controller should be stable in both cases, considering the sampling time of the V_{OC}, $R_2 \ll R$, and $C_2 \ll C$. In the next section, the mathematical model for both cases will be derived.

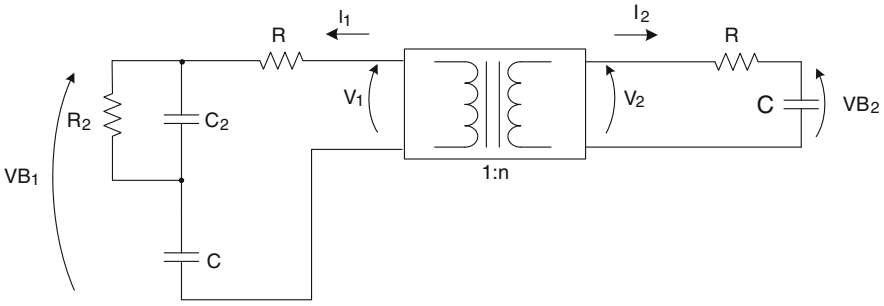

Fig. 6.40 Simplified electrical plant model, with V_{OC} error dominant in cell #1

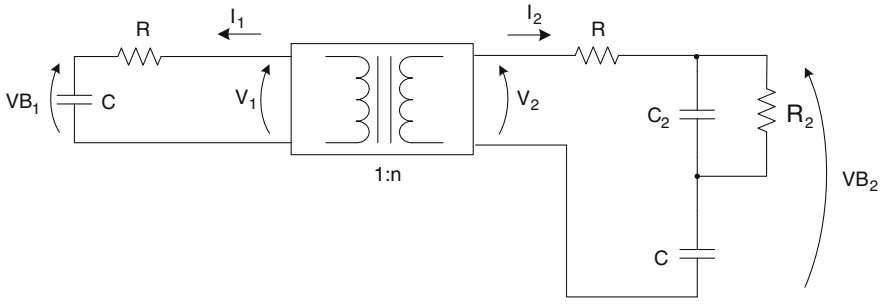

Fig. 6.41 Simplified electrical plant model, with V_{OC} error dominant in cell #2

6.5.9 Mathematical Derivation of the Cell Equalizer Controller

6.5.9.1 Plant Modeling for First Case, Shown in Fig. 6.40

Considering V_{OC} as the initial open circuit voltage, the voltages for the first circuit, using Laplace transform, can be expressed as:

$$V_1 = \frac{VOC_1}{S} + \frac{I_1}{S \cdot C} + I_1 \cdot R + \frac{I_1 \cdot R_2}{(1 + S \cdot R_2 \cdot C_2)} \tag{6.21}$$

$$V_2 = \frac{VOC_2}{S} + \frac{I_2}{S \cdot C} + I_2 \cdot R \tag{6.22}$$

$$VB_1 = \frac{VOC_1}{S} + \frac{I_1}{S \cdot C} + \frac{I_1 \cdot R_2}{(1 + S \cdot R_2 \cdot C_2)} \tag{6.23}$$

$$VB_2 = \frac{VOC_2}{S} + \frac{I_2}{S \cdot C} \tag{6.24}$$

Thereafter, considering the DC/DC transformer ideal equations, as defined in Eqs. 5.8 and 5.9, the following expression can be obtained for computing current through cell #1 (Ic_1):

$$Ic_1 = \frac{(-VOC_1 \cdot n + VOC_2) \cdot C \cdot (1 + SR_2C_2) \cdot n}{(n^2 + n^2S \cdot R_2C_2 + n^2S \cdot (R + R_2)C + n^2S^2RC \cdot R_2C_2 + 1 + S \cdot R_2C_2 + S \cdot RC + S^2RC \cdot R_2C)} \tag{6.25}$$

R_2 is much smaller than R, and in the stability analysis of this case, V_{OC1} is considered equal to V_{OC2}, which is the point where the system is nearly equalized. Hence, the following equation can be obtained:

$$Ic_1 = \frac{VOC \cdot (1 - n) \cdot C \cdot (1 + SR_2C_2) \cdot n}{(1 + S \cdot R_2 \cdot C_2) \cdot (1 + S \cdot R \cdot C) \cdot (1 + n^2)} \tag{6.26}$$

6.5.9.2 Plant Modeling for Second Case, Shown in Fig. 6.41

Using Laplace transform, the voltages for the second case, can be expressed as:

$$V_1 = \frac{VOC_1}{S} + \frac{Ic_1}{S \cdot C} + Ic_1 \cdot R \tag{6.27}$$

$$V_2 = \frac{VOC_2}{S} + \frac{Ic_2}{S \cdot C} + Ic_2 \cdot R + \frac{Ic_2 \cdot R_2}{(1 + S \cdot R_2 \cdot C_2)} \tag{6.28}$$

$$VB_1 = \frac{VOC_1}{S} + \frac{Ic_1}{S \cdot C} \tag{6.29}$$

$$VB_2 = \frac{VOC_2}{S} + \frac{Ic_2}{S \cdot C} + \frac{Ic_2 \cdot R_2}{(1 + S \cdot R_2 \cdot C_2)} \tag{6.30}$$

Again, considering the DC/DC transformer ideal equations, as defined in Eqs. 5.8 and 5.9, the following expression can be obtained for computing current through cell #1 (Ic_1):

$$Ic_1 = \frac{(-VOC_1 \cdot n + VOC_2) \cdot C \cdot (1 + SR_2C_2) \cdot n}{(n^2 + n^2S \cdot R_2C_2 + n^2S \cdot RC + n^2S^2RC \cdot R_2C_2 + 1 + S \cdot R_2C_2 + S \cdot (R + R_2)C + S^2RC \cdot R_2C)} \tag{6.31}$$

As R_2 is much smaller than R, and in the stability analysis of this case, V_{OC1} is considered equal to V_{OC2}, which is the point where the system is nearly equalized. Hence, the equation for the second case (6.31) becomes exactly the same as the one for the first case (6.16). This equation represents the response of the overall system.

6.5.9.3 Controller Modeling for First Case, Shown in Fig. 6.40

For the purpose of this thesis, n is defined in Eq. 6.19, as a voltage gain of V_2/V_1, the nominal value of which is 100 %.

The error signal is taken from the difference between the two-cell V_{OC} estimation (Eq. 6.32). The V_{OC} estimation method inherently possesses a slow first order sample and hold, which is about 1 min of sampling time (T_s). The gain, n, is kept constant during this sampling time. For the controller model, a simple PI is used, considered here without the limiters, as shown in Fig. 6.42.

The complete block diagram for the control analysis is shown in Fig. 6.43. A δ-signal applied to the input represents the initial error due to an unbalance of the cells. Conceptually, the transfer function represents the response of the error (the difference between the V_{OC} of each cell) to an initial unbalance.

Considering the error signal, before sampling:

$$Err = VB_2 - VB_1 \tag{6.32}$$

Thereafter, substituting VB_1 (using Eq. 6.23) and VB_2 (using Eq. 6.24) for the first case, the following error value can be obtained:

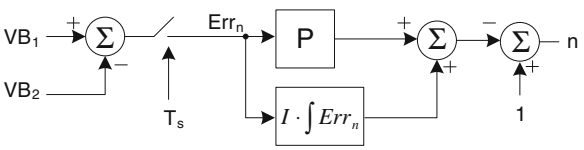

Fig. 6.42 Details of the controller

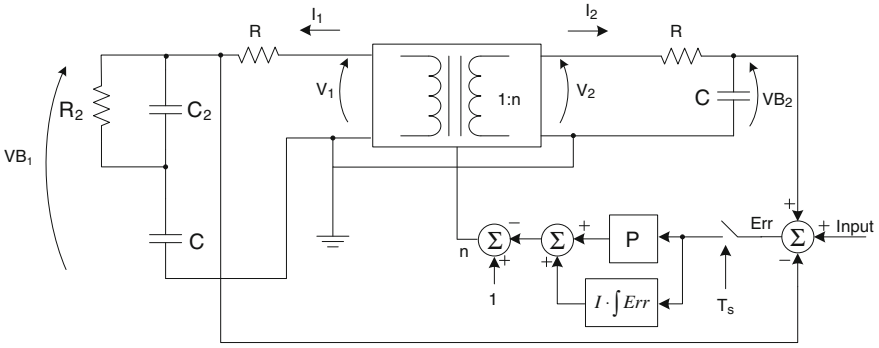

Fig. 6.43 Complete system diagram

$$Err = -Ic_1 \cdot \left[\frac{1+\frac{1}{n}}{SC} + \frac{R_2}{(1+S\cdot R_2\cdot C_2)}\right] \tag{6.33}$$

Substituting Ic_1, obtained from Eq. 6.26:

$$Err = \frac{-VOC\cdot C\cdot(1+SR_2C_2)}{(1+S\cdot R_2\cdot C_2)\cdot(1+S\cdot R\cdot C)} \cdot \left[\frac{(1-n)\cdot(1+n)}{(1+n^2)\cdot SC} + \frac{(1-n)\cdot n\cdot R_2}{(1+n^2)\cdot(1+S\cdot R_2\cdot C_2)}\right] \tag{6.34}$$

6.5.9.4 Controller Modeling for Second Case, Shown in Fig. 6.41

Repeating the procedure for the second case, and substituting Eq. 6.32 with Eqs. 5.8 and 5.9, the following error value can be obtained:

$$Err = -Ic_1 \cdot \left[\frac{1+\frac{1}{n}}{SC} + \frac{\frac{R_2}{n}}{(1+S\cdot R_2\cdot C_2)}\right] \tag{6.35}$$

Substituting Ic_1 from Eq. 6.26:

$$Err = \frac{-VOC\cdot C\cdot(1+SR_2C_2)}{(1+S\cdot R_2\cdot C_2)\cdot(1+S\cdot R\cdot C)} \cdot \left[\frac{(1-n)\cdot(1+n)}{(1+n^2)\cdot SC} + \frac{(1-n)\cdot R_2}{(1+n^2)\cdot(1+S\cdot R_2\cdot C_2)}\right] \tag{6.36}$$

6.5.9.5 System Modeling for Both Cases, Shown in Figs. 6.40 and 6.41

Due to the fact that n works in a very limited range (from 0.5 to 1.5), due to timing limitations, it is possible to approximate the following relationships:

$$\frac{(1-n)\cdot(1+n)}{(1+n^2)} \cong 1.7\ to\ 2.3 \cdot \frac{(1-n)}{2} \tag{6.37}$$

$$\frac{(1-n)\cdot n}{(1+n^2)} \cong 1 \cdot \frac{(1-n)}{2} \tag{6.38}$$

$$\frac{(1-n)\cdot n}{(1+n^2)} \cong 0.75\ to\ 1.4 \cdot \frac{(1-n)}{2} \tag{6.39}$$

Substituting Eqs. 6.37, 6.38, and 6.39 into Eq. 6.34, for the first case, and into Eq. 6.36, for the second case, the equation that covers both cases can be summarized as:

$$Err = \frac{-VOC \cdot C \cdot (1+SR_2C_2)\cdot(1-n)}{(1+S\cdot R_2\cdot C_2)\cdot(1+S\cdot R\cdot C)\cdot 2} \cdot \left[\frac{(1.7\ to\ 2.3)}{SC} + \frac{(0.75\ to\ 1.4)\cdot R_2}{(1+S\cdot R_2\cdot C_2)}\right] \tag{6.40}$$

From Fig. 5.14, using Laplace transform, Δn is calculated as:

$$n = \left(K_P + \frac{K_I}{S}\right) \cdot \left(\frac{1-e^{S\cdot T_S}}{S\cdot T_S}\right) \cdot Err - 1 \tag{6.41}$$

Substituting n, from Eq. 6.32, into Eq. 6.40, and using Eq. 6.41, the expression for the complete open loop transfer function is obtained as depicted in Eq. 6.42. The loop is open at the Err signal point, in Fig. 6.42, and considers A as a variable ranging between 1.7 and 2.3, from Eq. 6.37, and B ranging between 0.75 and 1.4, from Eq. 6.39.

$$\begin{aligned} T_{OL} &= \frac{Err_{out}}{Err_{in}} \\ &= \frac{VOC\cdot\left(K_P + \frac{K_I}{S}\right)\cdot\left(\frac{1-e^{S\cdot T_S}}{S\cdot T_S}\right)}{(1+S\cdot R_2\cdot C_2)\cdot(1+S\cdot R\cdot C)\cdot 2\cdot S} \cdot [A\cdot(1+SR_2C_2) + B\cdot SR_2C] \end{aligned} \tag{6.42}$$

For the open loop transfer function of the complete system, Err in Eq. 6.41 can be considered as input, and the corresponding Err, in Eq. 6.40, can be considered as output. Equation 6.43 depicts the closed loop transfer function:

$$T_{CL} = \frac{VOC \cdot \left(K_P + \frac{K_I}{S}\right) \cdot \left(\frac{1-e^{S \cdot T_S}}{S \cdot T_S}\right) \cdot [A \cdot (1 + SR_2C_2) + B \cdot SR_2C]}{(1 + S \cdot R_2 \cdot C_2) \cdot (1 + S \cdot R \cdot C) \cdot 2 \cdot S + VOC \cdot \left(K_P + \frac{K_I}{S}\right) \cdot \left(\frac{1-e^{S \cdot T_S}}{S \cdot T_S}\right) \cdot [A \cdot (1 + SR_2C_2) + B \cdot SR_2C]} \tag{6.43}$$

6.5.10 Cell Equalizer Controller Stability Analysis in Frequency Domain

Several variables exist in Eqs. 6.42 and 6.43. The closed loop control system must be stable in all possible scenarios, which are specified by the combinations of possible variable values. Table 6.5 summarizes the variable values obtained from measurements:

The goal of the controller design for this application is not to find the optimum equalizing time, but to define a set of K_P–K_I that obtains a robust controller, i.e., the variable variations of Table 5.1 or the noise of the analog measurements do not affect the stability of the system.

Given that the error in V_{OC} (R_2_C_2) estimation has a time constant close to T_S, R_2 will have the greatest influence on the stability of the system. In this analysis, a sampling time of 1 min is estimated. For the rest of the variables, which have smaller sensitivity, the worst case is considered, given $V_{OC} = 4.2$ V, $R = 100$ mΩ, $C = 20{,}000$ F, $A = 2.3$, and $B = 1.4$. For these conditions, the stability requirements in frequency domain (*Barkhausen Stability Criterion*) must comply with a minimum phase margin or gain margin [21, 22]. The minimum necessary K_I is used, in order to obtain a zero steady-state error (10 % of K_P). Figure 6.44 shows the gain of the open loop system, for different combinations of K_P and R_2.

In Fig. 6.44, A, B, and C correspond to different values of R_2 (A = 0 % of R, B = 20 % of R, and C = 80 % of R). The numbers 1, 2, and 3 indicate $K_P = 10$,

Table 6.5 Summary of controller variables

Variable	Value
Battery	
V_{OC}	3 ∼ 4.2 V
R	100 ∼ 150 mΩ
R_2	0 ∼ 20 % of R
C	20000 ∼ 50000 F
R_2 C_2	∼50 s.
Controller	
T_S	30 s ∼ 2 min
A	1.7 ∼ 2.3
B	0.75 ∼ 1.4

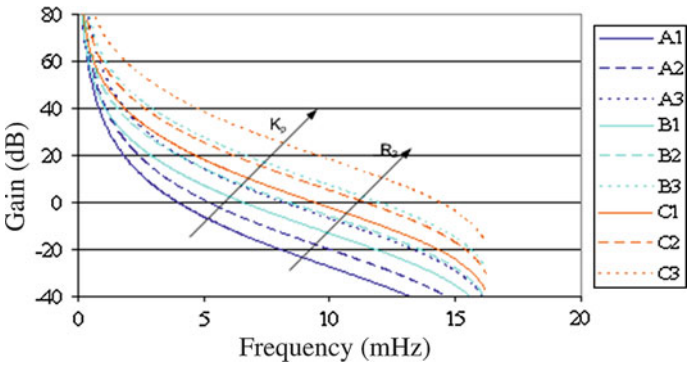

Fig. 6.44 System open loop gain, for different K_P and R_2 values

$K_P = 22$, and $K_P = 100$, respectively. Figure 6.45 shows the phase of the open loop system, for different values of R_2, which is independent of K_P.

In Fig. 6.45, A, B, and C correspond to different values of R_2 (A = 0 % of R, B = 20 % of R, and C = 80 % of R). It can be appreciated that the higher the gain or R_2 is, the less stable the system. Table 6.6 summarizes the stability indicators for each K_P–R_2 combination.

For a maximum acceptable V_{OC} estimation error, represented by the R_2 value, which is 20 % of R, the combination B_2, having about 50 degrees of phase margin and almost 20 dB of gain margin, is an excellent starting point. It is worthwhile mentioning here that if the error in V_{OC} estimation (represented by R_2) is not considered ($R_2 = 0$), the system might accept a much bigger K_P; as much as 4 or 5 times higher, as is the case in combination A3. Figure 6.46 shows the closed loop gain for the same combinations of K_P and R_2, as in Fig. 6.44.

In Fig. 6.46, A, B, and C correspond to different values of R_2 (A = 0 % of R, B = 20 % of R, and C = 80 % of R). The numbers 1, 2, and 3 indicate $K_P = 10$, $K_P = 22$, and $K_P = 100$, respectively. Again, it can be appreciated that the higher the gain or R_2 is, the less stable and faster is the system, which is proven in Fig. 5.18 by the higher peak gain and higher bandwidth, respectively. Table 6.7 summarizes the stability indicators for each K_P–R_2 combination.

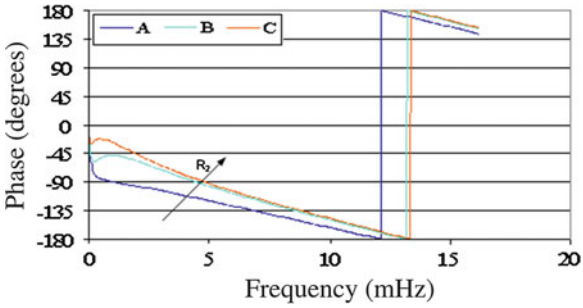

Fig. 6.45 System open loop phase, for different R_2 values

Table 6.6 Summary of stability indicators, for different K_P–R_2 combinations

Combination	R_2 (% R)	K_p	Phase margin (°)	Gain margin (*dB*)
A1	0	10	69	+ 36
A2	0	22	60	+29
A3	0	100	35	+16
B1	20	10	66	+26
B2	20	22	48	+19
B3	20	100	14	+6
C1	80	10	39	+15
C2	80	22	21	+9
C3	80	100	−9	−5

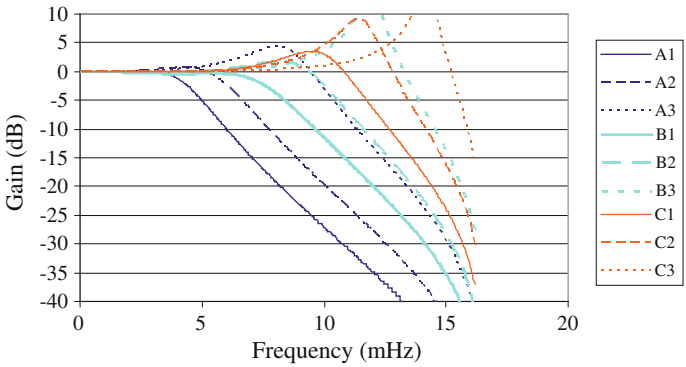

Fig. 6.46 System closed loop gain, for different K_P and R_2 values

As can be appreciated from Table 6.7, the combination B_2 (K_P value of 22 and $R_2 = 20$ % of R), presents a very good speed (high bandwidth), while maintaining the stability of the system (relatively low gain peak).

Subsequently, the effect of frequency sampling of V_{OC} estimation is studied. Section 6.5.2 explained a very simple V_{OC} estimation method, the main

Table 6.7 Summary of stability indicators for different K_P–R_2 combinations (closed loop)

Combination	R_2 (%R)	K_p	Peak gain (*dB*)	Bandwidth (mHz)
A1	0	10	+0.1	4.5
A2	0	22	+0.5	6.2
A3	0	100	+4.3	10
B1	20	10	0	7.8
B2	*20*	*22*	*+1.8*	*10.1*
B3	20	100	+12.9	13.6
C1	80	10	+3.5	11.4
C2	80	22	+9	13.2
C3	80	100	+ 17	15.5

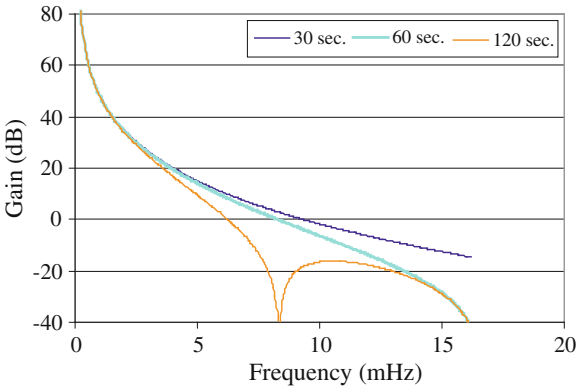

Fig. 6.47 System open loop gain, for different T_S values

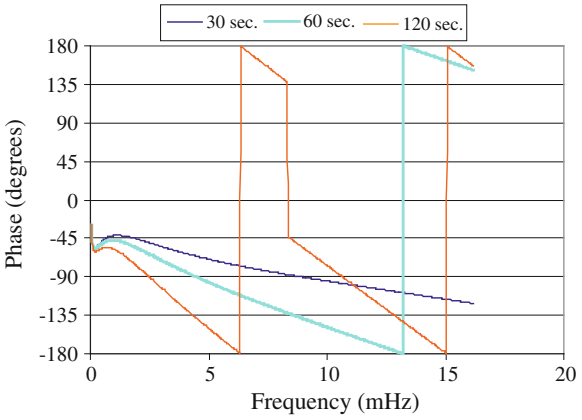

Fig. 6.48 System open loop phase, for different T_S values

disadvantage of which includes, turning off the equalizer for several seconds (in this case 4 s). This fact forces the reduction in sampling rate, from approximately 30 s to several minutes, in order to obtain a reasonable equalizing duty cycle.

Using the previously obtained K_P value of 22 and $R_2 = 20$ % of R, Fig. 6.47 shows the gain of the open loop system. Figure 6.48 the corresponding phase of the open loop system, with $T_S = 30$ s, 1, and 2 min, respectively.

As expected, a faster sampling rate makes the system much more stable. Table 5.4 summarizes the stability indicators for each sampling frequency and the resulting equalizer duty cycle.

From Table 6.8, it is clear that a maximum sampling rate of 1 min is necessary to obtain stable operating conditions. However, due to the 4 s turn-off during V_{OC} measurement, the equalizer duty cycle is negatively affected, as sampling rate tends to increase. As observed in Table 6.8, with a reasonable duty cycle of 93 %, a sampling rate of 1 min was found to perform satisfactorily.

Table 6.8 Summary of stability indicators for different sampling rates

Sampling rate (s)	Phase margin (°)	Gain margin (*dB*)	Equalizer duty cycle (%)
30	88	−40	87
60	48	−19	93
120	2	−1	97

Thus, critical control parameters have been extrapolated, in order to obtain a robust controller. After considering a possible error in V_{OC} estimation, the proportional factor was reduced to 25 % of the original value, in order to maintain stability of the system. In the next section, the stability of the system will be verified in time domain, considering nonlinear effects and variable limiters.

6.5.11 Cell Equalizer Controller Stability Verification in Time Domain

In order to verify the stability and dynamic performance of the controller, a full-time domain simulation is necessary. This is due to the presence of various system nonlinearities, such as the ones shown in Eqs. 6.37, 6.38, and 6.39, as well as the ones presented by the limitations of DC/DC ratio, n. It must be pointed out here that n is limited from 0.5 to 1.5, while the equalizer current and cell voltage are limited to 7 Amps and 4.2 V, respectively. As explained in Sect. 6.4.3.1, the maximum DC/DC ratio is limited, due to minimum and maximum switching times. This limitation is introduced in order to avoid overlapping between modes. The limitation in current is used to avoid saturation in the inductor. Furthermore, the limitation in maximum cell voltage is enforced to improve safety. If none of these limiters is active, then the system is considered to be in linear mode, and it usually occurs in the final stages of equalization.

The proposed novel equalizer is simulated using the dynamic model of the battery cells, reviewed in Sect. 6.5.3. The control method is explained in Sect. 6.5.6, using the parameters obtained from Sect. 6.5.10, and the V_{OC} estimation method, presented in Sect. 6.5.5. In order to reduce the complexity of the simulation, a system of two cells is used. This simulation represents the response of a bigger system fairly well, as validated later by practical measurements.

As seen in Sect. 6.5.5, V_{OC} estimation involves an equalizing current interruption for 4 s. This can be seen in the current plot as a "glitch," witnessing the small impact of the V_{OC} estimation method on the average equalizing current. Figure 6.49 shows the equalizing current in one of the two cells, with an initial unbalance, for three cases. The first case involves the original and most common controller, where the error signal is taken directly from the cell voltage, as demonstrated in Sect. 6.4, in Figs. 6.21 and 6.22. Here, the proportional and integral (K_P and K_I) factors are critically damped (this is called "*Method A*").

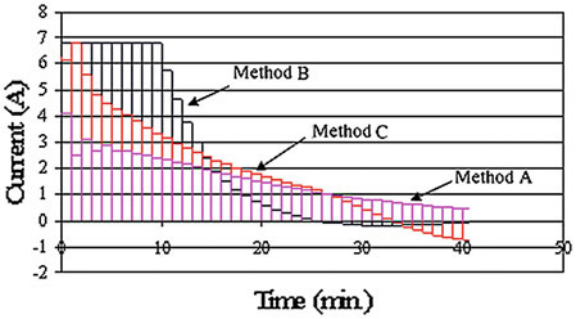

Fig. 6.49 Equalizer current in a cell, using: **a** cell voltage control, **b** V_{OC} control, and **c** reduced K_P factor V_{OC} control

The second case involves the ideal optimal controller, where the error signal is fed back from the estimated V_{OC}, as analyzed in Sect. 6.5.10 (combination *A*3), where K_P and K_I factors are critically damped ($K_P = 100$; this is called "*Method B*"). Finally, the third case involves a simulation with a more robust controller, in order to allow some error in the V_{OC} estimation. As explained earlier, in this scenario, K_P is reduced to 22, in order to maintain stability under all conditions (this is called "*Method C*"). Method C uses the same K_P as the experimental controller. Figure 6.50 shows the corresponding V_{OC} of each of the three systems.

The equalizing time can be seen in Fig. 6.49, when the current reaches zero, and in Fig. 6.50, when the V_{OC} peaks. The improvement in system response is obvious, based on V_{OC} estimation as an error signal ("method B"), in terms of equalizing time (25 min.). On the other hand, "method C" slows down the system, by reducing K_P (33 min.), in order to be stable in all situations. Even with reduction in K_P, the resulting system is much faster than the original one ("Method A," at 60 min.), which effectively reduces the overall equalizing time by nearly 50 %. The effect of limitation in equalizing current is critical to note, whereby the current is limited to 7 A, for safety, to avoid inductor saturation and for efficiency reasons (since the efficiency drops to less than 75 % at higher currents). This is clear in Fig. 6.49, during the first 10 min, in "Method B".

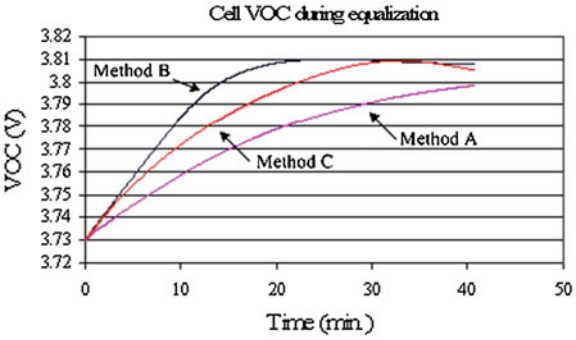

Fig. 6.50 Equalizer V_{OC} in a cell, using: **a** cell voltage control, **b** V_{OC} control, and **c** reduced K_P factor V_{OC} control

In addition, the controller should stop equalizing when the V_{OC} of each cell lies within the defined "deadband," specified to be 0.1 % of V_{OC}. This will be shown later, by means of experimental measurements. For example, in Fig. 6.50, the equalizer should have stopped, when the V_{OC} reached the equalizing voltage. In the next section, the experimental measurements performed on the proposed novel equalizer prototype will be presented.

6.5.12 *Proposed Novel Cell Equalizer Experimental Results*

The equalizer prototype, on which the measurements were performed, uses the modeled controller of "method C." These measurements validate the previous theoretical models. In order to prove the performance of the equalizer to a full extent, a string of five cells were used, where all cells were half charged, except one (cell #2), which was almost discharged. The charge difference was 2.5 Ah. For testing purposes, the total battery voltage was kept constant. This was achieved by using an external power supply, to provide a small current, proportional to the equalizer losses. Figure 6.51 shows the equalizing current on each cell during the equalization time.

In Fig. 6.51, it is clear that the equalizer provides current to cell #2 (positive current), while absorbing current (energy) from rest of the cells (negative current), in an almost equal manner. It is also clear that the equalizer is turned off (zero current) when the discharged cell comes closer to rest of the pack (inside the ± 0.1 % of V_{OC} difference window), to avoid forcing the equalizer to work in a low power transfer mode. This mode is not necessary in this application, in order to obtain a better efficiency (see Figs. 6.26 and 6.27). On the downside, there exists a certain amount of ripple in the measured current. This is mainly due to two sources: one is the error in V_{OC} estimation, as aforementioned, in section Cell Equalizer Controller Stability Analysis in Frequency Domain, which can also be seen in Fig. 6.51. The second source is the noise generated in the output PWM

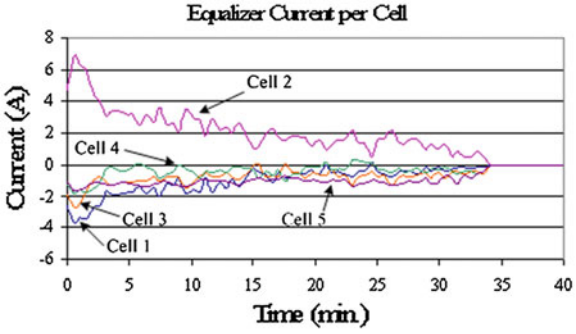

Fig. 6.51 Equalizer current per cell

counter, due to discretization. Figure 6.52 summarizes the estimated V_{OC} during the equalization time.

Figure 6.52 shows the V_{OC} equalization of cell #2, being completed in about 32 min. When the cells reach within a minimum voltage difference, defined by the specifications of 0.1 % of the V_{OC}, the equalizer is turned off, as shown in Figs. 6.51 and 6.52, in order to avoid low efficiency working points (Fig. 5.8, lower power transfer). It is clear that there exists a small remaining difference in V_{OC}, which does not justify further equalizing. Furthermore, there also exists some ripple in the estimated V_{OC}, which, as explained before, will affect the calculations. Again, as aforementioned, this is mainly due to small errors in V_{OC} estimation. The value of this error is approximately equal to the maximum error allowed by the specifications, of $\pm$ 0.1 %. Finally, when the cell voltages are within the "deadband," the equalizer is turned off. Hence, there exists no equalizing current, and the cell voltage is equal to the real V_{OC}. After 32 min, in Fig. 6.52, it can be appreciated that the change in V_{OC} is inside the allowable error, which perfectly validates the V_{OC} estimation method.

Section 6.5.13 discusses the novel equalizer simulations, using the "method C" control scheme, and will be compared with experimental measurements performed on the practical equalizer.

6.5.13 *Comparison Between Theoretical and Experimental Results*

The simulated and measured equalizing currents on cell #2 are shown in Fig. 6.53. The measured equalizing current and V_{OC} per cell are sampled once every 60 s, while the simulation is sampled once every second. Logically, this reduces the resolution of the measured current. Figure 6.54 shows the simulated and experimentally estimated V_{OC} on cell #2.

There also exist some visible differences; for example, there is a significant inaccuracy in the first 2 min of equalization. This is because cell #2 was nearly discharged when the equalization began (V_{OC} = 3.5 V, equivalent to less than

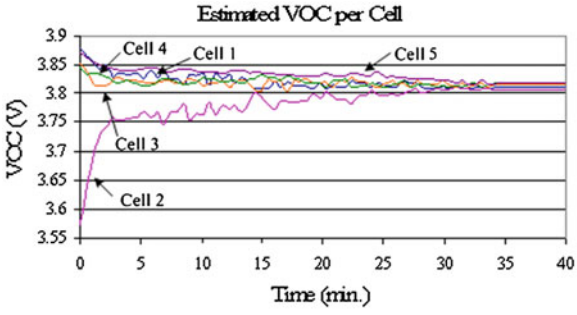

Fig. 6.52 Estimated equalizer V_{OC} per cell

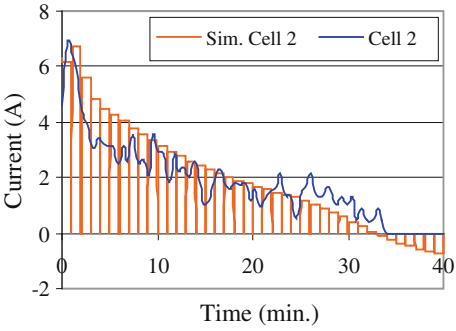

Fig. 6.53 Equalizing current on cell #2; simulated and measured

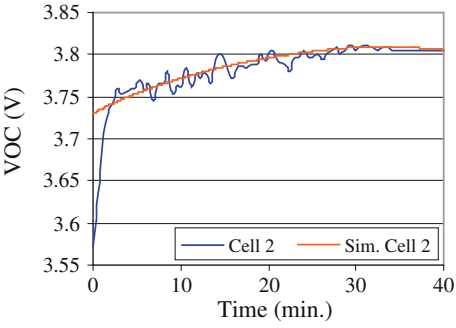

Fig. 6.54 V_{OC} on cell #2; simulated and estimated from measurements

10 % SOC; see Fig. 6.30). In this range of SOC, the electrical equivalent of the battery cell, used for simulation, was no longer valid (Figs. 5.3 and 5.5). Hence, the simulation is quite different from the experimental results, during the first 2 min of equalization. Again, it is worth mentioning here that this level of SOC is not generally used in EV/PHEV applications (as described in Sect. 6.3). Thus, making use of a more precise simulation in this range becomes fairly unnecessary.

Another important difference is the presence of relatively high noise in the measurements, which is around the maximum allowable specified noise (RMS value of 0.1 % of V_{OC}). Although in physical systems, noise is fairly unavoidable, in this case, there exist additional difficulties. The noise present in this system is generated from three primary sources: error in V_{OC} estimation (described in Sect. 6.5.8), the analog sources, like voltage and current measurements, and from quantization sources, like the resolution of the A/D converter, or the pulse width modulation (PWM) counter.

The noise due to PWM counter resolution, in particular, is critical in this implementation. In order to reduce component costs, the size of the equalizer inductors has been decreased. Because they work in CCM, the way to reduce the inductor sizes, without increasing the current ripple, is to increase the switching frequency. In this case, MOSFETs (and their drivers) are chosen to be fast enough; hence, theoretically there is no problem (except for the losses) in increasing the

switching frequency [21]. At the same time, there exists a problem in the microcontroller, the internal oscillator of which is running at a certain speed (in this case, 20 MHz). This frequency is fed to the PWM counters. In order to increase PWM switching frequency, the total count of the PWM counter must be reduced, which in turn reduces PWM resolution. For example, a total count of 200 will provide a 100 kHz switching frequency and a resolution of 40 ticks per PWM channel, in a 5-cell equalizer. This is barely enough resolution for the equalizer, and it is equivalent to a quantization error of 1/40th of the total time range, resulting in small noise in the desired current.

Although these noise sources are undesirable, they are not considered a major issue. This is because the equalization will still be performed accurately, but with slight variation in current, as demonstrated in Figs. 6.53 and 6.54. The only downside is the need to overdamp the system, by reducing K_P, in order to smooth the output, with a slight negative effect in equalizing time (Sect. 6.5.12). Possible techniques to improve equalizing time include: using a faster microcontroller; usually more expensive, bigger inductors and filter capacitors, which are also expensive, and/or using an additional external PWM modulator, which again increases the component count and total cost.

As in any engineering problem, there exists a trade off. In this case, the current ripple during equalization has to be balanced against the cost of the system. However, in a cost sensitive application, such as EVs/PHEVs, as discussed in Sect. 6.3, the balance is against the current ripple. As observed in Sects. 6.4.3.1 and 6.4.6, the current ripple increases idle losses, reducing the efficiency at lower current transfer levels. There exists a critical trade-off between this efficiency and cost. In the case of the developed prototype, the use of the "deadband" method, as seen in Sect. 6.5.12, avoided entering into low current equalization. Hence, a good efficiency at lower current transfer levels becomes unnecessary. Finally, the relatively precise prediction of current and V_{OC} in the normal SOC range is worth pointing out, even in the presence of current ripples. Thus, the control model for this application is successfully validated.

6.5.14 Summary

Based on the comprehensive control analysis and comparison with the experimental measurements, this chapter presented a detailed procedure to control an equalizer system, considering practical issues, such as cost and measurement errors (both numerical and physical). A simple V_{OC} estimation algorithm has been presented and validated. On the downside, the relatively small error of this method negatively affected the controller stability, forcing a slight increase in damping of the system. Thus, there is a slight increase in equalization time; however, this does not seriously affect the performance of the equalizer.

A suitable controller, integrated with the proposed equalizer, has been modeled, simulated, and validated against experimental measurements. Additional issues

appeared during experiments, such as analog noise in the voltage and current measurements and quantization noise in PWM timer. These issues are not large enough to justify changing the solution, which would inevitably involve a cost increase.

In this chapter, the objective of designing a low cost, robust equalizer controller has been successfully achieved. As a part of potential future work, an implementation of a more precise V_{OC} estimator, based on the methods proposed by [16, 17, 20] might be undertaken. However, issues such as computational load have to be overcome. The methods proposed in [16, 17, 20] will help reduce the sampling rate, without sacrificing the duty cycle of the equalizer. This will invariably increase the stability of the controller and improve the precision of V_{OC} estimation.

References

1. S. Moore, P. Schneider, A review of cell equalization methods for lithium-ion and lithium polymer battery systems. SAE technical paper series, 2001-01-0959, pp. 1–5, March 2001
2. A.C. Baughman, M. Ferdowsi, Double-tiered switched-capacitor battery charge equalization technique. IEEE Trans Ind Electron **55**(6), 2277–2285 (June 2008)
3. K. Nishijima, H. Sakamoto, K. Harada, A PWM controlled simple and high performance battery balancing system, vol. 1, in *Proceedings of the IEEE Power Electronics Specialists Conference*, June 2000, Galway, Ireland, pp. 517–520
4. Y. S. Lee, C. W. Jao, Fuzzy controlled lithium-ion battery equalization with state-of-charge estimator, vol. 5, in *Proceeding IEEE International Conference on Systems, Man, and Cybernetics*, Oct 2003, Washington, DC, pp. 4431–4438
5. Y.S. Lee, M.W. Cheng, Intelligent control battery equalization for series connected lithium-ion battery strings. IEEE Trans Industrial Electronics **52**(5), 1297–1307 (2005)
6. Y. S. Lee, M. W. Cheng, S. C. Yang, C. L. Hsu, Individual cell equalization for series connected lithium-ion batteries. IEICE Trans. Commun. **E89-B**(9), 2596–2607 (2006)
7. DigiKey Corp., http://www.digikey.com
8. U.S. DOE, Average retail price of electricity to ultimate customers: total by end-use sector, May 2009
9. X. Li, S. S. Williamson, Assessment of efficiency improvement techniques for future power electronics intensive hybrid electric drive trains, in *Proceeding of the IEEE Electrical Power Conf*erence, Oct 2007, Montreal, Canada, pp. 268–273
10. T. Markel, A. Simpson, Energy storage systems considerations for grid-charged hybrid electric vehicles, in *Proceeding of the IEEE Vehicle Power and Propulsion Conferene*, Sept 2005, Chicago, IL, pp. 344–349
11. M. Anderman, F. Kalhammer, D. MacArthur, Advanced batteries for electric vehicles: an assessment of performance, cost, and availability. *Technical* Report for the State of California Air Resources Board, June 2000
12. A123 systems, Inc., http://www.a123systems.com
13. LiFeBATT, Inc., http://www.lifebatt.com
14. Y.S. Lee, G.T. Cheng, Quasi-resonant zero-current-switching bidirectional converter for battery equalization applications. IEEE Trans Power Electron **21**(5), 1213–1224 (2006)
15. M. Chen, G.A. Rincon-Mora, Accurate electrical battery model capable of predicting runtime and I-V performance. IEEE Trans Energy Convers **21**(2), 504–511 (2006)

16. I.S. Kim, Nonlinear state of charge estimator for hybrid electric vehicle battery. IEEE Trans Power Electron **23**(4), 2027–2034 (2008)
17. C. R. Gould, C. M. Bingham, D. A. Stone, P. Bentley, Novel battery model of an all-electric personal rapid transit vehicle to determine state-of-health through subspace parameter estimation and a Kalman estimator, in *Proceeding of the IEEE International Symposium on Power Electronics, Electrical Drives, Automation and Motion*, June 2008, Ischia, Italy, pp. 1217–1222
18. AA Portable Power Corp., Li-Ion 18650, quantities of 50,000, Jan. 2009
19. Texas Instruments, "bq27500-system side impedance track fuel gauge," Sept. 2007
20. F. Xuyun, S. Zechang, A battery model including hysteresis for state-of-charge estimation in Ni-MH battery, in *Proceeding of the IEEE Vehicle Power and Propulsion Conference*, Sept 2008, Harbin, China
21. A. Affanni, A. Bellini, G. Franceschini, P. Guglielmi, C. Tassoni, Battery choice and management for new-generation electric vehicles. IEEE Trans Ind Electron **52**(5), 1343–1349 (2005)
22. I. Menjak, P.H. Gow, D.A. Corrigan, S. Venkatesan, S.K. Dhar, R.C. Stempel, S. R. Ovshinsky, Advanced Ovonic high-power nickel-metal hydride batteries for hybrid electric vehicle applications, in *Proceeding of the IEEE 13th Annual Battery Conference on Applications and Advances*, Jan 1, Long Beach, CA
23. R.C. Dorf, R.H. Bishop, *Modern Control Systems* 10th edn. (Prentice Hall, Englewood Cliffs)
24. G.F. Franklin, J.D. Powel, A. Emani-Naeini, *Feedback Control of Dynamic Systems,* 4th edn. (Prentice Hall, Englewood Cliffs)

Chapter 7
EV and PHEV Battery Charging: Grid and Renewable Energy Interface

7.1 Introduction

One of the biggest challenges in electric transportation is storing electrical energy for use in desired times and desired amounts. Batteries are mostly considered because of their high energy density compared to their counterparts and also their ability to get charged providing regenerative braking capability. The electrochemical nature of batteries has a highly nonlinear behavior and dependent on many factors such as state of charge, state of health, runtime, temperature, aging, load profile, and charging algorithm. A very important concern is related to storage, because in order to have a given amount of energy for a reasonable All Electric Range (AER), tens or hundreds of cells should be connected in series and parallel for the desirable voltage and current ratings of the battery pack. This causes the nonlinear behavior of cells to be more prominent. Furthermore, there are some phenomena that are observed only in battery packs and not in single cells, such as thermal unbalance among the cells in pack.

EV and PHEV battery packs are relatively expensive compared to the price of the whole car, because of high number of cells, chemistry types such as Lithium-based, and protection circuits. Accordingly, the life cycle of these battery packs are very important for a cost-effective user's point of view. Therefore, lower cost for final customer can be achieved with increasing the battery pack life cycle, resulting in less frequent replacements of the whole pack. As a real example related to Honda Civic, recently, there has been news [1] about Honda Company regarding the battery packs of Honda Civics produced during 2006–2008. Apparently, some of the battery packs in the second-generation Honda Civic hybrids are failing prematurely after 5 years. According to regulations in California, there is a 10-year, 150,000-mile warranty requirement on the components of the hybrid system. Although Honda Company took recall actions, some customers were not satisfied and preferred to change themselves the battery packs. It has been reported that those battery packs cost about $2,000 excluding tax, shipping, and installation.

This case shows the importance of the battery packs price in the commercialization of EVs and PHEVs in a large scale. A factor that highly impacts the life

S. S. Williamson, *Energy Management Strategies for Electric and Plug-in Hybrid Electric Vehicles*, DOI: 10.1007/978-1-4614-7711-2_7,

cycle of battery packs is the charging algorithm. There are other factors also involved such as the charging time that plays an important role in high attraction to EVs and PHEVs. These topics and all other ones related to this area should be mainly handled with a multilevel control and power system called Battery Management System (BMS) which takes care of all or some of the aspects affecting batteries in any way. While charging the battery pack, BMS works in collaboration with the charger. Depending on the architecture of the system, BMS can be integrated to the charger. The more accurate and comprehensive the BMS is the more reliable, safer, and faster the charging procedure can be done. Designing a highly efficient BMS needs very good understanding of the behavior of single cells according to the variations of different parameters and also parameter variation and behavior change in a packed large number of cells.

7.2 Charging Regimes for Batteries

7.2.1 Battery Parameters

7.2.1.1 Battery Capacity

Measured in Ampere-Hour (Ah), battery capacity indicates the amount of charge that can be drawn from a fully charged battery until it gets fully discharged. An important effect in batteries is that the higher amount of current drawn from a battery, the lower capacity the battery will have. Hence, theoretically, battery capacity is defined as the amount of current drawn from a battery that completely discharges it in 1 h. However, in practice battery manufacturers specify a table showing the amount of time the battery runs with different constant current loads and different constant power loads. In practice, this table provides more practical information rather standard definitions, because, after production different loads with different characteristics may be connected to the battery.

7.2.1.2 C Rate

This parameter is used to show the amount of current used for charging the battery. For example, for a 10 Ah battery, when it is mentioned to terminate the charging process while the charging current falls below C/10 rate (10 h rate), it means the charging should be stopped when current becomes less than the amount of current with which the battery is discharged after 10 h, or specifically 10Ah/10 h = 1 Amp.

7.2.1.3 State of Charge

State of Charge (SoC) is the percentage of charge available from a battery to the whole capacity of the battery. SoC is difficult to measure directly and usually some methods are used to estimate it indirectly. Besides, according to aging the rated capacity of the battery reduces over time, hence, for determining accurate SoC, the rated capacity should be measured or calculated regularly.

7.2.1.4 Depth of Discharge

Depth of Discharge (DoD) is defined as (100—SoC) in percentage, i.e., the percentage of total charge of the battery which has been utilized. This parameter is usually used in discharge patterns recommendations. For example, the battery manufacturer may recommend the user not to go over 70 % DoD according to lifetime issues.

7.2.1.5 Energy Density

Energy density can be defined based on volume or weight, i.e., Wh/L or Wh/Kg. The "Volumetric Energy Density", which is defined as the amount of available energy from a fully charged battery per unit volume (Wh/Liter). As we know Liter is used for measuring the volume of liquids, however, even for solid electrolytes such as Lithium Polymer batteries, the same unit is usually used. The other way of defining the Energy Density is "Gravimetric Energy Density" which is also referred as "Specific Energy" and defined as the available energy from a fully charged battery per unit weight (Wh/Kg). Based on application and based on the importance of the volume or weight, either definition can be used. In the case of EVs/PHEVs usually weight is a more important factor than volume, so, mostly Specific Energy is used.

7.2.1.6 Charging Efficiency

The chemical reactions inside the battery during charge and discharge are not ideal and there are always losses involved. Therefore, not all the energy used to charge the battery, is available during discharge. Some of this energy is wasted as heat dissipation. The charging efficiency can be defined as the ratio of available energy from the battery in a complete discharge to the amount of energy needed to completely charge the battery. This parameter may be mentioned by other names such "Coulombic Efficiency" or "Charge Acceptance". In general, the coulombic efficiency for a new battery is high, however, reducing as the battery ages.

Next section discusses some aspects of different battery types used in EVs and PHEVs regarding charging. This will help in designing more efficient and flexible

chargers based on battery behaviors, which will finally lead to improvement of battery packs lifetime.

7.2.2 Charging Methods

Charging in general is the action of putting energy back to the battery, i.e., restoring energy. It is important to know that different chemistries may require completely different charging methods. Other factors affecting choosing the charging method are capacity, required time, or other factors. The most common techniques are mentioned here:

7.2.2.1 Constant Voltage Charge

As it is clear from the name "Constant Voltage" or CV is when a constant voltage is applied to the battery pack. This voltage is a preset value given by the manufacturer. This method is accompanied with a current limiting circuit most of the time, especially for the beginning periods of charging where the battery easily takes high rates of current comparing to its capacity. The current limitation value mainly depends on the capacity of the battery. Depending on the battery type to be charged, this preset voltage value is chosen. For example, for Li-ion cells the value of 4.200 ± 50 mV is desirable, so the present value for the whole battery pack can be obtained by multiplying this value with number of cells in series. An accurate set point is necessary, since overvoltage can damage the cells and under-voltage causes partial charge which will reduce life cycle over time. Therefore, the circuit used for charging, which can be a simple buck, boost, or buck/boost topology depending on the voltage ratio of input and output, should be accompanied with a controller to compensate for source and load changes over time. When the cell reaches the preset voltage value, this causes the battery to be in a standby mode, ready for later use. The amount of this idle time should not be very long and should be limited based on the manufacturer recommendations. This method is usually used for lead-acid batteries, also for Li-ion batteries while using current limiter to avoid overheating the battery especially in the first stages of the charging process [2].

7.2.2.2 Constant Current Charge

Constant current charging method is applying a constant current to the battery with low percentage of current ripples independent of the battery state of charge or temperature. The abbreviation for this method is CC in the literature. This is achieved by varying the voltage applied to the battery using control techniques such as current mode control to keep the current constant. CC technique can be

implemented using a "Single Rate Current" or "Split Rate Current". In single rate only one preset current value is applied to the battery which is useful in balancing the cells. However, backup circuits must be used to avoid overcharging. In the split rate CC different rates of current are applied based on SoC, time of charge, voltage, or combination of them in different stages of charging. This gives more accurate and balanced charging and circuits should be used to avoid overvoltage of the cells. In some cases, for prolonging dead batteries, CC method with high rates and low duration can be utilized to extend the lifetime of the battery. But, this is a very cautious procedure and must be done carefully. Ni-Cd and Ni-MH batteries are charged using CC. Ni-MH batteries can be easily damaged due to overcharging, so, they should be accurately monitored during charging [3].

7.2.2.3 Taper Current Charge

This method can be used when the source is nonregulated. It is usually implemented with a transformer with a high output voltage comparing to the battery voltage. A resistance should be used to limit the current flowing to the battery. A diode can also be used to ensure unidirectional power flow to the battery. In this method the current starts at full rating and gradually decreases as the cell gets charged. This technique is only applicable to Sealed Lead-Acid (SLA) batteries.

7.2.2.4 Pulse Charge

This technique involves using short time current or voltage pulses for charging. By changing the width of pulses the average of the current or voltage can be controlled. Pulse charging provides two significant advantages, (I) it reduces charging time and, (II) the conditioning effect of this technique highly improves the life cycle. The intervals between pulses called rest times play an important role, they provide some time for chemical reactions inside the battery to take place and stabilize. Since in this method high rates of current or voltage can be used, it reduces undesirable chemical reactions that happen at the electrodes, such as gas formation and crystal growth, which are the most important reasons of life cycle reduction in batteries.

7.2.2.5 Reflex Charge

During charging procedure some gas bubbles appear on the electrodes, especially amplified during fast charging. This phenomenon is called "burping". Applying very short discharge pulses or negative pulses which can be achieved for example by short circuiting the battery for very small time intervals compared to charging time intervals in a current limited fashion, typically 2–3 times bigger than the charging pulses during the charging rest period resulting in depolarizing the cell

will speed up the stabilization process and hence the overall charging process. This technique is called with other names such as "Burp Charging" or "Negative Pulse Charging". Different control modes of charging along with waveforms and diagrams are described in [4]. There are other charging methods such as Current Interrupt or CI which will be thoroughly explained in the charging algorithm section.

7.2.2.6 Float Charge

For some applications when the charging process is complete and the battery is fully charged, the batteries should be maintained at 100 % SoC for a long time to be ready for time of use. Uninterruptable Power Supplies (UPS) are one of such applications where the batteries should always remain fully charged. However, because of self-discharge of batteries, they get discharged over time; for example, they may lose 20 or 30 % of their charge per month. To compensate for self-discharge, a constant voltage which is determined based on the battery chemistry and ambient temperature is applied permanently. This voltage is called "Float Voltage". In general, float voltage should be decreased with the increase of temperature. This causes a very low rate of current, for example C/300 to C/100 rate to the battery which continuously compensates for the self-discharge rate and also prevents sulfate formation on the plates. This technique is not recommended for Li-ion and Li-Po batteries and it is not necessary for EV/PHEVs which are frequently used every day. In addition, float charging involves a protection circuit which avoids overcharging. This circuit adjusts the float voltage automatically and interrupts charging at some intervals based on battery voltage and temperature.

7.2.3 Termination Methods

When the charging is in procedure, it is very important to decide when to terminate the charging. This is because of two main reasons. One is to avoid undercharge, i.e., making sure the battery is fully charged, not partially, in order to use the full capacity of the batteries. The other one is to avoid overcharging which is very dangerous especially in the case of high energy density Lithium-based battery packs. If not terminated on time, the overcharging of batteries can lead to over gassing of the cells, especially in liquid electrolyte cells which results in increase in the volume of individual cells, a situation that cannot be tolerated in a rigidly packed battery pack. Another issue is overheating of the cells especially in Lithium-based batteries which can easily lead to the explosion and firing of the whole pack, since; Lithium is a very active material and easily combines with oxygen in the air. The only thing needed to begin the combination is enough heat.

Choosing different termination criteria leads to different termination methods. Selecting the type of termination of charging process depends on different factors

such as the application and the environment where the battery is used. The conventional termination methods that can be used are mentioned here:

7.2.3.1 Time

Using time is one of the simplest methods which is mainly used as a backup for fast charging or normally used for regular charging for specific types of batteries. This method is very simple and inexpensive, but because of diminishing battery capacity over time due to aging, the time should be reset for a reduced capacity aged battery to avoid overcharging of old batteries.

7.2.3.2 Voltage

As mentioned before, voltage can be used as a termination factor, i.e., terminating the charging process when the battery voltage reaches a specific value. This method has some inaccuracies, because real open-circuit voltage is obtained when the battery is left disconnected for some time after charging. This is because chemical reactions happening inside the battery need some time to stabilize. Nevertheless, this method is widely used. In addition, this technique is usually used with constant current technique to avoid overheating damage to the battery.

7.2.3.3 Voltage Drop (dV/dT)

In some chemistries like Ni-Cd when charged using constant current method, the voltage increases up to the fully charged state point and then the voltage begins to decrease. This is due to oxygen build-up inside the battery. This decrease is significant, so the derivative of the voltage versus time can be measured to indicate overcharge. When this parameter becomes negative it shows that we have passed the fully charged state and the temperature begins to rise. After this point the charging method can be switched to trickle, or float charge, or terminated completely.

7.2.3.4 Current

In the last stages of charging, if constant voltage method is used, the current begins to decrease as the battery reaches fully charge state. A preset current value such as C/10 rate can be defined and when the current goes below this value the charging would be terminated.

7.2.3.5 Temperature

In general, during charging the battery temperature increases to some extent, however, extra increase in temperature is a sign of overcharge. Using temperature sensors highly adds to the cost of system. Nevertheless, for some chemistries such as Ni-MH, methods such as Voltage Drop is not recommended, since the voltage drop after full charge state is not significant to be relied on. In this case, temperature increase is a good indication of overcharge and can be used.

7.2.4 Charging Algorithm

Charging algorithm can be defined as the combination of what was mentioned up to here and controlling all or part of the parameters affecting battery performance and life cycle in such a way to achieve battery pack charging safely, efficiently, and terminated on time. Managing the charging procedure of a high power battery pack with hundreds of cells involves many issues as already discussed in this chapter. To control all of these parameters, efficient and accurate algorithms with reliable safety and backup circuits are required. The trend toward fast charging with huge amounts of current flowing to the battery pack producing lots of heat requires accurate and reliable supervisory control algorithms to ensure safe charge. Managing such complex task can be handled with advanced control techniques like fuzzy logic, supervisory control, and decentralized control, and so on. In general, each battery chemistry requires a unique charging algorithm. Depending on the algorithm it may be applied to some other types as well, however, this should be carefully done according to life cycle and safety issues.

For precise battery charging the charge/discharge profile of the battery provided by the manufacturer must be used. However, the profile is valid for brand new batteries, hence, some techniques like data acquisition methods must be used to acquire the charge/discharge profile of the battery with deterioration due to aging. Novel techniques regarding this issue are being introduced in the literature every often [5].

As mentioned before Lead-acid batteries have mature technology and infrastructure that already exist, but they still have poor life cycles in the order of 300–400 cycles. A lot of efforts have been put into research for increasing the life cycle of lead-acid batteries because of their advantages such as low cost and availability. This chemistry has a common charging algorithm which includes four different stages or three based on the application, as indicated in Fig. 7.1.

In the first stage a predefined constant current is applied to the battery pack which charges the cells rapidly. In this stage the cell voltages increase gradually because of SoC increase. This stage is called “Bulk Charge” stage. The process is continued until a predefined maximum voltage is reached. These values are all recommended by the manufacturer in the datasheet. In the next stage called “Absorption Charge” stage, a constant voltage is applied to the battery pack.

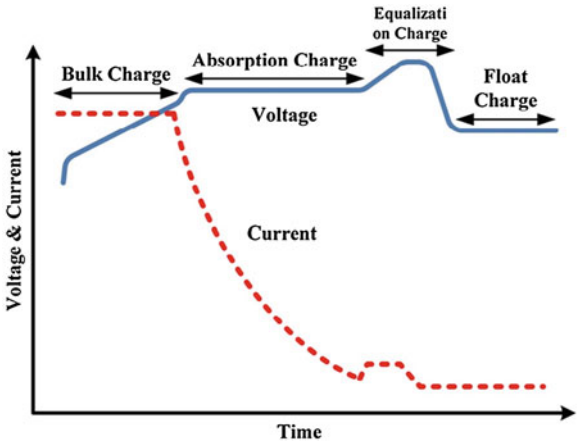

Fig. 7.1 Charging algorithm of a typical Lead-acid battery

At this stage the current decreases gradually until it reaches a predefined C rate value and the cells are approximately charged but not equalized because of cell imbalance. At this stage a relatively higher voltage than constant voltage in absorption stage can be applied to the pack for some time to balance all the cells inside the pack. This stage is called "Equalization Charge" stage. The equalization can also be achieved with other techniques as mentioned before. After some prescribed time, the charger applies a lower constant voltage in order to keep the battery in a ready to use state. This is called "Float Charge" stage and depending on the application it can be considered or omitted.

As the battery ages, its internal characteristics also change, hence, an adaptive charging algorithm could be used to take into account these parameters variations. Experimental results show that the value of voltage of the third stage should be increased over time to get the same amount of energy as the battery ages [6–8]. The equalization stage is the key part of this algorithm and has great influence on the life cycle of the battery. As mentioned before, the voltage of this stage should be increased but this increases the current and also the heat generated which has negative impact on the life cycle. One way to get the same amount of current with lower heat dissipation is by using pulses of current. Although this technique seems the same as pulse charging, it is actually different because the time intervals are significantly bigger than pulse charge time periods which are in the range of kilo hertz. This method is called "Current Interrupt" or "CI". This technique has shown significant life cycle improvements [9]. Using this algorithm, the battery can reach 50 % of the initial capacity after 500 cycles which is a significant improvement in life cycle. Although this algorithm is useful, it puts the battery under stress while it reaches the end of life because of permanently increasing the overvoltage value. This algorithm can be implemented in an alternative way. Instead of using this method for each cycle, which puts high stress on the battery, it can be utilized every 10 cycles. This algorithm is called "Partial-State-of-Recharge cycling (PSOR)" [9] and has approximately the same effect with the

advantage of less stress on the battery. This algorithm has been claimed to enable the battery deliver up to 80 % of initial capacity even after 780 cycles [9] which is a really noticeable improvement in life cycle.

As can be seen these complicated algorithms cannot be done using simple PI, PID controllers. They require DSP-based controllers to be programmable with numerical data dependent on the battery chemistry, state of health, and other factors.

Continuously, different algorithms are being proposed and tested for improving life cycle of the batteries. This is a vast research area and is currently under development, getting a lot of attention as EVs/PHEVs become popular and available in the market.

7.3 Charging from Grid

For practical purposes, connection of the carport to the grid is highly desirable, as such a connection would serve a number of useful purposes. The grid would primarily act as extended storage by collecting excess energy produced by the PV array. This will relieve the carport from the task of locally storing energy in batteries or flywheels. Second, the grid can supplement any deficiency in PV generation, during cloudy days or at night, for instance. Finally, storing energy during peak hours of grid utilization and the availability of connected batteries during the same period seems to be the optimal solution for the utility company for the many potential benefits described in [35], namely power factor improvement, backup power during grid failures, and peak shaving.

About the last point, it is well worth pausing on the realization that stand-alone installations, such as microgrids, must allow locally generated power to be stored in battery banks, as well as being converted to AC, in order to drive neighboring loads. At the same time, power must also be allowed to flow from the batteries to the AC line at times when PV generation is lacking. It appears then, that at least three out of the four power flow paths described above also apply to stand-alone systems. The order of importance for the power paths is not the same; nevertheless, it is still conceivable that many findings within this chapter may be applicable to microgrids as well. Keeping this fact in mind, this chapter will, henceforth, focus solely on PV grid-tied EV charging applications.

7.3.1 Line Stability Issues

As aforementioned in the introductory chapter, the grid could perform the function of “storing” excess energy produced by the PV resource of the carport, thus eliminating the need for local storage (batteries and flywheels). In fact, the scenario is somewhat more complicated than that. It is well-known that intermittent

generators, such as solar and wind installations, can potentially cause problems to the grid. In fact, should these generators become very widespread, or be connected to remote locations on the grid; the energy they produce may exceed the available load. Simple energy conservation theory dictates that such a condition is untenable and must be remedied either by storing the energy for later use or by decreasing power generation, thus underutilizing the generator's capacity. Even when produced energy is not in excess, the flow of current, back toward the power substation can cause the local point of common coupling to experience a voltage boost that can be severe when line impedance is significant.

Furthermore, and especially in the case of PV sources, the instantaneous level of generated power can experience rapid variations (up to 15 % per s, due to clouding) that cannot be compensated in real-time by the grid, thus causing voltage flicker. These serious issues concerning distributed generation are presently the object of intense study and mobilization by public and private parties and will not be addressed in this chapter. Nevertheless, it is important to consider the following points:

(1) Present grid penetration levels of distributed systems, in general, and photovoltaics, in particular, are very low, less than 2–3 % in North America. Several studies referenced in [36] have established that flicker and voltage boost are significant only when the penetration levels at the power substation are more than 5 and 15 %, respectively, in most cases.

(2) In the case of a carport, the load is intrinsically a storage type; EV/PHEV batteries. In other words, especially for large carports, there is a statistically high probability that the storage and the load are one and the same. Scenarios involving an empty carport and overproduction occurring simultaneously can be deemed so rare that decreasing production in such instances would be fairly acceptable. In fact, grid-connected EV/PHEV batteries could be beneficial to the utility company for the reasons mentioned in the introductory chapter.

7.3.2 Inverter Distortion and DC Current Injection

As the PV resource generates DC voltage, an inverter is needed in order to connect to the line. Several regulatory agencies, such as UL and IEC, have imposed common specifications for inverter performance. Minimally, the inverter must produce low harmonic distortion currents (less than 5 %) and near unity power factors (displacement PF compensation is not yet allowed in most cases). Furthermore, the inverter is not allowed to inject a DC current component into the grid, as this could cause distribution transformers to saturate. Commonly followed standards IEEE 929, IEC 61727, and EN 61000 specify between 0.5 and 1 % of rated output current as a maximum, while some national European standards add a 5 mA absolute requirement in addition to this minimum percentage.

7.3.3 Local Distribution Configuration

As a final note, the solutions considered in the previous sections assume the use of single-phase connections. The main appeal of the three-phase system is the enhanced power capacity, the fact that this power is delivered and absorbed without any line-frequency components, and the elimination of third harmonic currents in the distribution and grounding wiring. These features are quite attractive and include the advantage of potentially eliminating undesirable pulsating charging current to the EV battery. On the other hand, the single-phase configuration allows for less expensive and simpler distributed inverters. Especially considering the fact that PV can only provide 5 kW of power to the inverter, and that intervening DC/DC converters need to be added to can eliminate any pulsating current, it appears that a single-phase system is much better adapted to this application and will be assumed throughout this chapter.

7.4 Charging from Renewable Energy Sources

7.4.1 Basic Aspects of Battery Charging from Photovoltaic Systems

Solar energy is one of the most interesting types of renewable energy because of relatively well-established technology and efficiency enhancement every day with great efforts toward higher performance Photovoltaic (PV) panels. However, nonlinearity of PV panels characteristics and their dependence on atmospheric conditions such as sunlight irradiance level and temperature variations needs a Maximum Power Point Tracking (MPPT) unit, which is usually a converter to track the maximum power to ensure maximum efficiency of the system. Direct connection of PV panels to the load involves over sizing the panels to ensure load supply and in other words increased loss of the whole system. A typical PV panel characteristic is plotted in Fig. 7.2.

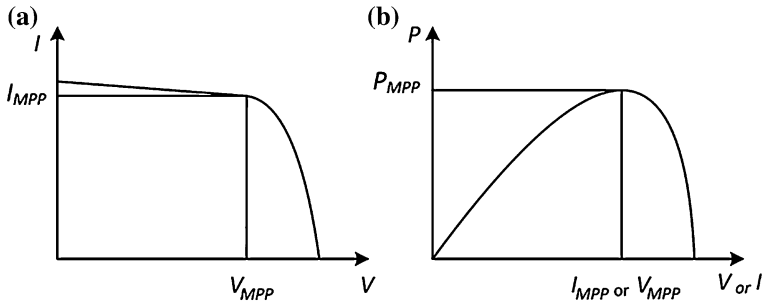

Fig. 7.2 Typical photovoltaic cell characteristics: **a** I–V curve, **b** P–V, or P–I curve

In general, the task of MPPT technique is to automatically shift the operating point to the maximum power point. There are numerous techniques in the literature. They may be categorized in different ways. In [10] MPPT methods are classified into two major groups based on the size of the system: (1) Large-scale PV systems which utilize digital signal processors (DSP) (2) Small-scale PV systems which do not use DSP-based methods. However, based on operation principals MPPT methods can be divided into various categories [11]: (1) Hill Climbing/P&O (2) Incremental Conductance (3) Fractional Open-Circuit Voltage (4) Fractional Short Circuit Current (5) Fuzzy Logic Control (6) Neural Network (7) Ripple correlation control (RCC) (8) Current Sweep (9) DC-Link Capacitor Droop Control (10) Load Current or Load Voltage Maximization (11) dP/dV or dP/dI Feedback Control (12) Array Reconfiguration (13) Mathematical Calculation of MPP (14) State-based MPPT (15) best fixed voltage (BFV) algorithm (16) linear reoriented coordinates method (LRCM), and etc. All these methods are summarized and briefly described in [12] along with their major characteristics such as PV array dependence, true or approximate MPPT, analog or digital implementation, periodic tuning, convergence speed, implementation complexity, and sensed parameters. Based on MPPT technique characteristics, one or more types are more suitable for a specific application.

One of the most common applications is battery charging which may be the main purpose of the whole PV system such as PHEV battery pack charger (stand-alone system), or a subsidiary part of the PV system as an energy storage element for storing extra energy produced, such as power injection to the grid in distributed generation systems (grid-connected system). A novel MPPT algorithm is introduced in this chapter and the first scenario is of interest of this thesis. However, this technique can be easily applied to more complex PV systems [13]. According to [14] among single pole double switch converters, the buck-boost converter has the highest energy conversion efficiency, however, since our goal here is not to investigate the energy conversion efficiency of the proposed algorithm among different topologies, we have chosen a simple buck converter as the MPPT stage just to prove the validity of the proposed algorithm. However, this algorithm is independent of the converter topology as will be described later. As concluded in [15] the MPPT can be achieved only with sensing one of the output variables, output voltage, or output current. This method mainly falls into load current maximization category, however, with some advantages such as independence from circuit topology and high degree of simplicity of low-level controller. Besides, it can be easily implemented using low-cost analog circuits with low implementation complexity.

7.4.2 PV Array Model

For designing and simulation purposes the PV model is required. Very accurate mathematical models such as double exponential model [16] exist which are not

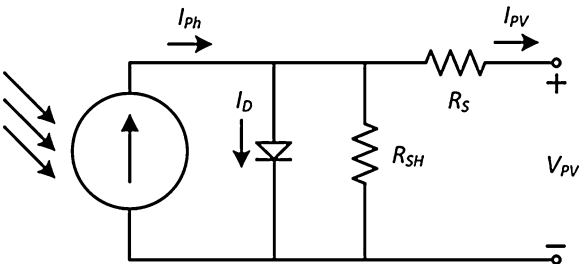

Fig. 7.3 Typical circuit based photovoltaic cell model

our concern here, since; our goal is not introducing an improved PV model. However, models with moderate complexity and acceptable accuracy exist [17] such as the one shown in Fig. 7.3 which are very suitable for circuit simulation purposes. The two main parts of the model are sunlight insolation-dependent current source and diode. The other two elements, namely, shunt resistance R_{SH} and series resistance R_S add to the accuracy of the model, however, for system level design purposes they can be assumed infinity and zero, respectively. We will consider these two elements because of higher degree of accuracy.

The main modeling approaches can be classified as mathematical models, circuit models, lookup tables (Data Sheets), and etc. Since we are using MATLAB/Simulink software and SimPowerSystems library, the use of power diode in the model will result in inaccurate results. This is because of the piece-wise linear model of the diode used in SimPowerSystems library which models the diode in on state as a negative voltage source in series with a resistance. This neglects the exponential curve of diode characteristics which is described with Shockley diode equation:

$$I_D = I_S * (e^{V_D}/(n * V_t) - 1) \tag{7.1}$$

where I_D, I_S, V_D, n, and V_t are diode current, reverse bias saturation current, diode voltage, ideality factor, and thermal voltage, respectively. To solve this problem, we use a hybrid type model which incorporates both circuit-based model and mathematical-based model. To consider the curvature of the maximum power point we use the Shockley equation for diode instead of using the diode block itself which gives acceptable degree of accuracy. This is illustrated in Fig. 7.4 which is the circuit implemented in Matlab/Simulink. As it can be seen, the controlled current source is used for modeling the dependence of PV on the insolation level and also for modeling the diode. For the insolation dependency a constant or variable signal can be fed to the model. The value of this signal is the short circuit current of the PV. For the diode, however, this approach introduces a problem called Algebraic Loop. An algebraic loop generally occurs when an input port with direct feed through is driven by the output of the same block, either directly, or by a feedback path through other blocks with direct feed through. As it is evident from Shockley equation and illustrated in Fig. 7.4, the voltage of the diode is used to decide the value of the diode current. This algebraic loop may generate error

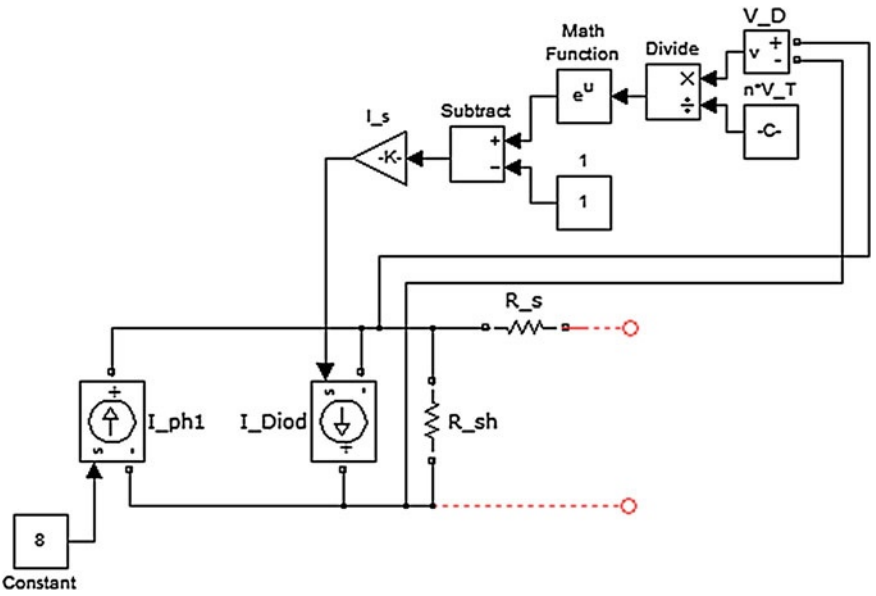

Fig. 7.4 Proposed hybrid PV model for simulation in MATLAB/Simulink

during simulations since for each step the data from previous step may be not available, because no state exists in the model. To deal with this problem we can add a capacitor to the output of the model, which is the practical case in real world to reduce the voltage ripple of the PV panel. This capacitor is an energy storage element and adds a state (capacitor voltage) to the model and solves the problem of algebraic loop since the value of the state for each step is available from the previous step.

7.4.3 Control System Design

The proposed method is based on maximizing the load power which leads to PV output power maximization assuming a lossless converter stage. In the case of constant voltage type battery load this is translated to maximizing the output current. To achieve this, a low-level current controller stage is designed to control the output current to the desired value and a higher level current reference maker is introduced which automatically finds the highest output current achievable and sets the current reference at that value. To describe this concept a buck converter is used as the MPPT stage and the battery is simply modeled as a DC source in series with internal resistance as illustrated in Fig. 7.5. There are some reasons for choosing this battery model. The MPPT stage is a fast dynamic system compared to the load which is considered a battery here as an example load. So battery is

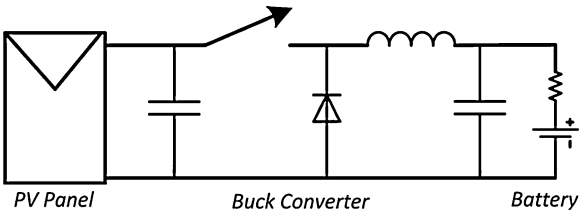

Fig. 7.5 Buck converter as MPPT stage

a slow dynamic system compared to the MPPT stage and can be considered as a constant source. Besides, our goal in this chapter is to validate the operation of the proposed MPPT method and not charging process of the battery. In addition, in our final battery pack charger system, this MPPT stage is not directly connected to the battery pack, rather, it is connected to another power stage which will be described in Sect. 7.5. So considering the battery as a constant voltage source in series with internal resistance is a valid model for verification of the proposed MPPT technique.

For designing the current controller we simply use a constant gain K_P. The first concern that may arise is about not using an integrator in the controller which will cause the output to have steady state error, however, this will not be the case for our algorithm, since, the higher level current reference maker controller will search for the highest output current possible even with the existence of the steady state error in the current control loop. This is an advantage of the proposed method which simplifies current loop to a very simple current controller involving only a simple gain. To understand this, the logic behind the algorithm is described here. The reference maker circuit increases the current reference exponentially to a high predefined value with an adjustable speed. Hence, the output current which is the inductor current in the case of buck converter will increase gradually. This cannot continue infinitely, since, the PV output has a limited maximum value based on atmospheric conditions, especially, sunlight intensity. Therefore, after some time the actual current cannot follow current reference and this will saturate the PWM regulator and current error begins to increase dramatically. Monitoring this saturation is the key point that when happens indicates that we have passed the maximum current value available. So we should set the current reference at the value which has caused saturation of the controller. How to implement this idea is a little tricky. According to what mentioned before, we want the current reference to have an exponential behavior beginning from a constant value and exponentially converging to another higher constant value. Suppose we want the output current, namely, "$y_{(t)}$" to begin from an initial condition $y_{(t\,=\,0)} = y_{(0)}$ and exponentially converge to the final value $y_{(t\,\rightarrow\,\infty)} = y_{(\infty)}$ with the time constant of $1/\alpha$. The infinite value for time is theoretical. In practice after four time constants we reach 97 % of the final value which can be considered as the steady state value. This behavior is the same as that of a first order system or circuit, such as voltage response of a RC circuit getting charged with constant current. This fact reminds the following equation for first order systems:

$$y_{(t)} = y_0 e^{-\alpha t} + y_\infty (1 - e^{-\alpha t}) \tag{7.2}$$

Expanding the equation and multiplying both sides by $e^{\alpha t}$ we get:

$$e^{\alpha t} y_{(t)} - y_0 = e^{\alpha t} y_\infty - y_\infty \tag{7.3}$$

Derivation of both sides gives us:

$$\alpha e^{\alpha t} y_{(t)} + e^{\alpha t} y'_{(t)} = \alpha e^{\alpha t} y_{(\infty)} \tag{7.4}$$

If we divide both sides by $e^{\alpha t}$ we will get:

$$\alpha y_{(t)} + y'_{(t)} = \alpha y_{(\infty)} \tag{7.5}$$

$$y'_{(t)} = \alpha \left(y_{(\infty)} - y_{(t)} \right) \tag{7.6}$$

$$y_{(t)} = \alpha \left(\int y_{(\infty)} - \int y_{(t)} \right) \tag{7.7}$$

Equation (7.7) is the key equation for the controller design. The parameter "α" determines the speed of convergence. The bigger the parameter "α" is, the faster the reference will be generated. However, implementation complexity increases. A trade-off should be considered between speed and complexity. We have chosen $\alpha = 20$ as an example. Implementation of (7.7) is clear using integrator; however, how to capture the reference value at which saturation happens is not that much obvious. There may be different ways to implement this; however, one way is using resettable integrator with adjustable initial condition in a configuration shown in Fig. 7.6.

As shown in Fig. 7.6 the output of the Integrator_1 is $y_{(t)}$ and that of Integrator_2 is $y_{(\infty)}$. In the startup time of the circuit, the pulse generator produces a very small duration pulse of a relatively high predefined value. This value should be set to the maximum possible short circuit current of the PV panel which can show up in the output. This happens in highest sun intensity (usually 1,000 W/m^2) and vertical position of the sun (Solar noon) which is available from PV datasheet and can be calculated for output stage of any converter like buck converter used here. In our case we assume this value equal to 20. This pulse at the circuit startup sets the initial value of integrator_2–20 and since it is integrating zero the output of this integrator will be equal to the initial condition. This output is then multiplied by 20 which produces a big value. As described before mathematically, this is the final value that output current should reach. Besides, the output of integrator_2 is $y_{(t)}$, in other words, the present value of current reference. In this way the current reference is increasing exponentially with a high speed and actual value of inductor current which is shown in Fig. 7.6 as I_L is tracking the reference by the current loop controller that is a simple gain of 2.5 which will be described in the following. The output of this gain is the variable (V(cont)*V_{PV}), hence, by dividing this signal by V_{PV} we get V(cont). This signal is fed into a limiter with an upper

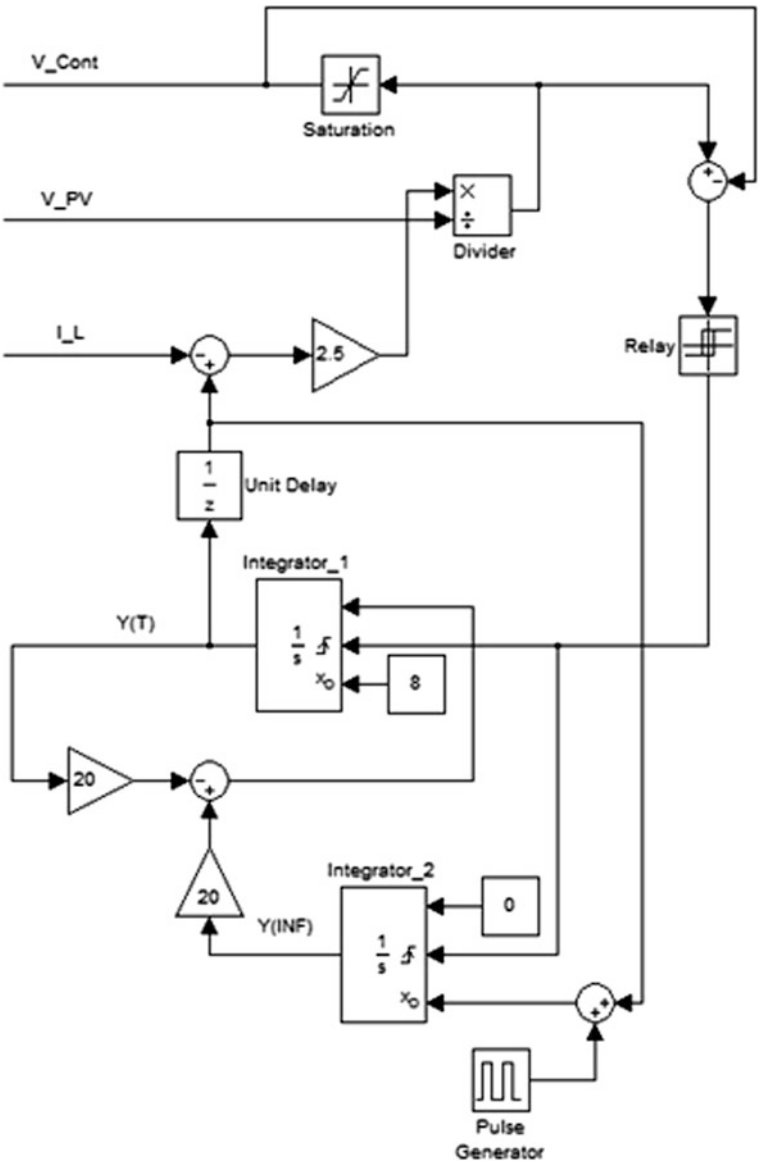

Fig. 7.6 The proposed block diagram configuration for capturing MPP

limit of 1 and lower limit of 0. To detect saturation the signal after the limiter is subtracted from the signal before limiter and fed into a relay to produce a signal indicating saturation. The procedure described here will continue until the saturation happens. At this time the value of $y_{(t)}$ is exactly the current reference signal at which saturation has happened. This value has been added to the output of pulse generator which now is zero because it has produced a pulse just at start up. This

means the output value of the summation going toward initial condition of integrator_2 is the current reference value at which saturation has happened. Because of reset signal produced by the relay and sensed by integrator_2, it will reset to its new initial condition which is the current value at which maximum power has been produced. This is the main idea of this algorithm.

Now the design procedure of current controller loop will be described. The current loop design procedure is as follows. First of all we need the model of the system. Here, we follow state space averaging approach. According to high switching frequency and the capacitor parallel to the PV the averaged state space equations can be written as follows:

$$L\frac{di_L}{dt} = d_{(t)}v_{PV} - v_c \tag{7.8}$$

$$C\frac{dv_C}{dt} = i_L - \frac{v_C - v_b}{r_b} \tag{7.9}$$

As it can be seen from state space equations, there is a multiplicative nonlinearity in the term ($d_{(t)}$ V_{PV}), hence, the system is nonlinear. To overcome this, the conventional approach is using small signal perturbation; however, this is not the approach we consider here. We utilize a heuristic technique. Let's consider the whole term ($d_{(t)}$ V_{PV}) as a variable. Looking at the system in this way changes the nonlinear system to a linear system. In other words, instead of $d_{(t)}$ we assume ($d_{(t)}$ V_{PV}) as the control parameter. Since our goal is to control the current, we need the control to output transfer function. Applying Laplace Transform and after some mathematical operations we get the transfer function as follows. For simplicity and clarity of the concept, we do not use the subscript "s" to show s-domain.

$$\frac{i_L}{d_{(t)}v_{PV}} = \frac{Cs + {}^1/_{r_b}}{LCs^2 + {}^L/_{r_b}s + 1} \tag{7.10}$$

Setting the switching frequency to 20 kHz as a trade-off between filter components size and switching losses, we choose 20 % of the switching frequency, 4 kHz as the cross over frequency of the compensated system. Choosing the typical values of C = 100 μF, L = 100 μH gives the corner frequency of 1.6 kHz for the filter which is small enough compared to switching frequency for good attenuation of switching ripples. Internal resistance of the battery approximately equal to $r_b = 0.1\Omega$ is chosen for a 3 volt single cell Li-ion battery.

The bode diagram of the plant transfer function is shown in Fig. 7.7. According to the –7.93 dB gain at 4 kHz a simple P controller with Kp = 2.5 will shift the cross over frequency to 4 kHz with a phase margin of almost 90° which is high enough for stability. As it is visible from Fig. 7.7, the slope of the magnitude diagram at low frequencies is zero, not 20 dB/dec or less which means steady state error, however, this is not important in our algorithm, since, it will automatically consider this error. This is one of the advantages of the proposed algorithm as mentioned before.

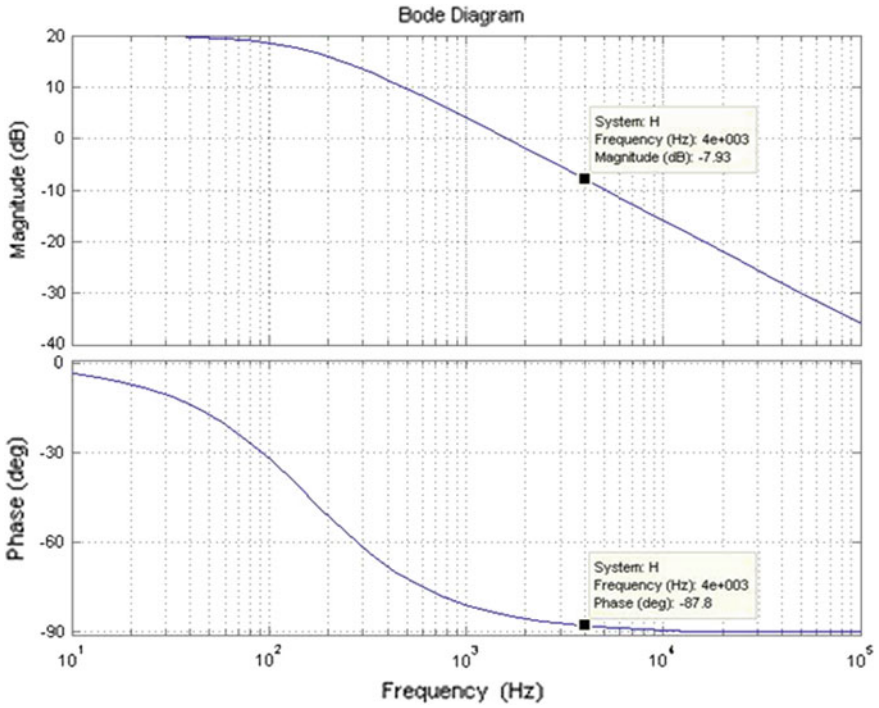

Fig. 7.7 Bode plot of Eq. (7.10)

7.4.4 Simulation Results

The system described in previous parts is simulated in MATLAB/Simulink to verify the performance of the control algorithm proposed. As will be shown in the results, the MPPT algorithm can simply handle large signal disturbances. For testing this case we change the value of short circuit current of the PV panel by changing the constant value signal feeding the controlled current source shown before in Fig. 7.4. First the simulation begins with the value of 18 amps. Results show good performance of the control in finding the maximum current value. Relatively high speed steady state is achieved. Then at the time of 0.4 s the short circuit current is reduced from 18 to 12 amps which is a large signal disturbance. Again after some time the operating point automatically shifts to the maximum power point. At the time of 0.7 s the short circuit current again reduces from 12 to 8 amps and the MPPT algorithm again finds the maximum power point. The instantaneous value of short circuit current of the PV panel, saturation detection by the relay, current reference, actual output current, instantaneous PV power, average PV power are all illustrated in Fig. 7.8 (a) through (f), respectively.

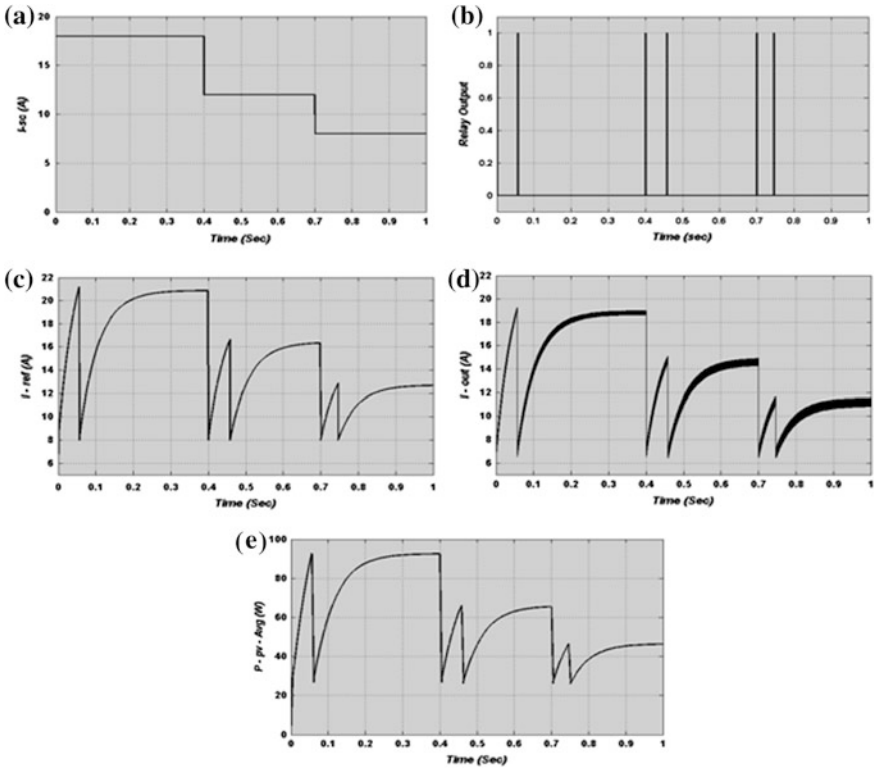

Fig. 7.8 Simulations results: **a** instantaneous value of short circuit current of the PV panel **b** saturation detection by the relay **c** current reference **d** actual output current **e** average PV power

7.4.5 Summary

In this section various MPPT techniques and their applications were studied. Pros and cons of each method were mentioned. A new PV model suitable for Simulink was proposed to avoid algebraic loop problem. A novel MPPT technique was proposed for battery charging applications. This method mainly finds the maximum power point of the PV panel by increasing the current reference of the power converter until the operating point which is unable to be tracked by the converter. This point will lead to saturation in the controller which will be used as a set point indicating the maximum power point. The main advantage of this method is its independency from the power converter topology. Simulation results verify the validity of the proposed technique.

7.5 Power Electronics for EV and PHEV Charging

7.5.1 Need of Power Electronics for PHEV Applications

As different electrical sources, loads and storage devices have different characteristics, power electronics plays a key role in reliable and efficient operation of electrical systems. Power electronics have dramatically developed over the previous decades in different aspects such as speed, reliability, performance, control and etc. Besides, enormous effort has been put into development in different areas of power electronics such as novel converter topologies, converter control and modeling and power flow management to improve the performance and increase the efficiency and reduce the cost of power converters. Without reliable and low-cost power converters, deployment of renewable energy sources for residential and industrial applications is impossible. Power electronic converter systems can be categorized based on different criteria. For single-input single-output converters power flow is a general criterion for classification which leads to two important classes, namely, unidirectional converters and bidirectional converters. Multi-input single-output, single-input multi-output, and multi-input multi-output converters are generally classified under multiport converters category.

For the EV/PHEV battery pack charger application using solar energy, PV panels are not used to charge the battery pack directly because of the intermittent nature of renewable sources. This is because of the necessity of the presence of enough power during the charging process. If the PV panels are directly connected to battery pack using an MPPT stage, when the required power by the battery pack is more than the available power from the PV panels, the battery pack cannot be charged based on the specified charging algorithm by the manufacturer. This will lead to battery degradation and reduced life cycle over time and also prolonged charging times which is not acceptable for users. Due to this fact, what is being applied in solar charging stations currently is injecting the available power from PV panels to the grid using inverters and charging the battery packs from the grid separately which can be considered an infinite source providing any amount of required power to the load. Using this method is like using the grid as a storage device which stores power from PV panels when available and delivers power to the load when required, specifically if the charging process does not coincide solar irradiation. This configuration has some problems or may cause some other problems for the grid in future. First, all of the injected power from the PV panels to the grid will not necessarily enter the battery pack and may flow through other paths and other loads far from the source which involves electric losses. In some cases the generation plant and charger can be very far from each other which will lead to lots of electrical losses in the transforming cables. Second, if the number of these charging stations increases a lot over time, assuming each house installs a solar charger and they all utilize the grid as storage, this can cause problems for the stability of the grid. What author has in mind is to propose a structure which forces

the available power from PV panels to enter the battery pack directly and obtain the remaining required power from the grid simultaneously.

7.5.2 Conventional Structures of PV Systems

In this section, we will have an overview on the existing PV structures. A general PV system consists of PV panels, power converters, filters, controllers, and electrical load or power system. Different configurations can be utilized to convert solar power to processed electrical power. They are mainly [18]: (a) Central inverters. (b) String inverters. (c) Module integrated inverters as shown in Fig. 7.9.

In Fig. 7.9 the converters are shown as DC-AC inverters. However, they do not have to be necessarily an inverter. They can also be DC-DC converters implementing MPPT based on the nature of the load, coupling of sources, or power system connected to the other side.

7.5.3 Central Inverters

In this configuration (usually for more than 10 kW), some PV strings are paralleled and connected to a single converter. This has some advantages and some disadvantages. According to initial and maintenance cost, it is beneficial because of single converter. On the other side, this topology has lower efficiency compared to

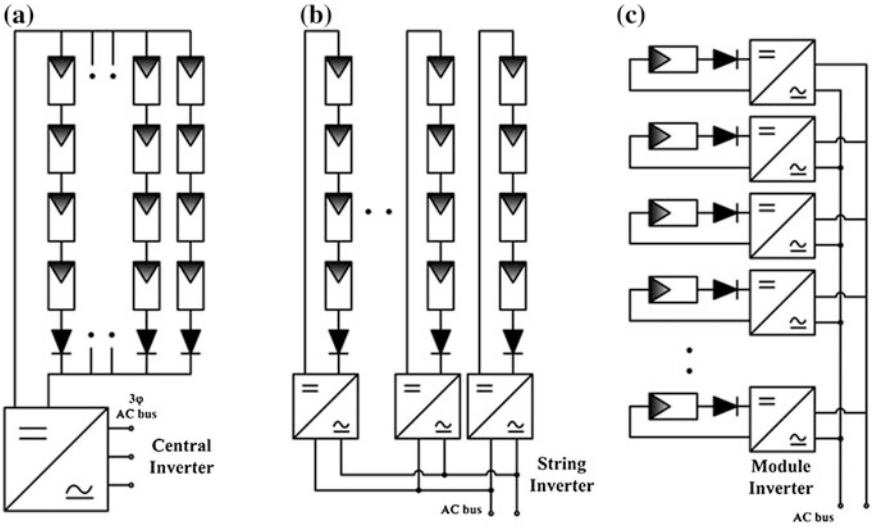

Fig. 7.9 Conventional PV structures: **a** central inverter (**b**) string inverter (**c**) module inverter

others because of inherent characteristic mismatch among different PV panels. In addition, partial shading in this case cannot be handled in an efficient manner [19]. After all, according to reliability point of view, this configuration is not reliable, since failure of the converter will result to failure of the whole system.

7.5.4 String Inverters

As depicted in Fig. 7.9b in the case of string inverters, the whole PV arrays are divided into parallel strings of series connected PV panels and each string is connected to a singular converter. This increases the whole energy harvested from solar energy due to better and more accurate MPPT capability, since each string is controlled separately and partial shading and PV panels mismatch can be considered in a more efficient manner. Because of utilization of multiple converters the whole system has higher reliability compared to centralized configuration.

A subclass of string converters exists and is called Multi-String Inverters. In this category a DC-DC converter is utilized for each string and finally only one DC-AC inverter is used for conversion to AC as shown in Fig. 7.10. This configuration combines the benefits of both string and centralized configurations. This multi-string topology allows the integration of different technologies of PV panel strings and also different orientations. The typical operating power range of multi-string topology is 3–10 kW.

7.5.5 Module Integrated Inverters

This configuration uses one converter for each PV panel and according to energy point of view the maximum possible electrical energy is harvested out of each panel because of implementing MPPT at panel level. This eliminates the losses due to panels mismatch. This system has a very high reliability; however, maintenance procedure is very complicated. Although this configuration is very costly at the moment, some researchers believe that according to progressing technology of packaging and every day decreasing price of semiconductors, this topology will be the most suitable one for the future of PV plants according to modularity and plug and play capability.

7.6 Topologies for PV Inverters

During recent years PV inverter technologies have evolved increasingly [20]. There are various power configurations possible. These can be summarized as shown in Fig. 7.11 [18].

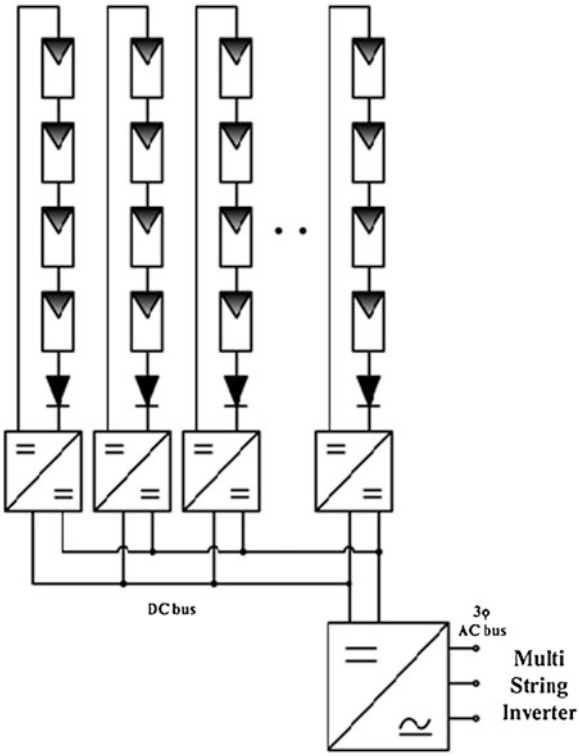

Fig. 7.10 Multi-string inverter structure

Using or not using a DC-DC converter depends of the configuration of PV panels and number of PV panels in series. If the number of PV panels in series is high enough to produce higher voltage than load side voltage for most of the times the use of a boost DC-DC converter can be avoided. The isolation depends on the safety standards and requirements.

7.6.1 PV Inverters with DC-DC Converter and Isolation

Isolation is usually achieved using a transformer. This transformer can be on the Low Frequency (LF) side (Fig. 7.12a) or interleaved in the High Frequency (HF) side (Fig. 7.12b) which is an intermediate AC stage. The second configuration is smaller and lighter due to smaller transformer; however, transformer should be of higher quality because of higher losses.

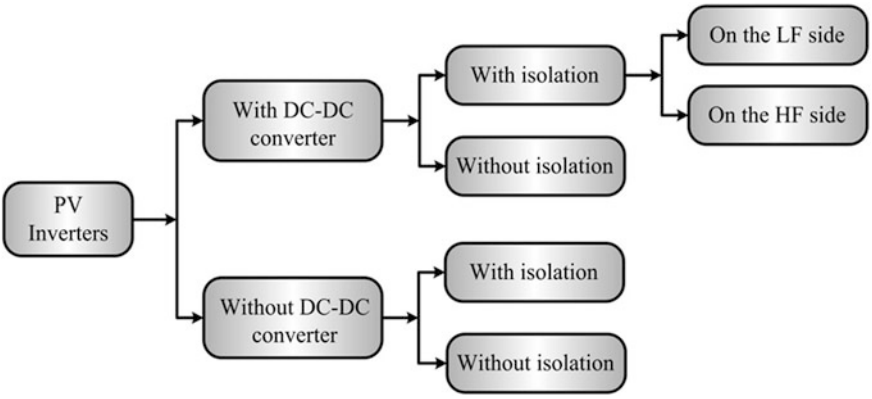

Fig. 7.11 Power configurations for PV inverters

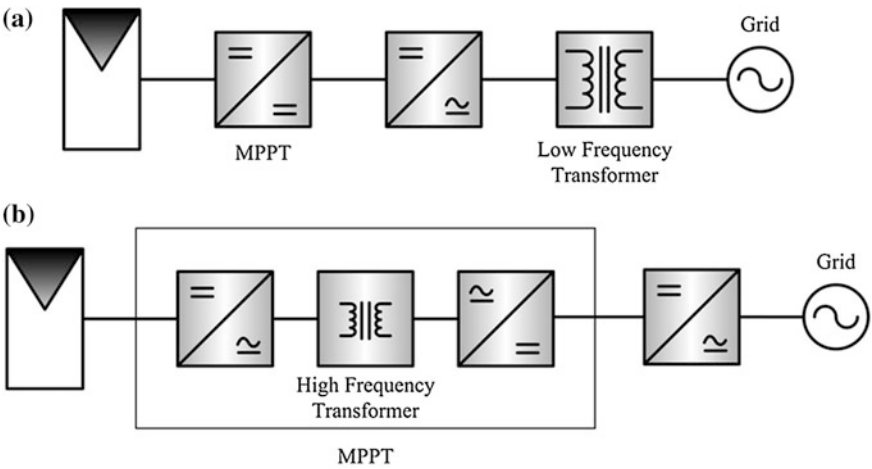

Fig. 7.12 PV inverter configurations with DC-DC converter and isolation: **a** transformer on LF side, **b** transformer on HF side

7.6.2 PV Inverters with DC-DC Converter and Without Isolation

Depending on the safety regulations, if isolation is not mandatory the transformer can be eliminated and a more simple system will be achieved as shown in Fig. 7.13.

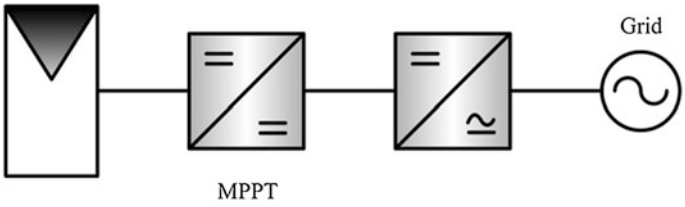

Fig. 7.13 PV inverter configuration with DC-DC converter and without isolation

7.6.3 PV Inverters Without DC-DC Converter and with Isolation

Eliminating the DC-DC converter stage and using only the DC-AC inverter involves MPPT and inversion stages to be integrated resulting in a more complex control algorithm. Besides, since the transformer is on the low frequency side it is bigger and heavier. A typical block diagram of this configuration is illustrated Fig. 7.14.

7.6.4 PV Inverters Without DC-DC Converters and Without Isolation

This configuration is the simplest configuration possible and at the same time has the least reliability comparing to its counterparts. Any fault in the source side or load side can easily expand to the other side and endanger the operation of the system. So an efficient protection system is required. Besides, any DC current can be injected to the load or power system side. This configuration can be utilized if the number of PV panels in series is high enough to produce a voltage higher than AC side voltage level. This configuration is shown in Fig. 7.15.

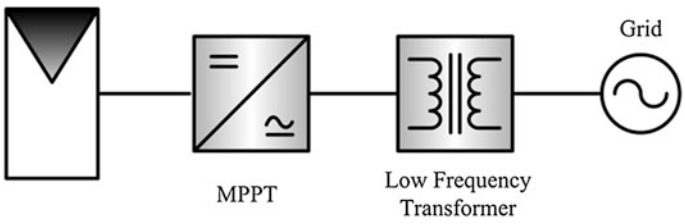

Fig. 7.14 PV inverter configuration without DC-DC converter and with isolation

7.6.5 Possible PV Interconnection Schemes

Comparing output power and energy results from PV systems obtained using simulations during design stages with the real experimental results over the previous decades has exposed a significant difference [21]. This is due to numerous reasons one of which is mismatch losses. Mismatch losses are mainly constituted of two main reasons [22–27]. The first reason is dispersion of electrical properties and nonuniformity PV cell illumination among the array. This is mainly due to manufacturer's tolerances or degradation processes. The other important reason is partial shading of the PV array and variation of the tilt angles of different PV panels. Test results from various commercially available inverters show that the power loss due to partial shading can be as high as 70 % [27]. If partial shading happens in a PV array or different PV panels with different angles are connected to one converter this will cause the power versus voltage/current characteristics of the PV array to have multiple local maximum point as shown in Fig. 7.12, however; only one of them is the global peak (GP) [28].

The existence of such local maximums can cause some Maximum Power Point Tracking Techniques (MPPT) especially Perturb and Observe (P&O) or Incremental Conductance methods to fail tracking the global maximum point ($P_{max,2}$ in Fig. 7.16). Eliminating or reducing this power loss resulting from mismatch of panels or different tilt angles can be performed by utilizing more efficient MPPT techniques, adding more converters or static/dynamic reorganizing cell/module

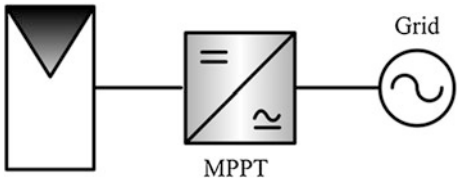

Fig. 7.15 PV inverter configuration without DC-DC converter and without isolation

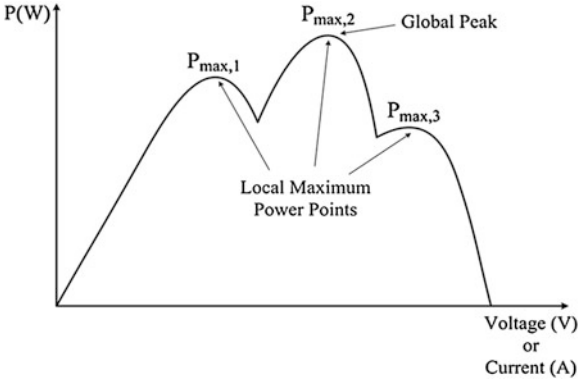

Fig. 7.16 A typical P-V curve of a partially shaded PV array

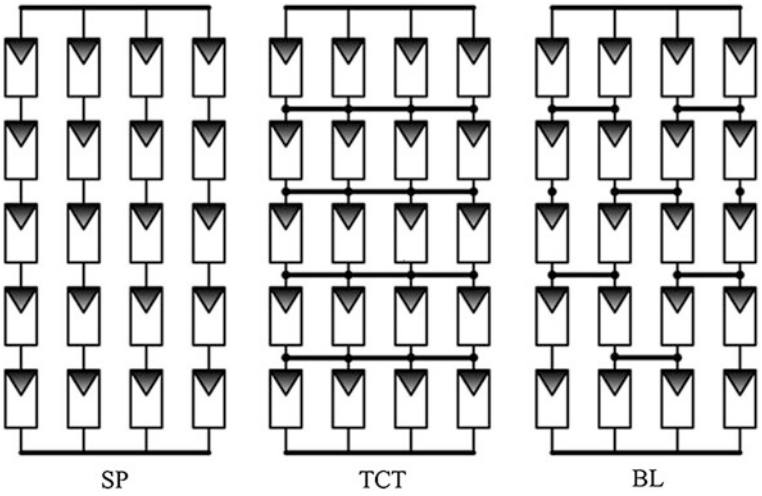

Fig. 7.17 Different cell interconnections: series–parallel (*SP*), total-cross tied (*TCT*), and bridge-link (*BL*)

connections. The usual interconnection of panels is connecting them in series and making strings of cells and paralleling the strings as was previously shown in Figs. 7.9 and 7.10. This interconnection is called Series–Parallel (SP). Other cell interconnections have been proposed which can reduce the mismatch power loss [22–24, 29–31]. They are called Total-Crossed Tied (TCT) and Bridge-Link (BL). They are shown in Fig. 7.17.

7.6.6 Proposed Structure

As mentioned in the introduction, our goal is to propose a structure which is able to inject the PV power directly to the battery pack and obtain the remaining power from the grid. The system diagram of the proposed structure is depicted in Fig. 7.18. This configuration has some advantages. First, the PV power can be directly injected to the battery pack and not to the grid then from the grid to the load which reduces the overall losses. Second, this configuration provides great flexibility for different power flows. Depending on the amount of available power from PV panels and required power by the battery pack, different modes of operation may happen. If available power from PV is more than the required power for charging the battery pack the remaining can be injected to the grid (mode 1). If PV power is not enough, grid will be involved to supply the remaining power (mode 2). If there is no power available from the PV panels battery pack can be charged solely by the grid (mode 3).

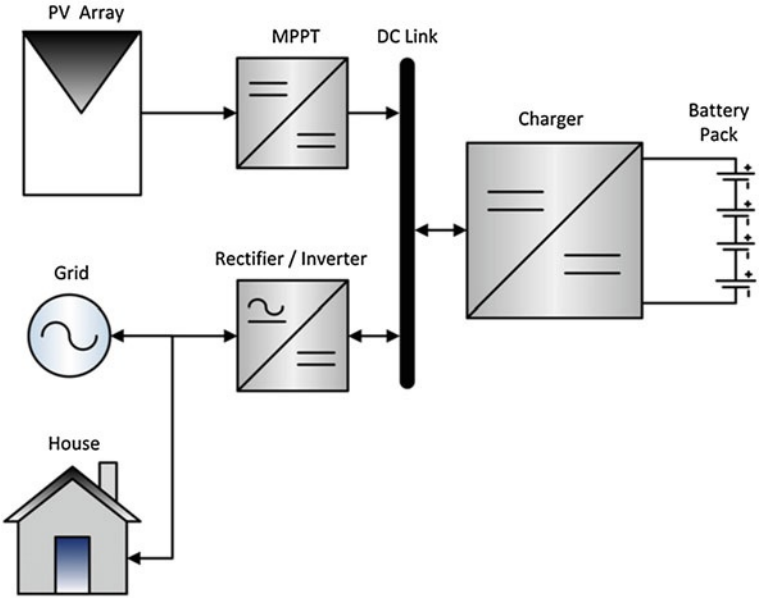

Fig. 7.18 System structure

If the battery pack is not connected to the system, PV power can be injected to the grid to reduce the electricity bill of the house (mode 4). If needed, the battery pack can be discharged to the grid during specified times performing as a configuration supporting Vehicle to Grid (V2G) (mode 5). Even in the case of blackouts the battery pack can perform as an energy source and supply the power to the house for some time depending on the battery pack capacity (mode 6). This flexibility in power flows and modes of operation facilitates implementing concepts like smart grid. Different modes of operation are illustrated in Fig. 7.19.

7.7 Power Converters Topology

There is variety of choices of converter topologies for the proposed configuration. There is not a unique best selection of topologies for this system like any other system; however, based on the operation principle of the configuration and nature of sources and loads the number of choices can be limited. According to the power flow directions depicted in Fig. 7.16 the category of the three converters in the system can be recognized.

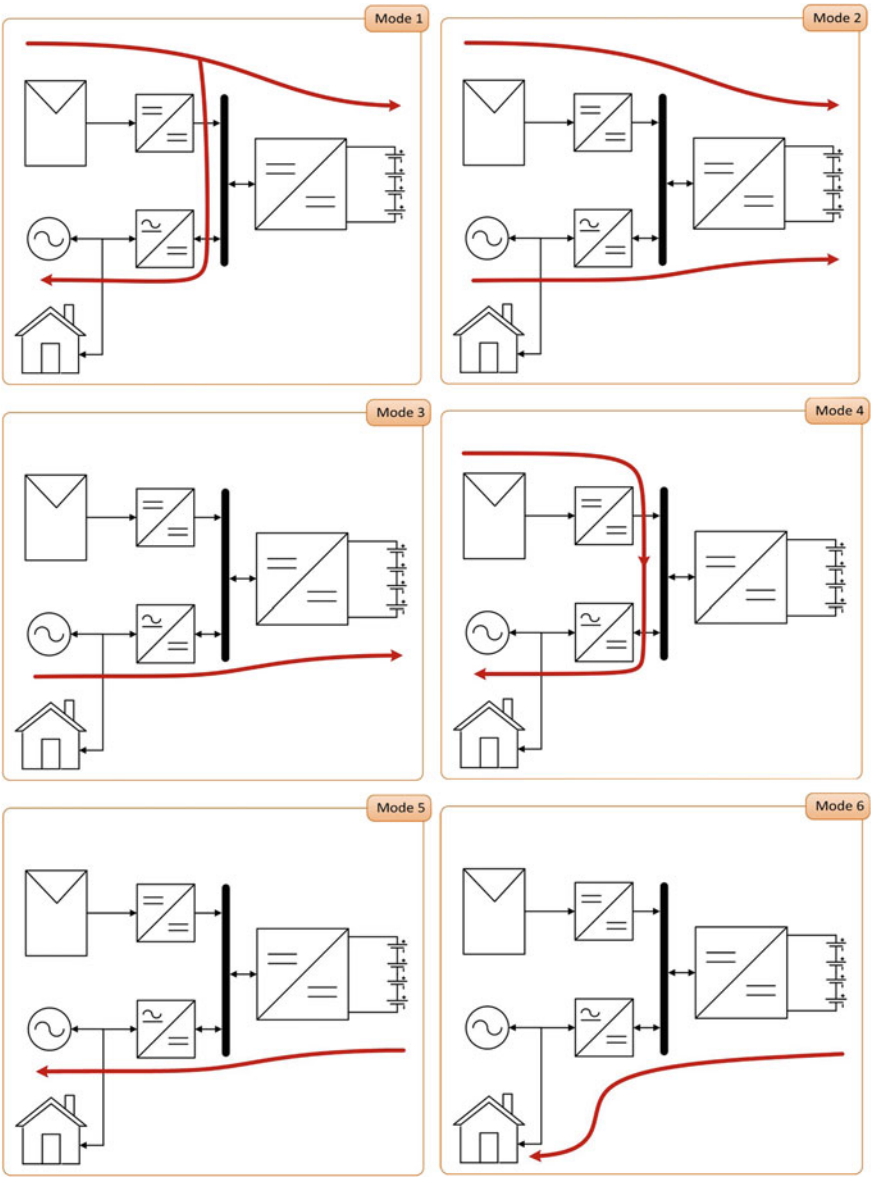

Fig. 7.19 Modes of operation

7.7.1 MPPT Stage

Since PV panels are unidirectional source of energy, the Maximum Power Point Tracker (MPPT) stage can be unidirectional and need not to be bidirectional. This

part of the system was described in detail in Sect. 7.3. Depending on the desired power rating of the system, maximum power and voltage rating of the PV panels, maximum number of possible PV panels to be installed in a limited area (roof of a house); different topologies can be chosen. In Sect. 7.3 a simple buck converter was used to show the validity of the proposed MPPT algorithm, however, as mentioned there the algorithm is independent of the converter topology as long as the topology can be current mode controlled. For example, nonisolated converters such as buck, boost, and buck-boost or their isolated topology such as flyback, forward, and push–pull converters can be used. Each one has its own advantages and disadvantages. Depending on the design criteria which can be cost, efficiency, filter requirements, control simplicity, durability, or other factors the topology can be chosen. PV panels can be connected in series/parallel and finally connected to the MPPT stage, or separate MPPT stages can be mounted on each PV panel and finally all of them connected in series or parallel or other combinations as was shown previously for inverters in Figs. 7.9 and 7.10. Any other conventional MPPT method such as perturb and observe can also be used.

7.7.2 Rectifier/Inverter Stage

As shown in Fig. 7.19 the rectifier/inverter stage should be bidirectional to be able to operate in both directions depending on the desired mode of operation. Full-bridge converter is a suitable candidate for this application, since it can operate both as a rectifier or an inverter with the same topology and just by changing the switching scheme. Different switching schemes are available for this topology and it has been widely analyzed in the literature. Because of the antiparallel diodes in full-bridge converter, all four quadrants of operation are accessible which provides reversible power flow direction. The rectifier/inverter stage is shown in Fig. 7.20.

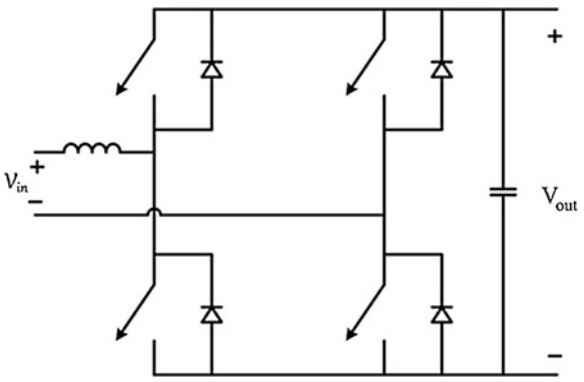

Fig. 7.20 Rectifier/Inverter stage

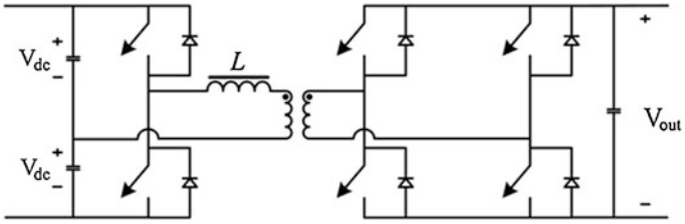

Fig. 7.21 DAB with half-bridge converter at one side

7.7.3 Charger Stage

As depicted in Fig. 7.19 the charger converter has to be bidirectional and DC at both sides. Our assumption for next generations of EVs/PHEVs is that we have direct access to the battery pack via DC terminal, eliminating AC/DC charger which is currently being used. This increases the efficiency of the overall system since one stage has been eliminated. Besides, because of the safety of the user, this converter should provide isolation, so in case of short circuit at the battery pack side the user remains safe. These features are all available in Dual Active Bridge (DAB). DAB was first introduced in [32–34] and modifications to this topology were later investigated. DAB is a bidirectional converter with high power density suitable for high efficiency applications. This converter has some desirable features such as bidirectional power flow, electrical or galvanic isolation, buck-boost operation, low device stress and low switching losses, small filter components because of high possible switching frequency, small and light isolation transformer because of high switching frequency, and utilization of transformer leakage inductance as inductive energy transfer component.

Based on the reverse voltage stress requirements of the switches other configurations can be recognized. For example, if the switches can tolerate the reverse voltages equal to input or output voltage, then the full-bridge converters can be substituted by half-bridge converters leading to Dual Half-Bridge (DHB) converter. Another possible configuration is to have one full-bridge converter on one side and one half-bridge converter on the other side as shown in Fig. 7.21.

References

1. Software Fix Extends Failing Batteries in 2006-2008 Honda Civic Hybrids: Is Cost Acceptable? *IEEE Spectrum*
2. L.R. Chen, in *Design of Duty-Varied Voltage Pulse Charger for Improving Li-Ion Battery-Charging Response*, vol. 56, no 2. (2009), pp. 480–487
3. S. Park, H. Miwa, B. Clark, D. Ditzler, G. Malone, N.S. S'souza, J.S. Lai, A universal battery charging algorithm for Ni-Cd, Ni-MH, SLA, and Li-Ion for wide range voltage in portable applications, in *IEEE Power Electronics Specialists Conference*, (2008), pp. 4689–4694

4. C. Hua, M.Y. Lin, A study of charging control of lead acid battery for electric vehicles, in *IEEE International Symposium on Industrial Electronics*, (2000), pp. 135–140
5. Z. Ullah, B. Burford, S. Dillip, Fast intelligent battery charging: neural-fuzzy approach. IEEE **11**(6), 614 (1995)
6. S. Altung, Z.C. B, Failure mode of the negative plate in recombinant lead/acid batteries. J. Power Sources **52**(2), 201–209 (1994)
7. D. Feder, J. Wem, Gas evolution, dryout, and lifetime of VRLA cells an attempt to clarify fifteen years of confusion and misunderstanding, in *IEEE International Telecommunications Energy Conference*, (1996), pp. 184–192
8. J. Wem, D. Feder, Behavior of VRLA cells on long term float. II. The effects of temperature, voltage and catalysis on gas evolution and consequent water loss, in *IEEE International Telecommunications*, (1996), pp. 358–366
9. N. RF, S. ED, O. JB, K. M, P. A, Search for an optimized cyclic charging algorithm for valve-regulated lead–acid batteries. J Power Sources **88**(1), 44–52 (2000)
10. L. Dong-Yun, N. Hyeong-Ju, H. Dong-Seok, I. Choy, An improved MPPT converter using current compensation method for small scaled PV-applications, in *Applied Power Electronics Conference and Exposition APCE*, (2003), pp. 540–545
11. T. Esram, J. W. Kimball, P. T. Krein, T. L. Chapman, P. Midya, Dynamic maximum power point tracking of photovoltaic arrays using ripple correlation control, IEEE Trans. Power Electron.**21**(5), 1292–1291 (2006)
12. T. Esram, P. L. Chapman, Comparison of photovoltaic array maximum power point tracking Techniques, IEEE Trans. Energy Convers. **22**(2), 439–449 (2007)
13. S.J. Chiang, K.T. Chang, C.Y. Yen, Residential photovoltaic energy storage system. IEEE Trans. Industr. Electron. **45**(3), 385–394 (1998)
14. J. Enrique, E. Duran, M. Sidrachdecardona, J. Andujar, Theoretical assessment of the maximum power point tracking efficiency of photovoltaic facilities with different converter topologies. Sol. Energy **81**(1), 31–38 (2007)
15. D. Shmilovitz, On the control of photovoltaic maximum power point tracker via output parameters, in *Electric Power Applications*, vol. 152, no 2, (2005) pp 239–248
16. J.A. Gow, C.D. Manning, Development of a photovoltaic array model for use in power-electronics simulation studies, in *Electric Power Applications*, vol. 146, no 2, (1999) pp. 193–200
17. F.M. Gonzalez-Longatt, Model of photovoltaic module in Matlab, in *2do congreso iberoamericano de estudiantes de ingenieriacute;a eléctrica, electrónicay computación, ii cibelec*, (2005), pp. 1–5
18. F. Iov, M. Ciobotaru, D. Sera, R. Teodorescu, F. Blaabjerg, Power electronics and control of renewable energy systems, in *7th International Conference onPower Electronics and Drive Systems, PEDS'07.*, 2007, pp.P–6, P–28, 27–30
19. T. Shimizu, O. Hashimoto, G. Kimura, A novel high-performance utility-interactive photovoltaic inverter system. IEEE Trans. Power Electron. **18**(2), 704–711 (2003)
20. H. Haeberlin, Evolution of Inverters for Grid connected PV systems from 1989 to 2000, in *Proceedings of Photovoltaic Solar Energy Conference*, (2001)
21. D. Picault, B. Raison, S. Bacha, J. De La Casa, J. Aguilera, Forecasting photovoltaic array power production subject to mismatch losses. Sol. Energy **84**(7), 1301–1309 (2010)
22. A. Chouder, et al. Analysis model of mismatch losses in PV systems. J. Sol. Energy Eng. **131**, (2009)
23. N. Gautam, An efficient algorithm to simulate the electrical performance of solar photovoltaic arrays. Energy **27**(4), 347–361 (2002)
24. N.D. Kaushika, N.K. Gautam, Energy yield simulations of interconnected solar PV arrays. IEEE Trans. Energy Convers. **4**(1), 127–134 (2003)
25. N. Kaushika, A. Rai, An investigation of mismatch losses in solar photovoltaic cell networks. Energy **32**(5), 755–759 (2007)
26. E. L. Meyer, E. E. Van Dyk, Assessing the reliability and degradation of photovoltaic module performance parameters. IEEE Trans. Reliab. **53**(1), 83–92 (2004)

27. N.J.C.M. Van der Borg, Energy loss due to shading in BIPV application, in *3rd World Conference on Photovoltaic Energy Conversion*, (2003) pp. 2220–2222
28. R. Bruendlinger, B. Bletterie, M. Milde, H. Oldenkamp, Maximum power point tracking performance under partially shaded PV array conditions, in *21st EUPVSEC*, (2006) pp. 2157–2160
29. W. X. W. Xiao, N. Ozog, W. G. Dunford, Topology study of photovoltaic interface for maximum power point tracking, IEEE Trans. Industr. Electron. **54**(3), 1696–1704 (2007)
30. E. Karatepe, M. Boztepe, M. Colak, Development of a suitable model for characterizing photovoltaic arrays with shaded solar cells. Solar Energy **81**(8), 977–992 (2007)
31. D.N.D. Nguyen, B. Lehman, An adaptive solar photovoltaic array using model-based reconfiguration algorithm. IEEE Trans. Industr. Electron. **55**(7) 2644–2654 (2008)
32. M.H. Kheraluwala, R.W. DeDoncker, D.M. Divan, Power conversion apparatus for dc–dc conversion using dual active bridges
33. R.W.A.A. De Doncker, D.M. Divan, M.H. Kheraluwala, A three-phase soft-switched high-power-density DC/DC converter for high-power applications, Inst. Electr. Electron. Eng. **27**(1), 63–73 (1991)
34. M.N. Kheraluwala, R.W. Gascoigne, D.M. Divan, E.D. Baumann, Performance characterization of a high-power dual active bridge DC-to-DC converter. IEEE **28**(6), 1294–1301 (1992)
35. S. De Breucker, P Jacqmaer, K. De Brabandere, J. Driesen, R. Belmans, Grid power quality improvements using grid-coupled hybrid electric vehicles, in *Proceedings IEEE Power Electronics, Machines, and Drives Conference*, Dublin, Ireland, April 2006, pp. 505–509
36. J. Newmiller, C. Whitaker, M. Ropp, B. Norris, Renewable systems interconnection: distributed PV systems design and technology requirements, U.S. Department of Energy, Oct. 2007

Chapter 8
Power Electronic Converter Topologies for EV/PHEV Charging

8.1 Grid and Photovoltaic (PV) System for EV/PHEV Charging

8.1.1 Introduction to Power Electronic Inverter Topologies

When defining the technical goals for a distributed power converter system to be used in a PV-powered, grid-tied carport, suitable compromises must be made, in order to contain costs while providing acceptable performance. Essentially, the main design objective is dictated by the fact that the carport will be a public or semi-public structure. Hence, it is crucial that the system is robust, reliable, and offers high availability. It was already ascertained that both the PV resource and the power conversion system must be distributed, providing flexibility and redundancy, while choosing topologies that are characterized by low component count and stress levels, in order to ensure a high Mean Time Between Failures (MTBF). MTBF will broadly be referred to as "reliability" henceforth, in this thesis.

Another important consideration is that renewable resources are not easily harnessed. This simple fact makes energy conservation through high conversion efficiency a priority. As mentioned above, the number of conversion stages should be minimized, at least for the most utilized power flow paths. In the case of a carport, the power will flow most frequently from the PV array to the EV battery and from the grid to the EV battery. Therefore, given a choice, the flow paths should be optimized in-line with the following priorities: in decreasing order of importance, array to battery, grid to battery, array to grid, and battery to grid. A schematic, showing possible power flow paths is depicted in Fig. 8.1.

Finally, it is reasonable to expect that the initial cost penalty would be more than offset by a design that is intrinsically low-maintenance, considering the application. This goal can be achieved by avoiding or minimizing the use of short-life components, such as electrolytic capacitors, electromechanical devices (relays,

S. S. Williamson, *Energy Management Strategies for Electric and Plug-in Hybrid Electric Vehicles*, DOI: 10.1007/978-1-4614-7711-2_8,

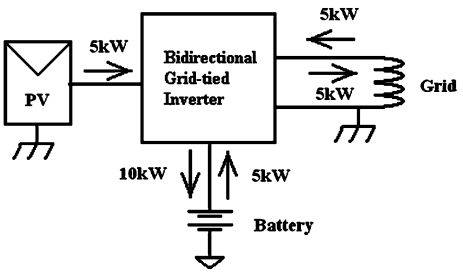

Fig. 8.1 Possible power flow paths with specified power level

fans, and power connectors), and fault detectors or suppressors (MOVs and GFID). In addition, the control scheme should be robust and rely as little as possible on critical sensing devices that have time stability limitations or require periodic calibration. These include thermistors, shunt resistors, hall-effect devices, and linear opto-electronics.

Having established the general design philosophy, the detailed specifications for the power conversion system, as have emerged in the discussion earlier in this study, are summarized here:

PV panel string peak power:	5 kW
PV panel voltage range*:	430 VDC $\pm$ 70V on full temperature range and 10–100 % insolation
PV operating temperature:	−20–65 °C
PV grounding	Required at either power conductors or as a center-tap
Grid nominal voltage:	Single-phase 220–240 VAC
Grid nominal current:	25 A
Current distortion:	<5 %
Power factor:	Unity
Charger voltage range	275 to 400 V (galvanically isolated)
Charging power	10 kW max
Discharging power	5 kW

The specifications shown above indicate a desirable range, as they guarantees a higher than line peak voltage for a transformer-less topology. The specifications also indicate the highest practical voltage allowed by code; of course, a higher voltage implies less cabling loss and higher efficiency.

8.1.2 Proposed Power Conversion Topologies

From the foregoing discussion, it appears that the ideal power processor would only have a single conversion stage between all power ports (i.e. the PV, the

inverter, and the EV battery). Furthermore, the power processor would also handle two DC levels simultaneously (EV battery and PV) and permit bucking and boosting to and from the grid. The Z-source/loaded converter (Z-converter) is known to possess all these attributes and will, therefore, attract most of the attention in this thesis; it will also be the first topology to be analyzed in detail. The Z-converter will be compared to another class of power processors that allows utilization of dedicated converters for the grid as well as the battery that can be isolated using small and highly efficient HF power transformers.

Safety and current shaping issues are easily resolved. However, the higher component count of the circuit can affect reliability. Finally, a third type of power processor will also be considered for comparison purposes. This third circuit represents the transformer-less topology; it allows direct connection to the grid distribution transformer without intervening isolation. However, the transformer-less topology is still not popular in North America, despite its broad acceptance in Europe. The good safety record of the transformer-less option in Europe, coupled with the objective advantages in the areas of cost and efficiency, will more than likely ensure its adoption worldwide. These topologies are simpler and more efficient than the previously discussed topologies. Nevertheless, they demand the use of sophisticated and precise control circuits, to avoid DC current injection onto the grid. In addition, safety requirements are more stringent for all the major components (panels, EV battery, and inverter). Although European standards do not require a ground on the PV string, the topology presented in this study has one, in order to satisfy the specifications.

For all topological options, the switching frequency is considered as 25 kHz. This choice allows the use of a fast IGBT technology, which is demonstrably better suited for power levels in the required range. Furthermore, given that physical size is not a priority for this application; higher frequency operation could be needlessly wasteful.

8.1.3 The Z-Converter

8.1.3.1 Background

The use of the Z-converter AC power absorption/injection, with simultaneously controlled battery charging, has been successfully demonstrated in literature [1]. The AC source/load could comprise of an EV electric machine, while the DC source could comprise of a fuel cell. The same concept can be extended to PV grid-tied systems. The grid-tied system, on the other hand has fewer degrees of freedom, because of two main reasons. First, in the case of the fuel-cell-battery HEV described in [2], the battery pack is native to the system, and therefore, its characteristics are fully known. In the case of a PV grid-tied carport, the PV and grid resources are expected to function with widely different battery technologies and characteristics. Second, the electric machine, used in [2] can be managed by

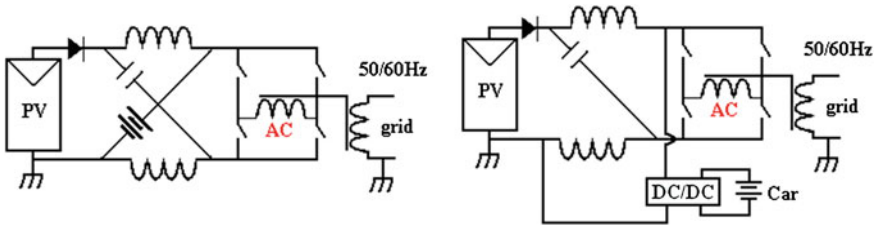

Fig. 8.2 Non-isolated grid-tied Z-converter (*left*); Grid-tied Z-converter with Isolated Charger (*right*)

the vehicle controller, while the grid behavior is an external variable. On the other hand, in the case of the PV carport, the EV battery will need to be isolated through a transformer, so that the turns-ratio can provide added flexibility. The schematic of the Z-converter system is shown in Fig. 8.2.

It is important to realize that the DC/DC converter was added to the original design, in order to solely provide galvanic isolation. In fact, the Z-converter possesses double modulation capability, and can shape the grid current while simultaneously regulating EV battery charging. This goal is achieved with a single conversion stage and can be considered as the main advantage of the Z-converter. An added advantage is the inherent buck-boost capability of this topology. However, given the presence of the isolation transformers to the grid and EV battery, this benefit is marginal in this application. Some of the drawbacks include:

(a) An outsized 60 Hz transformer is required, because a large common mode voltage would otherwise exist at the PV modules, making it impossible to meet leakage current specifications. A central 60 Hz transformer can possibly be used, to service all charging stations. Nevertheless, the single point of failure in this case would not be desirable.

(b) Single-phase power is delivered and absorbed in 120 Hz sinusoidal pulses. Because of the single stage of conversion, this power ripple must be stored at some point in the circuit. As the EV battery is by far the largest dynamic repository of energy in this circuit, it is likely to absorb most of this ripple. In fact, in the case of full PV production into the grid, the battery would not only experience AC current alone, but its amplitude would also be very large. As disturbing as this may appear, such an approach will be considered and even encouraged at times, because it allows the elimination of an additional large decoupling capacitor across the PV panels, improving cost and reliability. At the same time, the concern about the AC component can be rationalized in several ways. For instance, whenever PV production exceeds the demand of the battery, the local MPPT system can be bypassed, so that excess power is redirected to neighboring charging stations. This would not eliminate the ripple, but would at least avoid battery current reversal at line frequency. Otherwise, it could be assumed that future EVs will draw their energy from ultra-capacitor banks that are ripple-tolerant, rather than electro-chemical

devices. In either case, it is practical, that by storing the ripple in the battery by control methods is more complicated than simply introducing a large decoupling capacitor across the PV source. This method will therefore be considered, by default, in this thesis. Later, it will also be demonstrated that the ripple can easily be redirected from the battery to an added decoupling capacitor, if the design demands this requirement.

(c) In order to address the ripple problem more clearly, an additional DC/DC converter can be utilized in conjunction with the EV battery, to regulate the 120 Hz out of the charging current, with minimal decoupling. While this approach works in theory, it will require an added controller and the conversion efficiency may be reduced. In fact, the DC/DC converter would now have to be considered a second full conversion stage. This defeats the stated main advantage of the Z-converter and will only be considered briefly in 6.1.6. Therefore, no attempt will be made to completely eliminate this problem; rather, the 120 Hz ripple is accepted for this topology and will be managed using innovative techniques. These techniques involve modulation of the shoot-through duty cycle, D_o, with the intended purpose of directing the ripple either into the EV battery (or Z-circuit capacitors, when the battery is not connected) or into an added decoupling capacitor across the PV source, depending on the design requirements.

8.1.3.2 Static Design Equations and Control Scheme for the Z-Converter

The analysis of the operation of the bidirectional Z-inverter has been presented in [3, 4], and will not be repeated here. The only new addition is the DC/DC isolated converter needed for safety, as shown in Fig. 8.3.

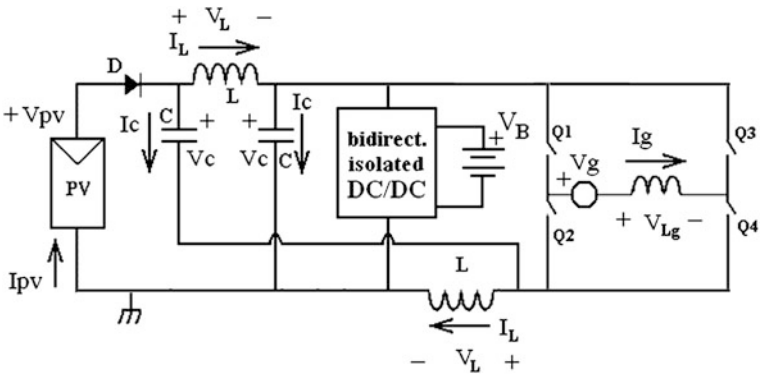

Fig. 8.3 Z-converter with added isolated DC/DC converter

In order to maximize efficiency, this added bidirectional converter is normally operated at 100 % duty cycle in open loop. Therefore, in normal operation, the voltage V_B is identical to voltage V_C, except for the static gain of the DC/DC converter. When no battery is present, and the PV feeds the grid with full available power, this converter does not operate, and appears as an open circuit. The three main static equations are derived in [5], and are restated below:

$$Vg_{(PK)} = V_C\left(\frac{D}{1-Do}\right) \tag{8.1}$$

$$Do = \left(\frac{V_C - V_{PV}}{2V_C - V_{PV}}\right) \text{ or } V_C = V_{PV}\left(\frac{1-Do}{1-2Do}\right) \tag{8.2}$$

$$I_L = \frac{D}{1-2Do} I_{\text{IN}} \tag{8.3}$$

Here, D is the modulation index or active duty cycle; D_o is the shoot-through duty cycle. Equation (8.2) is written in two ways. The first is more applicable when a battery is connected. In this case, the battery stiff voltage at V_C is independent of D_o. Rather, D_o depends on V_C. When the battery is not present, the DC/DC converter is replaced by its input capacitor alone. In this case, the capacitor voltage V_C depends on D_o, as shown in the second variation of (8.2).

Unfortunately, the validity of these equations is subject to strict operational conditions. In the first place, the circuit variables must be static or slow-changing. However, contrary to 3-phase systems, in 1-phase systems, the power is delivered to the load in a sinusoidal fashion. This causes substantial 120 Hz ripple on the Z-circuit components, and hence, static behavior within a cycle cannot be claimed. Second, the switching pattern, topology, or the operating point must be such that several undesirable conversion modes are avoided or contained. These are described exhaustively in [6, 7]. This scenario can be briefly explained here, as modes that cause either the diode, D, to turn off prematurely, during the active state, or the inverting bridge to short at the beginning of the active state, thus adding an un-programmed shoot-though subperiod. These modes, in conjunction with discontinuous conduction mode (DCM) conditions, at low AC loads, can cause the capacitor voltage to float much higher than that predicted by (8.2). However, the voltage rating of the capacitor must be kept as low as possible, in order to allow use of low-voltage semiconductors. A reasonable approach to this problem, as described in [7], proposes the use of a switch in place of diode D. The idea is to block conduction only during programmed shoot-through subperiods, while allowing reverse current under all other conditions. The subsequent revised topology is shown in Fig. 8.4.

It is worth noting here that the added diode would be needed anyway, in order to allow connections of adjacent PV panels. Furthermore, the added capacitor would also be needed, in order to buffer high frequency current from the PV panel and decouple the converter locally; its size depends on whether it will also be used to decouple the grid AC power, as discussed earlier.

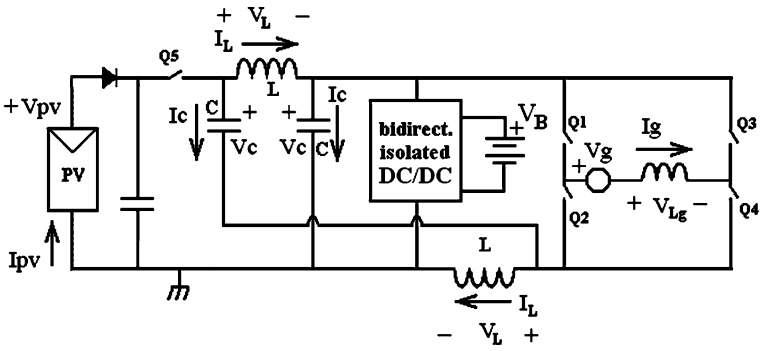

Fig. 8.4 Modified Z-converter topology to avoid undesired capacitor voltage boost

Equations (8.1) and (8.2) show the two variables, D and D_o, that control the grid and battery power flow, whereas the total power flow is controlled by the PV panel MPPT function. A simplified block diagram of the control system is depicted in Fig. 8.5. The PV MPPT will determine the appropriate current that should be drawn from the panels and generate a reference signal. This reference is compared to the measured PV current, and an error is generated, that represents the reference to an internal current loop. The controlled current in this case is the grid line current, whereby the grid current request will change with the MPPT request. At the same time, the EV on-board charge controller sends a current level request, which is a reference for the average battery current. This signal will be a DC signal in steady state. However, the actual battery charging current could have a sizeable AC component at line frequency. The error between requested and actual charge current produces the control signal D_o.

Figure 8.5 also shows the control strategy in case when there is no battery connected. The converter acts as a simple grid-tied inverter, and the modulating signal D_o is simply utilized as a means to regulate the capacitor voltage, at 550 V. This voltage level allows the use of commercially available high efficiency IGBTs rated between 900 and 1,200 V, for the inverting bridge. It must be noted that, although the specified PV voltage range does not allow the use of more efficient 600 V devices, the Switch Utilization Ratio (SUR) for the Z-converter is still high compared to alternate topologies.

8.2 DC/DC Converters and DC/AC Inverters for Grid/PV Interconnection

8.2.1 Design of the Isolating Bidirectional DC/DC Converter

Figure 8.6 shows the evolution of the Z-converter, from having the battery connected directly, in lieu of one of the Z-circuit capacitors having an intervening

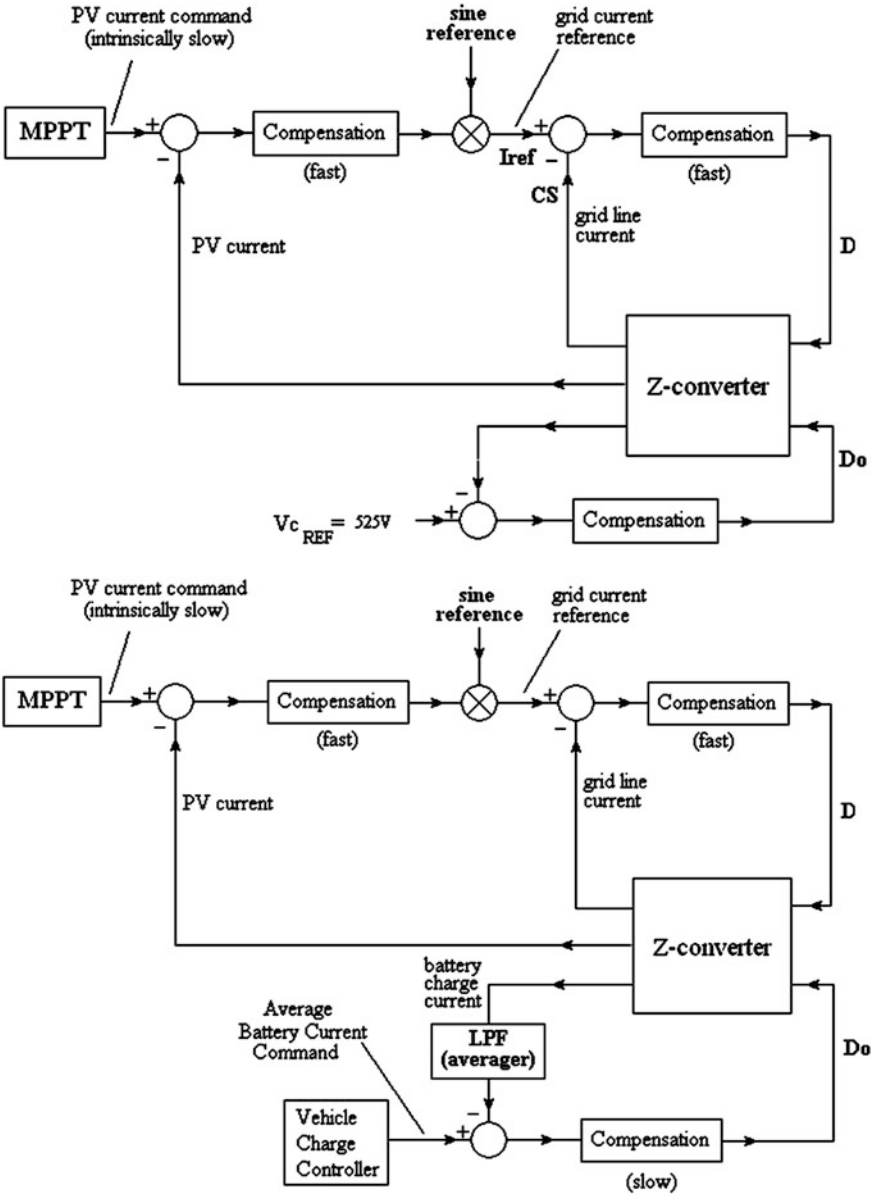

Fig. 8.5 Control strategies: With no battery (*top*), With battery (*bottom*)

isolating DC/DC converter. In both cases, the Z-circuit is no longer balanced and/or symmetrical. Although this scenario does not preclude acceptable operation, the presence of the converter allows the possibility of restoring symmetry. Figure 8.6 demonstrates this design aspect.

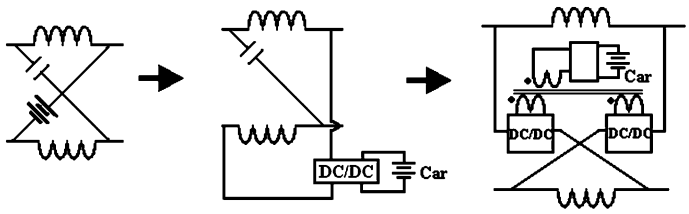

Fig. 8.6 Evolution of Z-circuit: Non-isolated (*left*), asymmetrically isolated (*center*), proposed symmetrically isolated (*right*)

This novel circuit topology adds a DC/DC converter with split primaries on the isolation transformer. However, a single secondary drives the EV battery, as depicted in Fig. 8.6. Two sets of primary switches are required. The switches conduct half of the current and can be sized accordingly. Also, because the converter operates at full duty cycle in open loop mode, very high efficiencies are obtainable by the use of simple soft-switching techniques, and various topologies, with similar costs and performance can be proposed to implement them. For the purpose of obtaining quantitative data, one such topology is proposed and analyzed without further justification, as long as it is made clear that other topologies can be substituted for this function. The chosen topology is shown in Fig. 8.7 and is based on using two half bridges, operating at a high frequency.

The converter of Fig. 8.7 uses 8 switches, with very low current and voltage ratings. However, different versions could use only 6 switches (or even 4), rated for higher voltages. Furthermore, as compared to popular push–pull topologies, the half-bridge topology does not suffer from transformer saturation, when operated in open loop full duty cycle, and has inherent zero-voltage switching (ZVS).

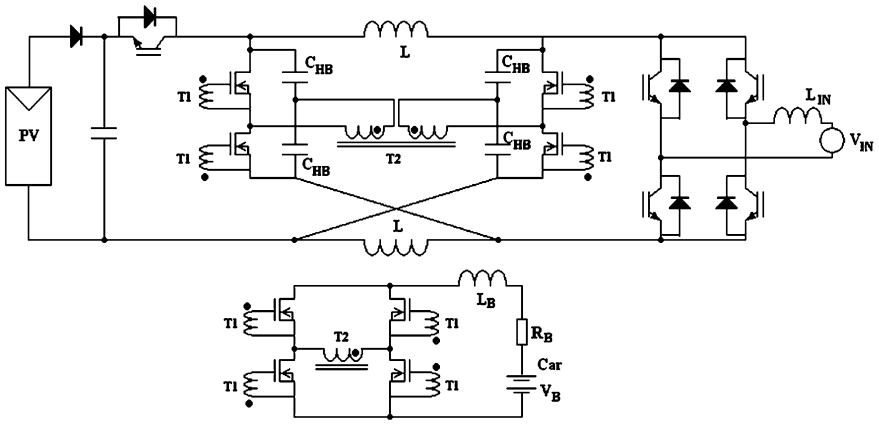

Fig. 8.7 Evolution complete detailed schematic for Z-converter including symmetrical DC–DC isolating converter

Despite the high number of MOSFETs, a single gate drive transformer can drive all switches simultaneously. In addition, there is no need to add two separate half-bridge capacitors. In fact, because of the required CV product, the Z-circuit capacitors are of the electrolytic type, which are commonly available with a 450 V maximum rating. Hence, two series capacitors must be used, given that the overall capacitor voltage can be expected to be higher than 600 V. Therefore, besides the high number of switches, the DC/DC converter can be kept compact. The operation of the half-bridge topology is well known and will not be addressed here. Nevertheless, the transformer turns ratio needs to be calculated and the equivalent average model obtained.

8.2.2 Calculation of the Turns Ratio

It is critical that the transformer turns ratio be kept to a minimum, in order to maintain the reflected battery voltage as low as possible, allowing the use of efficient devices. However, when the battery has low voltage ($V_{B(\min)} = 275$ V), the reflected voltage must still be higher than the maximum PV voltage ($V_{PV(\max)} = 500$ V). Thus, the turns ratio from each primary to the secondary winding is calculated as, $N = \frac{V_{PV(\max)}}{2V_{B(\min)}} = \frac{10}{11}$ where the factor of 2 is generated by the half-bridge operation. A ratio of unity will be adopted here for two main reasons: first, the half-bridge, operated in soft-switching mode, does not feature a perfect 100 % voltage transfer, due to the presence of parasitics. Second, a 1:1 ratio is optimal, because it allows all three windings to be arranged in trifilar configuration in the transformer, reducing leakage inductance to a minimum. The maximum voltage on the Z-circuit capacitors can now be calculated with $V_{B(\max)} = 400$ V and N = 1. Hence, $Vc_{(\max)} = 2N \cdot V_{B(\max)} = 800$ V. Thus, 900 V MOSFETs must be used in the primary circuit, while 500 V MOSFETs can be used in the secondary.

8.2.3 Derivation of the Equivalent Average Circuit of the DC/DC Converter

Each primary of the transformer can be simplified, as shown in Fig. 8.8. The average transformer current over one cycle can be considered zero, while the average current into the MOSFETs is ¼ I_{LB} (50 %, due to the parallel primaries sharing current, and another 50 %, due to the duty cycle). The average rectified secondary voltage is 50 % of V_C. Hence, the derived average model is straightforward, and is shown in Fig. 8.9.

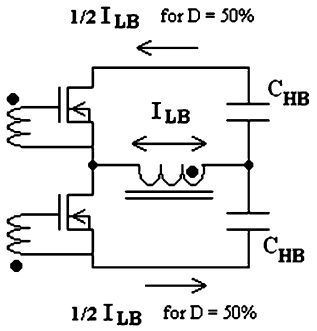

Fig. 8.8 Primary circuit for DC–DC section

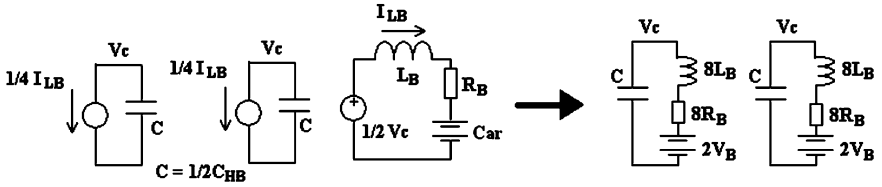

Fig. 8.9 Derivation of the average model for the DC–DC converter

Thus, the DC/DC converter and battery load can simply be modeled as a parallel branch on the Z-circuit capacitors, as shown in Fig. 8.9. Appendix A provides a detailed derivation of the equivalent battery circuit model.

8.2.4 Design of the Z-Circuit: Capacitor

The Z-circuit includes two capacitors and two inductors. The main function of the capacitors is to store and release reactive energy from and to the grid, when the EV battery is not connected. In this case, the PV cannot provide the sinusoidally pulsating power, leaving this task to the capacitors, since the inductors do not store appreciable energy. The voltage ripple at line frequency must be kept low, in order to reduce voltage stresses and allow proper operation of the inverter. A peak–peak ripple of 10 % is common for electrolytic capacitors at line frequency and will be adopted for the design. In order to calculate the ripple, it is necessary to determine the maximum levels of power flow in and out of the grid. The PV resource will provide a maximum of 5 kW. Thus, the inverter should be designed to allow this power to access the line. For optimal sizing of the inverter semiconductor devices, this should also be the amount of power that can be drawn from the line, so that a maximum of 10 kW can be used to charge the battery, if both the grid and the PV resource make their maximum contribution. From these considerations:

$Pg(t) = P_{PV}[1 + \sin(2\omega t)]$ and $Pc(t) = \frac{P_{PV}}{2}\sin(2\omega t)$ where the factor of 2 is added given that there are two capacitors in the Z-circuit.

$Pc(t) = Vc(t) \cdot i_C(t) = Vc(t) \cdot \frac{dVc(t)}{dt} C = \frac{P_{PV}}{2}\sin(2\omega t)$; hence:

$$\int_{\text{Vlow}}^{\text{Vhigh}} Vc(t)dVc = \frac{P_{PV}}{2C}\int_{0}^{\frac{\pi}{2\omega}} \sin(2\omega t)dt$$

or

$$\frac{1}{2}Vc^2\Big|_{\text{Vlow}}^{\text{Vhigh}} = -\frac{P_{PV}}{4C\omega}\cos(2\omega t)\Big|_{0}^{\frac{\pi}{2\omega}} = \frac{1}{2}(\text{Vhigh} - \text{Vlow}) \cdot (\text{Vhigh} + \text{Vlow}) = \frac{P_{PV}}{2C\omega}$$

(Vhigh − Vlow) is the peak–peak capacitor ripple voltage ΔV_C, while ½ (Vhigh + Vlow) is the DC component of the capacitor voltage V_C.

Hence: $\Delta Vc = \frac{P_{PV}}{2Vc \cdot C\omega}$ (the worst case) occurs when the DC component Vc is minimum. However, the capacitor voltage is regulated at 550 V, and therefore, the target ΔV_C is 55 V. With $P_{PV} = 5$ kW and ω= 377 rad/sec, a ΔVc of 55 V necessitates a minimum capacitor C = 220 μF. Considering tolerances and margins, a nominal value of 470 μF is reasonable. The capacitor current will be $Ic = \Delta Vc \cdot \omega C$, which computes to Ic = 4.54 A peak. Note that the value for calculated I_C does not include switching frequency ripple from the inductors in the Z-circuit. Rather, this includes only the line-frequency component. The voltage rating for the capacitor is determined by considering a connected EV battery, with maximum rated voltage of 400 V.

8.2.5 Design of the Z-Circuit: Inductor

The high frequency ripple current is generated during the shoot-though switching interval, when the full capacitor voltage is impressed on the inductors. The maximum ripple current is thus obtained for the widest shoot-through duty cycle, D_o, and maximum value of V_C. Maximum duty cycle, D_o, is obtained for minimum $V_{PV} = 360$ V. From (8.2):

$$Do_{(\text{MAX})} = \left(\frac{Vc_{(\max)} - V_{PV(\min)}}{2Vc_{(\max)} - V_{PV(\min)}}\right) = \left(\frac{800\ V - 360\ V}{1600\ V - 360\ V}\right) = 0.355$$

The limit on the switching ripple current on inductor L represents a somewhat flexible design choice, as the ripple is absorbed within the Z-circuit, and has only a moderate effect on the output quantities. Furthermore, the issue of DCM avoidance is managed by the use of the bidirectional switch in place of the diode. Possible limits on the ripple are current capability of the Z-circuit capacitors, the saturation level of the magnetic material used for the inductors, and additional conduction

loss in the semiconductor devices. However, a small L is preferable, in order to reduce the quality factor, Q, of the Z-circuit, for easier loop compensation. Therefore, an RMS current of 5 A is a reasonable choice, based on typical performance of high-voltage electrolytic capacitors. This corresponds to $\Delta I_L = 17.3$ A for triangular wave-shapes.

The maximum ripple is: $\Delta I_L = \frac{Do_{(\max)} \cdot Vc_{(\max)}}{F_{SW} \cdot L}$. Hence: $L = 650$ μH.

8.2.6 AC Analysis of the Z-converter

The Z-converter must be well understood in its AC behavior, in order to justify the choice of the power components, especially the inductors and capacitors. Moreover, in this application, the converter will have different operating regimes, corresponding to 3 distinct cases (PV to Grid with battery, PV to Grid no battery, and Grid to/from battery).

As will be seen, the full control system consists of as many as 4 control loops: these are the input current control loop, the MPPT PV current control loop, the I_B or V_C control loop (depending on the presence or absence of the battery), and, optionally, the current ripple reduction control loop. The analysis of all these loops is complicated by the fact that this is a MIMO system with two coupled control variables D and Do and two controlled outputs (grid current I_{IN} and charge battery current I_B or capacitor voltage V_C). Reference [4] provides useful insights on how the dual-modulated Z-converter can be decoupled, using nonlinear feedback schemes, that would likely require sophisticated application of DSP methods. Given that the objectives of this thesis are mainly geared toward an appreciation of the power topologies rather than the control mechanisms, a more traditional strategy, involving a number of iterations, is adopted. The small-signal model is studied and the first control loop is compensated, assuming single modulation of D, with D_o kept constant. The second loop is then compensated, with the first closed loop in place, and so on. With all compensated loops in place, coupled transfer functions can be optimized by iteration. Thus, in order to obtain a working model for simulation, analysis, and comparison, SISO techniques can still be employed rather than more involved methods, such as LQR or nonlinear feedback decoupling.

As mentioned earlier in 8.1.3.2, the control scheme can be made to direct the ripple current into the EV battery (Scheme 1) or into the PV source (Scheme 2). The former is more complex, and hence, its derivation will be demonstrated in more detail below. However, the latter will also be designed and simulated for verification.

8.2.7 Comments

Having fully modeled the Z-converter for this application, its performance will be evaluated in the Chap. 9. Some comments of a more qualitative nature can be introduced here.

8.2.8 Cost

The Z-topology allows distributing PV power to the grid as well as to the EV battery with a single stage of conversion. One of the hopeful consequences of this premise is a reduction in cost. Table 8.1 is a list of cost factors that are relevant for the Z-converter.

It appears that the cost balance may or may not be a positive one. The presence of the line-frequency transformer and larger enclosure weighs heavily on the negative side. However, this transformer may be required because of other criteria. For instance, the transformer-less topology is far from being universally accepted by safety agencies around the world. Utility companies may also rather see a galvanic barrier, prior to the interface point, in order to ensure both isolation and guaranteed elimination of DC current injection into the grid. In these cases, the Z-converter is certainly cost competitive.

8.2.9 Reliability

Voltage levels on the IGBTs and Z-circuit capacitors are relatively high. However, when appropriate ratings are used, the reliability of this topology is intrinsically very good, due to low component count. The presence of the 60 Hz transformer does not affect it in an appreciable manner, and there exist only four 450 V (standard availability) small value electrolytic capacitors, that are commercially available in various reliability and life ratings. This fact is possible due to the

Table 8.1 Cost factors for Z-converter

Cost reduction	Cost addition
Light cabling from PV (due to high PV voltage supported)	5 kVA 60 Hz isolation transformer
Relatively low power component count	High-voltage power capacitors
Simple drive method for DC/DC converter	High-voltage power semiconductors
Simple 1:1 isolation transformer for DC/DC converter	Large enclosure/sheet metal
Open loop operation of DC/DC converter (no isolated sensors)	Added protection circuits

introduction of the added ripple attenuating control described above, for allowing a design with very little capacitance across the PV source (Scheme 1)—large capacitors being otherwise necessary (Scheme 2) [8]. Worst-case voltage on the capacitors is 400 V (for maximum battery voltage of 400 V), while that on the IGBT, is 1,240 V, excluding any parasitic transients (with maximum V_B at 400 V and min V_{PV} at 360 V). Higher voltage devices are both more expensive as well as less performing than lower voltage ones; however, they do allow more design trade-offs.

Note that Fig. 8.7 shows the presence of 13 switches. Although this number is high, it can be reduced down to 9 by employing alternate common topologies for the DC/DC converter. On the other hand, the chosen topology for the DC/DC converter portion can be realized using high reliability, low-voltage/low-current devices. Because the converter runs in open loop, the driver is simple, and the control is devoid of isolation/sensing devices.

8.2.10 Dynamic Behavior, Interaction with PV Source, Interaction with Grid

It is evident that the control of the Z-converter is extremely complicated, due to the unavoidable relationship between the two control variables, D and D_o, and the fact that the energy storage components are present within the control equations. Also, the impossibility of effectively decoupling the power flow into the battery and the PV source from that of the Z-capacitor implies that the 120 Hz power ripple must be absorbed by either the battery or the PV source. For Scheme 1, this is achieved by decreasing the bandwidth of the charge current control system, with consequent slow response to external stimuli from the PV source and input line voltage. The PV source voltage itself changes rather slowly in response to irradiation level shifts and speed of the MPPT algorithm [9], thus causing only minor problems. A sudden change in the I_B request signal, however, is problematic for Scheme 1, and must be avoided externally. As such, changes cannot be easily handled using linear control. Should this become a critical issue, Scheme 2 can always be implemented, as it supports much quicker dynamics.

8.2.11 Design Flexibility

Another obvious shortcoming, originating from the close coupling of the battery to Z-circuit, and the use of linear control (compared to robust techniques, such as Sliding Mode Control), is the fact that the charge limiting resistance, R_B, becomes a nonnegotiable part of the control loop. It becomes impossible to optimize the loop response prior to knowing this resistance value. Unfortunately, different

battery technologies and even different states of charge have different characteristic resistances that would require different optimal compensations. In addition, the nominal battery voltage is also limited by the absence of a fully regulated DC/DC converter. Therefore, connection to a severely discharged battery, for instance, is not supported by this topology.

8.3 Novel Integrated DC/AC/DC Converter for EV/PHEV Charging

8.4 High Frequency Transformer-Based Isolated Charger Topology

8.4.1 Background

In specific cases, where a large 5 kVA, 60 Hz transformer is unacceptable, various topologies that retain galvanic isolation from grid to panels can be used. These are described in Refs. [1, 10]. A fair assessment, based on these references, is that there is no clear option among the competing topologies; rather, different approaches satisfy different design priorities. On the other hand, because the PV-powered charge infrastructure is not a straightforward grid-tied system, like those described in [1, 10], which include an added DC/DC charger, many of the proposed circuits are not easily exploitable. The otherwise attractive *pseudo-DC-link* topologies are an example, as are topologies using output current-fed inverters. Among those approaches that use a HF transformer for isolation, the benchmark is provided by the classic two-stage topology with DC-link, shown in Fig. 8.10.

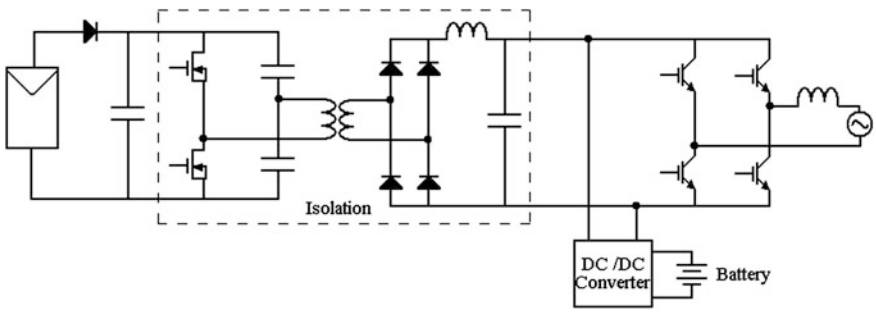

Fig. 8.10 HF transformer-isolated topology

For comparison purposes, this topology will be studied in the following chapters. The lengthy AC and dynamic response analysis for the inverter and DC/DC converter will not be included here, given that these are common topologies that have been treated at length in related literature.

8.4.2 Isolation and DC-Link

The main purpose of the isolation section shown in Fig. 8.10 is, of course, to offer isolation from the grid to the PV. Such an arrangement can also provide supplementary functions. For instance the half-bridge could be replaced by a regulated buck-boost converter stage. In this case, the DC-link voltage could be made to track the EV battery voltage and minimize switching losses in the DC/DC converter, while the buck-boost stage provides added flexibility, to deal with wider voltage ranges out of the PV panel. This can be implemented with few minor added costs, in terms of component stress and overall efficiency, which might be offset by the need to satisfy design requirements. In the case of this thesis, the requirements have been set, and can be satisfied by the isolated buck topology of Fig. 8.10, running in open loop at full duty cycle for ZVS and maximum efficiency. Due to ZVS, a very high frequency can be selected when MOSFETs are used, so that the filter components in the DC link can be minimized in size and cost.

8.5 Component Design

8.5.1 Isolation Transformer Turns Ratio Calculation

The steady-state voltage gain from the output of the PV source to the input of the inverter bridge is simply ½ N, where N is the turns ratio of the transformer. Because the voltage-source inverter (VSI) bridge can only buck, the defining condition is with minimum $V_{PV} = 360$ V and maximum $V_{\mathrm{IN}} = 370$ Vpk. A turns ratio of 3/7 will provide a minimum DC-link voltage of 420 V, corresponding to an overhead of 14 %, for dynamic control. The maximum DC-link voltage will be 580 V, allowing the use of efficient IGBT devices.

8.5.2 DC-Link Filter

The DC-link filter inductor can be considered a simple smoothing choke of very small value. This is due to the full duty cycle on the half-bridge. The capacitor, on

the other hand, will be sized to handle the pulsating power from the grid, and will therefore be as large as the combined size of the Z-circuit capacitors discussed earlier.

8.5.3 Inverter Bridge and DC/DC Converter Power Devices

As the DC bus voltage is limited to less than 600 V, very fast and efficient IGBTs as well as diodes can be used for the inverter bridge and the DC/DC converter. The architecture of the DC/DC converter is shown in Fig. 8.11. The arrangement is similar to that of the Z-converter, with the DC-link capacitor split, in order to accommodate a half-bridge converter. The main difference is that this converter has a full loop controlling duty cycle. Therefore, the smoothing choke will be relatively large and can be expected to detract from the efficiency number. A turns ratio for T2 of 1:2 will guarantee that a 400 V battery can be charged, when V_{PV} is minimum, at 360 V. The inductance L_B is calculated so as to provide $\pm$10 % ripple under worst-case; that is, when V_{PV} is maximum, at 500 V, and battery voltage is minimum, at 275 V. Calculation of the required inductance value is straightforward and yields 800 μH, at 50 kHz switching frequency.

This inductance can be less lossy than that of the Z-circuit, because it need not supply damping. An ESR of 0.03 Ω is chosen (or 50 % that of the Z-circuit combination).

8.6 Comments

8.6.1 Cost

Compared with the Z-converter, this topology replaces an expensive 60 Hz transformer with a small HF transformer. Considering that the primary winding is driven in ZVS, the frequency in question could be extremely high, thus virtually

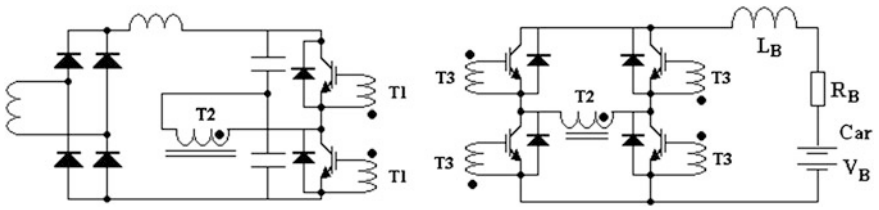

Fig. 8.11 DC/DC converter

eliminating the cost due to the isolating function. Additionally, the ensuing reduction in size should result in savings related to sheet metal.

Although this topology only has one large choke, L_B, in Fig. 8.11, it carries more current and has higher value than each of the Z-circuit inductors. Overall, the I^2L value is similar (compared to two 15 A, in 650 μH, to a single 18.5 A in 800 μH). A similar conclusion can be made for the Z-circuit capacitors, when compared to the DC-link capacitors for this topology. In both cases, they must be sized to deal with the same pulsed power from the grid.

Because of the double conversion stage and the AC/DC/AC/DC structure, this topology has high semiconductor content. Compared to the Z-converter, it includes an additional fast-diode full-bridge rectifier, and 5 IGBTs, accompanied by fast freewheeling diodes (note: all MOSFETs operating in ZVS are not considered here). Moreover, an extra control and drive circuit is needed for the additional conversion stage (see the comparison matrix below).

Considering the absence of the power transformer and, to a lesser extent the lighter sheet metal, cost should be much reduced compared to the Z-converter topology.

8.6.2 Reliability

Although the semiconductor component count is problematic, their electrical stress can be managed well, as all currents and voltages are precisely defined. This is not the case for the Z-converter, where the voltage stress on the bridge components, for instance, is strongly dependent on the operating point. A simple way of describing this is that this topology is inherently less reliable than the Z-converter. However, it can be easily upgraded by choosing better performing components. Considering that the cost is expected to be relatively lower, this may be quite acceptable in most cases.

8.6.3 Dynamic Behavior, Interaction with PV Source, Interaction with Grid

Because the battery charge current is controlled independently from the line current, dynamic behavior for this topology can be expected to be better than that of the Z-converter. Specifically, the EV battery current command can change rapidly and can be followed by a fast control. It is not clear how important this feature might be in practical terms, although it definitely provides an added degree of flexibility, when interfacing to the vehicle on-board controller. Moreover, the added conversion stage completely removes the AC component from the battery charge current.

As is the case for the Z-converter, interaction with the line presents no major problems. However, since the isolation transformer is placed prior to the inverting bridge, this topology is capable of injecting a DC current component into the line. Given the strict IEC and IEEE requirements for DC current injection, resolving this problem will necessitate a more sophisticated current sensor and very high-accuracy and low-drift components and circuits [11]. Periodic calibration may also be required, challenging one of the design goals established in Sect. 5.1.

8.6.4 Design Flexibility

This design comprises of two independently controlled power stages, including two isolation transformers that can be utilized to step-up or step-down critical voltages. As such, this configuration is extremely flexible, and can adapt itself to wide-range input/output requirements.

8.7 Transformer-Less Charger Topology

8.7.1 Background

The topologies described in the previous two sections use a power transformer to achieve two critical operational goals. The first is isolation and the second is to provide voltage amplification, in order to optimize power transfer and electrical stress levels; the former is a safety requirement, while the latter is a design requirement. However, it is practical to assume that the PV source, the grid, and the battery may all be available in voltage ranges that are already close-to-optimal, without the need for intervening amplification. Furthermore, if safety agencies allow the use of non-isolated inverters from PV source to grid, then the transformer-less topology becomes extremely attractive. The DC/AC/DC/AC configuration, described in Sect. 5.4, can then be reduced to a mere DC/AC.

Safety regulations in Europe have historically been lenient compared to North American standards, whereby PV panels may not be grounded as long as the switching topology guarantees small common mode voltages, thus reducing dangerous leakage currents. The additional problem of a safety hazard, following an insulation breakdown, is dealt with by using Ground Fault Interrupter devices. Many of the known transformer-less topologies, however, also allows direct grounding of the panels. This is the case for the topology selected in this study. Consider the simple buck topology shown in Fig. 8.12 (left).

During the positive half of the cycle, Q2 is off and Q4 on at all times. Then Q1 and Q3 switch complementarily, in a classic buck configuration. This topology has only 4 devices and drives the grid current in a unipolar fashion, for low harmonic

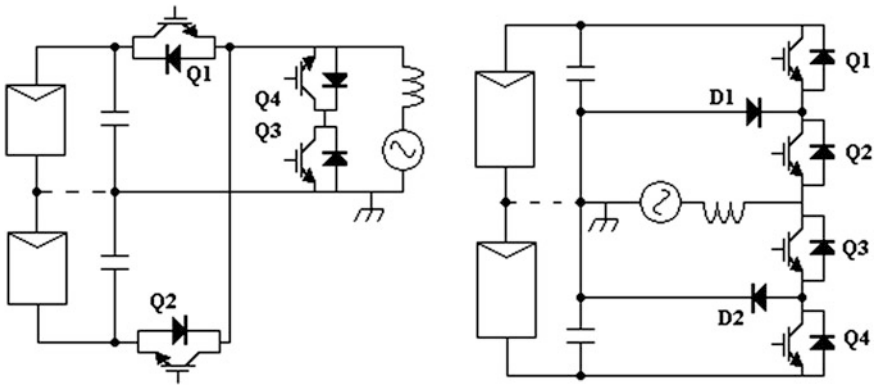

Fig. 8.12 Transformer-less topology (*left*); Neutral Point Clamped topology (*right*)

content and high efficiency. The only major drawback is that Q1 and Q2 must be rated at twice the maximum PV voltage. Thus, while Q3 and Q4 can be high efficiency, 600 V IGBTs, Q1, Q2 must be 1,200 V devices.

The Neutral Point Clamped (NPC) topology, shown in Fig. 5.28 (right), has increased conduction loss, because grid current is always driven through two series-connected semiconductor switches. In fact, during the positive half-cycle, Q2 is on and Q4 off at all times, while control is exercised by Q1 and freewheeling diode, D1. On the other hand, with the NPC, all devices can be rated at 600 V. Thus, the choice between the topologies shown in Fig. 5.28 is strongly affected by whether conduction or switching loss is dominant. Moreover, it is important to consider that both topologies may have to be modified, in order to allow bidirectional flow from the grid. In this respect, the NPC is at a disadvantage.

Both topologies presented in Fig. 8.12 would benefit from the PV panels being completely floating, without the connection shown as a dashed line. This is because both strings would deliver at the same time, at all times. By introducing a connection, each string tends to deliver the peak power during only half of the cycle. This is remedied, not without difficulty, by adding the large decoupling capacitors shown. Note that the panels should be left floating, the common mode voltage would be very small, so that the configuration could, in theory, pass safety requirements for leakage current. Unfortunately, only 600 V of ungrounded voltage is presently allowed, without incurring much higher costs, due to extra safety precautions. The ground connection, splitting the panels, is therefore non-negotiable. Because of its simplicity and lower conduction loss, the topology on the left, in Fig. 8.12, is adopted here, for comparative analysis.

Because of the lack of an intervening transformer between the PV source and the grid, voltage amplification cannot be performed. This imposes considerable restrictions on the value of operational input and output voltage ranges. When V_{PV} is at its minimum, at 360 V, the grid voltage cannot exceed 250 V (RMS). Considering semiconductor voltage drops and allowing for 10 % dynamic range for

the controlling duty cycle, the design is not feasible for the requirements expressed originally for this comparative study. Either the variability of the PV voltage is in some way narrowed, or the grid voltage must be nominally set to 220 V AC, instead of 220–240 V AC. The latter option is adopted here.

8.7.2 Component Design

The obvious presence of the split power source suggests, once again, the use of the half-bridge topology. In this case, however, high-voltage IGBTs must be used on the primary side. The DC/DC converter structure would then be as shown in Fig. 8.13.

A turns ratio for T2 of 4/5 will guarantee that a 400 V battery can be charged when V_{PV} is minimum, at 360 V. The inductance L_B is calculated so as to provide $\pm$10 % ripple under worst-case; that is, when V_{PV} is maximum, at 500 V, and battery voltage is minimum, at 275 V. Calculation of the required inductance value is straightforward and yields 1.7 mH, at 25 kHz switching frequency. Note that a lower switching frequency has been selected here, compared to the previous topology, because the primary switching devices are less-efficient, high-voltage IGBTs.

8.8 Comments

8.8.1 Cost

The cost structure for this transformer-less topology proves to be extremely good. The absence of a 60 Hz transformer as well as an isolation stage is the obvious strong point. These exists only a slightly offset due to the need for accurate sensing

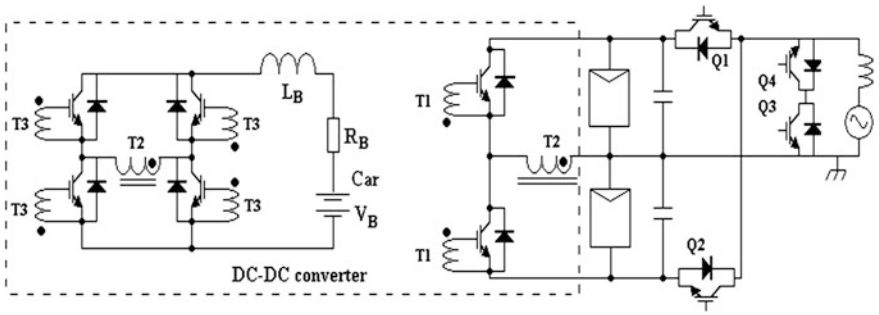

Fig. 8.13 Transformer-less topology showing DC/DC converter

and processing of control variables, in order to maintain DC current injection within acceptable limits, although some simple transformer-less topologies have been presented in [12] that deal with this problem topologically, rather than through control. Marginally higher costs may further need to be incurred due to the relatively large battery charge inductors (twice as large, compared to the previous topology). Finally, it must be noted that the split PV supply may require additional cost, for current sensing within the MPPT device. The expanded version of the cost matrix of Table 8.2 is depicted in the form of Table 8.3.

8.8.2 Reliability

The transformer-less topology, like the Z-converter, has a low part count and, like the HF-isolated topology, has well-controlled stress levels for all devices. Hence, due to these important advantages, the Z-converter depicts superior reliability.

Table 8.2 Cost comparison HT transformer versus Z-converter topologies

Component	Z-converter (LF transformer isolated)	HF transformer isolated
PV cabling	Good	Good
Transformers	Good	Better
Chokes	Good	Good
Capacitors	Good	Good
IGBTs	Good	Poor
Diodes	Good	Poor
Drivers	Good	Poor
Sheet metal	Good	Better
Overall	Good	Better

Table 8.3 Cost comparison HT transformer versus Transformer-less versus Z-converter

Component	Z-converter (LF transformer isolated)	HF transformer isolated	Transformer-less
PV cabling	Good	Good	Good
Transformers	Good	Better	Best
Chokes	Good	Good	Poor
Capacitors	Good	Good	Good
IGBTs	Good	Poor	Good
Diodes	Good	Poor	Good
Drivers	Good	Poor	Poor
Sheet metal	Good	Better	Better
Overall	Good	Better	Best

8.8.3 Dynamic Behavior, Interaction with PV Source, Interaction with Grid

From the point of view of dynamic response and interaction with the grid, the transformer-less topology is undistinguishable from the HF-isolated topology, as discussed in 5.4.4.3.

8.8.4 Design Flexibility

Arguably the weakest point of the transformer-less topology is its inability to adapt itself to different input and output voltage specifications. In fact, for the design presented here, the original grid voltage specification had to be relaxed, in order to allow the use of the assigned PV voltage range.

8.9 Modeling and Simulation Results of Test System

The PSIM software was used to validate the mathematical model and the overall operation under switch-mode regime. Steady state and transient behavior are verified and efficiency is calculated based on simulation results. It is important to mention that no attempts are made to model the MPPT/PV voltage-current characteristics in detail. Rather, the PV source is represented either as a voltage source, that remains constant under current changes at the MPPT power "knee," or as a diode string fed by a constant current source. One of the main results in [9] is that the MPPT has a fundamental effect on the overall system dynamic response. Therefore, although the simulations below confirm the fully controlled behavior of the converter, actual waveforms will vary in real life applications, depending on the type of MPPT strategy used.

8.9.1 The Z-converter

In 5.3.9.3, the dynamic limitations of the Z-converter were discussed. These will be highlighted in simulations involving changes in PV current demand, battery current demand, and line voltage. However, it is important to appreciate that the SISO linear control methods used in this thesis are probably not the best in terms of dynamic performance. Rather, nonlinear feedback and variable decoupling [4] or Sliding Mode Control [13] can improve response time and robustness. Nevertheless, it is demonstrated that more traditional techniques can produce an adequate behavior for this application.

In a system that includes the battery, there exist various combinations of line, PV, and battery voltages and currents that need to be considered. It is not convenient to present simulations for all these possibilities. Instead, typical combinations of critical variables will be used, while a given variable is swept from minimum to maximum level. Thus, in the course of this study, all significant extreme combinations have been simulated successfully using PSIM (electronic model) and SiMetrix (mathematical model), which were found to exhibit good matching.

Note that a specific line-frequency isolation transformer turns ratio was used in the simulations. This ratio must be as high as possible, in order to maximize duty cycle D for improved power transfer. Simply contrasting the minimum input voltage to the inverter bridge ($2Vc_{(\min)} - V_{PV(\max)} = 1{,}100–500\ \text{V} = 600\ \text{V}$) to the maximum peak of the line voltage (375 V), and adding 20 % margin for dynamic control of the duty cycle D, immediately yields an optimal turns ratio of 4/3. This is, in fact, the ratio used in all simulations related to the Z-converter, unless otherwise specified.

8.9.2 System Without Battery (Scheme 1)

Figure 8.14 shows the simulated response to a 40 % step in input voltage, with 2 different PV voltages, at maximum power generation of 5 kW. Note good regulation of V_C. The ripple current drawn from the PV source is approximately 15 % of the DC level.

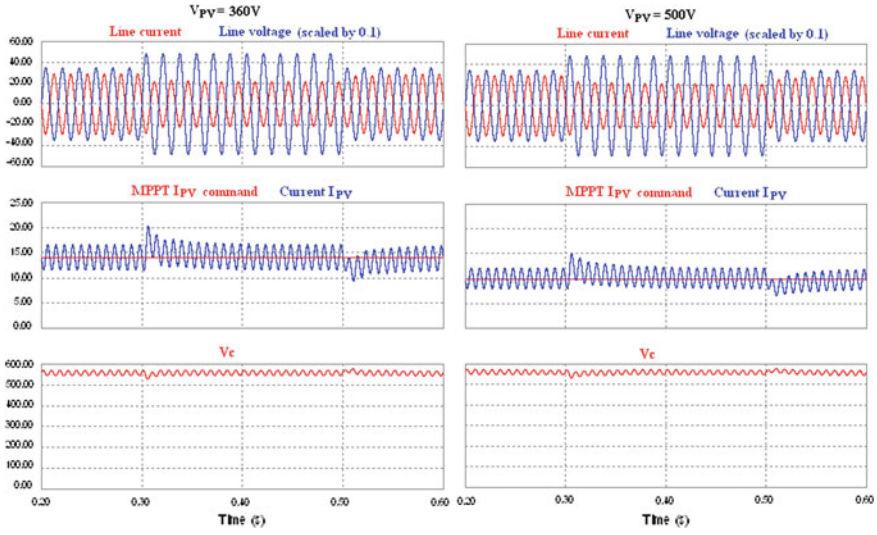

Fig. 8.14 System with no battery; response to 40 % step of input line voltage

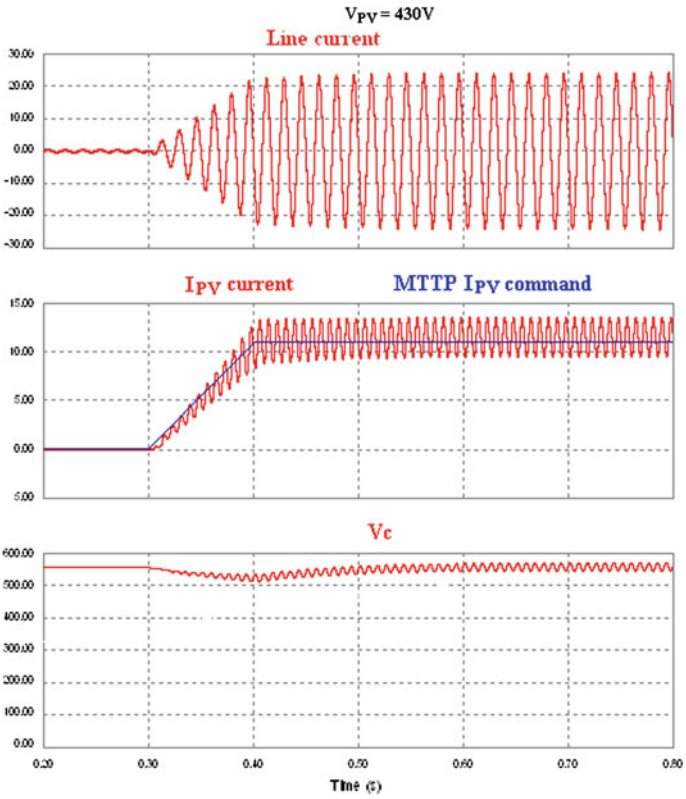

Fig. 8.15 System with no battery; response to 100 % step of MPP I_{PV} command (100 ms transition)

The ripple current can be further reduced by increasing the gain of the ripple cancelation amplifier, at the expense of low frequency harmonic distortion of the input current. Figure 8.15 shows the response to a 100 ms transition of the PV power output. The result is acceptable, considering that 100 ms is reasonably fast for an MPPT, tracking changes in irradiation.

8.9.3 System with Battery (Scheme 1)

Figure 8.16 shows the response of the input current, PV current, and battery charge current to a 100 % variation in MPPT current demand, in 100 ms. The battery demand is kept constant at 2.5 kW, so that at the beginning of the transition, the grid delivers power to the battery, and at the end of the transition, it absorbs power from the PV. This is clear from the phase reversal of the input current.

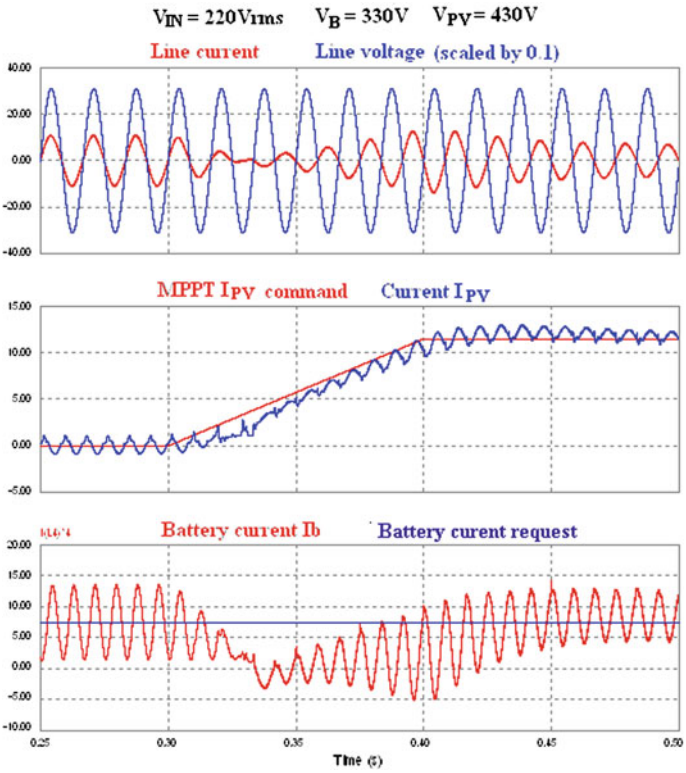

Fig. 8.16 System with battery; response to 100 % step of MPPT I_{PV} command (100 msec transition)

Note that the battery charge current is disturbed for approximately a mere 50 ms. Figure 8.17 shows the typical behavior, following a 40 % step in input voltage. The fast response of the input current loop produces predictably good results.

Finally Fig. 8.18 shows the response to a 1 Amp/sec change in battery charge current demand. Again, in this case, the grid changes from absorbing to supplying power. Note that the battery current cannot follow the changing demand voltage during the transition, due to the suppressed gain of the error amplifier. However, the current is still maintained at a safe level. In addition, Fig. 8.18 also depicts the same simulation run on SiMetrix, which strictly represents the average (mathematical) model. The match between the two simulations is a good indication that the derived mathematical models are fundamentally correct. This is indeed the case; the very minor differences in amplitude of the 120 Hz ripple and response can be attributed to the time step limitation of the PSIM engine as well as some simplifications used in modeling the state-space equations in SiMetrix.

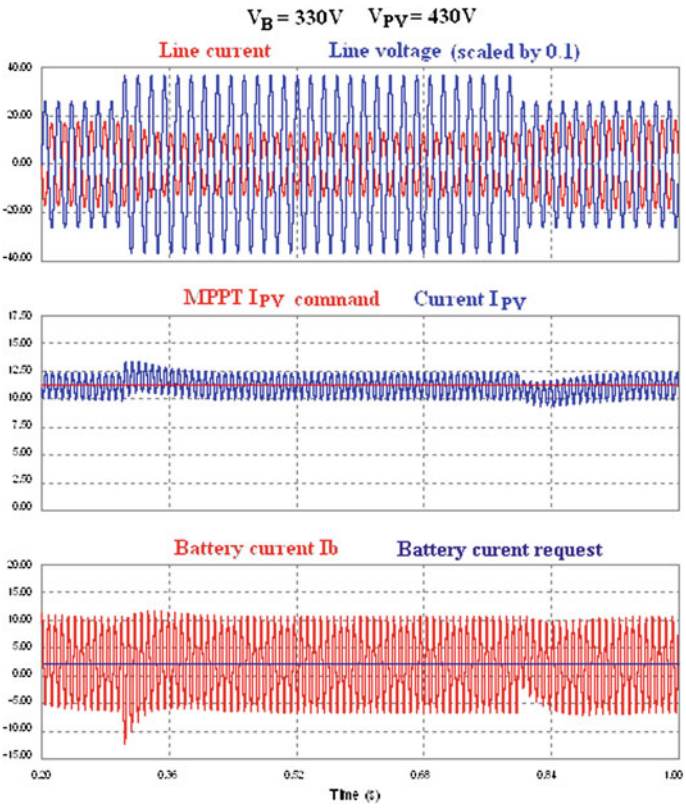

Fig. 8.17 System with battery. Response to 40 % step of input line voltage

The last simulation presented here corresponds to the atypical case, where the grid is fed by both the PV source and the battery as it discharges. In this case, battery average current will be negative. Note that the power levels are more or less accurate: the battery discharge power is 3.3 kW, and the PV power is 1.4 kW, for a total of 4.7 kW.

From Fig. 8.19, the power absorbed by the grid is found to be approximately 4.25 kW, for a conversion efficiency of 91 % (note that a factor of 1.33 must be used for the current waveform, due to action of the line transformer with its specific turns ratio).

8.9.4 System with Battery (Scheme 2)

If the design demands addition of a large capacitor at the PV terminals, in order to absorb the power ripple, the ripple cancelation circuit discussed in 5.3.8.5 could be

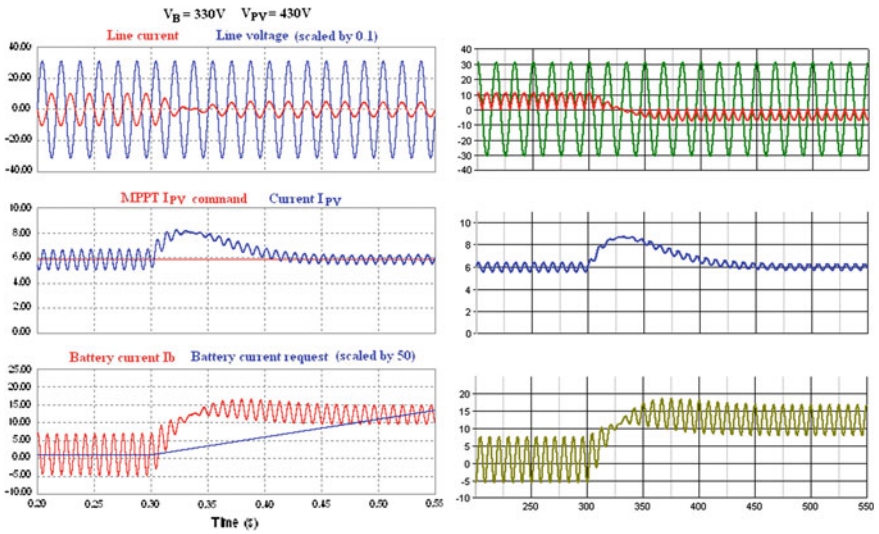

Fig. 8.18 System with battery; Response to a ramp in I_B demand; PSIM (*left*) and mathematical model set in SiMetrix (*right*)

eliminated. At the same time, the battery charge current control loop must be set to have appreciable gain at 120 Hz, in order to regulate out the ripple (5.3.8.5 and 5.3.8.9). This will redirect the ripple current from the battery to the PV; at the same time, the battery circuit becomes faster and more efficient. Using Scheme 2, Fig. 6.7 (left) becomes the counterpart of Fig. 6.3. While the line current behavior is similar, it is evident that the ripple content has been successfully transported from the battery to the PV source.

The counterpart of Fig. 8.18 for Scheme 2 is Fig. 8.20 (right). Note that the battery current command can be made to change much faster than that of Scheme 1.

8.9.5 IPV Ripple, PV Utilization Ratio, and MPPT

From the simulation results discussed above, it is safe to state that the Z-converter fulfils all general requirements stipulated at the start of this study. However, three specific outcomes are definitely less than desirable. The slow response of the battery current loop as well as the high ripple in the battery has been mentioned. The third drawback is the rather large 120 Hz ripple drawn from the panels that cannot be completely eliminated, despite the added control mechanisms, which in turn is much worse under Scheme 2. The presence of a ripple is not, in itself, a thoroughly objectionable occurrence. For instance, Ref. [14] draws on the switching ripple to perform the MPPT function. Reference [15] applies the same

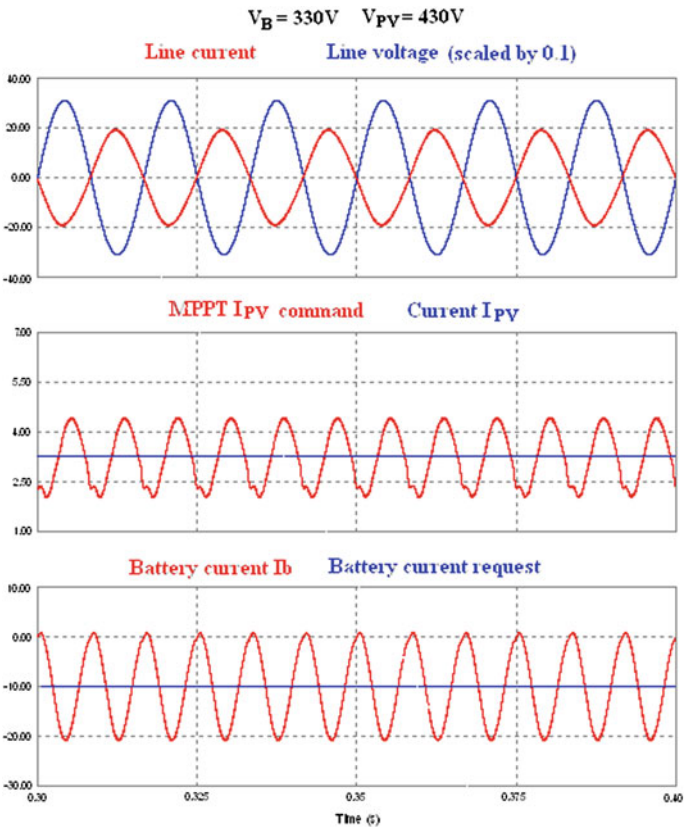

Fig. 8.19 System with battery; Battery discharges to provide grid power

principle to the 120 Hz ripple for single-phase systems—this being more applicable to this work. The problem lies in the extent of switching ripple present, especially at lower currents.

Figure 8.19, for example, shows a 30 % peak ripple. The utilization ratio, K_{PV}, is defined as the ratio of actual average power drawn from a PV source to the ideal maximum power achievable in the absence of ripple. Utilizations of more than 98 % are good. However, they can be achieved only with voltage ripples of less than about 8.5 % [16], corresponding to yet lower current ripples. Even in Scheme 1, it is well worth considering by adding a relatively small decoupling capacitor across the PV source. A 100 μF/600 V capacitor, for instance, would only have 1/30th the CV product of the Z-circuit capacitors, so that a film capacitor can be employed to maintain reliability, assuming size is not an issue.

In order to study the performance of the PV with the addition of this power decoupling capacitor (using the same example of 100 μF), a set of simulations using SiMetrix is performed, and the utilization factor is plotted and compared for

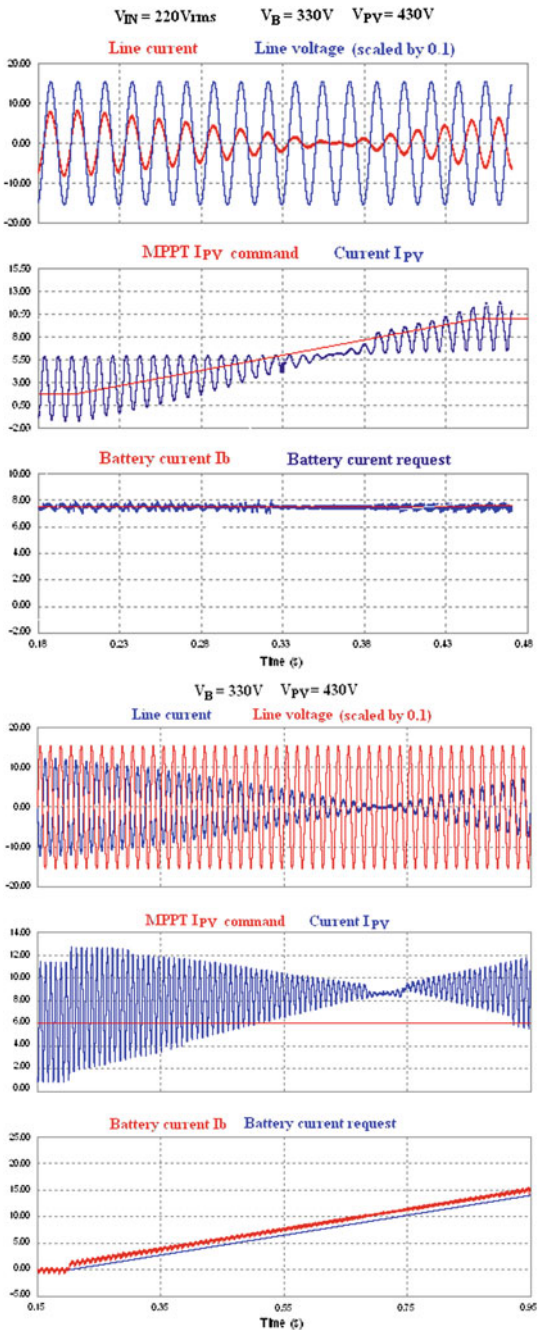

Fig. 8.20 System with battery; response to 100 % step of MPPT I_{PV} command (200 ms transition) (*left*); response to a 20 A/sec ramp in I_B demand (*right*)

different operating regimes. For this purpose, an ideal MPPT scheme is assumed, and the simulated values for I_{PV} under worst-case conditions are applied. Earlier simulation work reveals that the worst-case condition for I_{PV} ripple occurs during the atypical case of battery discharging to the grid, with maximum $V_{PV} = 500$ V. These conditions produce approximately a 1 A peak ripple for all values of I_{PV}. For the simulation, a bare-bone model of the PV panel, as shown in Fig. 6.8, is used, where the model diodes are of general purpose 20 A/1,000 V silicon type. Note that the absence of any series resistance will maximize ripple, representing worst-case (Fig. 8.21).

From Fig. 8.22, it is clear that unless the PV is used only with high levels of irradiance, a relatively small decoupling capacitor is necessary; even in Scheme 1.

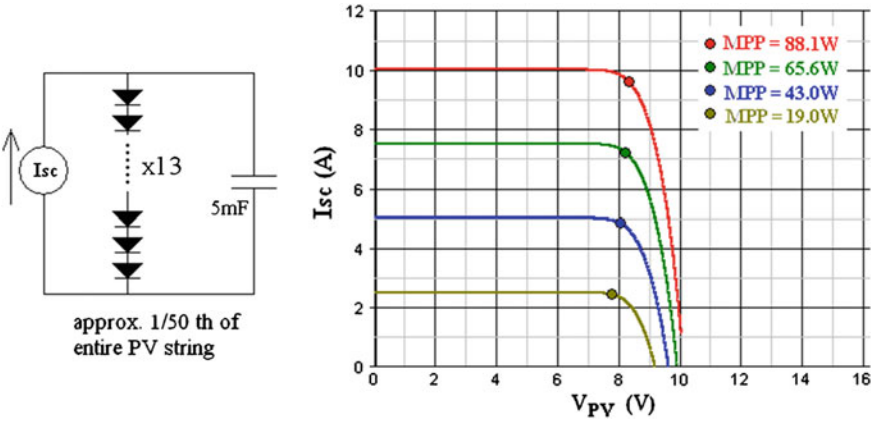

Fig. 8.21 I–V Characteristics of simulated solar panel (1/50th of entire string)

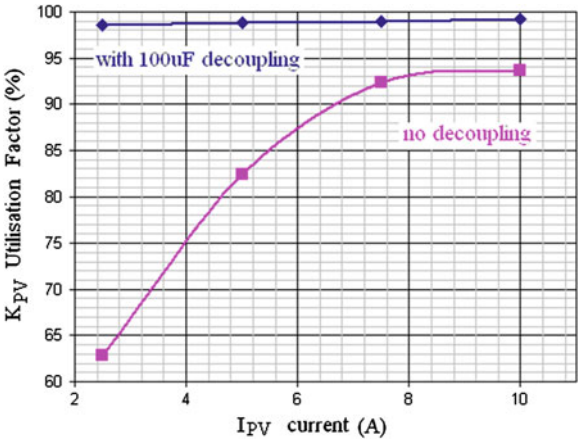

Fig. 8.22 Effect of capacitive decoupling on PV utilization factor for Scheme 1

This capacitor then, rather than being added, simply replaces the one already present that is needed for absorbing the HF switching current to the Z-circuit.

For Scheme 2, the ripple into the PV source is much higher than that discussed above. The worst case obviously occurs when the battery receives the full 5 kW from the grid, with a minimum PV voltage of 360 V. Thus, $I_{PV} = \frac{P_G}{V_{PV}} \sin(2\omega t)$, where P_G is the grid power (5 kW). The peak ripple is then found to be 13.9 A. Simulations with SiMetrix, using this current and the same model shown in Fig. 8.21, indicate that a 1 mF capacitor is needed to keep the voltage ripple below approximately 5 % peak, thus providing a utilization factor higher than 98 %. This capacitor must be rated at 500 V; the CV product is then higher than that of each of the Z-circuit capacitors.

8.9.6 Power Loss (Efficiency)

Power loss within the converter will be calculated using Scheme 1 for reference and by considering the following loss contributors:

(a) IGBTs (conduction and switching)
(b) IGBT body diodes
(c) Magnetics (conduction loss)

The results from the simulations will be used to describe all relevant RMS currents for the magnetic conduction losses, average currents for diodes, and IGBT conduction losses, as well as instantaneous currents and voltages for switching losses. Core loss for the inductors can be set arbitrarily small, if size concerns are less important, especially if many turns are needed to achieve the ESRs for better damping of the Z-circuit; they will not be considered here. For comparison purposes with other topologies, common commercially available semiconductor devices with equivalent chip-size will be chosen *ad hoc* for each topology. In the case of the Z-converter, the chosen IGBT will be IRG4PH50U. The relevant parameters from the datasheets are: IRG4PH50U: On-state = 3 V @20 A, E_{on} = 160 uJ @1,200 V, E_{off} = 1.8 mJ @1,200 V, 20 A.

As a first degree of approximation in the power loss calculations, the on-state voltages for the IGBTs and diodes will be kept constant at all currents. As such, PSIM can directly estimate all conduction losses. Unfortunately, this is not the case for switching losses. They will be calculated indirectly, by assuming that the switch-on loss energy, E_{on}, increases with the square of the switching voltage for IGBTs. Conversely, the switch-off energy for the IGBTs, E_{off}, is assumed to increase linearly with switching voltage and current. With this postulation, PSIM can calculate switching losses, starting with the instantaneous peak currents and voltages, by applying the formulae 6.1 and 6.2.

$$Psw_{\mathrm{ON}} = \frac{2f_G f_{SW} E\mathrm{on}}{V_R^2} \int_0^{\frac{1}{2F_G}} V(t)_{pk}^2 dt \tag{8.4}$$

$$Psw_{\mathrm{OFF}} = \frac{2f_G f_{SW} E\mathrm{off}}{V_R I_R} \int_0^{\frac{1}{2F_G}} V(t)_{pk} I(t)_{pk} dt \tag{8.5}$$

Here, $V(t)_{pk}$ and $I(t)_{pk}$ are the instantaneous switch voltage and current, f_G is the grid frequency, f_{SW} is the switching frequency, while V_R and I_R are the rated voltage and current. E_{on} is the switch-on loss, calculated at V_R, and E_{off} is the switch-off loss, calculated at V_R and I_R.

Before continuing with the power loss estimation, it is worth highlighting the switching sequence in the inverter bridge. In fact, switching losses can be minimized when a proper sequence is chosen, even without resorting to more sophisticated circuitry [8]. This can be done with no compromise on the harmonic distortion, by keeping the active state centrally placed within the cycle [17]. Also, given the shoot-through states that are responsible for the HF ripple on the Z-circuit inductors, they can be split evenly on either side of the active states, effectively doubling their frequency. Finally, as is usually preferable, only one of the four devices should need commutation, to obtain a state transition. The sequence shown in Fig. 8.23 possesses all the requirements, and is relatively simple to implement using analog carrier-based methods.

The most immediate result from Fig. 8.23 that affects power loss calculation is the fact that only one turn-on and one turn-off transition exists per switch and per switching period, even though these are "hard switching" transitions. The above statement is true for both line half-cycles. The manner in which the losses are estimated with PSIM will be demonstrated below in detail, for the input bridge. This procedure will then be repeated for all other devices; only the final results will be reported hereafter. Figure 8.24 shows the pertinent waveforms for one of the bridge IGBTs. The operation considers no battery, and 5 kW generated power.

The second graph (from top) of Fig. 8.24 is simply the running average of the conduction loss. It will converge to the average value of 24 W. The third graph (from top) is used to calculate the turn-on loss; its increase over a ½ cycle represents the definite integral in Eq. 6.1; in this case, it has a value of 6,600 V^2sec. Thus, the result of Eq. 6.1 can simply be estimated as 2.20 W. The same idea is used to compute turn-off losses, using the fourth graph (from top) and Eq. 6.2. The red trace is used over the ½ cycle when the IGBT current is positive and the blue trace over the ½ cycle when the antiparallel diode conducts. The result is a total turn-off loss of 27.1 W. The overall loss for a bridge IGBT is 53.3 W. As there are 4 IGBTs, these losses already amount to about 4 % in efficiency loss.

Continuing with the loss evaluation, the DC blocking IGBT was found to dissipate a total of 17.1 W, which is less than that for bridge IGBTs, because of zero-current turn-off. The MOSFETs used for the DC/DC converter do not really

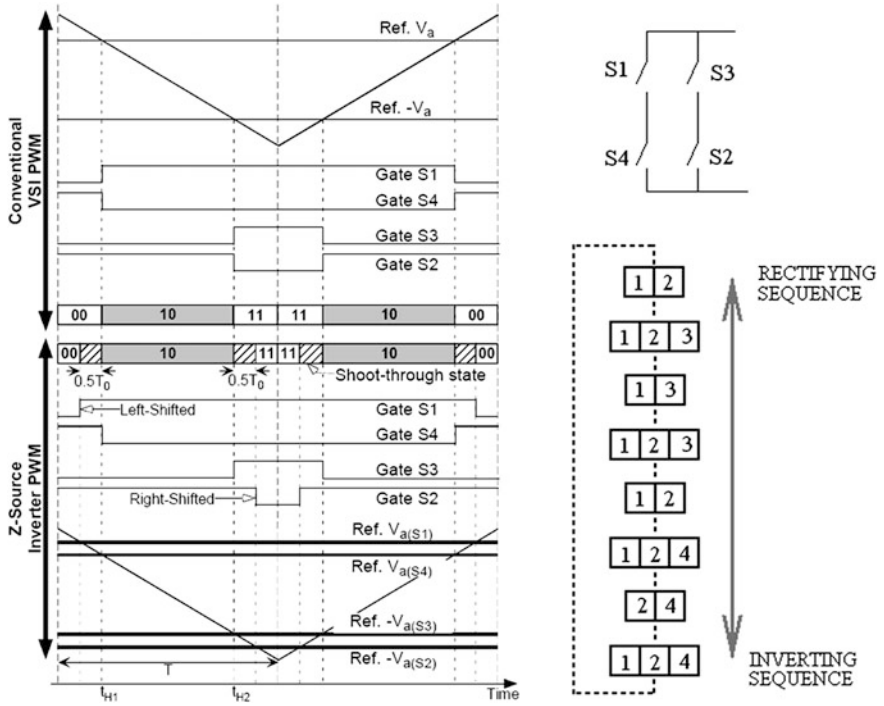

Fig. 8.23 Chosen switching sequence [27]

need to be simulated in order to estimate their power dissipation. Those on the Z-circuit side operate in ZVS, while those on the battery side are not active during charging, due to the conduction of the body diodes. It will be shown here that their loss is rather small. For example, for the FCB20N60 MOSFETs: $R_{ds,ON} = 0.15\ \Omega$, $E_{on} = 80\ \mu J$, $E_{off} = 40\ \mu J$ @ 1000 V. The RMS currents are calculated using Eqs. 6.3 and 6.4. For a battery current of 15 A, the total dissipation from all MOSFETs can be calculated at approximately 24 W. However, in the case being discussed here, the system does not include the EV battery. Hence, the dissipation is obviously zero.

$$Ib_{p(\mathrm{RMS})} = \frac{Ib}{2\sqrt{2}} \tag{8.6}$$

$$Ib_{s(\mathrm{AVG})} = \frac{Ib}{2} \tag{8.7}$$

Here, $I_{bp,\mathrm{RMS}}$ is the RMS current in the Z-circuit side MOSFETs (0.15 Ω) and $I_{bs,\mathrm{AVG}}$ is the average current in the battery side MOSFET body diodes (0.9 V on-state voltage, at 20 A).

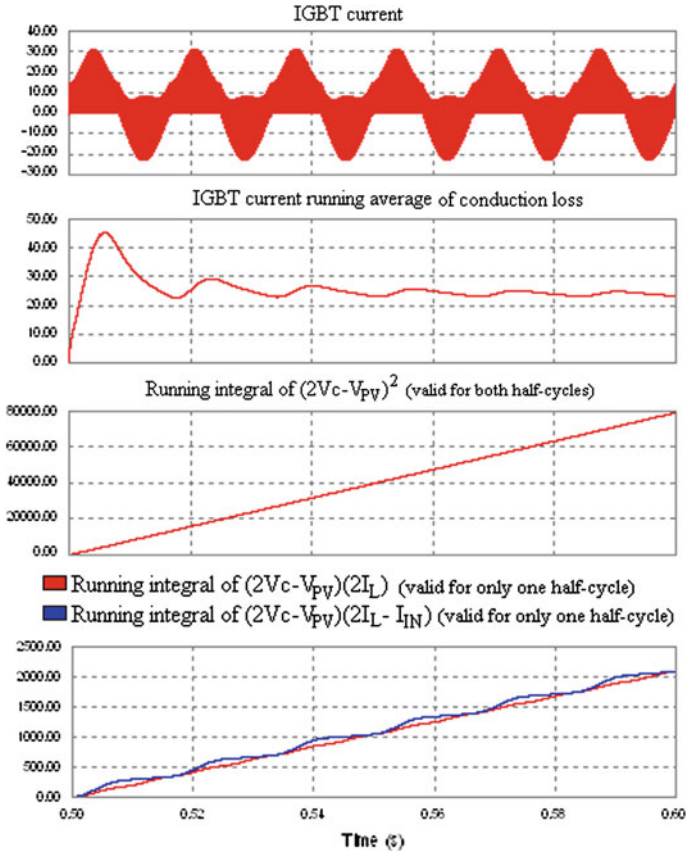

Fig. 8.24 Bridge IGBT power loss waveforms

Next, it is important to record the dissipations in the chokes and capacitors. These components possess high ESRs through design, because of damping requirements; the dissipations are expected to be high. Again PSIM is invoked to calculate RMS currents. From Fig. 6.12, the RMS currents in L, L_{IN}, and C can be estimated at 12.2, 15.3, and 9.8 A, respectively, corresponding to a total loss of 39.0 W.

The last critical component that needs to be considered is the 60 Hz isolation transformer. Again, if size and cost concerns are ignored, this component can be made arbitrarily efficient. Nevertheless, even when some compromises are made, due to real-world constraints, an efficiency of 98 % is reasonable for this part.

The final estimate of all losses treated above, for operation without the EV battery, can finally be completed. The losses amount to approximately 370 W of dissipation. Hence, the corresponding efficiency is estimated at 93.1 % (Table 8.4).

Table 8.4 Sample power loss mapping for Z-converter

Bridge IGBTs (W)	DC block IGBT (W)	Z-inductors (W)	Z-capacitors (W)	Input inductor (W)	Transformer (W)
213.2	17.1	8.9	23.0	7.0	100

Typical efficiency without battery: 93.1 % ($V_{IN} = 220$ V RMS; $V_{PV} = 430$ V) (Fig. 8.25).

The same PSIM-aided procedure described above can be applied to other significant simulations; the results for typical and worst-case operations with battery are reported below. However, more detailed numbers relative to all 4 power flow paths can be found in Appendix C. Note that efficiency is defined as the ratio of the sum of the powers delivered to the grid as well as to the battery to the power generated by the PV panel (Table 8.5).

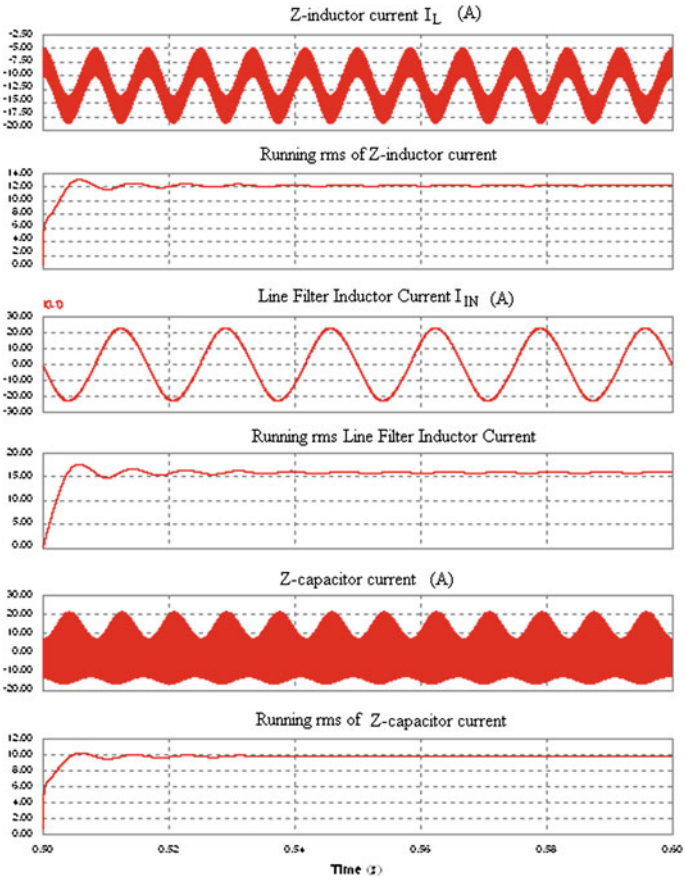

Fig. 8.25 RMS current estimation for inductors L, L_{IN}, and capacitor C

Table 8.5 Sample power loss mapping for Z-converter

Bridge IGBTs (W)	DC block IGBT (W)	Z-inductors (W)	Z-capacitors (W)	Input inductor (W)	Transformer (W)
188.0	16.5	3.6	19.5	1.8	50

Table 8.6 Sample power loss mapping for Z-converter

Bridge IGBTs (W)	DC block IGBT (W)	Z-inductors (W)	Z-capacitors	Input inductor (W)	Transformer (W)
308.0	19.3	12.4	35.8	10.1	100

Typical efficiency with battery: 94.7 % ($V_B = 330$ V, $V_{IN} = 220$ V RMS, $V_{PV} = 430$ V, $I_B = 7.5$ A).

Worst-case efficiency: 91.1 % ($V_B = 400$ V, $V_{IN} = 180$ V RMS, $V_{PV} = 360$ V, $I_B = 0$ A).

Note that worst-case condition is low input line and panel voltage, with power flow from panel to grid (Table 8.6).

8.9.7 *Efficiency Results for Alternate Z-Converter-Based Topology*

In view of the efficiency results, a different configuration for the Z-converter could be proposed. In fact, in related literature, the Z-converter has been acclaimed as an excellent method for obtaining buck-boost performance, for dealing with variable sources such as PV and fuel cells. Buck-boost operation is controlled by D and D_o and can, thus, be optimized. Instead, in the Z-converter configuration that was analyzed in this thesis, D_o was used in a novel fashion, for control of the EV battery current, so that it cannot be utilized for other purposes. For instance, this leads to the need for high-voltage devices in the inverter bridge that tend to be less-efficient than low-voltage devices. Consider the configuration evolution shown in Fig. 6.13. D_o is adjusted using Eqs. 5.1 and 5.2 to keep inverter input DC voltage below 600 V; this voltage being the threshold level for extremely efficient commercially available devices. On the other hand, the DC/DC converter in this new case is regulated, and thus, incurs higher losses, including switching loss and higher conduction losses, if MOSFETs are used. Moreover, a much larger smoothing inductor is needed, increasing the losses further. Thus, a popular controlled half-bridge, driven from a 430 V source using IGBTs, amounts to a nominal efficiency of 97 % (Fig. 8.26).

Then, in the case where the full power from the PV is directed to the battery, also 97 % will obviously be the total efficiency, constituting the best-case scenario. For comparison, two alternative operating regimes were simulated in PSIM, and

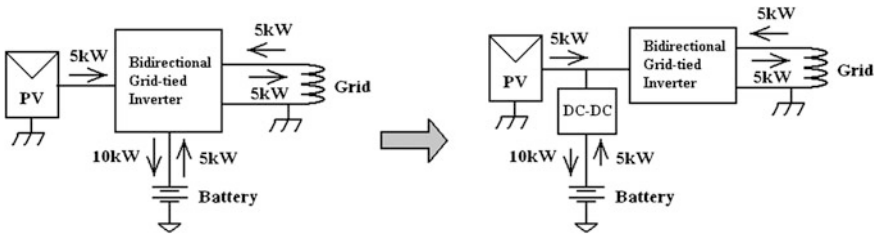

Fig. 8.26 Original (*left*) and alternate configuration (*right*) for Z-converter

the losses were evaluated. Note that, in this case, the choice for the transformer turns ratio is dictated by the ranges of the PV and grid voltage, the requirement of IGBT rated at less than 600 V, as well as the allowance for some dynamic range for control variable D. The new turns ratio is 1:0.94, compared to 1:1.333. The chosen devices are: IRG4PC40 W: On-state = 2.5 V @ 25 A, E_{on} = 170 μJ @ 600 V, E_{off} = 380 μJ @600 V, 25A; FCB20N60: $R_{ds,ON}$ = 0.15Ω, *E*on = 80 μJ, E_{off} = 40 μJ @ 1000 V; STTH15L06: On-state voltage = 1.0 V (Table 8.7).

Typical efficiency with battery: 95.7 % (V_B = 330 V, V_{IN} = 220 V RMS, V_{PV} = 430 V, I_B = 6 A) (Table 8.8).

Worst-case efficiency: 92.8 % (V_B = 400 V, V_{IN} = 180 V RMS, V_{PV} = 360 V, I_B = 0 A).

As can be seen, the alternate configuration can deliver efficiencies that are 1 % higher or more, at both nominal and worst-case operation. On the other hand, the use of 600 V devices is marginal and may not be possible in real systems. This is because D_o must still be partly modulated, to attenuate PV ripple in Scheme 1; this dynamic requirement imposes a minimum DC value of 0.1 on D_o, which pushes the minimum Z-capacitor voltage to nearly 560 V and the corresponding IGBT voltage to about 620 V. In addition, this topology cannot be considered "single-stage," and as such, requires additional control for EV battery charging as well as related driver circuits. Nevertheless, it was included briefly in this study, for comparison purposes.

Table 8.7 Sample power loss mapping for alternate Z-converter topology

Bridge (W)	DC IGBT (W)	Z-inductors (W)	Z-capacitors (W)	Input inductor (W)	DC–DC Conv. (W)	Transformer (W)
66.2.0	6.4	4.3	4.2	5.4	87.0	50

Table 8.8 Sample power loss mapping for alternate Z-converter topology

Bridge IGBTs (W)	DC block IGBT (W)	Z-inductors (W)	Z- capacitors	Input inductor (W)	Transformer (W)
205.0	16.4	18.2	22.1	26.3	100

8.10 Conclusion

Simulations confirm the mathematical model developed previously for the Z-converter (see Fig. 6.5), especially the relatively sluggish behavior of the battery current regulation loop in Scheme 1. Apart from this drawback, the converter performs satisfactorily, as expected. It was found that a mid-sized decoupling capacitor, in the order of 100 μF, is needed in Scheme 1, in order to eliminate the strong interaction with the PV I–V characteristics. However, this addition is rather small, and does not contradict the original cost and reliability premises. In Scheme 2, this capacitor must be much larger (about 1mF), in order to achieve the same MPPT performance. Because this is very likely to be an electrolytic capacitor, reliability and cost are affected.

The power losses were estimated directly (conduction losses) or indirectly (switching losses) through PSIM, following a simple method, and provide a fairly good idea of the overall efficiency, especially for comparison with other topologies. Even considering a worst-case number, and for a seldom used power flow path, the efficiency of about 91 % is somewhat disappointing for a single-stage topology. This can be attributed to the unavoidable use of high-voltage devices, with their poorer performance in terms of conduction and switching loss, as well as the presence of the 60 Hz transformer.

An alternate topology was briefly considered, to allow the use of more efficient, low-voltage devices. Indeed the efficiency can be improved by 1 % or so, but other technical difficulties arise.

8.11 High Frequency Transformer-Isolated Topology with DC-Link

The topology, as described in Sect 5.45.4, is rather uncomplicated. The dynamic behavior can be closely associated with that of the DC/DC buck converter, for the EV battery charger and voltage-fed inverter (another form of the buck converter), for the line conditioner. Because these are well known and loop compensation is straightforward, simulation results relating to the dynamic response will not be shown here. In fact, comparable results will be shown in Sect 6.3, when discussing the transformer-less topology, which is also based on the buck design; similar performance can be expected for the HF transformer-isolated topology.

The efficiency estimation for typical operation, based on the PSIM simulations, is summarized in Appendix C and Fig. 7.1. Although Table 8.9 reports that the worst-case condition for this topology includes the grid to EV battery power flow path, the reverse flow (battery to grid) is actually worse, by approximately a percentage point. However, this scenario is not considered, because this path can be considered atypical, or nearly anomalous. However, the heat sinks and power devices must be sized accordingly.

Table 8.9 Sample power loss mapping for HF transformer-isolated topology

Bridge IGBTs (W)	DC–DC IGBT (W)	Diodes (W)	Chopper IGBTs (W)	Inductors (W)	HF transformer (W)
145.6	172.3	0	0	57.9	50

Worst-case efficiency with battery: 92.1 % ($V_B = 275$ V, $V_{IN} = 180$ V RMS, $V_{PV} = 360$ V, $I_B = 18$ A).

The grid to battery path, quantified in Table 8.9, is a more critical path than the one corresponding to the worst case for the Z-converter. Hence, the Z-converter is better optimized for this application. However, the efficiency number itself is higher for the HF-isolated topology.

8.12 Transformer-Less Topology

As is the case for the HF transformer-isolated topology, no AC analysis is presented, due to the simple and thoroughly well-known transfer functions that can be expected from the buck converter. It will be proven that the transformer-less topology, comprising of two power conversion stages, provides a superior dynamic performance. Again, modeling and simulation results are also used to estimate losses. Note that the same bare-bone model for the PV panel, used in section IPV Ripple, PV Utilization Ratio, and MPPT, is also used here.

8.12.1 Dynamic Behavior

Figures 8.27 and 8.28 immediately confirm that the dynamic behavior is excellent, as expected.

Fast changes in commands (<0.1 sec) from the battery charger and the MPPT scheme, as well as the line voltage, are serviced cleanly and promptly by the control loops. As mentioned earlier, similar results can be expected for the HF transformer-isolated converter.

8.13 Efficiency

Typical efficiencies for all modes of operation are found in Fig. 7.1 and Appendix C. The worst-case condition is again grid to EV battery. However, the results are significantly better than the proposed alternatives (Table 8.10).

Worst-case efficiency with battery: 94.0 % ($V_B = 275$ V, $V_{IN} = 180$ V RMS, $V_{PV} = 360$ V, $I_B = 18$ A).

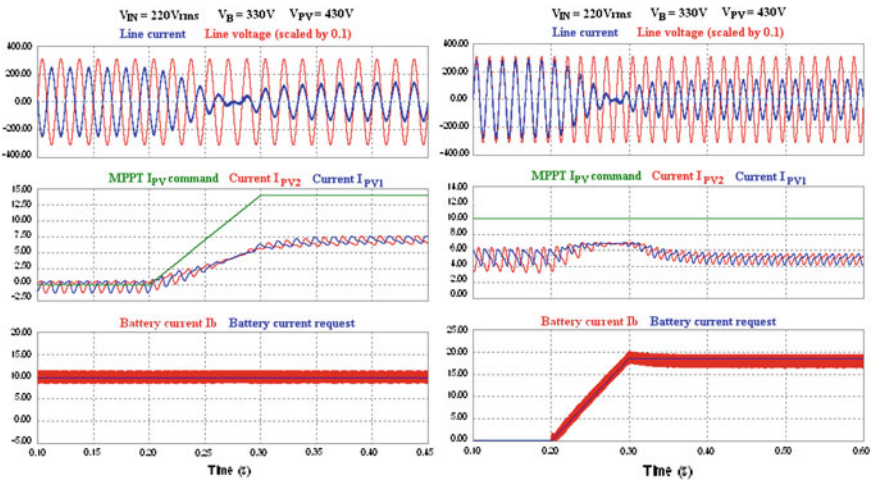

Fig. 8.27 System with battery; response to 100 % step of MPPT I_{PV} command (100 ms transition) (*left*); response to a ramp in I_B demand (100msec transition) (*right*)

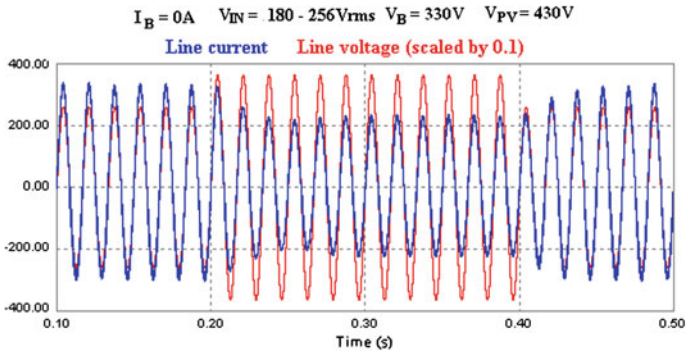

Fig. 8.28 System with battery; response to 40 % change in grid voltage

Table 8.10 Sample power loss mapping for the transformer-less topology

IGBTs (W)	DC–DC IGBT (W)	Diodes (W)	Transformer (W)	Inductors (W)
89.9	92.3	37.1	50	48.9

References

1. S. B. Kjaer, J. K. Pedersen, F. Blaabjerg, A review of single-phase grid-connected inverters for photovoltaic modules. IEEE **41**(5), 1292–1306 (2005)
2. F. Z. P. F. Z. Peng, M. S. M. Shen, K. Holland, Application of Z-source inverter for traction drive of fuel cellamp; mdash; battery hybrid electric vehicles. IEEE **22**(3), 1054–1061 (2007)
3. P. Fairley, Electric-car maker touts 10-minute fill-up. IEEE Spectr. (2007)
4. G. Carli, S. Williamson, On the elimination of pulsed output current in Z-loaded chargers/rectifiers, in *Applied Power Electronics Conference and Exposition*, pp. 1754–1760
5. F. Z. P. F. Z. Peng, Z-source inverter. IEEE **2**(2), 504–510 (2002)
6. M. S. M. Shen, F. Z. P. F. Z. Peng, Operation modes and characteristics of the Z-source inverter with small inductance or low power factor. IEEE Trans. Industr. Electron. **55**(1), 89–96 (2008)
7. X. Ding, Z. Qian, S. Yang, B. Cui, F. Z. Peng, A high-performance Z-source inverter operating with small inductor at wide-range load, in *Applied Power Electronics Conference and Exposition*, pp. 615–620
8. C. M. Wang, C. H. Su, M. C. Jiang, Y. C. Lin, A ZVS-PWM single-phase inverter using a simple ZVS-PWM commutation cell. IEEE Trans. Industr. Electron. **55**(2), 758–766 (2008)
9. Y.T. Tan, D.S. Kirschen, N. Jenkins, A model of PV generation suitable for stability analysis. IEEE Trans. Energy Convers. **19**(4), 748–755 (2004)
10. Y. Xue, L. Chang, S. B. Kjaer, J. Bordonau, T. Shimizu, Topologies of single-phase inverters for small distributed power generators: an overview. IEEE Trans. Power Electron. **19**(5), 1305–1314 (2004)
11. IEEE, *IEEE Standard for Interconnecting Distributed Resources with Electric Power Systems*. 2003, p. Std. 1547
12. R. Gonzalez, J. Lopez, P. Sanchis, E. Gubia, A. Ursua, L. Marroyo, *High-Efficiency Transformerless Single-phase Photovoltaic Inverter*. 2006
13. Z. Chen, X. Zhang, J. Pan, An integrated inverter for a single-phase single-stage grid-connected PV system based on Z-source. Bull. Pol. Acad. Sci. Tech. Sci. **55**(3), 263–272 (2007)
14. T. Esram, J.W. Kimball, P.T. Krein, T.L. Chapman, P. Midya, Dynamic maximum power point tracking of photovoltaic arrays using ripple correlation control. IEEE Trans. Power Electron. **21**(5), 1291–1292 (2006)
15. D. Casadei, S. Member, G. Grandi, C. Rossi, Single-phase single-stage photovoltaic generation system based on a ripple correlation control maximum power point tracking. IEEE Trans. Energy Convers. **21**(2), 7 (2006)
16. S.B. Kjaer, *Design and Control of an Inverter for Photovoltaic Applications* (Aalborg, Denmark, 2004)
17. J. Takesuye and S. Deuty, Introduction to insulated gate bipolar transistors

Chapter 9
EVs and PHEVs for Smart Grid Applications

9.1 Introduction

The challenge for the next few years is to reduce greenhouse gas (GHG) emissions from vehicles for global warming curtailment. GHG emissions are mainly due to internal combustion engines (ICE) used in transportation. To decrease this emission, a viable solution lies in using non-polluting electric vehicles. New transportation penetration has affected energy production in a major way. Energy production is already reaching peaks. At the same time, load demand has drastically increased. Hence, it has become imperative to increase daily energy production. It is well known that the world energy requirement is mainly catered by nuclear and thermal power plants, which are not environment friendly. There is a need to go for renewable energy sources that are both environment friendly and cheap at the same time. This chapter considers a control strategy including converter efficiencies, which consists of the local network, where the home is connected to renewable sources, in addition to the grid.

9.2 Vehicle-to-Grid and Grid-to-Vehicle Issues

There are several issues to be addressed in Vehicle to Grid (V2G) [1]. In this chapter, the Vehicle to Grid (V2G) power flow is more specifically called vehicle-to-home, V2H. When the home is supplied using an EV battery pack, household peak consumption can be reduced. Moreover, the EV battery can be charged during the night, when energy consumption is low.

The aim of the home control (HC) energy control (EC) Fig. 9.1 strategy is to process, which energy fits best for electrical consumption. There exists a choice between the renewable energy source, the grid, or the PHEV's battery. The choice depends on availability of renewable energy, the battery SoC of the battery, and grid cost operation. The first choice is, obviously, the renewable energy source, since its cost is zero. In case the available power from renewable energy sources

S. S. Williamson, *Energy Management Strategies for Electric and Plug-in Hybrid Electric Vehicles*, DOI: 10.1007/978-1-4614-7711-2_9,

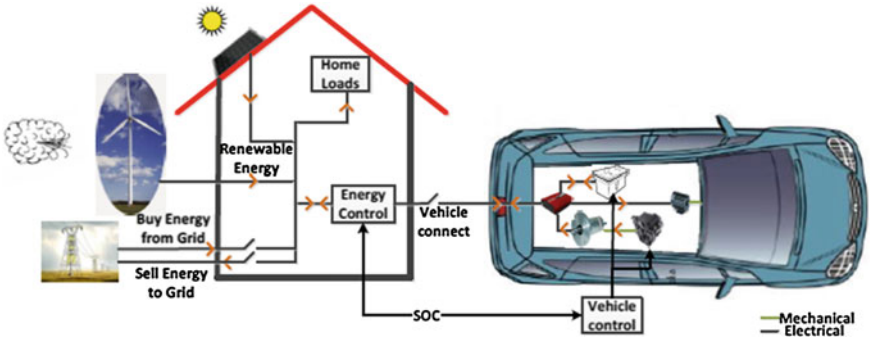

Fig. 9.1 Global diagram

falls short of the requirement, the controller has to select between the battery and the grid, based on the battery SoC as well as grid cost operation.

An optimization algorithm has been developed in the past by authors [2], using the dynamic programming technique developed by Sundstrom and Guzzella [3] to identify the most appropriate energy source from the available options. However, the system has two major concerns: the converter losses which include losses at every step of conversion and hence reduce the overall efficiency of the system, and the battery life cycle. In Sect. 3, the losses in each component of the converter is discussed and calculated. The battery life cycle is not discussed in this section, it will be discussed in detail in a future edition.

To make a more accurate choice, the controller must have knowledge of the exact amount of energy it can obtain from each of these sources. To determine the accurate amount of available power, the efficiencies of the power electronic converters have to be considered. Figure 9.2 shows the system configuration under study, along with the converters, which are essentially sources of losses.

Fig. 9.2 System diagram

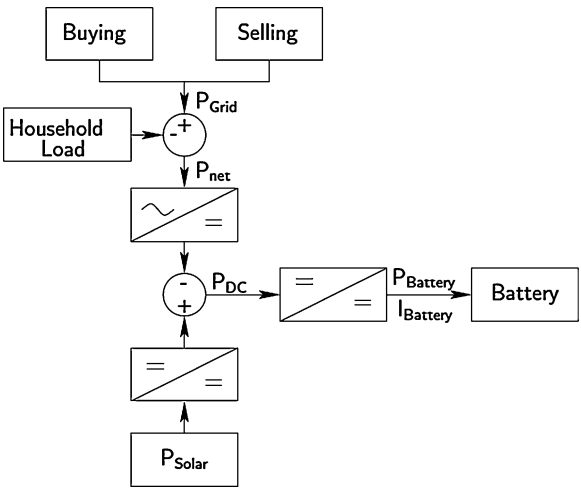

9.3 Ancillary Services from V2G

The PHEV's battery can be connected to home, either to charge the battery, or to transfer its energy to the home (V2H), depending upon its state-of-charge (SoC) and the energy requirements of the home load. The more recent electricity utility trend is to make use of electric, hybrid electric, and plug-in hybrid electric vehicles (EV, HEV, and PHEV) [4], for storage and/or production of energy (Fig. 9.1 [2]). Power conditioning efficiency values can typically be higher than 90 % [5]. EV/PHEV batteries can supply the electric motor of the vehicle, when it is not connected to the house. When the EV/PHEV is connected to the house, it can assist the supply grid for household loads. This power flow is called vehicle-to-grid, V2G.

9.4 Vehicle-to-Home and Home-to-Vehicle Concept

When the PHEV is connected to home, the battery can be charged either from the renewable energy source, or the grid, or both. This energy flow is called home-to-vehicle (H2V). The battery can also supply home loads, which in turn helps back-up the grid. This energy flow is called vehicle-to-home (V2H). When the PHEV is disconnected from home, the vehicle is propelled either by the battery, or the engine, or both.

9.5 Interconnection Requirements

9.5.1 Converter Losses Calculation

The converter efficiency depends upon several factors including the components used and switching frequency. Converter losses include conduction, blocking, and switching losses [1, 6–8]. The converters in the case are a bidirectional DC/DC converter, a unidirectional DC/DC converter, and an inverter. The conduction and switching losses in all the components are calculated separately and summed up to obtain the total losses. The efficiency is then calculated in (9.1)

$$\eta = \frac{\text{Input Power} - \sum(\text{Losses})}{\text{Input\_Power}} \tag{9.1}$$

9.5.1.1 IGBT Losses

IGBT losses is divided into two categories, conduction losses and switching losses.

Conduction losses: The conduction losses is determined by the equivalent IGBT diagram: voltage source in series with a resistance. The equation to calculate the conduction losses $P_{\text{conduction}}$ is given in (9.2) [1, 9]

$$P_{\text{conduction}} = F_{\text{sw}} \cdot \int_0^{\frac{1}{F_{\text{sw}}}} (V_s + R_{\text{on}} \cdot I_c) \cdot I_c \cdot dt \tag{9.2}$$

where

V_s Forward voltage drop (V)
R_{on} On state resistance (Ω)
I_c Collector current (A)
F_{sw} Switching frequency (Hz)

Switching losses: The switching losses can be calculated from the datasheet details as explained in [9]. First and foremost appropriate polynomial equation in Ic, for E_{on}, E_{off} and E_{rr} are obtained from the graphs provided in the datasheets (Fig. 9.3). This procedure includes noting down the values from the curves and then fitting a second order polynomial approximate equation by using a math tool, such as the Trendline tool in Microsoft ExcelR. Figure 3 shows the IGBT switching approximation giving the turn-on (E_{on}) and turn-off (E_{off}) IGBT energy and the diode reverse recovery energy Err plots. By using the Trendline tool,

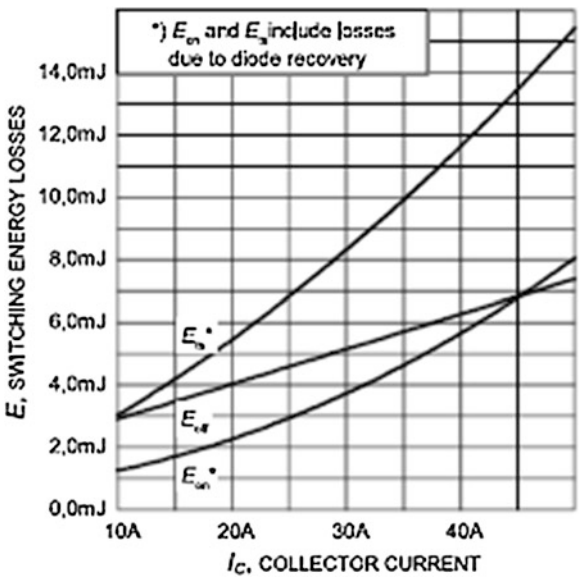

Fig. 9.3 IGBT datasheet

quadratic equations approximating the loss curves E_{on}, E_{off} andE_{rr} are obtained. For the IGBT [10] these equations are obtained as given below (9.3, 9.4 and 9.5)

$$E_{on} = 0.00218 \cdot I_c^2 + 0.041 \cdot I_c + 0.6105 \tag{9.3}$$

$$E_{off} = -8 \times 10^{-5} \cdot I_c^2 + 0.118 \cdot I_c + 1.7095 \tag{9.4}$$

$$E_{rr} = 0.0021 \cdot I_c^2 + 0.1659 \cdot I_c + 0.9329 \tag{9.5}$$

The switching losses fitted curves should be checked with the original curves to ensure they are close approximations. This checking is performed by placing the approximated curves obtained by mathematical tool on the same graph of the manufacturer datasheet.

9.5.1.2 Inductor Losses

This study includes the copper losses in the inductor [6] P_{induc} which is calculated as in (9.6).

$$P_{induc} = R_L\left(I^2 + \frac{\Delta I^2}{12}\right) \tag{9.6}$$

where
R_L Equivalent series inductor resistance ()
I Current through the inductor (A)
ΔI Ripple current

9.5.1.3 Diode Losses

The diode conduction losses are calculated as in (5)

$$P_D = R_D \cdot I_{on}^2 + V_D \cdot I_{on} \tag{9.7}$$

where
P_D Diode conduction losses (W)
I_{on} On state diode current (A)
R_D On state diode resistance (Ω)
V_D Diode voltage (V)

9.5.2 Converter Topology

9.5.2.1 DC/DC Converters

In this study basic DC/DC converters are used, a bidirectional converter with the topology as shown in Fig. 9.4: Bidirectional DC/DC Converter Fig. 9.4 and the other a buck converter with the topology as shown in Fig. 9.5: Buck converter

First, the efficiency is relating to the switching frequency. According to the following graph (Fig. 9.6), for both buck and boost converters, the maximum efficiency is obtained when the switching frequency is 40 kHz (Fig. 9.7).

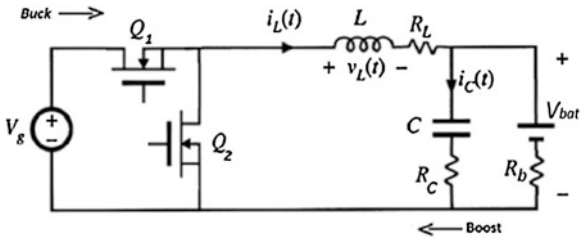

Fig. 9.4 Bidirectional DC/DC converter

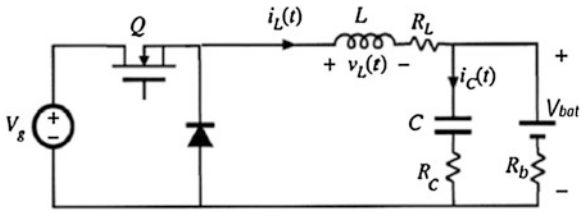

Fig. 9.5 Buck converter

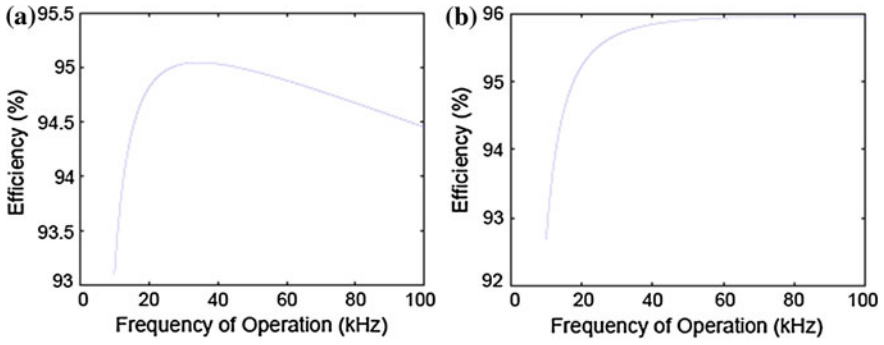

Fig. 9.6 Buck and Boost frequency characteristic (**a**) Boost frequency characteristic (**b**) Buck frequency characteristic

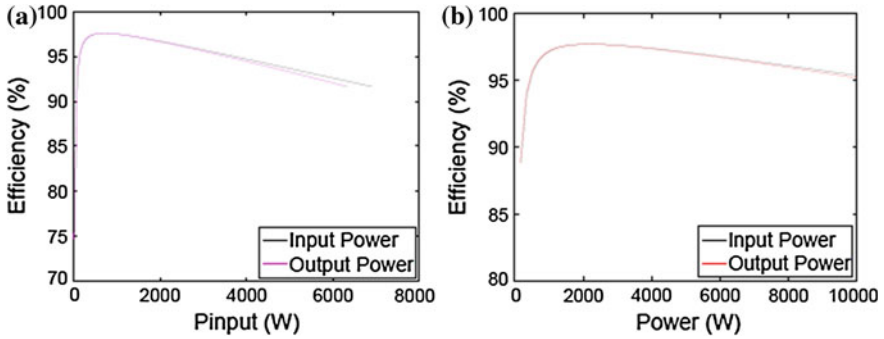

Fig. 9.7 Buck–Boost efficiency characteristic (**a**) Boost efficiency characteristic (**b**) Buck efficiency characteristic

Secondly, the boost mode should work between 500 and 1000 W (Fig. 9.7b), whereas the buck mode between 1000 and 3000 W (Fig. 9.7a) to have the best efficiency.

Curve fitting has been done for the efficiency curve for boost operation and the equation for the same is given in (9.8) and, similarly for buck operation, the equation is as given in (9.9).

$$\eta_{\text{boost}} = -0.0006739 \cdot P_{\text{in}} + 97.12 \tag{9.8}$$

$$\eta_{\text{buck}} = -0.001087.P_{\text{in}} + 89.83 \tag{9.9}$$

9.5.2.2 Inverter

The topology used is an H bridge inverter. The plot in Fig. 9.8 shows the optimum switching frequency that the inverter should work. In this case the switching frequency, at which the efficiency is maximum is 20 kHz. To use the best efficiency of this inverter, the input power should work between 250 and 500 W (Fig. 9.9).

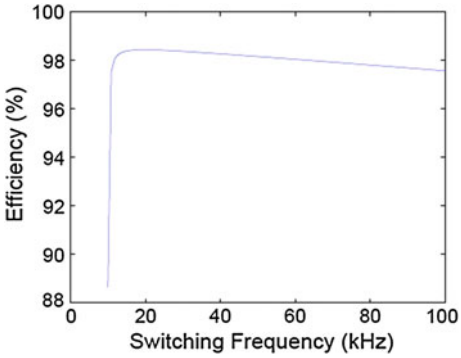

Fig. 9.8 Inverter frequency characteristic

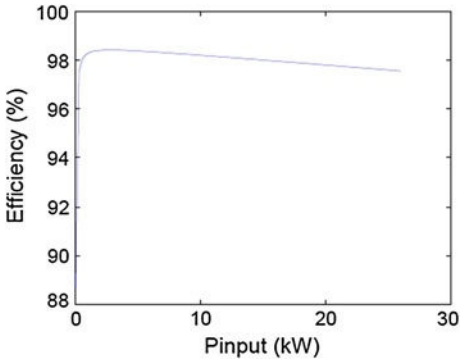

Fig. 9.9 Inverter efficiency characteristic

The curve fitting of the inverter is given in (9.10)

$$-1.066 \times 10^{-05} \cdot P_{\text{in}} + 98.1 \tag{9.10}$$

9.6 Study Case

This section describes the scenario used for testing the algorithm, including the fit equations of converters.

9.6.1 Scenario

The simulation starts at 6 AM in the morning and finishes at 6 AM the next day morning, considering a normal routine day. The schedule is given in Table 9.1. The driver goes for work at 8 AM and comes back home at 5 PM. The travel home to work is simulated by using the Japan 10–15 drive cycle (Fig. 9.10a) and the travel work to home is modeled by the reverse Japan 10–15 drive cycle (Fig. 9.10b). The vehicle battery size is 25 Ah.

In France, the grid on-peak and off-peak hours are defined as in Fig. 9.11; between 10 PM and 6 AM it is the off-peak period and the rest of the day it is on peak period (Fig. 9.11).

Table 9.1 Table schedule example

Hour of departure	Drive cycle
8	Japan drive cycle 10–15
17	Inverse Japan drive cycle 10–15

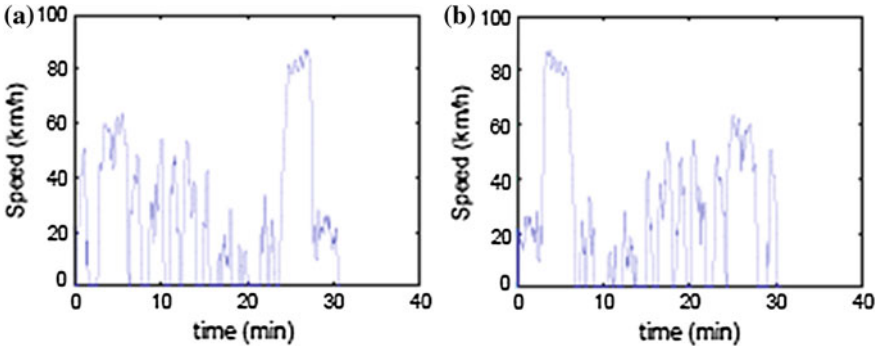

Fig. 9.10 Drive cycle **a** Japan 10–15 drive cycle (home to work) **b** Inverse Japan 10–15 drive cycle (home to work)

Fig. 9.11 Grid cost

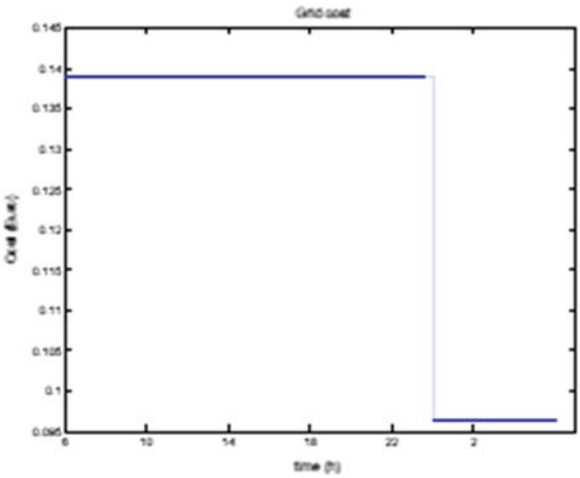

In Fig. 9.12a and b, the solar power and the household consumption respectively, which are used in this simulation are shown.

9.6.2 Results

The battery behavior shown in Fig. 9.13 describes the best behavior of a battery. Indeed, the battery discharges during the on-peak power, before the driver leaves home. Then, the battery continues to discharge from home to work; the vehicle does not use the ICE. Once the vehicle is parked there is no further change in the battery state. In this study the battery charging at business place is not considered. At the

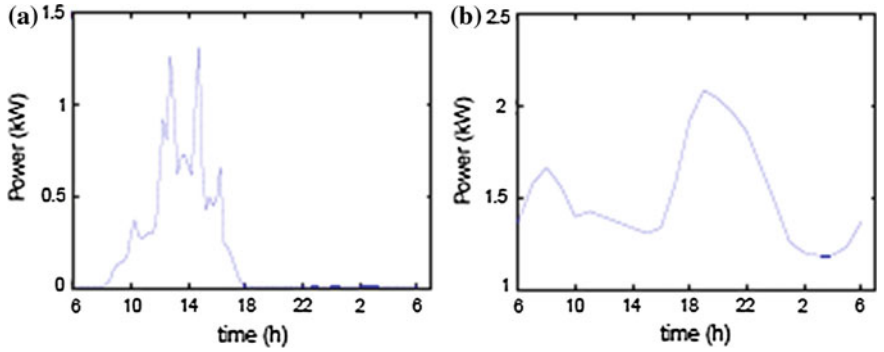

Fig. 9.12 Household production and consumption **a** Solar production **b** Household load production

Fig. 9.13 Battery state of charge

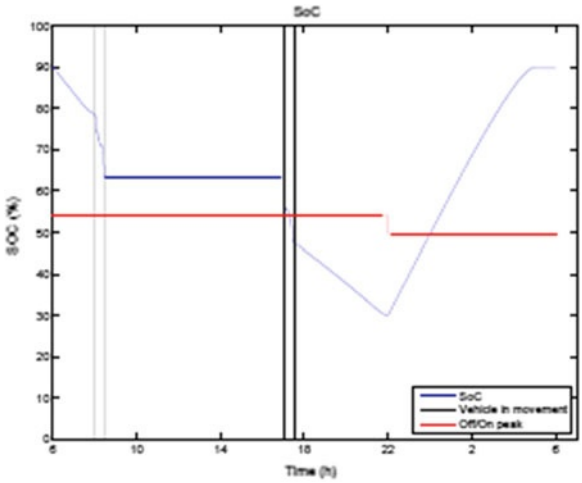

end of the business day, the driver comes back home and the battery is only used to propel the vehicle to home. Once back at home, the battery helps the grid to supply the household load until the off-peak hours start. During this time the battery is charged to prepare for the next day. To prepare for the next day, a constraint has been implemented in the optimization algorithm, that is, the initial SoC has to be the same as the final SoC. This constraint allows to have a repeatable system. From 10 PM to 6 AM, the grid energy is greater than the household consumption and the battery will be charged since it is off-peak power (Fig. 9.14).

In Fig. 9.15 the buck–boost converter, which is implemented between the Pdc and the vehicle battery (Fig. 9.2), the efficiency varies if the battery is supplying household load or if the battery is charging from the grid. In the boost mode the converter is working always around its maximum efficiency, whereas in the buck mode it is not always the case. To work at this efficiency allows to smooth the grid

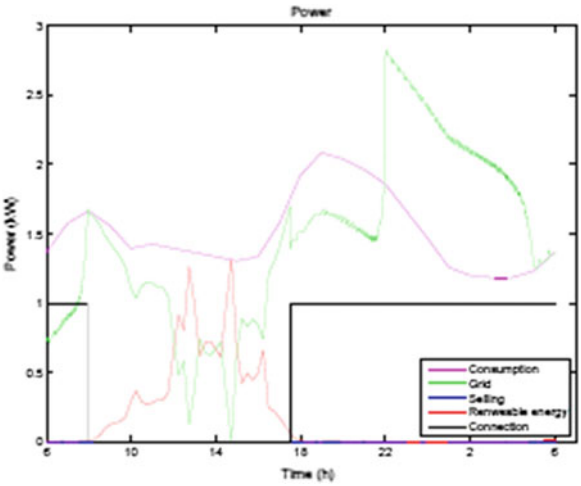

Fig. 9.14 Powers

power when the vehicle is charging. If the losses are not taken into account the control strategy can allow the converter to work at low power and that generates energy losses.

The other converter graphs do not play a significant role in the losses because they work always at the same efficiency.

9.7 Summary

The converter efficiency plays an important role in determining the exact amount of power available to the user. The efficiencies of various converters have been estimated by taking into consideration the non-idealities of the components of the respective converter.

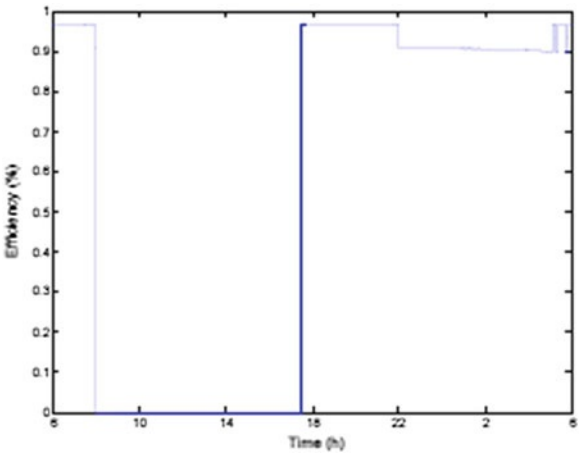

Fig. 9.15 Buck–Boost operation

The graphs and plots presented in this chapter correspond to basic converters. But the procedure can be adapted to any converter once the converter is chosen, since the losses calculation procedure or approach for each component of the converter remains the same. Moreover, to implement converter losses allows the grid power to be smooth and then uses a significant amount of energy from the electric grid.

This system has more losses than the regular system because of the step conversion. However the losses are less compared to the gain of reducing the peak power during the evening, when the vehicle helps the grid to supply household load.

References

1. D. Graovac, M. Purshel, IGBT power losses calculation using the data-sheet parameters (2009)
2. A.M.F. Berthold, B. Blunier, D. Bouquain, S. Williamson, Offline and online optimization of plug-in hybrid electric vehicle energy usage (home-to-vehicle and vehicle-to-home), in *IEEE Transportation Electrification Conference and Expo* (*ITEC*), pp. 1–6 (2012)
3. O. Sundstrom, L. Guzzella, A generic dynamic programming Matlab function, in *IEEE Control Applications CCA Intelligent Control ISIC*, pp. 1625–1630 (2009)
4. A. Emadi, K. Rajashekara, S.S. Williamson, S.M. Lukic, Topological overview of hybrid electric and fuel cell vehicular power system architectures and configurations. IEEE Trans. Veh. Technol. **54**(3), 763–770 (2005)
5. A. Emadi, S.S. Williamson, A. Khaligh, Power electronics intensive solutions for advanced electric, hybrid electric, and fuel cell vehicular power systems. IEEE Trans. Power Electron. **21**(3), 567–577 (2006)
6. A.M. Kabalo, D. Paire, B. Blunier, D. Bouquain, M.G. Simoes, A. Miraoui, Experimental validation of high-voltage-ratio low-inputcurrent- ripple converters for hybrid fuel cell supercapacitor systems, IEEE Trans. Veh. Technol. **61**(8), 3430–3440 (2012)
7. R. Modak, M.S. Baghini, A generic analytical model of switching characteristics for efficiency-oriented design and optimization of CMOS integrated buck converters, in Proceedings of *IEEE International Conference on Industrial Design*, Australia (2009)
8. S. Pam, R. Sheehan, S. Mukhopadhyay, Accurate loss model for DC–DC buck converter including non-linear driver output characteristics. in Applied Power Electronics Conference (APEC 2012), (Orlando, Florida, 2012), pp. 721–726
9. J. Pou, D. Osorno, J. Zaragoza, C. Jaen, S. Ceballos, Power losses calculation methodology to evaluate inverter efficiency in electrical vehicles. 7th International Conference on Workshop Compatibility and Power Electronics CPE'11, (Tallinn, Estonia, 2011), pp. 404–409
10. IGBT datasheet, TrenchStop IKW2RT120 (2008)

Chapter 10
EV and PHEV Well-to-Wheels Efficiency Analysis

10.1 Interest in Well-to-Wheels Efficiency Analysis

A major portion of current research in the automotive industry involves the study of the overall efficiency of advanced vehicular power trains. The improvement of overall energy efficiency is one of the most important subjects for developing hybrid electric, fuel cell, and battery electric vehicle (HEV, FCV, and BEV) technologies. This chapter aims at developing a basis for comparison of overall efficiencies of advanced vehicular topologies for the above-mentioned advanced vehicular systems. The main idea behind efficiency comparisons between HEVs and FCVs is the analysis of their respective well-to-tank (WTT) and tank-to-wheels (TTW) efficiencies, the product of which reveals the true well-to-wheels (WTW) efficiency, which is one of the deciding factors for market penetration [1]. Finally, the overall efficiency analysis performed in this chapter will lay down the foundation for a concrete conclusive comparison between advanced vehicular topologies of the future. The WTW efficiency analysis approach starts with the well, where the raw material is first extracted from the ground and ends with the power finally delivered to the wheels of the vehicle [1, 2]. This comprehensive comparison is essential in order to accurately and fairly compare the available future advanced automotive options.

As mentioned earlier, a complete WTW fuel cycle is used in the analysis of the advanced vehicular technologies. As shown in Fig. 10.1, this cycle includes raw material production, transportation and storage, fuel production, fuel transportation/storage/distribution, and finally the vehicle operations, useful work generated at the wheels, and the actual power delivered to the wheels [2]. This approach is essential for a fair comparison of future transportation options.

The main idea of this chapter is to present a comprehensive comparative analysis of HEV and FCV propulsion systems in order to determine the best future vehicular option in terms of WTW efficiency and greenhouse gas (GHG) emissions. In addition, a brief comparison from the point of view of performance parameters, such as acceleration and energy usage for advanced HEV and FCV systems, are presented. Through the simulation results presented in the latter

S. S. Williamson, *Energy Management Strategies for Electric and Plug-in Hybrid Electric Vehicles*, DOI: 10.1007/978-1-4614-7711-2_10,

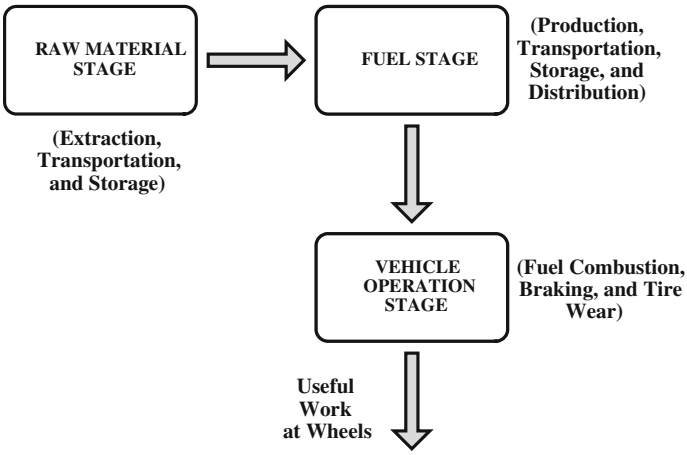

Fig. 10.1 Schematic diagram showing stages involved in complete WTW vehicular efficiency analysis

sections of this chapter, it will be clear that FCVs are not as highly efficient as their promoters claim them to be. In fact, under the current technological situation, HEVs seem to be a much more viable option at least for the next 10–20 years. Currently, FCVs are highly impractical and their operation is proven to be too expensive for the auto industry to consider commercialization.

Before considering the overall WTW efficiencies of the proposed HEV and FCV topologies, it is essential to form a concrete approach to perform the study aimed at in this chapter. This involves conducting a basic back-of-envelope TTW efficiency calculation for individual drive trains based on the products of the theoretically proven efficiencies of individual drive train components. The ensuing section of the paper presents the theoretical TTW efficiencies of conventional ICE vehicles and the proposed HEV and FCV drive train topologies.

10.2 Theoretical Efficiency Calculations for Advanced Vehicular Drive Trains

It is a well-known fact that on a theoretical average only about 20 % of the total fuel that is fed at the input of a conventional ICE based vehicle is available at the wheels as useful work. This is because of the extremely low efficiency of the engine and the overall losses in the vehicular drive train components. In the case of conventional vehicles, engines transform heat released in combustion into useful work that ultimately turns the vehicle's wheels enabling useful propulsion force [3, 4]. A basic diagrammatic representation of the theoretical TTW efficiency of a conventional ICE vehicle is shown in Fig. 10.2.

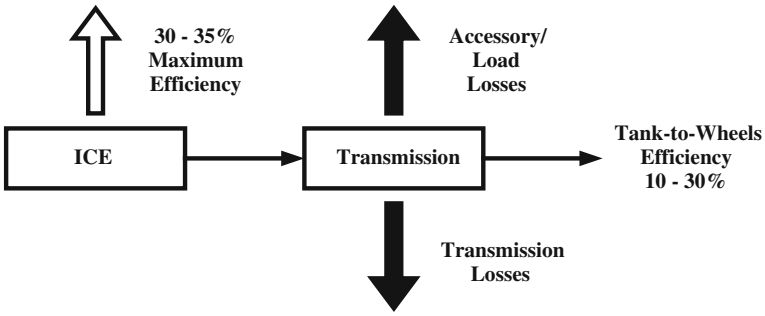

Fig. 10.2 Theoretical TTW efficiency of a typical gasoline engine vehicle

In order to compare the TTW efficiency of the ICE-based vehicular power train with those of the proposed HEV and FCV power trains, similar theoretical TTW efficiency calculations are performed. A diagrammatic representation of the theoretical efficiency calculation for a parallel HEV is shown in Fig. 10.3.

In case of a full HEV power train, the major advantage is that the ICE is mostly running at its optimal combination of speed and torque thereby, having a low fuel consumption and high efficiency. In addition, in a full hybrid vehicle, the size of the engine is much smaller (nearly 50 % of the size of its conventional counterpart). Besides, HEVs also possess the unique advantage of regenerative braking [3–5]. Figure 10.4 shows a pictorial representation a fuel cell hybrid vehicle (FCHV) with secondary energy storage battery system. A mean voltage efficiency of about 50 % is considered for proton exchange membrane (PEM) fuel cells, which are commonly proposed for automotive fuel cell traction applications.

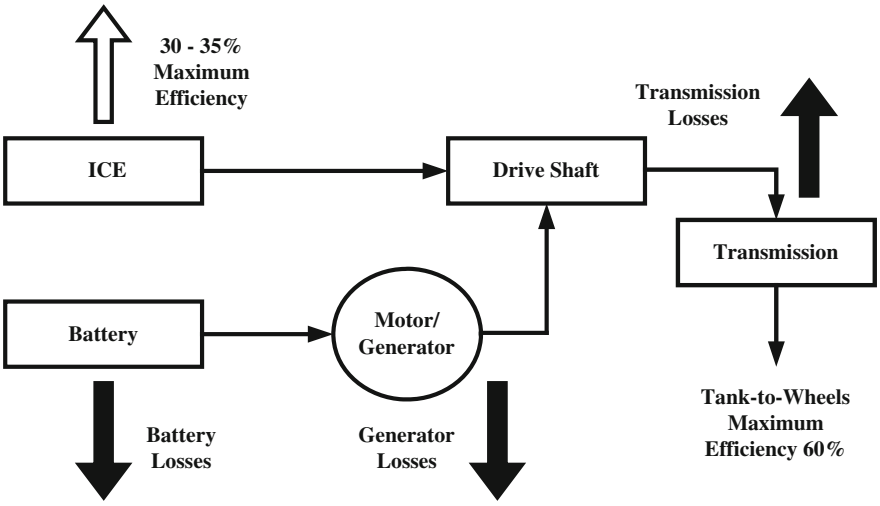

Fig. 10.3 Theoretical TTW efficiency of a typical gasoline fuelled parallel HEV power train

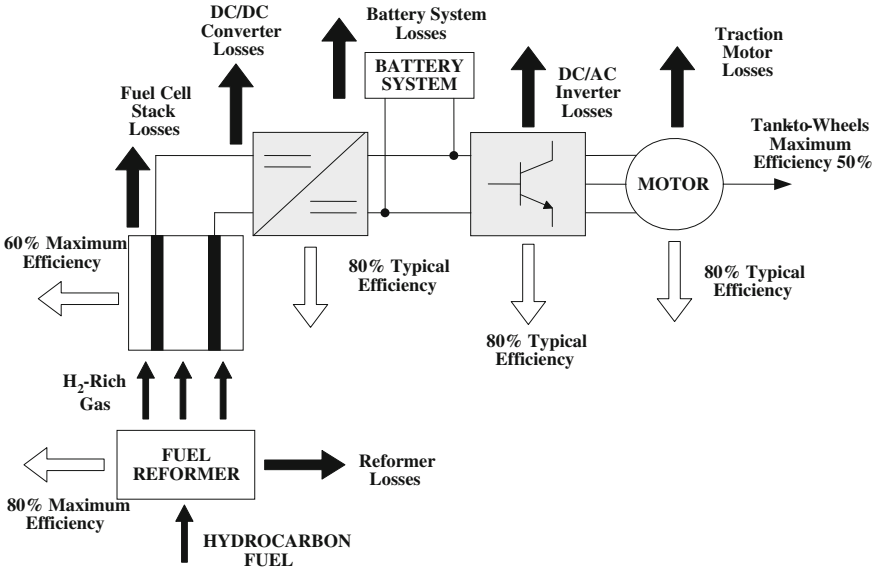

Fig. 10.4 Theoretical TTW efficiency of a typical FCHV drive train

Also, energy is always lost in the electric system between the fuel cell and wheels. The overall efficiency of the electric drive train in most cases depicts a maximum value in the range of about 85–90 % [6–10]. In the recent past, it has often been claimed that the power train of an FCV is highly efficient and that it can reach values as high as 60–70 %. However, when the overall system losses and ancillary subsystems necessary to make practical FCVs are taken into consideration, the actual efficiency reduces drastically from the popularly acclaimed 60–70 % to the order of a mere 30 % or an even lower. Unfortunately, for FCV promoters, these meager efficiency values do not even come close to those depicted by HEV power trains and at best happen to be only similar to those of some advanced gasoline (spark ignition, SI) and diesel (compression ignition, CI) engine-based vehicular systems.

For an FCHV, the overall TTW efficiency is higher (maximum value of about 50 %), as shown in Fig. 10.4. This TTW efficiency, which is higher due to the HEV concept applied to the FCV, is still less than that of gasoline or diesel-based HEVs. In order to prove the trend depicted by the above theoretical calculations, simulations were performed on a medium-sized sport utility vehicle (SUV) in the Advanced Vehicle Simulator (ADVISOR) software, the results of which are summarized in the following sections.

10.3 Simulation Setup for the Vehicle Under Study

For the purpose of TTW efficiency calculations, the ADVISOR software, developed by National Renewable Energy Laboratory (NREL), was used [11]. The vehicle chosen for the study was a typical medium sized sports-utility vehicle (SUV), which was simulated under city and highway drive cycles. For the city driving simulations, the vehicle was simulated for the urban dynamometer driving schedule (UDDS) drive cycle, whereas for the highway simulations, the vehicle was simulated for the highway fuel economy test (HWFET) drive cycle. A brief summary of the parametric description of the medium-sized SUV considered for simulation purposes is given in Table 10.1.

For the FCV power train simulations, the gasoline-based FCV/battery hybrid vehicle was considered since, as mentioned earlier, this arrangement is indeed the real-world option for FCV market penetration, as and when FCVs do become commercially available [12, 13]. The main reason that the auto industry is considering using the gasoline FCV hybrid arrangement is due to the major challenges faced by H_2 based FCVs, namely, insufficient fueling infrastructure, overcoming on-board H_2 storage issues, huge system start-up times, and extremely expensive equipment and accessories for fuel cell system operation. In a gasoline-based hybrid FCV, an on-board fuel reformer is required, which is normally used to obtain hydrogen from any hydrocarbon (hydrogen-rich) fuel [13–15]. It is worthwhile mentioning here that the above power train topologies were simulated for the TTW efficiency calculation for both, gasoline (spark ignition, SI) as well as diesel (compression ignition, CI) engines, the results of which are summarized in the ensuing sections.

10.4 Overall Efficiency Analysis Based on Simulation Results of the HEV and FCV Drive Train Architectures

The vehicle under study was run through the city (UDDS) and highway (HWFET) driving schedules. The results summarized in this section are for the simulations performed on both gasoline-based vehicles as well as diesel-based vehicles. Upon running the simulation for the city and highway driving schedules, the achieved fuel economies (miles per gallon, MPG–gasoline equivalent) are shown in Fig. 10.5.

Table 10.1 Physical specifications of the representative medium-sized SUV

Parameter	Value
Drag coefficient	0.4
Frontal area (m^2)	3.22
Vehicle length (m)	4.4
Vehicle width (m)	1.82
Vehicle height (m)	1.77
Wheelbase (m)	2.62
Total mass (kg)	2,050
Total propulsion power (kW)	170

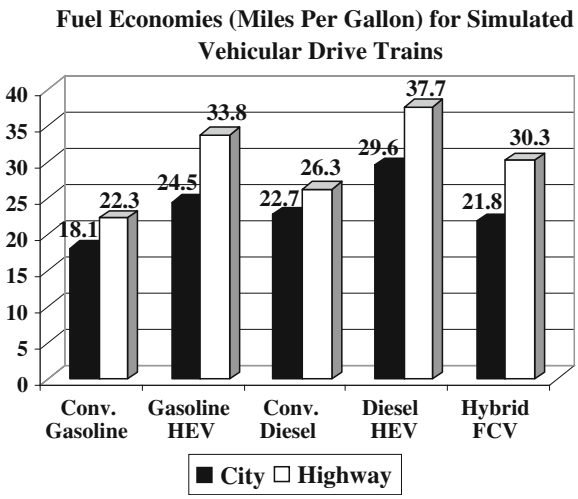

Fig. 10.5 Fuel economy comparison for city and highway driving

It is interesting to note here that the hybrid FCV topology depicts fuel economies almost similar to those depicted by a diesel or gasoline HEV. In fact as seen in Fig. 10.5, compared over the same driving pattern, the HEV is slightly more economical compared to the hybrid FCV. It must be noted that the HEV simulated here is more like a practical vehicle. If its hybridization factor (HF) were to be increased further, then it would depict even better fuel economies [15, 16].

Based on this theoretical background, the TTW efficiencies were also obtained upon simulation for city and highway driving cycles. Again, the TTW efficiencies of the vehicles show different values for city and highway driving schedules since, as mentioned earlier, the ICE works at higher efficiency regions when the vehicle is run on a high-speed highway drive cycle [17]. The TTW efficiencies for the gasoline HEV, diesel HEV, and gasoline hybrid FCV drive trains (city and highway) are shown in Fig. 10.6.

As shown in Fig. 10.6, there exists a clear difference of about 6–10 % in TTW efficiencies between the gasoline HEV and the hybrid FCV depending on driving conditions (city or highway). A much larger difference is obvious when considering TTW efficiencies of diesel HEVs, as is clear from Fig. 10.6.

Now, based on the simulation results for TTW efficiencies, it is possible to determine the actual WTW efficiencies for the advanced FCV and HEV drive trains, as shown in Fig. 10.7. It must be pointed out here that the results in Fig. 10.7 are plotted only for city driving.

As shown in Fig. 10.7, the true WTW efficiency for the hybrid FCV is lower than that of the gasoline and diesel HEVs. In fact, even the conventional diesel vehicle depicts a higher WTW efficiency than the hybrid FCV. Although fuel cell promoters have claimed that fuel cell systems depict efficiencies in the range of 50–60 %, it must be kept in mind that they usually refer to chemical-to-electric conversion efficiencies. However, for automotive applications, mechanical energy is required for propulsion and, hence, as is clear from the simulation results of Fig. 10.7, the

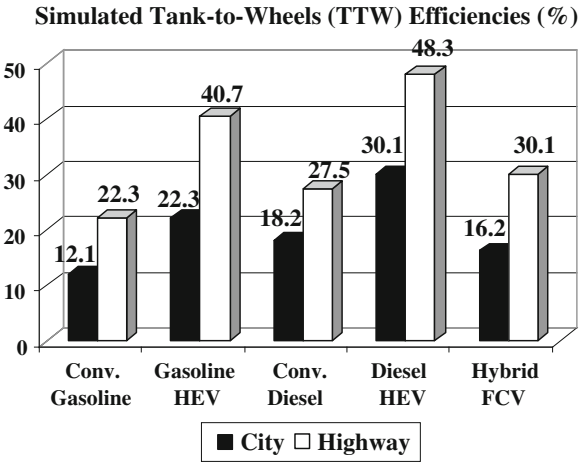

Fig. 10.6 TTW efficiencies for the simulated vehicles (city and highway)

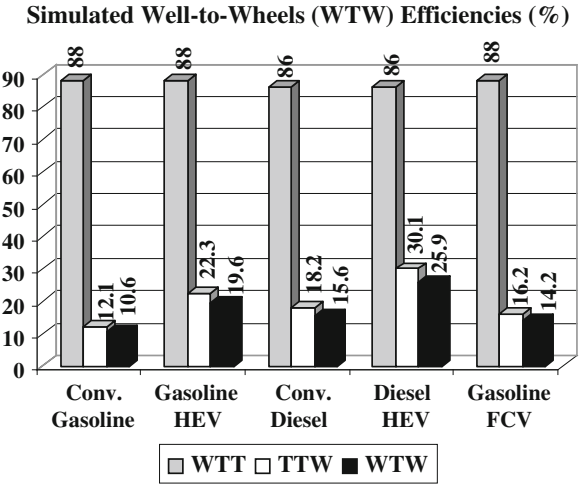

Fig. 10.7 WTW efficiencies for the simulated vehicles (city driving)

overall efficiency of a fuel cell-based propulsion system is extremely lower [18–20]. A further increase in TTW efficiency can be achieved in parallel HEVs by using a continuously varying transmission (CVT) system, instead of a fixed step transmission. With this technique, it is possible to choose the most efficient operating point for the ICE at given torque demands freely and continuously [19].

Simulation results (not presented here) with the usage of a CVT system show almost a 5 % gain in TTW efficiencies for the parallel HEV drive train. Thus, the TTW efficiency for a parallel HEV reaches 27.3 % in the city and 45.7 % for highway driving. This results in an overall WTW efficiency (considering only city driving) of about 24 %, which implies a major efficiency gain over the hybrid FCV. A direct implication of the overall WTW efficiencies of the above-mentioned advanced vehicular drive trains is the total energy that is used at both

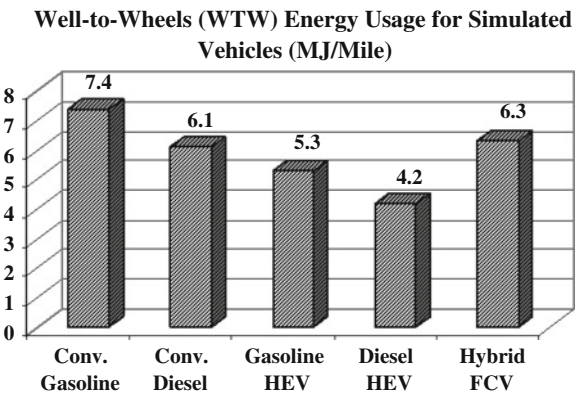

Fig. 10.8 WTW energy usage for the simulated vehicles (city driving)

stages, the WTT delivery of the fuel as well as TTW energy loss/usage, the sum of which in turn depicts the total WTW energy usage (in Million Joules/mile). The simulation results for the overall WTW energy usage for the various HEV and FCV power trains are shown in Fig. 10.8.

The critical observation in this case is that the WTW energy usage of the hybrid FCV (6.3 MJ/mile) is higher than that of both the diesel HEV (4.2 MJ/mile) as well as the gasoline HEV (5.3 MJ/mile) [16]. This study further emphasizes the fact that diesel HEV drive trains are better suited for SUV applications as compared to gasoline-based HEV drive trains. It is well understood thus far that the WTW efficiency plots for diesel HEVs maintain the same trend as those of gasoline-based vehicles, with the only difference being that the WTW values for the diesel-based HEV is almost 5–7 % higher than that of the gasoline-based HEV.

The benefits of newer compression-ignition direct-injection (CIDI) diesel engines are quite obvious. For diesel HEV applications, they offer about 10–15 % improvements in fuel economy compared to gasoline-based HEVs, thus, resulting in about 15–20 % average lower emissions [19, 20]. As far as the market for diesel HEVs is concerned, it is a well-known fact that diesel engines are dominant in the heavy-duty vehicle sector because of higher capabilities in terms of power, efficiency, durability, and reliability. The heavy-duty applications that would benefit most from the diesel HEV technology are those that are driven mostly in stop-and-go conditions, such as SUVs, pick-up and delivery trucks, and heavy-duty transit buses [20].

10.5 Acceleration Performance and Well-to-Wheels Greenhouse Gas Emissions for HEV and ECV Drive Trains

In order that the consumers of future advanced vehicles have a clear vision of performance capabilities, further simulations related to acceleration capabilities and GHG emissions were performed in addition to the efficiency calculations. The

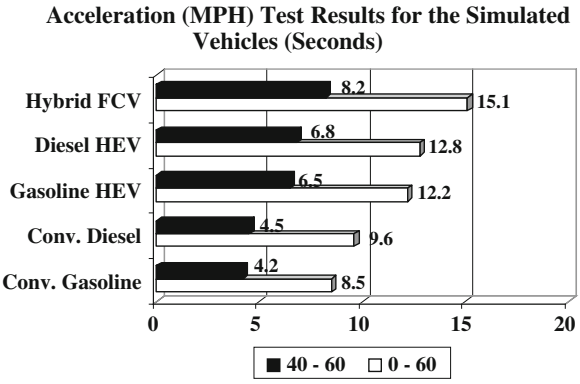

Fig. 10.9 Acceleration test results for different simulated vehicular drive trains

various acceleration capabilities based on the simulations performed on the different HEV and FCV drive trains are summarized in Fig. 10.9. Two sets of acceleration tests were aimed at; 0–60 and 40–60 m/h. Again, it must be kept in mind that the vehicle under study is a medium-sized SUV with a manual transmission. As is clear from the acceleration results of Fig. 10.9, hybrid FCVs are the slowest to accelerate amongst the proposed future vehicular technologies.

The parallel HEV can be driven with the ICE or the electric motor, or both at the same time and, hence, it is possible to choose the combination freely to feed the required amount of torque at any given time [20, 21]. This scenario is not true for the hybrid FCV due to the operational restriction on the fuel cell system. Thus, due to their inherent control flexibility, the acceleration performance of HEV drive trains is better than those of FCV drive trains.

Another major parameter that needs to be analyzed when considering the performance of advanced future automotive power trains is the overall WTW GHG emission analysis. Based on simulations done in the GREET model from ANL, the overall GHG emissions (g/mile) are summarized in Fig. 10.10.

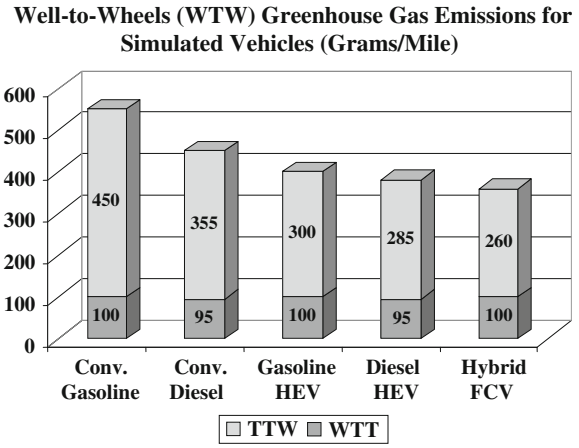

Fig. 10.10 WTW GHG emissions of the simulated vehicles (g/mile)

As is well hyped, promoters of FCVs claim that they are zero-emission vehicles, just like pure BEVs [21, 22]. However, this is not true from a WTW perspective, as seen in Fig. 10.10, which depicts GHG emissions of higher than 300 g/mile of driving for a hybrid FCV.

10.6 Prospective Future Work

One of the major uncertainties that remain to be concretely addressed with regard to HEV and FCV technologies is overall efficiency. As seen in the results presented in this chapter, in terms of TTW efficiency, the HEV easily scores over its FCV counterparts. In addition, addressed in the literature of this paper is the fact that the calculation of TTW efficiencies alone is not enough to evaluate the overall efficiency. For this purpose, the true WTW efficiency analysis needs to be done on a much more regular basis.

Based on the overall WTW results summarized here, the FCV option looks much less promising than its promoters often portray it to be. Based on the studies conducted in this paper, HEVs depict WTW efficiencies almost 1.5–2 times that of FCVs. Furthermore, it is clear that diesel HEVs look to be more promising for stop-and-go HEV applications, such as light trucks, SUVs, and transit buses. An interesting aspect from the point of view of future research would be to investigate the comparative WTW efficiencies of alternatively fuelled FCV and HEV topologies, whereby the fuelling options could include natural gas, methanol, and ethanol.

Considering the stage at which automotive technology stands at this point, commercial FCVs are not a clear feasible superior option given that they have a lower WTW efficiency than the gasoline and diesel HEV technologies. In addition, one of the most difficult issues in case of FCVs is their overall cost, including the cost of developing an infrastructure to support the distribution of hydrogen fuel. Another challenge faced by the hydrogen FCV is the energy storage. As a cryogenic liquid, hydrogen occupies nearly four times as much space as gasoline for the same amount of energy stored.

Although future research may provide solutions to the problems related to usage of FCVs as commercial vehicles, the technology is not yet ready for commercialization. Even if FCVs become practically available in the automotive market, as seen through the results in this paper, they are not efficient enough to compete with HEVs. Thus, it is safe to say that at least for the next decade, the HEV technology seems to be the most viable and sensible advanced automotive option from a technical and social point of view, as verified by the comprehensive analytical study conducted in this chapter.

References

1. A. Rousseau, P. Sharer, Comparing apples to apples: well-to-wheel analysis of current ICE and fuel cell vehicle technologies, in *SAE Technical Paper Series* p. 21 (2004)
2. F. Stodolsky, L. Gaines, C.L. Marshall, F. An, J.J. Eberhardt, Total fuel cycle impacts of advanced vehicles, in *SAE Technical Paper Series* **724**, (1999)
3. A. Emadi, M. Ehsani, J.M. Miller, *Vehicular Electric Power Systems: Land, Sea, Air, and Space Vehicles*. (Marcel Dekker, New York, 2010)
4. C. C. Chan, An overview of electric vehicle technology. IEEE Trans. Veh. Technol. 81(9), 1202–1213 (1993)
5. F. An, D. Santini, Assessing tank-to-wheels efficiencies of advanced technology vehicles, in *SAE World Congress and Exhibition,* Detroit, Michigan, United States, March 3, 2003
6. B. Min, R. Matthews, M. Douba, H. Ng, B. Larson, Direct measurement of power train component efficiencies for a light-duty vehicle with a CVT operating over a driving cycle in *SAE Powertrain and Fluid Systems Conference and Exhibition*
7. Z. Juda, Simulation of energy conversion in advanced automotive vehicles, in *Automotive and Transportation Technology Congress and Exhibition* (2011)
8. M. Brekken, E. Durbin, An analysis of the true efficiency of alternative vehicle power plants and alternative fuels, in *SAE International Spring Fuels and Lubricants Meeting and Expo* (1998)
9. U. Bossel, Efficiency of hydrogen fuel cell, diesel-SOFC-hybrid and battery electric vehicles. Eur. Fuel Cell Forum 1–4 (2003)
10. K. Rajashekara, Power conversion and control strategies for fuel cell vehicles. Paper presented in 29th annual conference of the IEEE industrial electronics society (2003) pp. 2865–2870
11. T. Markel, A. Brooker, T. Hendricks, V. Johnson, K. Kelly, B. Kramer, M. O'Keefe, S. Sprik, K. Wipke, ADVISOR: a systems analysis tool for advanced vehicle modeling. J. Power Source **110**(2), 255–266 (2002)
12. S. Williamson, A. Emadi, Fuel cell vehicles: opportunities and challenges, in *Power Engineering Society General Meeting*
13. T. Matsumoto, N. Watanabe, H. Sugiura, T. Ishikawa, Development of fuel-cell hybrid electric vehicle, in *SAE World Congress and Exhibition* (2002)
14. F. A. Wyczalek, Driving schedules influence electric and hybrid vehicle efficiency. Paper presented at the SAE 34th intersociety energy conversion engineering conference (1999)
15. F. Kreith, R. E. West, B.E. Isler, Efficiency of advanced ground transportation technologies. ASME J. Energy Res. Technol. **124**, 173–179 (2002)
16. J. Burns, T. Cors, B. Knight, B. Thelen, Evaluating advanced automotive energy technologies: a multivariate mobility contribution metric. Int. J. Energy Technol. Policy **2**(3), 262–271 (2004)
17. M.J. Atkins, C.R. Koch, A well-to-wheels comparison of several power train technologies, in *SAE World Congress and Exhibition* (2003)
18. M. Douba, H. Ng, R. Larson, Characterization and comparison of two hybrid electric vehicles (HEV)—Honda insight and toyota prius, in *SAE World Congress and Exhibition* (2001)
19. J. M. Tyrus, R. M. Long, M. Kramskaya, Y. Fertman, A. Emadi, Hybrid electric sport utility vehicles. IEEE Trans. Veh. Technol. **53**(5), 1607–1622 (2004)
20. I.J. Albert, E. Kahrimanovic, A. Emadi, Diesel sport utility vehicles with hybrid electric drive trains. IEEE Trans. Veh. Technol. **53**(4) (2004)
21. N. Imai, N. Takeda, and Y. Horii, Total efficiency of a hybrid electric vehicle. Paper presented at the IEEE power conversion conference (1997), pp. 947–950
22. U. Bossel, Well-to-wheels studies, heating values, and the energy conservation principle. Eur. Fuel Cell Forum (2003)